

Oleochemicals and cellulose nanocrystals in solvent-free coatings

by

Anna Magdalena Hubmann

A thesis submitted in partial fulfillment of the requirements for the degree of

Doctor of Philosophy

in

Bioresource Technology

Department of Agricultural, Food & Nutritional Science
University of Alberta

Abstract

Since prehistoric times, unsaturated plant oils, referred to as drying oils, have been used as a natural film forming material as result of oxidation-induced polymerization. Here, the use of oleochemical reactions and photo-chemistry to develop three coating systems with low volatile organic compound (VOC) emissions and up to 100% biobased content targeting improved drying time and durability is reported.

The ozonolysis of canola oil and linseed fatty acid methyl esters (FAME) produced compounds that were shown to be effective in directly adding to conjugated carbon-carbon double bonds resulting in faster polymerization. The drying time reduction effect was found to be strongly dependent on the concentration of ozonized lipids but not greatly influenced by the ozonolysis time or the lipid source. When used as a dual-use drying agent and reactive diluent in tung oil, ozonized linseed FAME demonstrated up to a 90% reduction in curing time and viscosity, which allows the replacement of up to 65% of the tung oil with a lower cost, locally sourced ozonized linseed oil. The addition of 5 wt% to 65 wt% of ozonized linseed FAME reduced the glass transition temperature (T_g) of the dried films by 2 °C to 49 °C. However, the T_g of dried films with 25 wt% of ozonized linseed FAME in tung oil reached that of a pure linseed oil film, suggesting a similar degree of cross-linking but with the benefit of faster polymerization and lower viscosity than either of the two pure oils. At the same time, a 100% biorenewable content and air-induced polymerization could be maintained.

While offering a biobased solution to significantly reducing the drying time of tung oil to 1 h at 60 °C, photo-induced polymerization is still a faster alternative. A drying oil analogue was developed from epoxidized linseed lipids with curing times of about 5 min under ultraviolet (UV) or solar irradiation, when photosensitized with curcumin. However, oxygen inhibition of this plant-based photosensitizer was found to limit cross-linking on wood and in thin films unless a tertiary amine was present to bind oxygen. Owing to the formation of ether cross-links at high conversion rates of the epoxy groups ($\geq 80\%$) during photoinduced poly-

merization, hydrolytic (abiotic and enzymatic) degradation compared to air-dried linseed oil was reduced by 20 % whilst maintaining a >93 % biorenewable content.

As a result of near-instantaneous polymerization in UV-curable coatings, polymerization stresses can build up and significantly reduce adhesive strength. Using a solvent-exchange approach, unmodified CNC could be kinetically stabilized in a photo-curable urethane-based prepolymer. The hydrogen bonding interactions between the coating components and CNC likely reduced internal stresses during UV-polymerization. At a loading level of only 0.3 wt %, this increased the adhesive strength by more than 150 % without sacrificing mechanical properties. The formation of a structured fluid also imparted thixotropic flow behavior that could prevent sagging of the resin prior to UV-curing.

In summary, this thesis demonstrates three new pathways to use plant biomass for performance improvement of solvent-free coatings with regards to drying time, viscosity, hydrolytic stability, and adhesive strength.

Preface

This work was carried out between 2015 and 2020 in the Lipid Chemistry Group (LCG) at the University of Alberta under the supervision of Prof. Jonathan M. Curtis. He assisted in manuscripts preparations and editions.

Chapter 2 resulted from an initial project funded by Phytola, an Alberta Innovates Bio Solutions centre based at the University of Alberta. The idea of using ozone to accelerate the curing of drying oils was initiated by Dr. Jonathan M. Curtis. The concept of using ozonized lipids as a drying agent was developed by Magdalena Hubmann. We would like to thank Ereddad Kharraz for the assistance in the experimental setup for lipid ozonolysis. We also acknowledge the support of Natural Sciences and Engineering Research Council of Canada (NSERC) through a Discovery Grant awarded to J.M. Curtis [RGPIN-2018-04602]. A manuscript has been submitted as "A biobased reactive accelerant and diluent for solvent-free drying oils" to Progress in Organic Coatings and has been accepted with subject to minor revisions.

Chapter 3 was developed from an initial interest of our group to better understand the (bio)degradation of plant-based epoxy materials. Magdalena Hubmann took this input as an opportunity to combine the study of photo-induced cationically cured epoxy coatings with the development of a drying oil alternative with improved durability. She developed the experimental design and performed the thermo-mechanical and gravimetric analyses, while elemental analysis of the obtained suspensions using inductively coupled plasma mass spectrometry (ICP-MS) to determine the extent of leaked photoinitiator products was performed by Dr. Konstantin von Gunten from the Alessi Research Group in the Department of Earth and Atmospheric Sciences, University of Alberta. A manuscript has been prepared for submission as "UV-curable epoxidized linseed lipids as a fast curing and more durable alternative to traditional linseed drying oils" to Progress in Organic Coatings.

Chapter 4 is collaborative work with Dr. Xiaohua Kong, a research associate at LCG at the time, and has been published as "Hubmann, Magdalena, Xiaohua Kong, and Jonathan M. Curtis. Kinetic stabilization of cellulose nanocrystals in a photocurable prepolymer for application as an adhesion promoter in UV-curable coatings. *Progress in Organic Coatings* 129 (2019): 101-115". The work is based on a proposal accepted as part of the CNC 2.0 Challenge by Alberta Innovates, submitted by Drs. Xiaohua Kong and Jonathan M. Curtis. We wish to express our gratitude for the generous funding obtained from Alberta Innovates to support early-stage work to investigate technical feasibility of CNC in applications with potential for

commercialization. Magdalena Hubmann was responsible for creating the experimental design, performing the experiments, and analyzing the data. During this process, the focus of the study was changed towards polymerization stress development and the impact of cellulose nanocrystals (CNC) on the resulting adhesion properties. We thank Rahn AG and IGM Resins USA Inc. for providing various samples of photoinitiators and reactive diluents. We would also like to thank Dr. Frederick R. van de Voort for his valuable inputs on how to interpret the FTIR spectra with regard to photopolymerization, Dr. Daniel S. Alessi for providing the ultrasonicator probe, and Emanuel Hubmann for the valuable inputs to interpret the SEM images of the fracture surfaces and internal stress development in the nanocomposites. This work was awarded with the RadTech Europe Advanced Development Award 2019.

This thesis is dedicated to all the amazing people who joined me on this journey. Thank you for always being there for me.

Acknowledgements

Firstly, I would like to express my sincere gratitude to my advisor Dr. Jonathan M. Curtis for the continuous support of my PhD study and related research, for his patience, motivation, and knowledge. His guidance helped me through all this time of research and writing of this thesis. Thank you for letting me dive into a new research area and explore opportunities to pursue our shared goal of developing more environmentally-friendly materials from locally sourced biomass. I also greatly appreciate the opportunity to present this research at multiple national and international conferences. The past five years have been an immense learning experience, not only through conducting research in a entirely new field, but also developing personally as an independent scientist.

Besides my advisor, I would like to thank the rest of my thesis committee: Drs. Feral Temelli and David Bressler, for their insightful comments and encouragement, but also for the hard question which inspired me to widen my research from various perspectives and to think critically about my research questions. It has been such a privilege to work with you.

A PhD is not a PhD without long nights in the lab or stimulating coffee breaks with colleagues. I want to thank my labmates, in particular Dr. Nuanyi Liang, Lucie Nečasová, Dr. Yuan Yuan Zhao, Savanna Won, Beiyi Shen, and Siew Meng Liew for all the fun we have had in the last five years despite how stressful some days were. It is one of best feelings to know that you can always count on your colleagues and I am so grateful for the around-the-clock support, as well as the many memories from our "extra-curricular" activities. Thank you, Dr. Mohammad Hossein Tavassoli Kafrani for all the help to get started with my PhD, and Ereddad Kharraz for the unlimited technical support in the lab. A big thanks also goes to Dr. Xiaohua Kong, who has been an important mentor and friend. Her knowledge in polymer chemistry has been so valuable and many of our intense discussions have resulted in solutions to some challenges I faced during this work. No matter how our lab-days went, we never forgot to smile and laugh, which truly made a difference every single day! Thank you!

I would also like to thank Drs. Anja Rutishauser and Kirk Scanlan for being amazing friends and supporters. In fact, I should be thanking the University of Alberta, as we probably wouldn't have met any time soon if it wasn't for them to offer all four of us an opportunity to do our PhD's here. You have been an inspiration as a couple, scientists, and outdoor enthusiasts.

To Evan Oxland and Alireza Farrokhi at Alberta Culture and Tourism, Government of Alberta, I would like to express my sincere gratitude for letting me help analyzing a million of paint layers from Hewko House at the Ukrainian Cultural Heritage Village in Edmonton, Alberta. Not only did I learn a lot about the history and application techniques of paints and finishes, the gained experience even helped me solve the issue of how to get reliable drying time data for drying oils using a drying time recorder (later parts in the thesis will be self-explanatory regarding the relevance of this finding). I also got an amazing opportunity to be awarded with APT Miami 2019 scholarship and present the results of our analyses at the conference. I would also like to thank Ron Anthony for being my official mentor for this conference and beyond. In the short period of time, I learned so much from you and look forward to keep swapping ideas and thoughts.

Canada has been such a welcoming country, and my husband and I feel so extremely grateful for all the opportunities and adventures we were given. We have not only pursued exciting careers but also met friends for life from outside of our "academic bubble". To our Russian crew - we are going to miss everything: dancing, partying, camping, and climbing the mountains. You have no idea how much your friendship helped with my thesis, whether it was for a much needed distraction, to celebrate small steps of success, or simply to boost energy and creativity.

However, I would have never gotten this far in my life without my family. I would like to thank my parents Katharina and Hanspeter, and my brother Emanuel for all the unconditional love, kindness, and support I have received.

This journey was intense. For every up and down I always knew that I was not alone but together with the best person I can imagine: Kostja. In the past 10 years, life gave us a couple of mountains to climb, but it's all about putting the boots on and starting the hike. Our PhD's have been a hard climb (more so for me than for you) but one never climbs a mountain so that people can see you but that one can see the world. We certainly did - the good and the not so good. We even managed to spend a total of four weeks in a rudimentary field station in the middle of the Brazilian Atlantic Rainforest and publish a scientific paper together about it. Even though we didn't end up having furry co-authors, at least we could acknowledge our two research stray dogs for their significant contribution to this project. Now it's time to open a new chapter in our lives. I hope we will continue to strive and explore the world, find joy, love, and value in what we do.

And before closing this section, my heartfelt gratitude goes to anyone who takes the time to have a look at this thesis. With my name as the author, I take all responsibility for the contents of this thesis. But for any potential value you will find, please remember how many people contributed to it in the one or other way. And I am so grateful for all these amazing people to exist and be a part of my life. Thank you all!

Contents

Abstract	ii
Preface	iv
Acknowledgements	vii
List of tables	xiv
List of figures	xvi
Nomenclature	xix
1 General introduction	1
1.1 Coating systems with low VOC emissions	2
1.1.1 Air-drying: drying oils	2
1.1.1.1 Overview of autoxidative polymerization	3
1.1.1.2 Yellowing	7
1.1.1.3 Derivatizations: plant oil-based, semi-synthetic coatings	8
1.1.1.4 Other natural and organic film forming materials used in traditional coatings and paints	8
1.1.2 Radiation curing: radical polymerization	8
1.1.2.1 Radical reactions	9
1.1.2.2 Radical photoinitiators	10
1.1.2.3 Oxygen inhibition	11
1.1.2.4 Effect of volumetric shrinkage on adhesion	12
1.1.3 Radiation curing: cationic polymerization	12
1.2 Lipid derivatization reactions for use in polymers	15
1.2.1 Transesterification	15
1.2.2 Epoxidation	15
1.2.3 Epoxy ring opening reaction to yield polyols	16

1.2.4	Polyurethanes	17
1.3	Cellulose nanocrystals	17
1.3.1	Dispersibility	18
1.4	Thesis outline	19
1.4.1	Project overview	19
1.4.1.1	Chapter 2	20
1.4.1.2	Chapter 3	20
1.4.1.3	Chapter 4	21
2	A biobased reactive accelerant and diluent for solvent-free drying oils	22
2.1	Introduction	22
2.2	Materials and methods	26
2.2.1	Materials	26
2.2.2	Methods	26
2.2.2.1	Ozonolysis reaction	26
2.2.2.2	Attenuated total reflectance Fourier transform infrared spectroscopy	27
2.2.2.3	Gel permeation chromatography	28
2.2.2.4	Decomposition enthalpy	28
2.2.2.5	Dry-through time determination	28
2.2.2.6	Viscosity determination	29
2.2.2.7	Modulated differential scanning calorimetry	29
2.2.2.8	Experimental design and statistical analysis	29
2.2.2.9	Preparation of the model nanocomposites	30
2.3	Results and discussion	31
2.3.1	Drying agent synthesis and analysis	31
2.3.1.1	Decomposition enthalpy	32
2.3.2	Systematic drying agent performance analysis in tung oil	33
2.3.2.1	Viscosity reduction	33
2.3.2.2	Drying time reduction	35
2.3.2.3	Effect on the glass transition temperature	38
2.3.3	Performance beyond the Box-Behnken design boundaries	40
2.3.3.1	Effect on tung oil at room temperature	40
2.3.3.2	Use of higher concentrations of ozonized lipids in tung oil	40
2.4	Outlook and future work	42
2.4.1	Dispersion of CNC and formation of bionanocomposites	42
2.5	Conclusion	44
3	Epoxidized linseed lipids as a durable and fast-curing alternative to drying oils	45
3.1	Introduction	45
3.2	Materials and methods	48

3.2.1	Materials	48
3.2.2	Methods	48
3.2.2.1	Central composite experimental design	48
3.2.2.2	Resin rheology	49
3.2.2.3	Film preparation and curing	49
3.2.2.4	Epoxy conversion	50
3.2.2.5	Film properties	50
3.2.2.6	Hydrolytic stability	51
3.2.2.7	Desirability assessment	52
3.2.2.8	Preliminary suitability assessment of curcumin-sensitized solar curing	53
3.2.2.9	Scanning electron microscopy	54
3.2.2.10	Additional tests	54
3.3	Results and discussion	54
3.3.1	Central composite experimental design	54
3.3.2	Resin rheology	54
3.3.3	UV-curing kinetics	54
3.3.4	Glass transition temperature and pencil hardness	58
3.3.5	TABER abrasion resistance	59
3.3.6	Hydrolytic stability	60
3.3.7	Desirability assessment	63
3.3.8	Preliminary suitability assessment of curcumin-sensitized solar curing	64
3.4	Conclusion	64
4	Low concentration CNC as an adhesion promoter in a UV-curable coating	66
4.1	Introduction	66
4.2	Materials and methods	70
4.2.1	Materials	70
4.2.2	Methods	70
4.2.2.1	Polyol-CNC suspension	70
4.2.2.2	Prepolymer synthesis and characterization	71
4.2.2.3	Photocurable nanodispersion	73
4.2.2.4	CNC-matrix interaction	74
4.2.2.5	Statistical analyses	75
4.3	Results and discussion	76
4.3.1	Prepolymer synthesis	76
4.3.1.1	ATR-FTIR monitoring of the grafting reaction	76
4.3.1.2	Molecular size distribution analysis by GPC	78
4.3.1.3	Prepolymer viscosity	78
4.3.2	Photocurable nanodispersion	79
4.3.2.1	Resin viscosity	79

4.3.3	CNC-matrix interaction	80
4.3.3.1	Modulated dynamic scanning calorimetry	80
4.3.3.2	Tensile properties	80
4.3.3.3	Abrasion resistance	83
4.3.3.4	Pull-off adhesion strength	83
4.4	Conclusions	86
5	General conclusion	87
5.1	Three new low-emission coating systems	87
5.1.1	A fully biobased reactive accelerant and diluent for drying oils	87
5.1.2	Epoxidized lipids as a durable and fast-curing alternative to drying oils	88
5.1.3	Biobased nanotechnology for improved adhesion of UV-cured coatings	89
5.2	Potential implications on coating sustainability	91
5.2.1	Emissions	91
5.2.2	Recyclability	91
5.2.3	Leaking of non-volatiles	92
5.3	Summary	93
A	Appendix Chapter 2	117
A.1	Materials and methods	117
A.1.1	Methods	117
A.1.1.1	Demonstration of penetration and film appearance on wood	117
A.2	Results and discussion	118
A.2.1	Drying agent synthesis	118
A.2.2	Systematic drying agent performance analysis in tung oil	118
A.2.2.1	Results from the drying time recorder	118
A.2.2.2	Effect of the drying agent on the kinetics of tung oil drying	119
A.2.2.3	Structural and chemical changes after film formation	122
A.2.3	Control experiments in cold-pressed linseed oil	122
A.2.4	Performance beyond the Box-Behnken design boundaries	126
A.2.4.1	Effect on tung oil at room temperature	126
A.2.5	Demonstration of penetration and film appearance on wood	127
A.2.6	Statistics	128
A.2.6.1	Box-Behnken Design	128
A.2.6.2	Independent <i>t</i> -tests	136
B	Appendix Chapter 3	139
B.1	Materials and methods	139
B.1.1	Materials	139
B.1.2	Methods	139

B.1.2.1	Identification of the metal drier in boiled linseed oil	139
B.1.2.2	ECOSAR ecotoxicity characterization	140
B.1.2.3	UV-VIS spectroscopy	140
B.1.2.4	Hot and cold check resistance	140
B.1.2.5	Effect of household chemicals	140
B.2	Results and discussion	140
B.2.1	Boiled linseed oil digestion	140
B.2.2	ECOSAR ecotoxicity characterization	141
B.2.3	UV-VIS spectroscopy	143
B.2.4	Preliminary suitability assessment of curcumin-sensitized solar curing	143
B.2.5	Hot and cold check resistance	144
B.2.6	Effect of household chemicals	144
B.2.7	Statistics	146
B.2.7.1	Data transformation	146
B.2.7.2	Model accuracy and selection	146
B.2.7.3	Regression coefficients and derived models	147
B.2.7.4	Diagnostic plots	150
B.2.7.5	Pairwise comparison of means	152
C	Appendix Chapter 4	154
C.1	Results and discussion	154
C.1.1	Prestudy: photopolymerization kinetics and oxygen inhibition	154
C.1.2	CNC-matrix interaction	158
C.1.3	Statistics	158
C.1.3.1	Levene's Test	158
C.1.3.2	Pair-wise comparisons	159

List of tables

1.1	Fatty acid composition of the most common drying oils.	3
2.1	Overview of common metal driers used in drying oils.	24
2.2	Box-Behnken design for Chapter 2.	30
3.1	Central composite design matrix of the parameters and levels tested.	50
3.2	Desired range for the responses considered for estimating the overall desirability.	52
4.1	Review of selected properties of UV-nanocomposites reinforced with CNC.	69
4.2	Overview of the used photoinitiators.	70
4.3	Resin formulation for the CNC-reinforced model coating system.	73
4.4	Wear index and effect of CNC.	84
A.1	Adequacy of different models to fit the data for the drying time.	129
A.2	Adequacy of different models to fit the data for the viscosity.	129
A.3	Adequacy of different models to fit the data for T_g	130
A.4	Coded coefficients for the linear model with squares to fit the drying time data.	131
A.5	Coded coefficients for the linear model with interactions to fit the viscosity data.	131
A.6	Coded coefficients for the linear model to fit the T_g data.	132
A.7	ANOVA of the dry-through time data.	132
A.8	ANOVA of the viscosity data.	133
A.9	ANOVA of the T_g data.	133
A.10	Pair-wise two-tailed independent t -test for the decomposition enthalpy (ΔH_{dec}).	137
A.11	Pairwise two-tailed independent t -test for the peak decomposition temperature.	138
B.1	Composition of metal elements in the boiled linseed oil resin ($n = 2$).	141
B.2	Ecotoxicological characterization of the used photoinitiator using ECOSAR.	142
B.3	Test report for the resistance to household liquids.	145
B.4	Test statistics for the different models to fit the rate constant k (first-order reaction).	146
B.5	Test statistics for the different models to fit the final conversion.	146
B.6	Test statistics for the different models to fit the T_g	146

B.7	Lack of fit test for the modelling the rate constant k (first-order).	147
B.8	Lack of fit test for the modelling the final conversion.	147
B.9	Lack of fit test for the modelling the T_g .	147
B.10	Coded coefficients for the linear model with squares to fit the data of the rate constant k .	148
B.11	ANOVA for the linear model to fit the rate constant k (first-order).	148
B.12	Coded coefficients for the linear model with squares to fit the final conversion data.	148
B.13	ANOVA for the linear model to fit the final conversion.	149
B.14	Coded coefficients for the linear model with squares to fit the T_g data.	149
B.15	ANOVA for the linear model with squares to fit the T_g .	149
B.16	Bonferroni test statistics for the pairwise comparison of the mean total wear index.	152
B.17	Bonferroni test statistics to study the curing time dependence on the curcumin concentration.	152
B.18	Bonferroni test statistics to study the curing time dependence on film thickness.	153
C.1	Levene's test statistics for different analyses of the nanocomposites.	158
C.2	Pair-wise comparisons for different analyses of the nanocomposites.	159

List of figures

1.1	Overview of the global coating market segments and the main raw materials (2017).	2
1.2	Simplified mechanism of the autoxidative polymerization of drying oils.	4
1.3	Illustration of secondary and tertiary radicals, and the effect of hybridization.	10
1.4	Relationship between polymerization shrinkage and stress development.	13
1.5	Illustration of hydrogen bonding in CNC and particle configuration in the dry and liquid state.	18
1.6	Radiation- and air-curable coatings and common problem areas.	19
1.7	Biomass use and polymer systems studied in the three thesis projects.	20
2.1	Schematic overview of Chapter 2.	25
2.2	Simplified process flow diagram for Chapter 2.	27
2.3	Scheme of the apparatus used for the ozonolysis.	28
2.4	Monitoring of drying agent synthesis by ATR-FTIR and GPC.	31
2.5	Decomposition enthalpy and temperature of peak decomposition.	33
2.6	Scatter plot of response variables and trend of reduced viscosity/drying time.	34
2.7	Response surface plots and effect sizes.	34
2.8	ATR-FTIR analysis of the drying kinetics at 60 °C of pure tung oil and with ozonized lipids.	36
2.9	TGA monitoring of film weight change during drying and evolution of the T_g over 24 h.	39
2.10	PCA analysis to study the differences in top and bottom film surfaces' chemistry.	40
2.11	Effect of using higher concentrations of FAME _{oz,20min} and 95 % prediction bands.	41
2.12	Effect of CNC on rheological properties and T_g	43
3.1	Schematic overview of Chapter 3.	47
3.2	Chemical structure of the cationic photoinitiator Silcolease UV Cata 243 (CAS 1115251-57-4).	48
3.3	Simplified process flow diagram for Chapter 3.	49
3.4	Epoxy resin viscosity dependence on the ELOME:ELO ratio	55
3.5	Selected epoxy group conversion profiles.	56
3.6	Rate constant k dependence on the photoinitiator concentration and the ELOME:ELO ratio.	57
3.7	DSC analysis and pencil hardness in comparison to dried films of boiled linseed oil.	58
3.8	T_g dependence on the photoinitiator concentration and the ELOME:ELO ratio.	59
3.9	Comparison of wear resistance of air-dried films of boiled linseed oil and the epoxy resin.	60

3.10	Gravimetric monitoring of hydrolytic film stability and leaching of driers and photoinitiators.	61
3.11	Overall desirability plot based on the ELOME:ELO ratio and photoinitiator concentration.	63
3.12	Solar drying time dependence on curcumin concentration and film thickness.	65
4.1	Schematic overview of Chapter 4.	67
4.2	Simplified process flow diagram for Chapter 4.	71
4.3	Experimental setup for the prepolymer synthesis.	72
4.4	Chemical structure of the polyol and the grafting reaction with TMI.	72
4.5	Photographs of the produced CNC suspensions.	75
4.6	Calculated isocyanate conversion during prepolymer synthesis.	76
4.7	ATR-FTIR analysis of the prepolymer and suspensions with CNC to study hydrogen-bonding.	77
4.8	GPC traces of the polyol and prepolymer obtained through grafting with TMI.	78
4.10	Dependence of T_g and stress-strain curves on the CNC concentration.	81
4.11	Effect of CNC on selected tensile properties.	82
4.12	SEM images of the fracture surfaces and the effect of CNC.	83
4.13	Increased tensile strength due to CNC and a simplified illustration of the acting stresses.	85
5.1	Comparison of M_w/T_g of the developed coating systems with industrial coating polymers.	90
A.1	Photographs of the synthesized drying agents.	118
A.2	Needle tracks of the films for the Box-Behnken experimental design.	119
A.3	Contour plot of changes in the ATR-FTIR spectra during drying.	120
A.4	Individual ATR-FTIR spectra recorded during film drying.	121
A.5	Changes in the ATR-FTIR spectra with prolonged oxidation.	122
A.6	Needle tracks for the control experiments with linseed oil polymerization.	123
A.7	Changes in the ATR-FTIR spectra recorded during autoxidative polymerization.	124
A.8	ATR-FTIR analysis of linseed oil drying kinetics.	125
A.9	Effect of the drying agent on linseed oil weight change and T_g during polymerization.	126
A.10	Needle tracks for drying experiments at room temperature.	127
A.11	Coated spruce specimen and demonstration of improved wood penetration.	128
A.12	Fitted <i>versus</i> experimental values for the dry-through time, viscosity, and T_g .	130
A.13	Interaction plots of the mean viscosity.	134
A.14	Diagnostic plots for the drying time regression analysis.	135
A.15	Diagnostic plots for the regression analysis of the viscosity.	135
A.16	Diagnostic plots for the regression analysis of the T_g .	136
B.1	UV-VIS spectra for the cationic photoinitiator and curcumin in acetonitrile.	143
B.2	Illustration of colour change and film formation on wood under solar irradiation.	143
B.3	Illustration of surface defects upon hot and cold check testing.	144
B.4	Illustration of reduced yellowing upon 6 months of sample storage.	145
B.5	Diagnostic plots for the regression analysis of the rate constant k .	150

B.6	Diagnostic plots for the regression analysis of the final conversion.	151
B.7	Diagnostic plots for the regression analysis of the T_g	151
C.1	ATR-FTIR spectra of TMI and Genomer 1225.	155
C.2	Curing behavior compared based on terminal C=C bond conversion.	156
C.3	Illustration of oxygen inhibition using ATR-FTIR.	157
C.4	Trace contaminants as potential cause for increased resin turbidity.	158

Nomenclature

Symbols

α	alpha level, type I error rate, or significance level	[-]
ΔH_{dec}	decomposition enthalpy	[J g ⁻¹]
ε	strain	[-]
η	dynamic viscosity	[Pa s]
λ	spectral absorption	[nm]
ϑ	temperature	[°C]
E	elastic modulus	[MPa]
T_g	glass transition temperature	[°C]

Indices

dec	decomposition
e	elastic
oz	ozonized
p	plastic
res	resulting

Acronyms and abbreviations

ANOVA	analysis of variance
ASTM	American society for testing and materials
ATR	attenuated total reflectance
BDE	bond dissociation energy
CC	concern concentration

ChV	chronic value
CI	confidence interval
CMF	microfibrillated cellulose
CNC	cellulose nanocrystals
CNF	nanofibrillated cellulose
<i>d</i>	Cohen's measure of effect size
<i>df</i>	degrees of freedom
DIY	do-it-yourself
DMHA	2-hydroxy-2-methyl-1-phenylpropan-1-one
DMPA	2,2-dimethoxy-2-phenylacetophenone
DSC	differential scanning calorimetry
ELO	epoxidized linseed oil
ELOME	epoxidized linseed fatty acid methyl ester
<i>F</i>	F-ratio
FAME	fatty acid methyl ester
FTIR	Fourier transform infrared
GPC	gel permeation chromatography
ICP-MS	inductively coupled plasma mass spectrometry
ISC	intersystem crossing
LCL	lower control limit
$\log K_{ow}$	octanol/water partition coefficient
<i>M</i>	sample mean
MDSC	modulated differential scanning calorimetry
MS	mass spectrometry
M_w	molecular weight
NA	not applicable
<i>ns</i>	not significant
OEM	original equipment manufacturer
OOC	oxirane oxygen content
<i>p</i>	<i>p</i> -value
PCA	principal component analysis
PGX	pressurized gas expanded liquid
PI	photoinitiator
<i>q</i>	<i>q</i> -value (corresponding to an adjusted <i>p</i> value)

Q1	lower (first) quartile
Q3	upper (third) quartile
ROI	region of interest
<i>SD</i>	standard deviation
SEM	scanning electron microscopy
sp	sp hybridization
<i>t</i>	<i>t</i> -test value
TAG	triacylglycerol
THF	tetrahydrofuran
TMI	3-isopropenyl- α,α -dimethylbenzyl isocyanate
TPO	2,4,6-trimethylbenzoyl-diphenylphosphine oxide
UCL	upper control limit
UV	ultraviolet (light)
VOC	volatile organic compound

Chapter 1

General introduction

As one of the oldest industries dating back to at least 20 000 yr [1], the coating and paint industry today is a ~200 billion CAD business with a volume of ~42 billion litres [2]. Coatings are applied as a covering to the surface (referred to as substrate) of objects for decorative and/or functional purposes, such as corrosion protection or improved wear resistance. An overview of volumes and values of architectural (decorative) and industrial original equipment manufacturer (OEM) coatings is given in Figure 1.1a). Of the raw materials used in coatings and paints, solvents constitute ~20 % of the total volume (Figure 1.1b)). While urban air pollution is typically associated with exhaust air from transportation, a recent study by McDonald et al. [3] revealed the important contribution of household items and building materials to volatile organic compound (VOC) emissions. These contributions become more evident as transportation is becoming "cleaner" and mitigation technologies are implemented. According to their study, in the US alone, 2.4 ± 0.6 T g of VOC were emitted from coatings in 2012, which accounts for 30 % of total VOC emissions from volatile chemical products. These also include pesticides, printing inks, adhesives, cleaning agents, and personal care products. In comparison, total VOC emissions from mobile sources and upstream emissions (petrochemical facilities and oil/gas production) is estimated to be 3.5 ± 1.1 Tg and 4.8 ± 1.4 T g, respectively.

VOC emissions from coatings and paints are mostly related to the presence of solvents and mainly affect indoor air quality [3]. Conventional paints contain between 45 % to 65 % solvents [5]. In particular, aromatic and chlorinated hydrocarbons can cause health issues [3]; the use of latter is already restricted in several countries [6, 7]. Solvents are used in coatings and paints to dissolve the polymeric film forming agents. Such physically drying coatings not only contain high amounts of solvents, but also undergo an energy-intensive drying process. Solvent contents in waterborne paints are considerably lower (8 % to 18 %) [5], nonetheless, the energy requirements for drying remain substantial [8].

This work aims at improved coating sustainability by using renewable lipid and cellulosic feedstocks to develop coating components for two "green" curing technologies: air- and photo-polymerization. Unlike conventional systems, the energy is not used to dry the coatings but to initiate their polymerization when exposed to

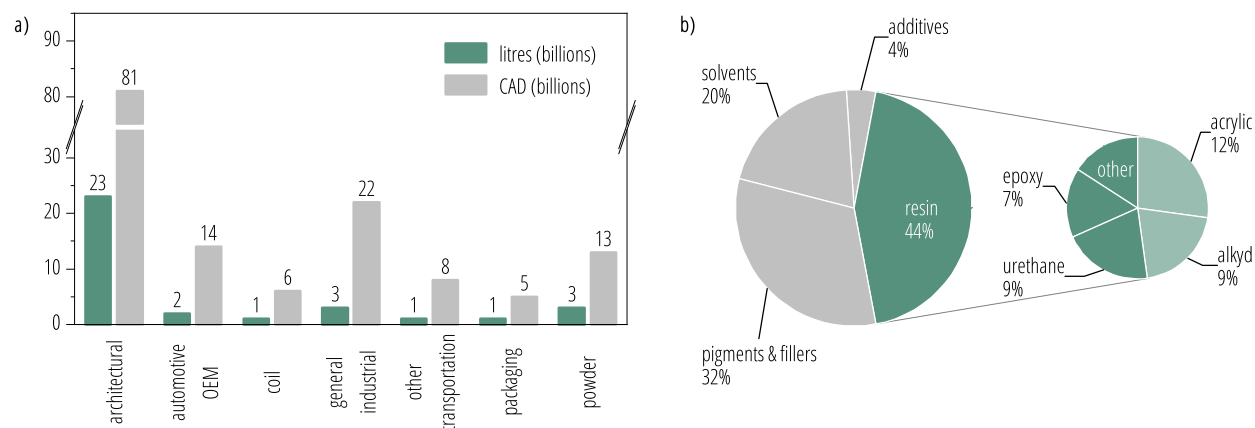


Figure 1.1: Overview of the global coatings industry. **a)** Volume and value of architectural coatings/paints and sub-segments of industrial OEM coatings (2017). **b)** Volumes of coating raw materials (2017) and most common resins (dark green colour indicates the subcategories relevant to this thesis). Graphs are based on data published by Vincentz Network's Coatings Team [2, 4].

high-intensity ultraviolet (UV) light or polymerization is induced upon contact to atmospheric oxygen (O_2). This reduces the energy requirements significantly and low solvent emissions occur since most components of the resin become part of the polymer network.

The following sections are summarizing some of the main principles of air- and photopolymerization, as well as the utilization of lipid and cellulosic feedstocks for polymeric and nanotechnological applications. They are meant to provide an overview of the major problem fields relevant to this thesis, as well as some background information on the main chemical principles, and the history of coatings and paints. Additionally, the thesis outline and hypotheses are presented.

1.1 Coating systems with low VOC emissions

This thesis focuses on solvent-free liquid resins. However, it is important to note that solvent-free coatings also include powder coatings. They are applied as solids before being melted and forming films in a baking oven [5]. Due to the often required high melting temperatures, these coatings are not suitable for thermally sensitive substrates such as wood, which is one of the most important substrates for lipid-derived coatings.

1.1.1 Air-drying: drying oils

The most important natural materials used as binders in coatings and paints are unsaturated plant oils. As drying oils, they have been used since prehistoric times and might therefore be one of the first thermosetting binders used by humankind. Chiriu et al. [9] detected drying oils on mid-third Millennium B.C. Mesopotamian clay pottery, and suggested that drying oils were applied as a primer and also used in subsequent painting decorations due to the presence of cyclopropenoid fatty acids, which are typically found in cottonseed oil.

Table 1.1: Fatty acid composition of the most common drying oils ([wt %]) [15].

drying oil	linolenic	α -eleostearic	α -lipoic	linoleic	oleic	ricinoleic
cottonseed	-	-	-	40	24	-
castor	-	-	-	3	7	87
linseed	52	-	-	16	22	-
oiticia	-	-	78	-	6	-
safflower	1	-	-	75	13	-
soybean	9	-	-	51	25	-
sunflower	2	-	-	52-75	14-34	-
tung oil	3	80	-	4	8	-

Synchrotron-based analyses also identified drying oils as the paint binder in 12 out of the 50 caves behind the recently destroyed gigantic Buddhas of Bāmiyān in Afghanistan (5th to 9th century A.D), long before drying oils were "discovered" in Europe [10–12].

1.1.1.1 Overview of autoxidative polymerization

The fatty acid composition of the most common drying oils is given in Table 1.1. While natural castor oil is a non-drying oil, good drying properties are only obtained through chemical dehydration and formation of a double bond conjugate. Its commercial use in the US dates back to the mid-1930s as a result of the volatile price and availability of tung oil [13], the fastest curing natural drying oil also known as (China) wood oil. Linseed oil, on the other hand, is the most popular and widely used drying oil in the paint industry to date [14].

Autoxidation involves the addition of O₂ to unsaturated fatty acids and a sequence of radical reactions resulting in cross-linking and eventual film formation. Autoxidation is moved forward by a free-radical chain mechanism, consisting of initiation, propagation, and termination reactions, governed by the formation of hydroperoxides, the decomposition of these compounds, and their subsequent cross-linking in primary reactions [16, 17] as outlined in Figure 1.2. Initiation of the chain reaction follows an enzymatic oxidation, photooxidation, or the production of radicals by initiators such as metals or UV light. These radicals can react with O₂ to form peroxy radicals. Through hydrogen (H) atom abstraction, they can form hydroperoxides and regenerate free alkyl radicals to further react with O₂.

Initiation Direct oxidation of unsaturated lipids (RH) by molecular oxygen is spin forbidden due to the different spin states of their ground states (*i.e.* triplet oxygen ³O₂ versus singlet ground state of lipids). Instead, the reaction with ³O₂ requires free radical intermediates [18] provided by initiators (I) such as heat, light, free radical generators, or metal catalysts [19]. In contrast, the direct reaction of unsaturated lipids

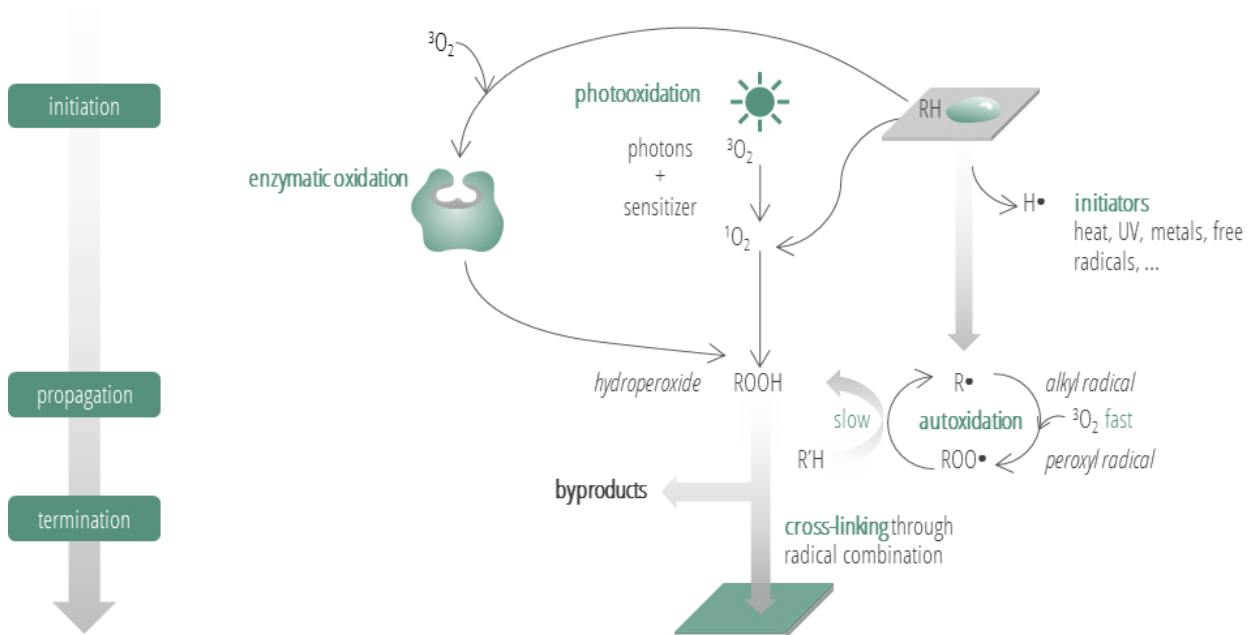


Figure 1.2: The autoxidative film forming process of unsaturated (non-conjugated) lipids (RH) is moved forward by a free-radical chain mechanism, consisting of initiation, propagation, and termination reactions. Initiation typically follows an enzymatic oxidation or photooxidation with subsequent formation of hydroperoxides or the direct production of radicals by initiators, which react with O_2 to form peroxy free radicals. Through H atom abstraction, they can form hydroperoxides and regenerate a free alkyl radical to further react with O_2 . Decomposition of hydroperoxide compounds and their subsequent cross-linking are primary reactions resulting in film formation.

and O_2 requires its excitation to singlet oxygen (1O_2) in the presence of metal catalysts, photosensitizers or through enzymatic catalysis [20, 21].

Once the peroxy radicals are formed, the process then proceeds most favourably with the abstraction of *bis*-allylic hydrogen atoms ($H\cdot$), resulting in the formation of hydroperoxides and alkyl radicals. The alkyl radicals of fatty acids with isolated double bonds can isomerize to conjugated systems (Eq. 1.1) due to conjugative resonance stabilization [22]:



Addition of O_2 to these carbon-centred radicals is "diffusion-controlled" with essentially no energy barrier for formation of a new peroxy radical [23], and the oxidation process is therefore of autoxidative nature [24]. Depending on the reaction conditions, the peroxy radicals can have a considerable half-life ranging from milliseconds to seconds, making it possible to engage in several different pathways [25]. In a reverse reaction to oxygen addition, the peroxy radicals can convert back into the carbon radical by β -fragmentation (bond cleavage in the β -position relative to where the radical is located) and compete with H atom abstraction to form hydroperoxides, resulting in a distribution of *cis/trans* stereoisomers [26, 27] with a driving force towards *trans/trans* double bonds due to the greater thermodynamic stability [28].

Propagation and termination The dominant and also rate-limiting pathway for peroxy radicals during the early stages is H atom abstraction [29] and the formation of a free alkyl radical, which reacts with oxygen to form another peroxy radical and thereby accelerating the autoxidative process (Eqs. 1.2 and 1.3) [24]:



The decomposition of the formed hydroperoxides (Eqs. 1.4 and 1.5) [20] and subsequent radical combination are considered the primary reactions leading to film formation.



Direct addition of alkoxy or hydroxyl radicals to alkenes with isolated $-\text{CH}=\text{CH}-$ does not occur to a noticeable extent [30, 31]. For conjugated oils like tung oil, however, direct radical addition to conjugated $-\text{CH}=\text{CH}-$ contributes significantly to the observed fast drying rate [32], as this reaction results in direct cross-linking without terminating the reactive chain. Accordingly, O_2 plays a less important role in the polymerization of conjugated oils as will be discussed in more detail in Chapter 2.

For drying oils with isolated $-\text{CH}=\text{CH}-$, cross-linking occurs mainly through termination reactions, *i.e.* the dimerization of radicals at high enough concentrations resulting in the formation of carbon-carbon, peroxy, and ether cross-links (Eq. 1.6-1.11).

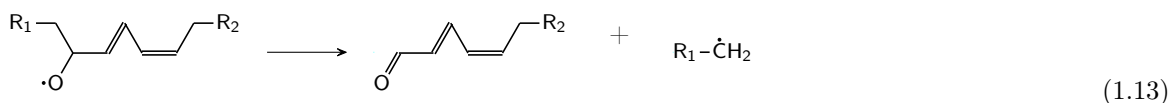


Combination reactions to form carbon-carbon cross-links are not typically observed at ambient temperature [24]. However, carbon-carbon cross-links can be formed *via* a Diels-Alder pathway (Eq. 1.12) [24, 33, 34], a cycloaddition reaction of a conjugated diene and another fatty acid acting as a dienophile.



In addition to these primary oxidation reactions resulting in cross-linking through radical combination, a multitude of secondary oxidation reactions not resulting in cross-linking render drying oils prone to yellowing and embrittlement over time. For example, upon β -scission at either side of the carbon bearing oxygen (Eq. 1.13) of an alkoxy radical, both an aldehyde and an alkyl radical can be formed at cost of chain length. In addition to radical combination, bimolecular radical termination can also occur through disproportionation reactions. A β -H atom is transferred from one carbon-centred radical to the other to form non-radical

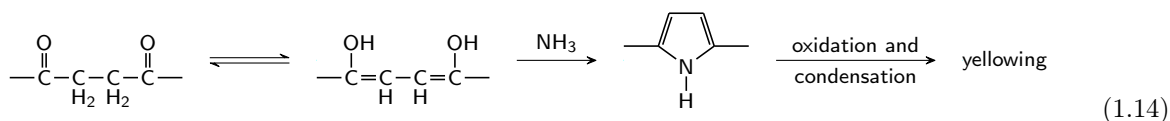
products without cross-linking [24], a reaction which competes with combination reactions of carbon-centred radicals [35].



1.1.1.2 Yellowing

The question of which factors determine the progressive yellowing of drying oil films has caused much debate over the years [36]. Yellowing, and hence, the formation of chromophoric groups, occurs when a clear or pigmented drying oil film is exposed to the atmosphere under both diffusive daylight as well as total darkness ("dark-yellowing") [37]. However, this type of yellowing is partially reversible by exposure to daylight, likely due to attack of the chromophores by radicals formed during the photo-induced homolytic cleavage of labile peroxide cross-links [38, 39].

In 1962, O'Neill et al. [40] suggested that yellowing in aged drying oil films is caused by atmospheric nitrogenous contaminants (*e.g.* ammonia NH_3), which form pyrroles through the enolization with oxidation products bearing carbonyl groups (Eq. 1.14), although the exact mechanism of this reaction is not yet clear [36].



However, a growing body of literature suggests the presence of oxidatively formed colourless precursors, which undergo further reactions to eventually give yellow compounds, possibly through condensation reactions [41]. Alternatively, impurities present in the oil could be oxidized in later stages of drying oil polymerization and also evolve into yellowing compounds [36].

As a result of the high extinction coefficients ϵ (a measure for light absorption) of these unsaturated coloured bodies, they lead to visible yellowing at very low concentrations but on the other hand, they are not considered to significantly affect the physical aging of drying oil films [36]. It becomes clear that yellowing of drying oil-based films is a result of complex chemical mechanisms and difficult to prevent. In fact, the economic breakthrough of synthetic resins for coatings and paints is to a certain extent related to improved yellowing resistance [5].

1.1.1.3 Derivatizations: plant oil-based, semi-synthetic coatings

After the introduction of nitrocellulose lacquers (mid-1920s) and phenol-formaldehydes (late 1920s), oxidizing alkyds were introduced in the 1930s [42]. These so-called "drying" alkyds are polyesters modified with unsaturated fatty acids and continue to be the dominant binder in most "oil-based" paints available nowadays. They can be produced at relatively low cost through either a) the fatty acid process or b) alcoholysis/mono-glyceride process [5]. In the first case, free fatty acids are reacted with acid anhydrides and polyols, while in the second processing type, raw vegetable oil combined with polyol is transesterified to produce a mixture of mono- and diglycerides, which are then polymerized with acid anhydrides [24]. They can be modified with different monomers such as acrylates for faster polymerization and improved coating performance [15]. Due to higher M_w , alkyds are typically solvent-borne binders but they can be prepared at high solid content and also as waterborne coatings. Previously, waterborne paints were developed through the maleinization of drying oils in the early 1950s [43, 44]. The reaction with maleic anhydride proceeds by two routes: a) allylic addition and b) ene-reaction [45, 46]. Traditionally, the acid groups were then neutralized by ammonia or amines to produce water soluble oils [47]. In a more recent study, Diels-Alder adducts (*cf.* Eq. 1.12) were obtained when maleinizing tung oil for further grafting with UV-curable monomers [48].

1.1.1.4 Other natural and organic film forming materials used in traditional coatings and paints

Traditionally, drying oils have also been used in combination with tree/insect resins (oil varnishes) and as enamels (with high amounts of ground zinc oxide) in the late 19th century. While higher contents of oils impart more flexibility and durability, the presence of resin increases curing speed, gloss, and hardness [42]. Natural tree resins (*e.g.* rosin, sandarac, copal, and mastic) are composed of terpenoids referred to as resin acids, while shellac is a resin-excretion from the lac beetle and consists mostly of laccolic lactone and shelloic acids [49]. Although these natural resins are non-polymerizing, they are easily oxidized and therefore also discolour on aging [42].

As naturally water-soluble binders, proteins were one of the first binders used by human kind along with drying oils. Film formation is related to protein denaturation, resulting in the formation of inter- and intramolecular hydrogen bonds and covalent cross-links. Casein paints and animal glues have a long history in paints, but more and more also plant-derived proteins are used in distempers [47]. In contrast to drying oils, protein-based binders undergo little chemical changes due to their oxidative stability, but suffer from lower water resistance [49].

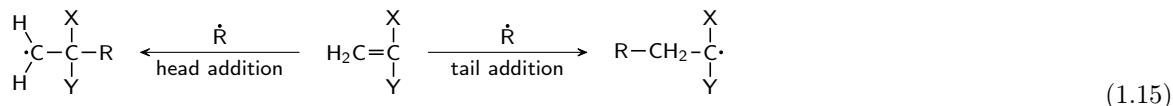
1.1.2 Radiation curing: radical polymerization

While a typical drying oil takes days up to weeks until a tack-free surface is formed, radiation-curing provides near instant polymerization, enabling immediate processing of the cured surfaces, and therefore improves productivity through shorter production times. Currently, radiation-curing is also the fastest growing alternative technology in the coatings industry with wood coatings having the biggest estimated volume share of applications (~32% in 2005) [50].

Unlike conventional systems, the energy is not used to dry the coatings but to initiate their polymerization when exposed to high-intensity UV light or electron beam sources. This reduces the energy requirements significantly and minimal VOC emissions occur as all components of the resin become part of the polymer network. The basic properties of the eventual coatings are imparted by the oligomer, the main component (25 % to 90 %) of radiation-curable formulations. Film-forming monomers (0 % to 60 %) are mainly added to reduce the resin viscosity. UV-curable coating formulations also contain photoinitiators and various additives (*e.g.* defoaming or wetting agents), as well as fillers/pigments [51].

1.1.2.1 Radical reactions

Radical polymerization in combination with acrylate-based monomers is the most commonly used chemistry in UV-curable coatings. The polymerization proceeds *via* a free-radical chain mechanism as in drying oils involving initiation, propagation, and termination (combination and disproportionation) reactions. However, the radicals involved have a much higher tendency to add to double bonds as opposed to H atom abstraction as in drying oils, resulting in a faster increase in molecular weight (M_w) and therefore faster curing (*cf.* Section 1.1.2.3). During initiation and propagation, the free radicals add to the predominantly less substituted end of the double bonds ("tail-addition") in the photocurable moieties of the film-forming coating components as outlined in Eq. 1.15.



These radicals are transient species and their stability is influenced by a complex combination of different factors including bond strength, polar, and steric terms [52]. In addition to acrylates, also methacrylate, allyl, and vinyl oligomers and monomers are used. However their rates of cure decline in the order [53]:



The lower curing speed of methacrylates compared to acrylates is commonly associated with radical stabilization *via* the α -methyl group (*cf.* Figure 1.3a)) and therefore reducing its reactivity [51]. This influence by the degree of substitution on radical stability (tertiary > secondary > primary) is rationalized by hyperconjugation [35], the stabilizing interaction of an extended molecular orbital due to the overlapping of double-occupied σ -bonding orbitals (usually C-H) with the the single-occupied non-bonding p orbital as shown in Figure 1.3b). However, the polymerization kinetics of acrylate monomers is complicated by a variety of radical transfer reactions, which affect the kinetics and the molecular features, a phenomenon which has not been discovered until recently [54]. This behaviour is related to a mechanism known as "backbiting" and relates to intramolecular chain transfer within the polymer, which leads to branching and formation of tertiary radicals in proximity to the chain end [55]. The higher stability of these radicals reduces their propagation rate and therefore slows down the polymerization rate [56].

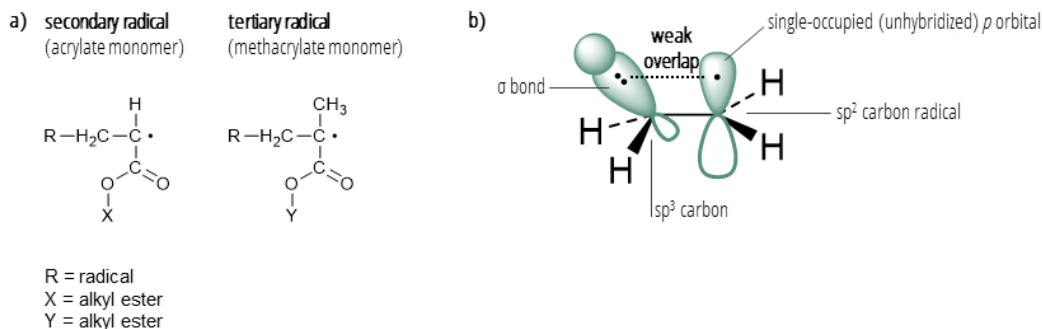
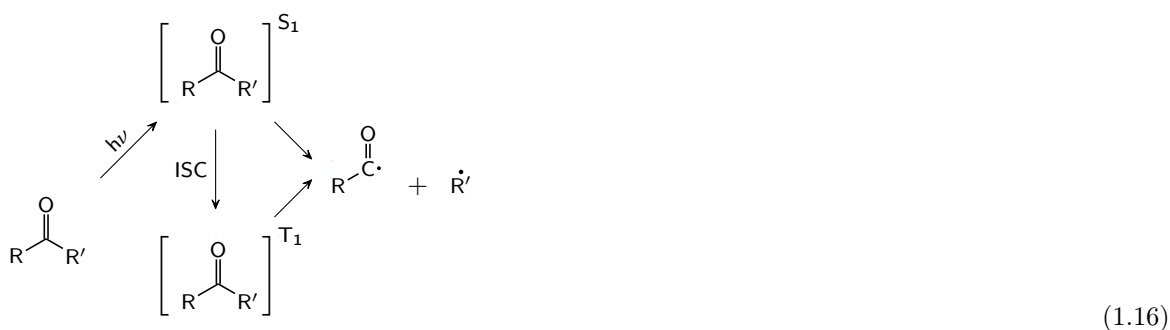


Figure 1.3: a) Formation of secondary and tertiary radicals upon radical attack (R) *via* tail-addition for acrylates and methacrylates, respectively. X and Y denote alkyl ester R group for the generalized monomers. b) Illustration of hyperconjugation stabilization as the rationale behind the increased stability of tertiary radicals compared to secondary radicals.

1.1.2.2 Radical photoinitiators

In contrast to electron beam curing, radical and cationic UV-curing is typically initiated by photoinitiators, which absorb UV light and decompose to form radicals. Two types can be distinguished: type I photoinitiators (*e.g.* 1-hydroxy-cyclohexylphenylketone) yield two free radicals upon Norrish type I α -cleavage (Eq. 1.16), and type II photoinitiators (*e.g.* benzophenones/amines), which form an excited state and abstract a H atom from the donor molecule (synergist). The synergist then acts as the initiating species [57]. In the case of the former, the triplet excited state of the ketones or aldehydes can be obtained through intersystem crossing (ISC) and the two radical fragments (alkyl and an acyl radical pairs) are obtained through the unimolecular cleavage of the α -carbon. Cleavage from the singlet excited state occurs in competition with the rate of intersystem crossing [58].



Radical photoinitiators are used at concentrations of 0.5% to 15%, depending on film thickness, UV light source, or pigmentation [59]. Due to decreased resin penetration of higher frequency radiation [60], typically a mixture of photoinitiators is used in order to guarantee surface and through cure. For type I photoinitiators, usually only one of the photoinitiator fragments is reactive. Therefore, the non-initiating radicals remain in the films as extractables, which can cause migration issues, such as in food packaging [51]. While type I

photoinitiators are the most widely used, photoinitiators absorbing visible-light typically belong to type II photoinitiators. Absorption in visible light implies a yellow colour of the photoinitiator, a problem which can be solved if the photoinitiator undergoes bleaching during activation due to cleavage of the chromophore [61, 62]. Additional yellowing commonly observed in UV-cured films can originate from a phenomenon referred to as "initial photo-yellowing". Analogous to the yellowing of drying oils, this effect is related to remaining photoinitiator-fragments, which are likely involved in condensation or oxidation reactions. While this type of yellowing occurring shortly after curing is partially reversible, the effect is worse for type II photoinitiators with tertiary amines as the synergist [63]. However, tertiary amines have an important role in reducing oxygen inhibition as discussed below [63].

1.1.2.3 Oxygen inhibition

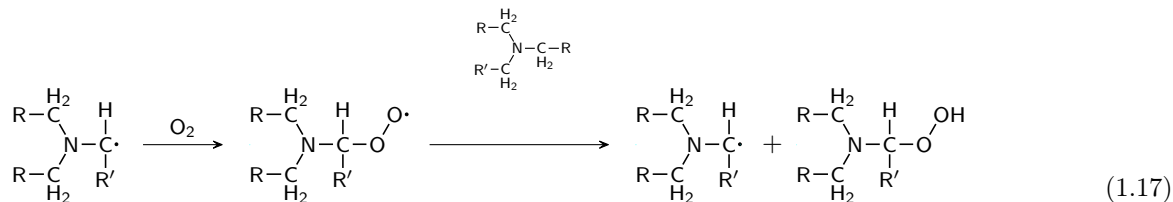
Radical polymerization can be affected by the presence of O_2 . It is generally accepted that the photoinitiators in their excited state can be quenched by O_2 , thereby reducing the rate of cleavage from the triplet state. Accordingly, fewer initiating radical species are formed. Subsequently, 3O_2 reacts rapidly with carbon-centred free radicals and converts them into weakly propagating peroxy radicals, causing a further decrease of the polymerization rate. As discussed in Section 1.1.1.1 for the autoxidative polymerization of drying oils, peroxy radicals engage in H atom abstraction reactions. Typically, heteroatom-centred radicals have a higher H atom abstraction:addition ratio when compared to carbon-centred radicals [35]. The relative propensity of radicals to abstract H atoms (chain transfer) as opposed to radical addition to double bonds (cross-linking) has a big effect on polymerization rate and M_w .

Generally, inhibition by O_2 is observed as a prolonged induction time and surface tackiness, in particular for thin films, where O_2 is replenished as it is consumed [64], as well as in resins of low viscosity [65]. The following three main routes are used to combat O_2 inhibition [51, 59, 65]:

1. removal of O_2 from the zone of curing by use of an inert gas or physical barrier (*e.g.* wax migrating to the surface)
2. increasing the photoinitiator concentration and/or light intensity to increase the concentration of photoinitiator fragments to initiate polymerization
3. use of chemicals, which can react with the peroxy radicals (*e.g.* tertiary amines).

Amine synergists have long been known as an effective measure to combat O_2 inhibition either as an additive or grafted onto acrylates *via* Michael addition, which reduces plasticization and odour by un-bound amines [66]. A generalized mechanism of the reaction is shown in Eq. 1.17. As efficient H donors, their

radicals can scavenge O_2 and regenerate their reactive form through H atom abstraction by the peroxy group.



1.1.2.4 Effect of volumetric shrinkage on adhesion

During the chemical curing of a resin coated onto a substrate, the molecular distance between the monomers and oligomers is reduced upon covalent bond formation. Due to adhesive forces with the substrate and increasing rigidity of the solidifying film, this volumetric shrinkage is restricted and the polymeric matrix can no longer accommodate the voids by relaxation, resulting in the build up of internal stresses. Therefore, this effect is more pronounced as the glass transition temperature (T_g) approaches the reaction temperature [67] (reduced chain mobility). Internal stresses have been attributed to the observed poor adhesion of some radiation-cured materials [68], where it can lead to deformation, delamination, or even adhesive failure [51].

Polymerization shrinkage stresses have long been known to cause adhesion issues in UV-curable dental resin restorations, where volumetric contractions between 2% to 13% can occur [69, 70]. As reviewed by Giachetti et al. [71], clinical consequences are not limited to reduced adhesion. Also micro-cracking in the restorative material and even potential damage to the tooth substrate due to stress transfer can occur. In UV-curable coatings, adhesion issues related to stress accumulation are often controlled by reducing the functionality of the film-forming monomer [59]. On the other hand, dental restorative resins are often hybrid materials with considerable amounts of inorganic fillers. In addition to improving the wear resistance, the fillers can also reduce stress development during volumetric shrinkage [72]. This concept will be important in Chapter 4, where nanoparticles were explored as a new route to increase the adhesive strength of UV-curable coatings. The effect of fillers on internal stresses in dental adhesives is twofold: polymerization shrinkage is reduced due to the lower fraction of resin, while the elastic modulus of the composite is increased and thereby creating more stresses at the interface [71, 73, 74]. Upon reaching the gel point, polymerization stresses accumulate due to the reduced ability of the growing polymer chains to yield and slip into new positions without damaging the internal structure or bonding to the substrate (Figure 1.4) [75–77].

1.1.3 Radiation curing: cationic polymerization

Better adhesive properties and the absence of oxygen inhibition in cationically-curable systems are some of the advantages over radically-cured UV coatings, which lead to increasing interest in cationic UV curing. However, these coating systems are still a niche market including metal decorations and inks [79]. Consequently, the raw materials are more limited.

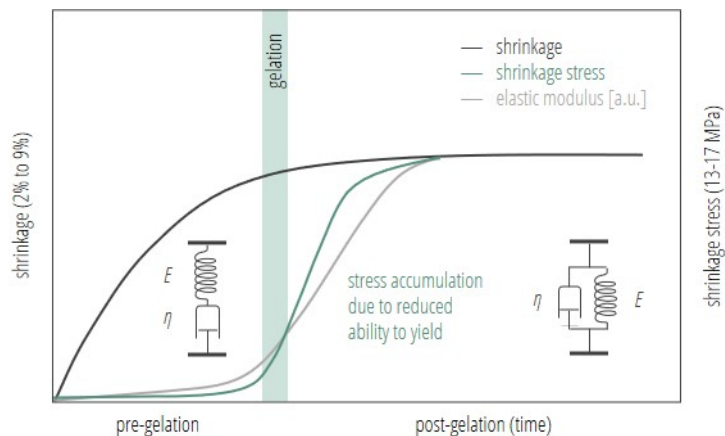
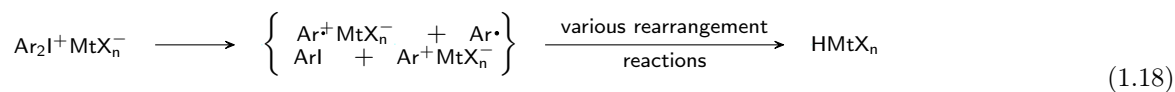


Figure 1.4: Simplified relationship between polymerization shrinkage and stress development for UV-curable dental composite resins (adapted from Abdulsamee et al. [78]). The viscoelastic properties of the resin can be represented by a Maxwell and Kelvin-Voigt model prior and after the gel point, respectively, consisting of a dashpot (Newtonian fluid) and spring (following Hooke's law) connected in series or in parallel (reversible deformation of the viscoelastic solid) [75]. E corresponds to the elastic modulus and η is the viscosity.

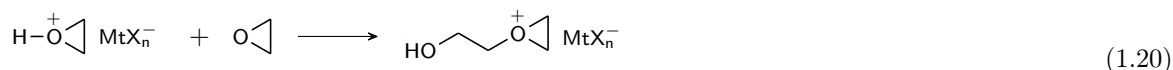
Cationic photoinitiators use UV radiation to generate strong acids, which will initiate ring-opening polymerization of epoxy monomers. It is generally accepted that their excitation, fragmentation, and the initiation of the cationic polymerization of epoxides follows the mechanism outlined in Eq. 1.18 to Eq. 1.21 [80–82]. Cationic and radical species from the fragmented photoinitiator react with monomers to yield the Brønsted acid HMtX_n (Eq. 1.18) [81], in the present case $\text{HB}(\text{C}_6\text{F}_5)_4$ (Chapter 3).



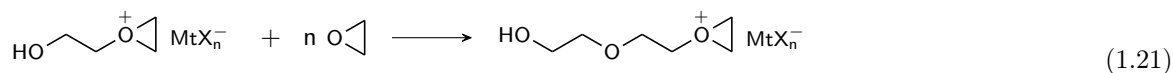
The epoxy monomer is rapidly protonated by this superacid to form secondary oxonium species (Eq. 1.19).



Cationic ring-opening polymerization then proceeds *via* an $\text{S}_{\text{N}}2$ attack resulting in the formation of tertiary oxonium species (Eq. 1.20).

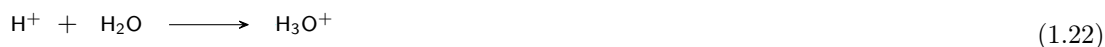


Chain growth occurs by the repetitive addition of monomers to the active chain end (Eq. 1.21).

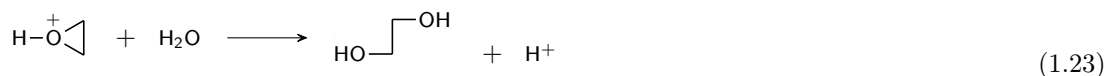


While the polymerization rate of radically-cured UV coatings is usually higher than for cationic systems [83], their adhesive properties are reported to generally be superior [51, 59]. Since the oxonium ions do not react with themselves, termination reactions are less likely to occur compared to radical systems. This is considered to be the primary reason for the longevity of the active centres and therefore the presence of dark cure polymerization, which can make up >80% of epoxy conversion [84, 85]. This is a main advantage for application of 3D objects, which cannot be fully irradiated. Unlike radical polymerization, this reaction mechanism is also not inhibited by O_2 . However, polymerization can be affected by the presence of nucleophiles, in particular H_2O as follows [82, 86, 87]:

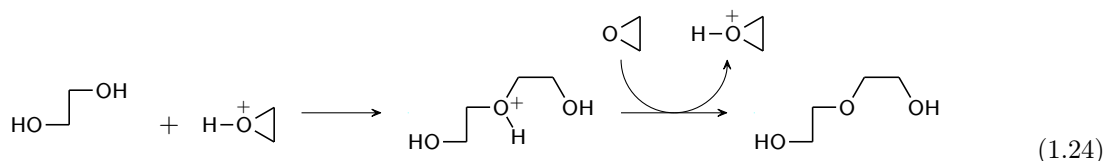
1. The polymerization can be inhibited by the reaction of H_2O with the generated Brønsted acid forming the hydronium ion and thereby reducing the concentration of the initiating superacid:



2. H_2O can also act as a chain transfer agent when oxonium ions preferably react with water (rather than the monomer), which reduces the effective H_2O concentration:



3. Subsequently, polymerization acceleration can occur through an activated monomer mechanism (fewer steric constraints than for the addition of an epoxide monomer):



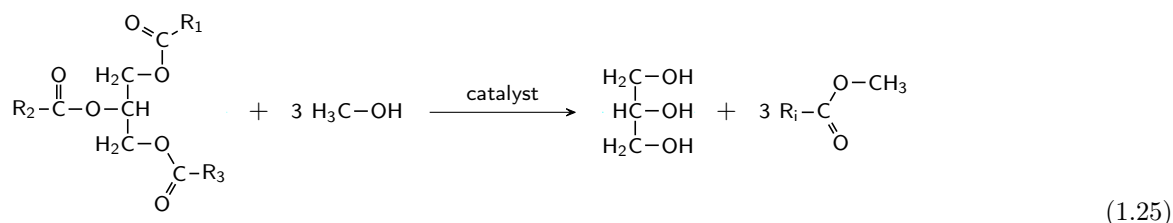
A more in-depth discussion of monomer and photoinitiator reactivity is provided in Chapter 3.

1.2 Lipid derivatization reactions for use in polymers

As highlighted in the sections above, plant oils have been and continue to have an important role in the coatings industry. The research presented here will expand on the chemical modification of oilseed lipids as a sustainable chemical feedstock for coating materials with improved performance. Their potential in polymer chemistry is given from the perspective of their monomeric character, worldwide availability, and suitability for chemical transformation because of unsaturation [88]. This allows to synthesize monomers with structures similar to petrochemical-based monomers [89]. The sections below briefly discuss the main derivatizations used in this work.

1.2.1 Transesterification

Despite the relatively simple manufacturing at an up to 100% biobased content and the much reduced viscosity compared to triacylglycerols (TAG), fatty acid methyl esters (FAMES) are relatively new as a raw material for coatings [90]. They are derived by the transesterification of TAG with methanol to yield their mono alkyl esters with glycerol as the byproduct as shown in Eq. 1.25.

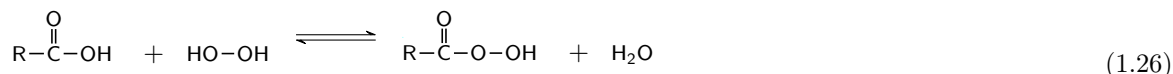


Typically, homogeneous catalysts like sodium hydroxide (NaOH)/potassium hydroxide (KOH) and sulfuric acid, or heterogeneous catalysts like solid acids or metal oxides are used [91]. However, the latter are often associated with issues of toxicity and difficulties in their recovery [92]. Under supercritical conditions, transesterification with methanol can also be achieved at high yield in the absence of a catalyst [93].

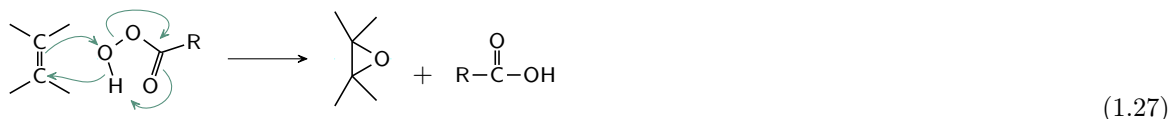
1.2.2 Epoxidation

Epoxy monomers contain one or more epoxy (oxirane) functional groups per molecule. In the coatings industry, epoxy resins based on bisphenol A and epichlorohydrin are the most commercially important resins for high-performance applications [15]. Acid-catalyzed epoxidation of plant oils is considered an environmentally-friendly process, and is economically viable when following the Prilezhaev reaction through an *in-situ* acid

catalysis using H_2O_2 [94]. In the first stage (Eq. 1.26), a peroxy acid is formed upon reaction of H_2O_2 with performic ($\text{R}=\text{H}$) or peracetic ($\text{R}=\text{CH}_3$) acid.



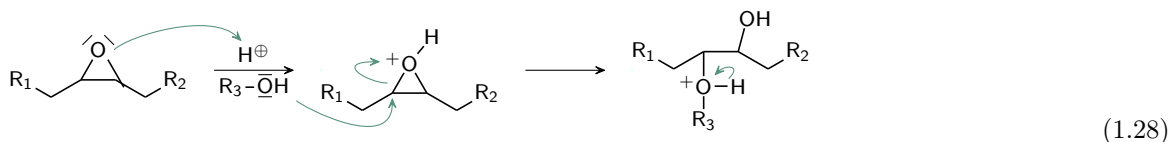
In the second step (Eq. 1.27), the peroxy acid reacts with the unsaturated lipid and the carboxylic acid is regenerated.



However, the epoxy groups are prone to ring-opening reactions. During their synthesis, a high molar ratio of acid: H_2O_2 catalyses the ring-opening with the acid *via* protonation of the oxirane oxygen [95]. Alternatively, reaction with H_2O can occur and yields vicinal (bonded to two adjacent carbon atoms) -OH groups [96], which are also secondary -OH groups, and therefore not very reactive for further derivatization.

1.2.3 Epoxy ring opening reaction to yield polyols

Ring-opening reactions of epoxides as the side-reactions described during their synthesis above, are used as a route to obtain polyols from epoxidized plant oil, most commonly through ring-opening reaction with alcohols (hydroxylation or alcoholysis). In Eq. 1.28, the mechanism for acid-catalyzed ring-opening *via* nucleophilic attack of the alcohol after protonation is given.



The reaction with monoalcohols is most often performed with methanol in the presence of a strong acid (*e.g.* sulfuric acid), which results in the formation of one secondary hydroxyl group (-OH) [97]. Using diols (*e.g.* 1,3-propanediol) or triols as the nucleophile for the ring opening of epoxidized lipids, also primary and therefore more reactive -OH functional groups are inserted in addition to the secondary -OH, which is formed during the ring-opening reaction. However, the use of multifunctional alcohols for epoxy ring opening to

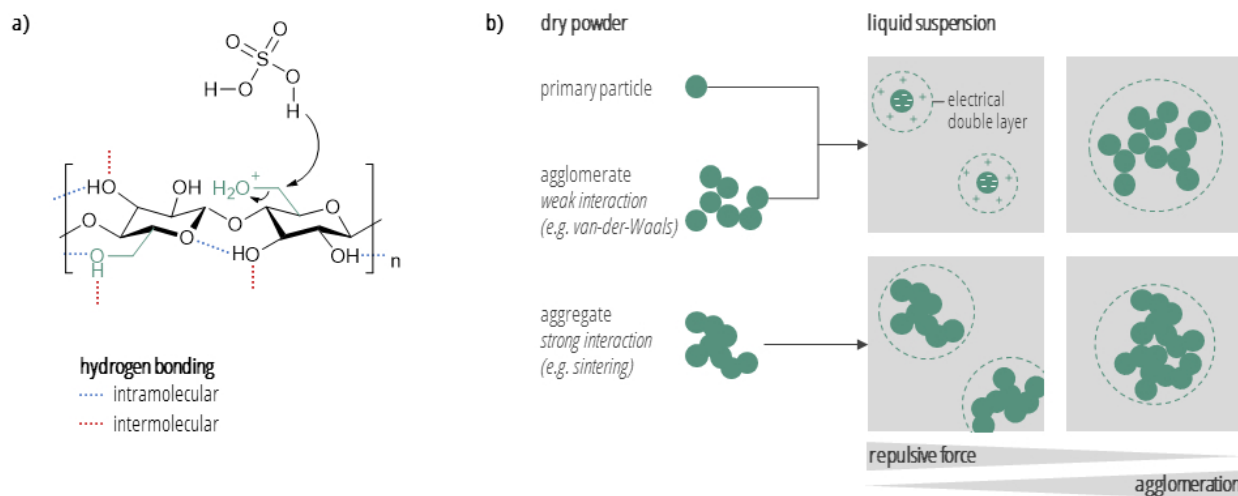


Figure 1.5: **a)** Illustration of intra- and intermolecular H bonding in crystalline cellulose and esterification with sulfuric acid during acid hydrolysis (green: primary -OH). **b)** Illustration of particle configuration in the dry and liquid state. Depending on interactive and repulsive forces, particles can be redispersed as primary particles or they form agglomerates. The degree of aggregation during the drying of the particles will further affect, the effective particle size in solution.

delaminated to yield stretched bundles of elementary nanofibrillated cellulose (CNF) with a higher flexibility compared to CNC imparted by the presence of amorphous domains and a reduced width of about 20 nm to 50 nm when compared with CMF [105].

Both intra- and intermolecular hydrogen bonding in the crystallites result in the high strength but also in the inaccessibility of water and other reagents [104] (Figure 1.5a)), making it possible to selectively hydrolyze the amorphous domains and release the nanocrystals. If the reaction is performed with sulfuric acid, CNC can undergo esterification through its primary surface -OH groups [106]. As a result, the CNC surface is partially grafted with negatively charged sulfonic groups, which can aid in dispersibility as discussed below.

1.3.1 Dispersibility

While esterification with sulfuric acid reduces the thermal stability of CNC [107], the negative surface charge was found to be effective in preventing the aggregation of CNC *via* hydrogen bonding due to repulsion forces of the electrical double layer [106]. When using CNC in non-waterborne systems, the prevention of CNC agglomeration in the polymer matrix is essential to nanoreinforcement. In the present work (Chapter 4), CNC was used as an aqueous dispersion to circumvent drying-induced agglomeration/aggregation, which would require more energy-intensive dispersion processes to obtain redispersibility for maintaining the particles at a nanoscale in the eventual coating resin (Figure 1.5b)). As reviewed by Zimmermann et al. [108], the main drying processes to obtain CNC in a powder form include:

- solvent evaporation: low cost but considerable agglomeration
- spray drying: low operational costs but formation of clusters up to micrometer size range

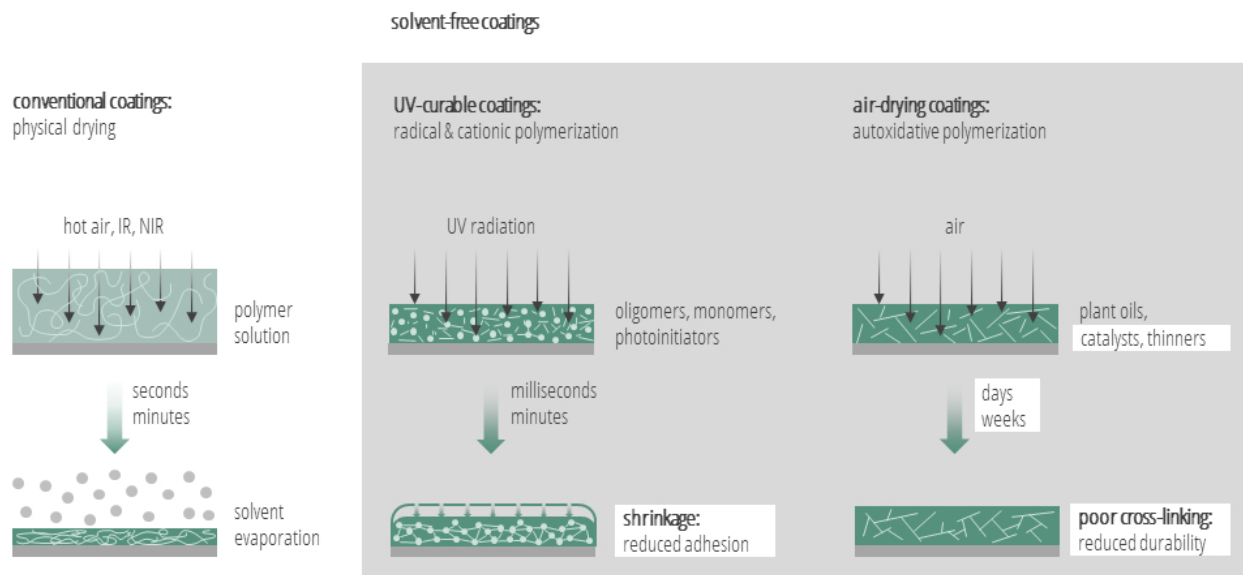


Figure 1.6: Comparison of UV- and air-curable coatings with conventional coatings and illustration of the targeted problem areas (white boxes) to use plant biomass for improved performance of solvent-free coatings. Adhesion issues in radically polymerized coatings are addressed, as well as the slow drying time and relatively poor durability of drying oils.

- lyophilization: slow with some agglomeration
- supercritical drying: high cost but very efficient in drying and preserving the nanoscale [109]

1.4 Thesis outline

1.4.1 Project overview

Generally speaking, fast curing and durability (*e.g.* resistance to biodegradation and good adhesion) are some key properties needed for competitive advantages of coating materials. Figure 1.6 summarizes the previously discussed key principles of UV- and air-curable coatings in comparison to conventional coatings. The problem areas which limit their performance are highlighted; these are targeted in the work described in this thesis.

Possible solutions to these problems are investigated in the next three chapters, with a focus on the use of plant oil lipids and CNC derived from (local) biomass as summarized in Figure 1.7. Transesterification of the plant oil TAG with methanol offers the possibility for viscosity reduction due to lower M_w of the formed FAME. The projects are suitable for different levels of lipid modification starting from native oils (TAG and FAME), to epoxidized oils, and *via* polyols to polyurethanes. However, the associated increase in strength is somewhat compromised by a loss of biobased content as photoinitiators are needed for UV-polymerization, and in the polyurethane-based prepolymers, also due to the derivatization with isocyanate and use of synthetic film-forming monomers for reduced viscosity.

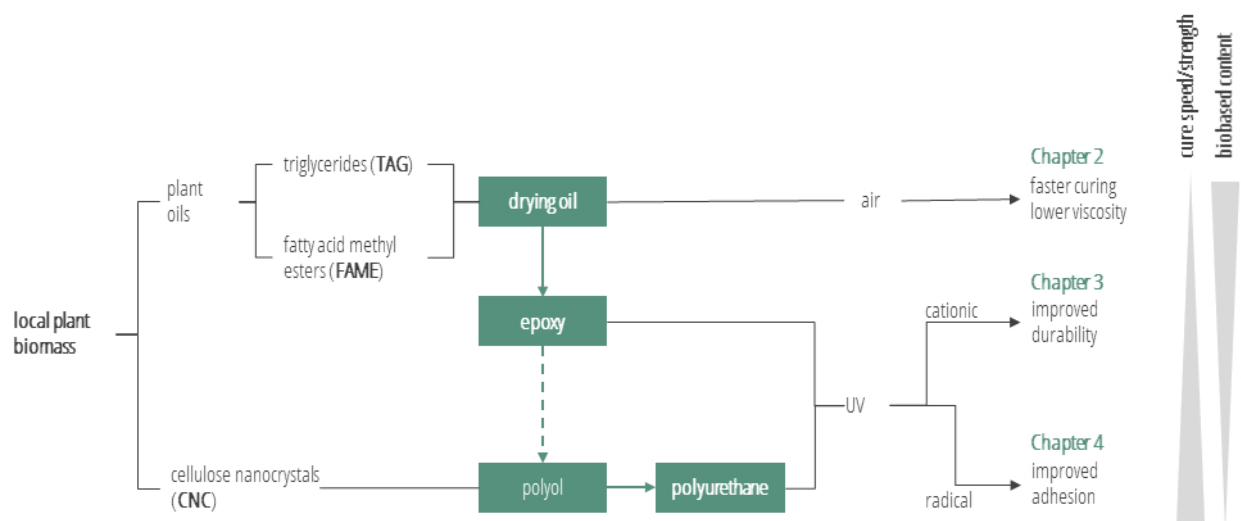


Figure 1.7: Overview of targeted plant biomass utilization and polymer matrices for the three solvent-free coating systems investigated in this thesis.

1.4.1.1 Chapter 2

This project aimed at the development of a lipid-based drying time and viscosity reducing agent as an alternative to metal driers and solvent-based thinners in drying oils while maintaining the air-induced drying. The idea was to functionalize lipid double bonds with ozone to introduce ozonide (1,2,4-trioxolane) functional groups. The general objective was to test the applicability of such derivatized lipids by studying the drying behaviour and T_g depending on relevant processing and formulation parameters using a Box-Behnken experimental design. It was hypothesized that ozonized plant lipids can serve as drying agents for drying oils through the decomposition into radicals and presence of other unstable moieties introduced during the ozonization, which can then participate in the free radical autoxidation polymerization.

1.4.1.2 Chapter 3

While providing a fully biobased wood finish, drying oils do not only suffer from relatively long drying times but are also susceptible to microbial colonization and subsequent staining, which requires the drying oil finishes to be reapplied regularly. To reduce drying oil susceptibility to hydrolytic degradation (hydrolysis of ester cross-links) as a potential limiting factor for microbial colonization, this project was designed to test the applicability of transesterification and epoxidation of linseed oil to formulate a UV-curable substitute for drying oils. The goal was to systematically study the structure-property relationships of mixtures of epoxidized TAG/FAME and a cationic photoinitiator using a central composite experimental design. It was hypothesized that formulations of epoxidized linseed TAG and FAME can be cationically photopolymerized to form linseed drying oil alternatives with similar mechanical properties but higher resistance to hydrolytic degradation due to the formation of ether cross-links. Using a desirability optimization methodology, the

overall suitability of such formulations as a faster drying and potentially more durable alternative to drying oils was investigated.

1.4.1.3 Chapter 4

In the third project, the concept of biobased nanoreinforcement combined with solvent-free curing was applied to a polyurethane-based model system. While lipid-based polyols could be used as an intermediate, it was decided to use a commercial petroleum-derived polyol for the simplification of the model system. It was hypothesized that nanoreinforcement effects can be induced at very low loading levels and without the need for CNC surface modification if CNC can be maintained at a nanoscale throughout the dispersion in the resin and subsequent UV-curing. As the main coating component, a photocurable polyurethane-oligomer was synthesized as a carrier for CNC and tested for its ability to kinetically stabilize CNC to prevent its agglomeration. A variety of thermomechanical and mechanical analyses were performed to determine potential nanoreinforcement effects.

Chapter 2

A biobased reactive accelerant and diluent for solvent-free drying oils

Drying oils are unsaturated plant oils, widely used in paints and varnishes. The inclusion of solvent thinners and metal catalyst accelerators in drying oil formulations may be problematic from an environmental perspective. Here, the development of a biobased alternative that can act as both a reactive accelerant and a viscosity modifier for solvent-free drying oil systems, is reported. The ozonolysis of canola oil and linseed fatty acid methyl esters (FAME) produced compounds that were shown to be effective in directly adding to conjugated carbon-carbon double bonds (-CH=CH-) resulting in faster polymerization. For tung oil, substitution with 25 wt % of ozonized linseed FAME reduced the drying time by 70 % and the viscosity by 60 %, while the glass transition temperature approached that of a pure linseed oil film. The drying time reduction effect was found to be strongly dependent on the concentration of ozonized lipids but not greatly influenced by the ozonolysis time. For tung oil, a conjugated drying oil, incorporation of up to 65 wt % ozonized lipids was possible, resulting in dried films within less than 1 h at 60 °C and a 90 % viscosity reduction while maintaining up to 100 % biorenewable content and air-induced polymerization.

2.1 Introduction

Solvent evaporation makes a large contribution to the emission of volatile organic compounds (VOCs) during the physical drying of coatings. This source of urban air pollution [3] can be greatly decreased by using solvent-free polymerizable resins. Drying oils are probably one of the oldest cross-linkable paint binders [110] and have been used since prehistoric times [9]. They are still important components of film-forming industrial products but are associated with relatively long drying times. While combinations of metal catalysts and oxidative pretreatments can considerably reduce drying times for drying oils, these maybe associated with issues of toxicity [24, 111] and high viscosity [112, 113], respectively.

Drying oils such as linseed oil, tung oil, or poppy seed oil, are highly unsaturated and polymerize when exposed to molecular oxygen through a free-radical chain mechanism known as autoxidation (see Section 1.1.1.1). For non-conjugated oils, it is well known that the amount of *bis*-allylic methylene groups determines the ability to undergo autoxidative polymerization resulting in film formation.

Autoxidation follows a free radical chain mechanism, which includes lipid radical formation (initiation) and propagation through their reaction with oxygen to form lipid peroxy radicals which can abstract hydrogen atoms from lipids, regenerating a lipid radical. Ultimately, termination of the process occurs through radical-radical reactions resulting in cross-linking [24, 114]. Following the abstraction of hydrogen atoms, isolated carbon-carbon double bonds (*i.e.* -CH=CH-) can readily isomerize to form conjugated systems [24]. Also, due to the higher bond dissociation energy (BDE) of *mono*-allylic hydrogen atoms (322 kJ mol⁻¹) in conjugated systems compared to *bis*-allylic hydrogen atoms (272 kJ mol⁻¹) in lipids with isolated -CH=CH-, direct radical addition by peroxy radicals to a conjugated bond (BDE = 284 kJ mol⁻¹) is more favourable in conjugated lipids [32]:



This process can result in direct cross-linking without terminating the radical chain and is considered an important factor to explain the much faster drying of tung oil compared to linseed oil despite the similar degree in unsaturation.

Various methods have been used to accelerate the drying time of drying oils including the use of driers, and thermal/oxidative pretreatments of the oils. For coating driers, solubility is often imparted to the metal-based catalysts by reaction with organic acids, especially 2-ethyl hexanoic acid and versatic acid, to form metallic soaps [111]. Their classification and mechanisms are summarized in Table 2.1. In most cases, they are not considered true catalysts, as they can alter the course of the drying mechanism for example by altering the amount O₂ absorption [115] or causing delayed skinning (Table 2.1). Linseed oil is an example where thermal and oxidative treatments have been employed to accelerate drying. Boiled linseed oil has been prepared by heating linseed oil to 150 °C in the presence of driers (as in Table 2.1), resulting in increased viscosity [112]. Blown linseed oil is prepolymerized linseed oil obtained by blowing air through the oil at elevated temperatures (up to 130 °C) [113]. In contrast, in the absence of oxygen, thermal polymerization at temperatures above 270 °C [116] results in the isomerization into conjugated -CH=CH- systems, with subsequent Diels-Alder addition reactions [117] and possible interesterifications [118]. This results in a very viscous oil known as stand oil, which is more durable and less prone to yellowing [113]. Thinners like turpentine, mineral spirits, and naphtha have been commonly used in oil paints and varnishes [119–121], while "citrus solvent" containing limonene, introduced in the 1990s [122], is now sometimes promoted as a natural thinner alternative to mineral spirits.

Here, the development of a new type of combined solvent- and metal-free drying agent through the use of ozonized lipids is described. In this work, the fully biorenewable nature of drying oils is maintained by only

Table 2.1: Overview of common metal driers used in drying oils.

drier type [24]	most common metal ions [123]	likely mechanism	effects
surface driers (top driers, oxidative driers)	Co ²⁺ , Mn ²⁺ , Ce ³⁺ , V ³⁺ , Fe ²⁺	oxygen complex formation [124], Haber Weiss mechanism for peroxide decomposition [125]	induce drying from the top down [24], catalysis of peroxide formation and/or decomposition [123, 125, 126]
through driers (secondary driers)	Pb ²⁺ , Zr ⁴⁺ , Al ³⁺ , Bi ³⁺	Lewis acid co-catalysts to surface driers [24]	cannot initiate polymerization but control cross-linking anisotropy [24]
auxiliary driers (promoters, coordination driers)	Ca ²⁺ , K ⁺ , Li ⁺ , Zn ²⁺	cation adsorption onto pigments/fillers, reducing sites for surface drier inactivation [24]	increased drying rate [24]; zinc: delayed skinning, which allows for better O ₂ uptake and through drying [24, 127]

adding a drying agent comprised of partially ozonized lipids as outlined in Figure 2.1. It was hypothesized that the thermal decomposition of ozonides into radical species would accelerate autoxidative polymerization. To test this theory, drying agents were developed by subjecting canola triacylglycerides (TAG) and linseed fatty acid methyl esters (FAME) to ozonolysis, resulting in a range of compounds with different reactivities and molecular weights.

Although they are commonly manufactured derivatives of TAG oils, the use of FAME in drying oils has rarely been described. Biermann et al. [128] reported on the use of different fatty acid esters from calendula oil and tung oil as reactive diluents in a linoleic acid-based alkyd and other commercial resins. The low molecular weights and presence of conjugated -CH=CH- bonds in these FAME successfully lowered the viscosity of the resins and accelerated their polymerization, but also reduced the hardness of the cured films. Variations to the alcohol type in the transesterification reaction, including alcohols substituted with allyl or vinyl groups rather than straight chain alcohols (including methanol, as used in the present study) gave no additional advantage to curing rate. Similarly, Stenberg et al. [129] reported on the viscosity reduction potential and film softening when using linseed FAME in linseed oil. Furthermore, they found that the amount of residual isolated *cis* -CH=CH- was reduced in the presence of the reactive diluent, which could indicate improved film through-drying.

Lipid ozonolysis has been widely studied in connection to structure determination (first described by Harries [130]) and in organic synthesis (such as ozonides [131, 132], aldehydes/ketones [133, 134], and acids [135, 136]). Ozonized lipids have been used as disinfectants, anti-inflammatories, and in skin treatments [137–141]. Ozonolysis is usually performed in inert solvents and often at temperatures below 0 °C [142]. It is generally accepted [143, 144] that the reaction of O₃ with olefinic compounds follows the mechanism (Scheme 2.1) first proposed by Criegee [145]. A cyclic 1,2,3-trioxolane intermediate, referred to as the primary ozonide (**1**), is formed through the cycloaddition of O₃ to the double bond. This decomposes into a zwitterion (**2a**), and a carbonyl fragment (**2b**). The zwitterion can recombine with the carbonyl to form the more stable 1,2,4-trioxolanes or secondary ozonides (**3a**). However, there are other reaction products, including various oligomeric (**3b**) or polymeric ozonides (peroxide oligomers [146]). The yield of ozonides is reduced

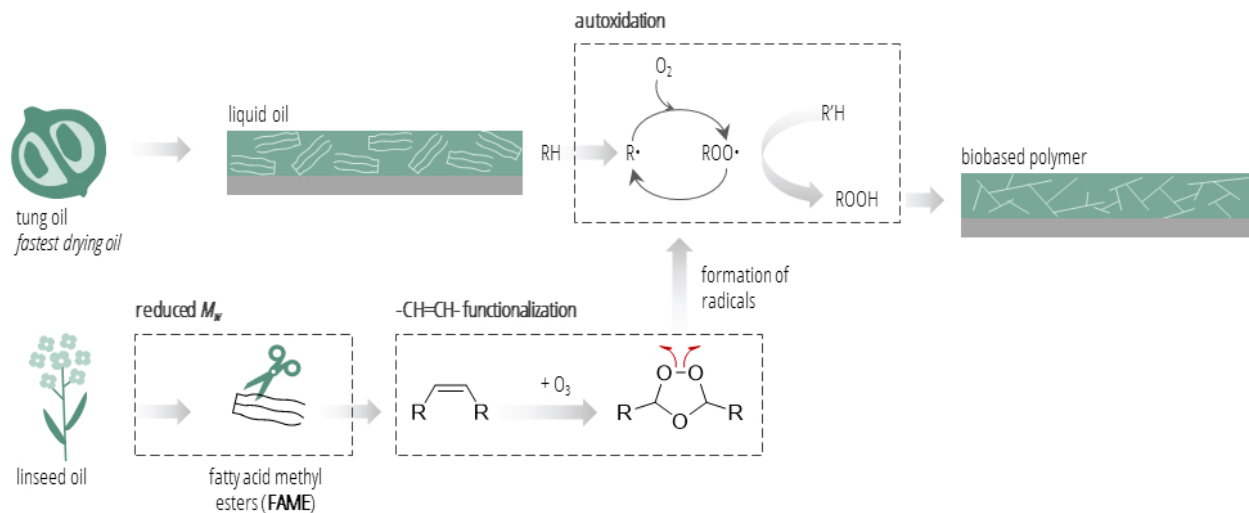
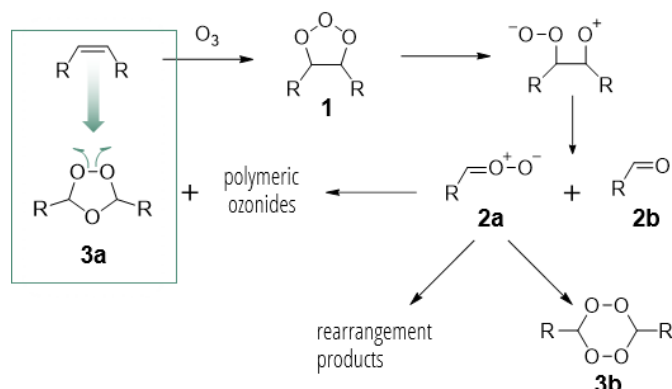


Figure 2.1: Schematic overview of the approach used to develop accelerants for drying oils using ozonized lipids, which can participate in autoxidative polymerization through decomposition into radical species. To obtain dual purpose as a reactive diluent, the functionalization of FAME as a drying agent for tung oil was investigated.

when solvents of higher polarity are used; this may depend on their relative stabilization of the zwitterion, preventing the formation of secondary ozonides [147, 148]. While most available literature is based on the ozonolysis of vegetable oil and their derivatives in organic solvents, ozonide formation has also been achieved in liquid CO_2 [149, 150]. The concept of using ozone in drying oils is mentioned in some reports dating back to the late 19th century [151, 152]. In various technical publications from the early half of the 20th century, ozone-treated drying oils were described as fast-drying and being of high viscosity, but these were mostly prepared for linoleum production rather than in oil paints [153–155].

The present work explores the use of ozone to accelerate the curing of drying oils *via* the synthesis of a novel lipid-based drier. In order to achieve a system with a high polymerization rate, the initial study uses the drier in combination with a conjugated plant oil (tung oil). However, in Canada at least, the use of non-conjugated, locally-grown unsaturated oils (canola and linseed) as raw materials for the drier, decreases the overall cost of the mixture with imported tung oil, and increases the content of locally sourced biomass. In order to optimize the new drier and its possible application in coatings, response surface methodology was used to study the effects of ozonolysis time, lipid structure, and drier/tung oil composition on the drying time and viscosity of formulations, as well as on the glass transition temperature (T_g) of cured films. Fourier transform infrared (FTIR) spectroscopy was extensively used to study changes at the molecular level occurring during ozonolysis and curing.



Scheme 2.1: Simplified reaction of O₃ with olefinic -CH=CH- according to the Criegee mechanism in an inert solvent. Formation of the secondary ozonide is the targeted functionalization of the lipid -CH=CH- for the synthesis of the drying agents in this study.

2.2 Materials and methods

2.2.1 Materials

Pure tung oil by Real Milk Paint Co. was obtained from Harvest Haven (Lethbridge, Alberta, CA). Food grade canola oil (ACH Food Companies Inc., Memphis, Tennessee, USA) and cold-pressed linseed oil (Winsor & Newton, London, UK) were purchased from a local supermarket and artist store, respectively. The plant oils were used as supplied. Linseed FAME were prepared as described previously [156]. Hexanes (reagent grade, CAS 110-54-3) was purchased from Caledon Laboratories Limited (Georgetown, Ontario, CA). CaCO₃ (light powder) was purchased from ACP Chemicals (Montreal, Quebec, CA). Polystyrene standards (EasiVial PS-M, Agilent Technologies) with molecular weights between 282 g mol⁻¹ and 113 300 g mol⁻¹ were used to generate a calibration curve for gel permeation chromatography. Ozone generation is described in Section 2.2.2.1.

2.2.2 Methods

An overview of the conducted experiments and analyses is illustrated as a process flow diagram in Figure 2.2. The two main aspects of this research concern the synthesis of the drying agents, and the systematic study of their mode of action and impact on tung oil-based films.

2.2.2.1 Ozonolysis reaction

Canola oil and linseed FAME were ozonized in hexanes (10 wt%) at an initial temperature of 10 °C. The setup of the apparatus for the ozonolysis reaction is illustrated in Figure 2.3. The reaction was performed in a jacketed three-neck vertical round-bottom flask (500 mL) with a magnetic stirrer. Cooling of the reactor flask was carried out using a circulating chiller (Julabo F25, Julabo USA Inc., USA) and the initial temperature of lipid-solvent mixture (200 mL) was 10 °C. Ozone was generated by passing dry oxygen as the feed gas

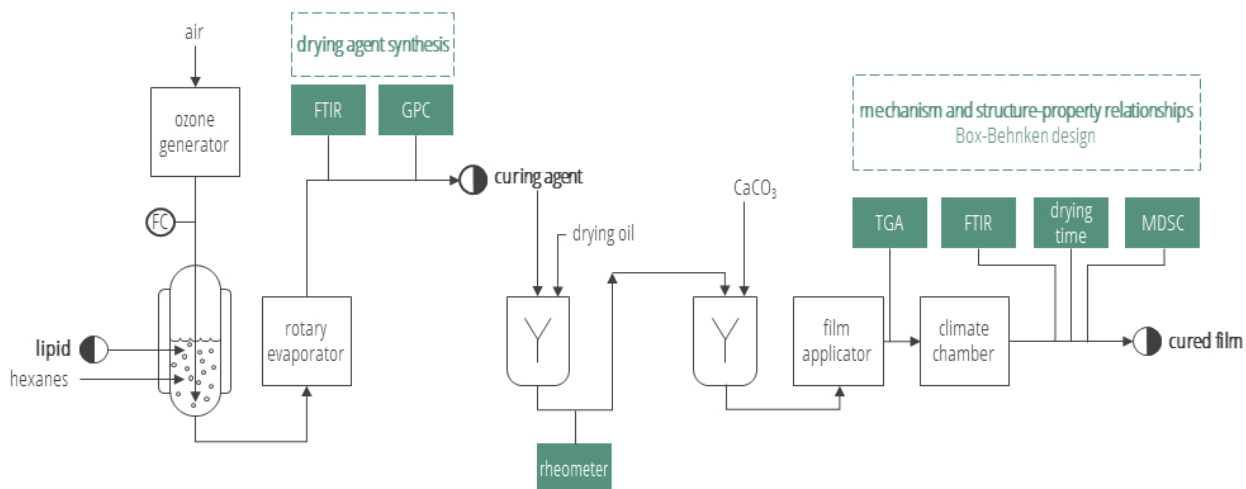


Figure 2.2: Simplified process flow diagram of the experimental setup and analyses to develop lipid-based accelerants, and to investigate their effect on the drying behaviour of tung oil.

through an ozone generator (ATLAS Ozone Generator,) coupled to a controller unit (Ozone monitor 454H, Teledyne API, San Diego, USA) at a concentration of 100 g m^{-3} . A stainless steel inlet solvent filter was used as the diffuser to feed the gas into the bottom of the reactor. Ozone was introduced into 200 mL of the lipid-solvent mixtures at a flow rate of 1.5 L min^{-1} .

As the gas escaped the liquid, it was neutralized through a gas bubbler and discharged through the fume hood exhaust. While the ozone concentration of 100 g m^{-3} could be maintained throughout the reaction with linseed FAME, the effective concentration for canola TAG dropped with time (down to 70 g m^{-3} after 35 min) due to deposits of higher molecular weight product on the diffuser. The solvent (and other volatiles) were then removed using a rotary evaporator at $25 \text{ }^\circ\text{C}$ until and the ozonized lipids were stored at $-5 \text{ }^\circ\text{C}$ until further use.

2.2.2.2 Attenuated total reflectance Fourier transform infrared spectroscopy

Attenuated total reflectance Fourier transform infrared spectroscopy (ATR-FTIR) was used to monitor the change in functional groups during the synthesis of the drying agents, as well as to compare the surface functionality of the dried films. A total of 16 interferograms at a resolution of 4 cm^{-1} were summed before Fourier transformation (Platinum ATR Alpha, Bruker). Automatic baseline correction using the OPUS software (Bruker) was performed for the spectra of the linseed FAME and canola oil after 0 min, 5 min, 20 min, and 35 min of ozonolysis. The local maximum method and the second derivative algorithm were used for automatic peak detection (OriginPro 2019b). For the dried films, the spectra were normalized by the total absorbance in order to account for inhomogeneities due to the presence of filler particles (CaCO_3). For kinetic analysis, second derivatives with a Norris filter (gap-segment = 1-2) were calculated when band separation was needed instead of band area determination.

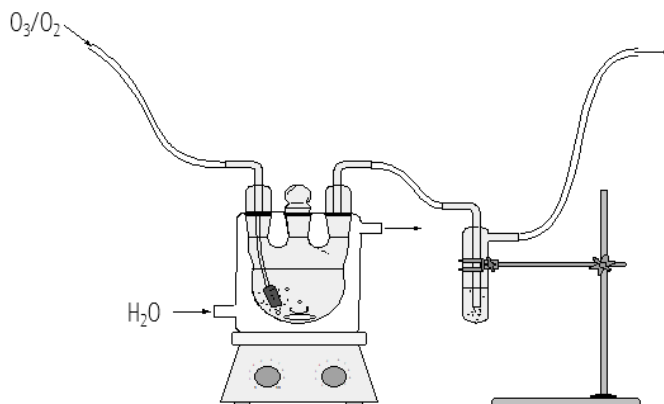


Figure 2.3: Apparatus for the ozonolysis of the lipids, the reaction products of which were tested as an accelerant and reactive diluent.

2.2.2.3 Gel permeation chromatography

A 1200 series high performance liquid chromatograph from Agilent Technologies (Agilent Technologies Inc, USA) equipped with an evaporative light scattering detector (Alltech ELSD 2000, Mandel Scientific Company, CA) at a drift tube temperature of 60 °C was used to monitor the change in the molecular weight distribution of the lipids during ozonolysis. A GPC column ((300 × 4.6) mm² i.d.) with a particle size of 5 μm (Styragel HR 4E THF, Waters Corporation) was used under isocratic conditions: mobile phase of tetrahydrofuran (THF, HPLC-grade) at a flow rate of 0.5 mL min⁻¹ and an injection volume of 10 μL. The sample preparation included diluting about 0.3 mg of the ozonized lipids into 10 mL of THF. Polystyrene standards with known MW (Agilent EasiVial GPC/SEC Calibration Standards, Agilent Technologies Inc, USA) were used to generate a calibration curve. The chromatographs were normalized by dividing the curves by the total peak area.

2.2.2.4 Decomposition enthalpy

A differential scanning calorimeter (TA Q100, TA Instruments) was used to determine the drying agents' decomposition enthalpy (ΔH_{dec}). Samples of 4 mg to 5 mg of the ozonized lipids were scanned at a temperature ramp of 10 °C min⁻¹ from 25 °C to 250 °C in hermetic aluminum crucibles under nitrogen flow. The decomposition enthalpy was determined as the area below the exothermal peak using the TA analysis software (Universal Analysis 2000) with linear interpretation.

2.2.2.5 Dry-through time determination

The drying progress was studied using a drying time recorder (TQC Drying Time Recorder, Paul N. Gardner Company, Inc.) based on ASTM D5895 [157]. Calcium carbonate (CaCO₃) is often used as an "inert" pigment and filler in drying oils [158]. In this study, CaCO₃ was used at a 1:1 weight ratio to overcome the crawling (de-wetting) of oil films on the glass slides used for the drying time recorder. Films with a wet

thickness of 30 μm were applied to the glass slides using a cube film applicator of 30 μm gap size (Paul N. Gardner Company, Inc.). Drying was conducted in a climate chamber with controlled temperature (60 $^{\circ}\text{C}$) and humidity (20 % relative humidity), and 5 g weights were applied to the needles. Drying oil coatings continue to cure during their lifetime, hence, the dry-through time (where the needle no longer leaves a track) was used as a proxy to quantify the drying time. It was previously established, that the dry-through time was reproducible using the conditions described above for tung oil ($M = 6.8$ h, $SD = 5$ min, $n = 3$), with M being the sample mean and SD the standard deviation.

2.2.2.6 Viscosity determination

The viscosities of the drying agents and mixtures with tung oil were determined by rotational rheology (Advanced Rheometer AR 2000, TA instruments) at 25 $^{\circ}\text{C}$ using a plate/cone geometry (2 $^{\circ}$, 40 mm, truncation gap distance of 52 μm) over a shear rate range from 1000 s^{-1} to 100 s^{-1} (downramp) under steady state conditions. Linear regression was used to determine the viscosity in the tested shear rate range (first Newtonian plateau). For the suspensions containing CNC, up- and down-ramps were applied to the sample. The analyses were preceded by a 5 min conditioning step at the measurement temperature.

2.2.2.7 Modulated differential scanning calorimetry

Modulated differential scanning calorimetry (MDSC) was used to determine the glass transition temperature (T_g) of the cured films (24 h at 60 $^{\circ}\text{C}$) using a differential scanning calorimeter (TA Q100, TA Instruments) and standard aluminum sample pans. The samples were directly cooled to -90 $^{\circ}\text{C}$ at a rate of 10 $^{\circ}\text{C min}^{-1}$. Then, a modulated heating profile up to 40 $^{\circ}\text{C}$ was applied using a linear heating rate of 2 $^{\circ}\text{C min}^{-1}$ and a modulated heating rate with a 60 s modulation period and 1 $^{\circ}\text{C}$ temperature amplitude. The glass transition temperatures were determined from the reversing heat flow curve using the TA analysis software (Universal Analysis 2000) from the inflection point between onset and endpoint of the glass-rubber transition range.

2.2.2.8 Experimental design and statistical analysis

Box-Behnken design Response surface methodology was used to map how the response (drying time, viscosity, and T_g) is dependent on ozonolysis time, drying agent concentration, and the ratio of $\text{FAME}_{\text{oz}}:\text{TAG}_{\text{oz}}$. A Box-Behnken design with three centre points was chosen as an effective tool to determine the influence and interaction of ozonolysis time, drying agent concentration, and drying agent type (FAME and TAG) at three levels (Table 2.2). A total of 15 experiments were conducted analyzed using the "Design of Experiments" app (file version 1) for OriginPro 2019b (significance level $\alpha = 0.05$).

Spectral principal component analysis Spectral principal component analysis (PCA) was used to compare the ATR-FTIR spectra of dried oil films (with baseline correction and normalization, see Section 2.2.2.2) using the "Principal Component Analysis for Spectroscopy" app (file version 1.3) for OriginPro 2019b. The PCA was performed based on the covariance matrix and 2 components were extracted.

Table 2.2: Box-Behnken design matrix with coded (-1, 0, and 1 for the three levels) and real values for ozonolysis time (X_1), drying agent concentration (X_2), and FAME_{oz}:TAG_{oz} ratio of the drying agent (X_3).

	X_1		X_2		X_3	
	coded	real [min]	coded	real [wt%]	coded	real [%]
1	0	20	0	15	0	50
2	1	35	0	15	-1	0
3	0	20	-1	5	-1	0
4	0	20	-1	5	1	100
5	1	35	-1	5	0	50
6	1	35	0	15	1	100
7	0	20	1	25	1	100
8	-1	5	-1	5	0	50
9	-1	5	0	15	1	100
10	1	35	1	25	0	50
11	0	20	0	15	0	50
12	-1	5	1	25	0	50
13	-1	5	0	15	-1	0
14	0	5	0	15	0	50
15	0	20	1	25	-1	0

Comparing two means To test whether the means of two independent samples are equal, independent two-sample t -test analysis (two-tailed, significance level $\alpha = 0.05$) was performed using OriginPro 2019b. The analysis was considered "inconclusive" for statistical power < 0.8 as a result of the low sample size (triplicate or duplicate).

2.2.2.9 Preparation of the model nanocomposites

Linseed FAME and canola TAG ozonized for 35 min (expected higher polarity due to longest ozonization time) were chosen to investigate the dispersibility of PGX-CNC (obtained from Ceapro Inc., Edmonton, CA), a CNC aerogel obtained through supercritical fluid drying (*cf.* Section 1.3.1) in combination with pressurized gas expansion (PGX) technology. Small batches of 0.5 wt % CNC in the drying agents were prepared and sonicated for a few seconds by applying pulsed ultrasonication (Sonic Dismembrator Model 100, Fisher Scientific) until a transparent suspension without microscopic particles was obtained. The obtained CNC-drying agent suspensions were mixed with tung oil at a weight ratio of 1:1 to prepare drying oil-nanocomposites. Their T_g and viscosity was determined as described in sections 2.2.2.7 and 2.2.2.6, respectively.

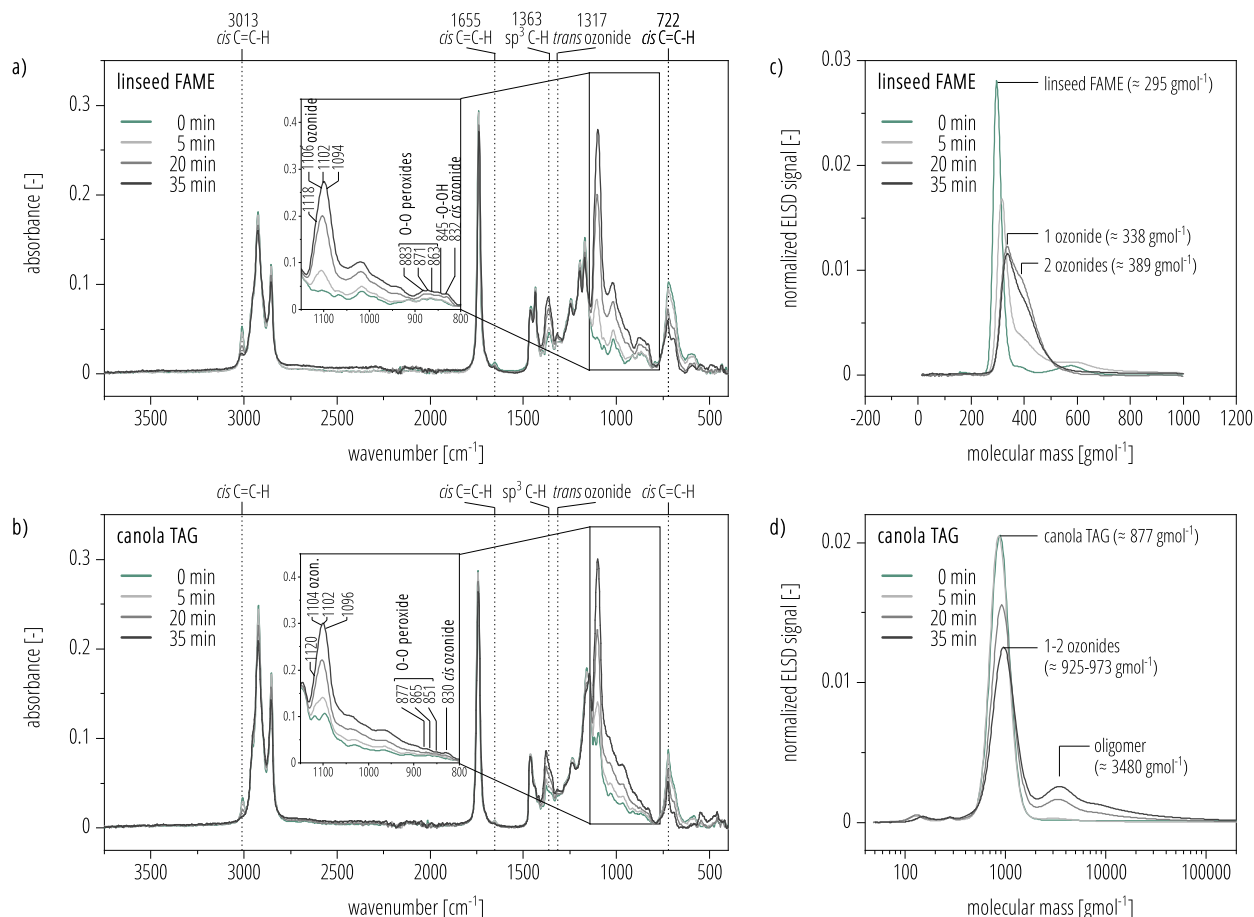


Figure 2.4: Monitoring of lipid functionalization during ozonolysis (up to 35 min). **a)** FTIR spectra of ozonized linseed FAME. **b)** FTIR spectra of ozonized canola TAG. The inset graphs show overlapping bands specific to ozonide and peroxide moieties. **c)** Transformed GPC traces of ozonized linseed FAME. **d)** Transformed GPC traces of ozonized canola TAG.

2.3 Results and discussion

2.3.1 Drying agent synthesis and analysis

Here, ozonized species of the linseed FAME and TAG are referred to as FAME_{oz} and TAG_{oz}, respectively. During the course of ozonolysis, canola TAG and linseed FAME were bleached to pale yellow and clear liquids after removal of the solvent (images are given in A.2.1). Figure 2.4a) and 2.4b) show how the ATR-FTIR spectra of FAME_{oz} and TAG_{oz} change during the 35 min of ozonolysis. A progressive loss of absorbance from -CH=CH- bonds following attack by ozone can be seen at approximately 3013 cm⁻¹, 1655 cm⁻¹, and 722 cm⁻¹. The subsequent formation of ozonides and peroxides resulted in the appearance of overlapping bands in the range of 1200 cm⁻¹ to 800 cm⁻¹ (see inset graphs).

The appearance of a strong band in the range of 1110 cm⁻¹ to 1105 cm⁻¹ during the ozonolysis is attributed to the formation of the 1,2,4-trioxolane ring (ν C-O) in ozonides [146, 159, 160]. In the present case, the broad

and overlapping bands in this region suggest the formation of a multitude of products with the likely ozonide band appearing at 1106 cm^{-1} and 1104 cm^{-1} for the FAME_{oz} and TAG_{oz}, respectively. In addition, increases in bands attributed to *trans* and *cis* isomers of ozonides were seen at about 1320 cm^{-1} and 830 cm^{-1} [161], respectively. The absorbances between 900 cm^{-1} and 800 cm^{-1} were higher for FAME_{oz} when compared to TAG_{oz}. Vacque et al. [162] showed that $\nu\text{O-O}$ vibrations of peroxides occur in this region, more specifically from 885 cm^{-1} to 845 cm^{-1} . The formation of peroxidic bonds would be expected through further reactions of ozonides (*e.g.* oligomeric ozonides, see Scheme 2.1). Overall, ATR-FTIR analysis demonstrated the successful functionalization of the lipids with ozonide and some peroxide moieties, which might be sources of radical decomposition products to accelerate the autoxidation of drying oils.

Ozonide formation was further supported by the observed change in the molecular weight distribution upon reaction of ozone with linseed FAME and canola TAG (Figures 2.4c) and 2.4d)). The shift in the main peaks during the reaction are consistent with the electrophilic addition of one and two molecules of ozone ($+48\text{ g mol}^{-1}$ and 96 g mol^{-1}). The formation of high-molecular weight oligomers was only observed for ozonized canola TAG with increasing duration of ozonolysis. Canola TAG was selected because when the ozonolysis of the highly unsaturated linseed TAG was attempted, a more rapid formation of high-molecular weight oligomers and gelation was observed. DSC analysis (see 2.3.1.1) suggests a similar degree of total oxidation for canola TAG and linseed FAME. Therefore, comparing mixtures with different ratios of canola TAG and linseed FAME will reveal the effect of molecular weight (TAG *versus* FAME and corresponding oligomerization) with a smaller contribution from residual unsaturation and differences in the type of oxidative functional groups formed.

2.3.1.1 Decomposition enthalpy

Ozonized vegetable oils are considered stable at room temperature [146]. This was also demonstrated for the synthesized drying agents using DSC analysis. During thermal decomposition, homolytic cleavage of the O-O bond is the rate-determining step for the subsequent formation of aldehydes and carboxylic acids, as well as other by-products [163]. As shown in Figure 2.5, the average peak degradation temperature was significantly ($p \leq 0.006$) higher in the ozonized canola oil samples ($153\text{ }^\circ\text{C}$ to $155\text{ }^\circ\text{C}$) compared to linseed FAME ($145\text{ }^\circ\text{C}$ to $148\text{ }^\circ\text{C}$) during the 5 min to 35 min of ozonolysis (data for the independent *t*-test are listed in Table A.11, A.2.6.2.). This corresponds to the reported temperature range of approximately $110\text{ }^\circ\text{C}$ to $160\text{ }^\circ\text{C}$ [146, 164, 165]. There was no statistical difference in ΔH_{dec} of the two lipid types, except for 25 min of ozonolysis (data for the independent *t*-test are listed in Table A.10, A.2.6.2.). According to Cataldo [146], this indicates a similar degree of total oxidation reached due to the heat released being reportedly unaffected by the proportions of different oxygenated species present. The analysis suggests equal energy potential for both types of ozonized lipids, as well as non-explosive character despite the presence of chemical groups associated with explosive properties. With the highest observed ΔH_{dec} of 209 J s^{-1} in a decomposition temperature range $<190\text{ }^\circ\text{C}$, the ozonized lipids would not be classified as Class 1 explosives [166].

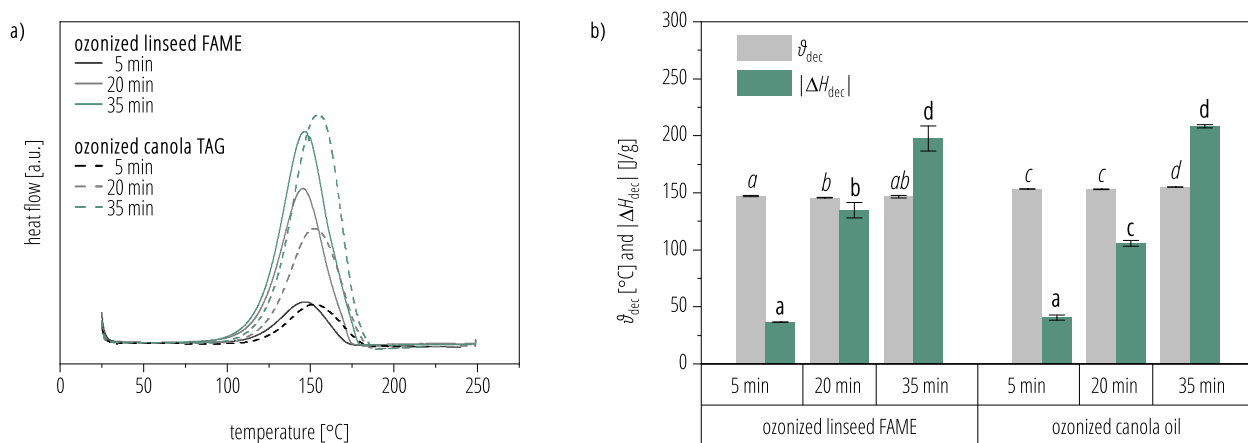


Figure 2.5: **a)** Representative heat flow graphs for the linseed FAME_{oz} and canola TAG_{oz} (exo up). **b)** Grouped box plot showing the increasing decomposition enthalpy (ΔH_{dec}) with ozonolysis duration and difference in peak degradation temperature depending on the lipid feedstock. The error bars represent the standard deviation ($n = 3$). Means with different letters are significantly different (t -test with Welch correction, $\alpha = 0.05$).

2.3.2 Systematic drying agent performance analysis in tung oil

A Box-Behnken design was used to study the effect of ozonolysis time, lipid type (FAME_{oz} versus TAG_{oz}), and concentration on three response variables: dry-through time, viscosity, and T_g . The data collected from the 15 experiments is plotted in Figure 2.6, along with the properties of a pure tung oil sample. The observed trends of reduced viscosity and dry-through time for the mixtures of tung oil with the drying agents are investigated below by response surface methodology. All response surface models had $R^2 \geq 0.96$ and non-significant lack-of-fit tests indicating a good fit for the models [167]. Detailed results of the statistical analyses can be found in A.2.6.1.

2.3.2.1 Viscosity reduction

The viscosities of almost all ozonized FAME/TAG mixtures were lower than the viscosity of pure tung oil, with the exception of the canola TAG-based drying agent with longest ozonolysis time (35 min), which contained more high-molecular weight reaction products (Figure 2.7b)). Thus, drying agent mixtures containing high proportions of FAME_{oz} are the most suitable for use as a reactive diluent. These would be expected to have improved penetration into wood, without the use of additional solvents. In a preliminary qualitative study, it has indeed been demonstrated faster penetration of tung oil with 25 wt % FAME_{oz,20min} into spruce specimens (longitudinal to fibre orientation), as seen in Figure A.11, A.2.5. For other applications where a higher viscosity might be beneficial (*e.g.* imparting body to a paint), a high proportion of ozonized TAG species could be used.

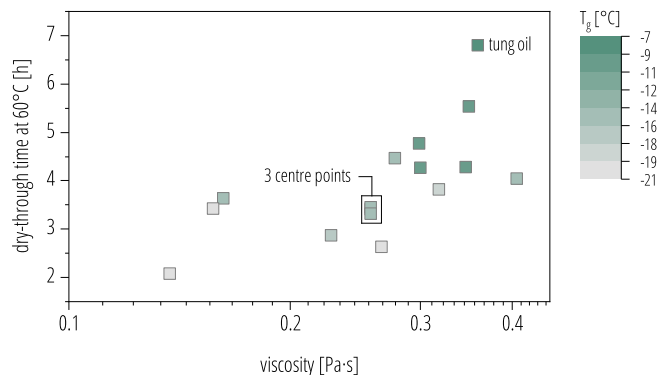


Figure 2.6: Overview scatter plot of the recorded response variables for the different formulations of the Box-Behnken design. The colour map indicates the effect on T_g . Most formulations had a lower viscosity (25 °C) and shorter drying times at 60 °C, but a lower T_g compared to pure tung oil.

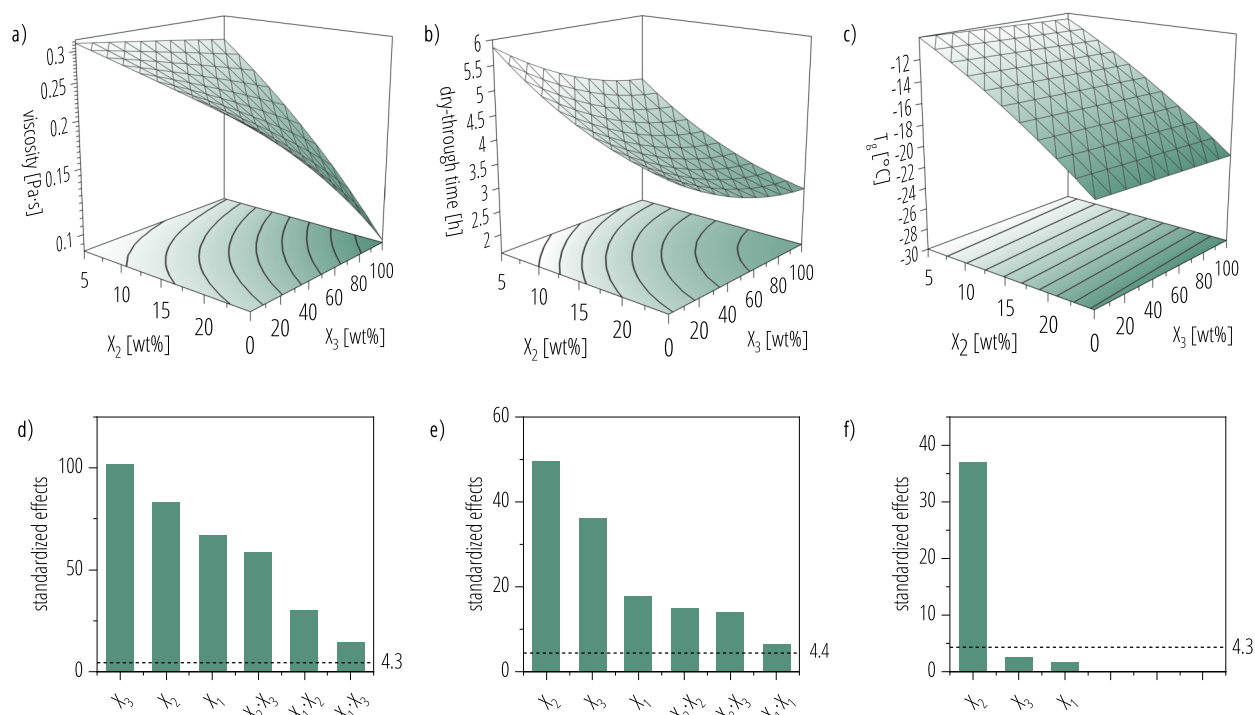


Figure 2.7: Response surface plots for a) the viscosity at 25 °C, b) the dry-through time, and c) the T_g after 24 h drying at 60 °C. An ozonolysis time of 5 min was used in all three surface plots. Graphs d)-f) show the Pareto plots of the absolute values of the standardized effects. The factors of the Box-Behnken design are denoted as X_1 for the ozonolysis time, X_2 for concentration of ozonized lipids in tung oil, and X_3 for the FAME_{oz}:TAG_{oz}. In all cases, the drying agent concentration and FAME_{oz}:TAG_{oz} ratio had the strongest effect on the response variables.

2.3.2.2 Drying time reduction

The dry-through time for films of tung oil/drying agent were measured using a drying time recorder, as described in Section 2.2.2.5. Photographs of typical glass slides and needle tracks are also shown in Figure A.2, A.2.2.1. The shortest dry-through time achieved was 2.1 h, observed in the presence of 25 wt % of FAME_{oz,20min}. This represents a remarkable 70 % reduction in drying time compared to the 6.8 h measured for pure tung oil. In the control experiment with non-conjugated cold-pressed linseed oil (A.2.3), no shortening in drying time was observed.

The drying agent concentration had the strongest effect on drying time reduction, followed by the FAME_{oz}:TAG_{oz} ratio, and ozonolysis time. Increasing drying agent concentration, relative content of FAME_{oz}, and ozonolysis time reduce the drying time but the effect becomes smaller at higher levels, as evidenced by their significant quadratic terms. While the degree of oxidation was significantly increased for FAME_{oz} and TAG_{oz} with increasing ozonolysis time (Figure 2.5, Section 2.3.1.1), it did not have a very strong effect on the drying time reduction.

Reduced induction time and higher polymerization rate In order to investigate how the presence of the ozonized drying agent changes the curing process in tung oil, FTIR spectroscopy was used. FTIR data was obtained throughout the drying of tung oil containing 25 wt % FAME_{oz,20min}, which had the shortest observed drying time. Similar data were also obtained for cold-pressed linseed oil (A.2.3). In Figure 2.8, the changes in abundances of diagnostic absorbances in the FTIR spectra for the tung oil-based system are plotted against drying time at 60 °C (see Figures A.3 and A.4 in A.2.2.2 for the full spectra). Figure 2.8 shows the occurrence of some distinct changes in the chemical composition over time, characteristic of the onset of free radical oxidative chain reactions. It is well-known that the induction time for lipid oxidation processes can be delayed by the presence of antioxidants or accelerated by pro-oxidants [24]. In the case of tung oil, the onset is recognizable by the disappearance of conjugated trienes (Figure 2.8d)), which are present in high abundance in tung oil as α -eleostearic acid (9*cis*-,11*trans*-,13*trans*-octadecatrienoic acid). In addition, the disappearance of isolated *cis* -CH=CH- bonds from linoleic and oleic acids which are present in tung oil at low amounts (<10% each) is evident (Figure 2.8b)). It can be seen from Figure 2.8d) that the presence of 25 wt % FAME_{oz,20min} (green line) significantly reduces the induction times for these oxidative processes compared to pure tung oil (grey line) from approximately 170 min to <50 min. Similarly, the induction time has also been significantly reduced in cold-pressed linseed oil (A.2.3).

The induction time of drying oils can be reduced through the deactivation of antioxidants and by pro-oxidants [169, 170], leading to the formation of singlet oxygen or peroxy radicals [24, 41]. However, the observed reduction in induction time does not completely account for the total measured dry-through time reduction of 280 min (derived from the drying time recorder), which was found for conjugated tung oil and not observed using the drying agents in (non-conjugated) linseed oil, even though solid films were still obtained. This implied involvement of conjugation in the acceleration mechanism suggests that radical decomposition products from the ozonized drying agent add to conjugated -CH=CH- bonds (Equation 2.1) prior to the the expected initiation of radical chain reactions *via* hydrogen atom abstraction, as seen with isolated -

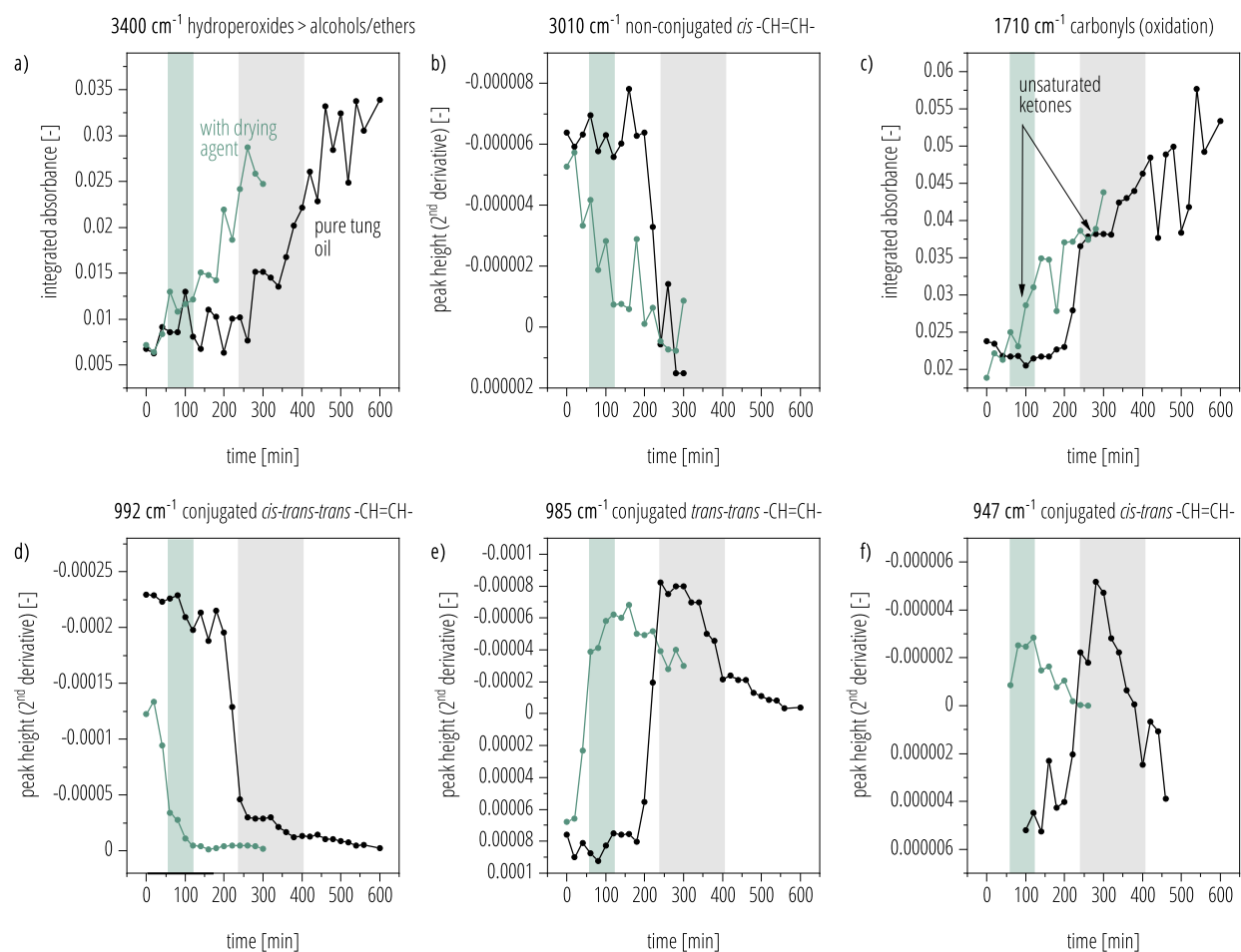


Figure 2.8: ATR-FTIR analysis ($n = 1$) of the drying kinetics at 60 °C of pure tung oil (dark grey) and with 25 wt % FAME_{oz,20min} (green) for the upper surface of the films. The shaded areas represent the observed time for tack-free surface to the measured dry-through time. **a)** and **c)** Integrated peak area for the following regions of interest: 3400 cm⁻¹ (3692 cm⁻¹ to 3136 cm⁻¹), and 1710 cm⁻¹ (1734 cm⁻¹ to 1672 cm⁻¹) based on De Viguerie et al. [168]. **b)** and **d)-f)** Peak height of second derivatives with Norris filter (segment length 1 and gap of 2) for different double bond configurations at 3010 cm⁻¹, 992 cm⁻¹, 985 cm⁻¹, and 947 cm⁻¹.

CH=CH- systems. The ratio addition:hydrogen abstraction, which is important in determining molecular weight in radical polymerization, is thought to be higher for carbon-centred radicals as opposed to heteroatom-centred radicals [35], such as those formed during the homolytic scission of the O-O bond in ozonides or peroxides [164]. However, increasing electrophilicity for heteroatom-centred ($\text{HO}\cdot > \text{ROO}\cdot > \text{RO}\cdot$) has been associated with a higher tendency for addition to double bonds [35, 171, 172]. Hence, it remains to be investigated whether radicals from the homolytic cleavage of the peroxide bonds (-O-O-) in ozonides are directly involved in radical addition or whether this observation is a result of carbon-centred radicals formed through a variety of decomposition reactions involving β -scission, as described in the literature [173, 174].

Consistent with the idea of direct radical addition, it was found that the rate of *cis*-CH=CH- disappearance due to isomerization (Eq. 1.1, Section 1.1.1.1) into conjugated systems after H-atom abstraction (Figure 2.8e) and f)) is reduced in the presence of the drying agent (Figure 2.8b)) and did not show the abrupt drop observed during pure tung oil drying right before film formation. Direct radical addition results in cross-linking and therefore an increase in molecular weight before the radical concentration is high enough for termination reactions. This might explain why the drying time was reduced by considerably more than the decrease in induction time despite the absence of the triacylglycerol structure in the FAME-based drying agent which has correspondingly fewer ester linkages.

An initial broadening of the carbonyl bands (1710 cm^{-1} , Figure 2.8c)) was found to be dominated by the formation of unsaturated ketones at 1696 cm^{-1} [175]. As recently reviewed by Honzík [38], ketones and alcohols, may not be formed by the widely described Russell termination mechanism involving peroxy radicals, but through H atom transfer involving two alkoxy radicals [176] and H atom abstraction in the α -position to a hydroperoxide group [38]. As discussed below, it was observed that the main O_2 uptake during the air-drying of tung oil/drying agent mixtures at 60°C occurs after film formation. The observation of initially lower and more gradual formation of ketone by-products in the presence of the drying agents (Figure 2.8c)) during film formation further supports that the involved radical decomposition products are less likely to be involved with H atom abstraction reactions. Direct radical addition to *cis-trans-trans* conjugated trienes first converts them to dienes before these dienes can undergo further reactions themselves. The observed faster drop in conjugated *cis-trans* dienes compared to *trans-trans* dienes (Figure 2.8e) and f)) may reflect the rearrangement of the conjugated hydroperoxides from *cis,trans* to *trans,trans* [177]. This can proceed via β -fragmentation during which rearrangement into a *transoid* conformation occurs, driven by greater thermodynamic stability [28]. However, the band at 975 cm^{-1} for isolated *trans*-CH=CH- [178] did not appear until the main uptake of oxygen as discussed in the following section.

Ozonides such as ozonized isoprene or diisobutylene ozonide have been previously reported as polymerization catalysts for various monomers with conjugated -CH=CH- systems, such as styrene. These ozonides were found to initiate polymerization [179, 180] and to be more reactive than benzoyl peroxide [181], which is also known to catalyze tung oil polymerization [182]. Although the ozonolysis of lipids is well studied, little has been reported about the effects of ozonized lipids on promoting lipid oxidation. Ewing et al. [183] showed that allylbenzene ozonide can effectively increase the rate of methyl linoleate autoxidation (in the absence of antioxidants) as monitored by the formation of conjugated dienes. They reported that the autoxidation

rate of methyl linoleate is significantly lower in the presence of ozonized methyl oleate compared to ozonized allylbenzene, where ozonolysis occurs at the terminal position. This suggested that the structure of the ozonide can have a strong influence on reactivity and potentially on the addition:hydrogen abstraction ratio.

Faster onset of O₂ absorption Acceleration of the autoxidative drying of tung oil due to the inclusion of 25 wt % FAME_{oz,20min} was also seen by thermogravimetric analysis (TGA) under dry air at 60 °C (Figure 2.9a)). The rapid weight increase of a film of tung oil (with CaCO₃ filler) due to O₂ absorption occurred considerably earlier when the ozonized drying agent was present. The observed onsets of oxygen uptake were found to approximately correspond to the measured dry-through times.

These results are also consistent with the observations from the FTIR spectra of the upper surface of the films taken after 24 h of drying at 60 °C (Figure A.5, A.2.2.3). These show that for tung oil, both with or without the drying agent, significant oxygen uptake occurs after film formation. This can be seen by the large increase in oxygen-containing functional groups beyond film formation, for example an increase in ketone absorbances, accompanied by significant further decreases in conjugated double bonds. Hence, in contrast to linseed oil where the main uptake of O₂ is an indication of the induction time [158, 184], conjugated tung oil exhibits an earlier onset of autoxidative polymerization that is more accurately represented by the FTIR data (Figure 2.8 and shaded areas in Figure 2.9a)).

In order to rule out any contribution from the filler (or aluminum sample pan) and to confirm the general applicability to lignocellulosic substrates, the TGA analysis was successfully repeated on a bamboo surface (Figure 2.9a) III). Despite the poor signal-to-noise ratio of this trace (the low relative humidity in the TGA chamber results in some water evaporation, requiring data processing against a blank sample) it clearly shows a similar time for rapid oxygen uptake, demonstrating that the effectiveness of the drying agent is not influenced by the filler or greatly affected by the bamboo (or wood) substrate. It is seen in Figure 2.9a) that there is a lower net absorption of oxygen in the presence of the drying agent, leading to only about half as much weight gain. At the same time, a much higher net loss of weight due to the emission of volatile oxidation products was observed over the 1 day time period. It has been reported previously that drying oils (even in the absence of thinners) can give off volatile oxidation products on drying, such as the emission of hexanal and propanal from linoleic and linolenic acid-rich oil paints [185]. Possibly this was enhanced by the inclusion of low molecular weight ozonized linseed FAME (*versus* TAG).

In summary, the above results suggest that the proposed drying agents result in direct radical addition to oils containing conjugated double bonds, while the overall autoxidative polymerization mechanism is preserved. As such, they can be considered as reactive diluents, since they can be incorporated into the drying oil at high loading levels but drying time acceleration is limited to conjugated oils.

2.3.2.3 Effect on the glass transition temperature

The T_g after 24 h of drying at 60 °C was mostly affected by the concentration of drying agent, decreasing from approximately -9 °C for pure tung oil to -20 °C for tung oil including 25 wt % of FAME_{oz}/TAG_{oz} (see Figure 2.7 c)). However, neither the ozonized lipid type (FAME_{oz} *versus* TAG_{oz}) nor the ozonolysis time

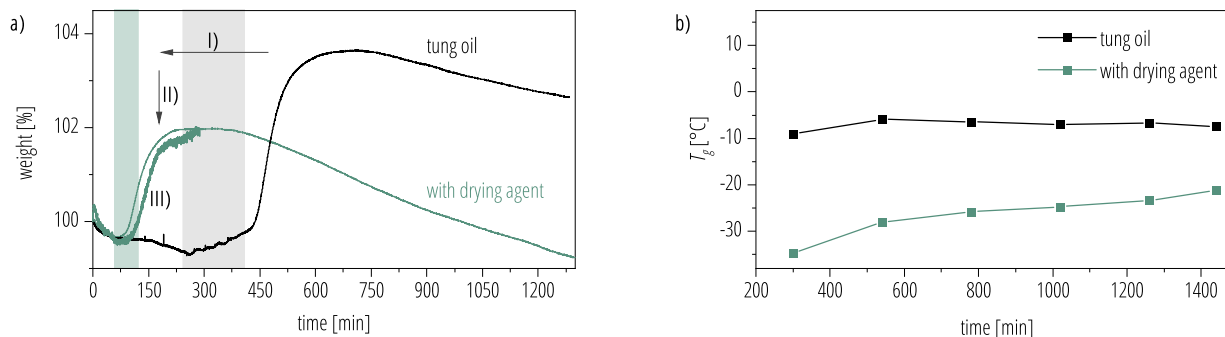


Figure 2.9: **a)** Percentage weight change over time recorded by TGA for tung oil and its mixture with 25 wt % FAME_{oz,20min} and CaCO₃ as filler at 60 °C. I) Reduction in the induction time. II) Lower net O₂ uptake. III) Replication of 25 wt % FAME_{oz,20min} in tung oil on a woody substrate in the absence of CaCO₃. The shaded areas indicate the onset of a track-free surface until the dry-through time. Representative TGA traces are shown from duplicate measurements. **b)** Evolution of T_g ($n = 1$) after film formation for pure tung oil and a formulation with 25 wt % ozonized (20 min) linseed FAME at 60 °C.

had a statistically significant effect on T_g . Both, the incorporation of FAME and TAG of lower iodine values might be expected to reduce T_g compared to pure tung oil, due to fewer available sites for cross-linking. Also, oxidative by-products from ozonolysis or drying agent decomposition may have further plasticized the films. The possible role of these low molecular by-products appear more evident when monitoring the change in T_g over time. After film formation, the T_g remained relatively constant for pure tung oil over 24 h at 60 °C (Figure 2.9b)). In contrast, for tung oil containing 25 wt % FAME_{oz,20min}, the T_g was found to increase by more than 10 °C over this period. As previously mentioned in Section 2.3.2.2, the TGA data shows a corresponding reduction in weight over this period, suggesting that the loss of volatile oxidation products results in this reduction in molecular mobility. Nevertheless, the T_g of the tung oil films with 25 wt % of FAME_{oz,20min} reached that of a pure linseed oil film after 16 h of curing, suggesting that a degree of cross-linking comparable to a linseed oil film (Figure A.9b), A.2.3) could be obtained when using 25 wt % FAME_{oz,20min} in tung oil but with benefit of faster polymerization than either of the two pure oils.

ATR-FTIR spectra recorded at the upper and bottom side of the films prepared for T_g analysis after 24 h of drying at 60 °C in the Box-Behnken design did not provide further insight into the observed difference in T_g upon addition of the drying agents. However, by using PCA on all of the spectra, it was revealed that between formulation differences (over the range of 0 wt % to 25 wt % drying agents) were less pronounced than the spectral differences between the top and bottom side of the films (Figure 2.10a)). The corresponding loading plots in Figure 2.10b) show a strong negative influence on PC 1 by bands for sp³ C-H stretching vibrations and ester bonds. As reviewed by De Viguerie et al. [168], several authors report the loss of alkane C-H stretching bands due to cleavage reactions, while ester bonds are shown to form and later decrease (as observed in this study). Under the conditions used, it is unlikely that hydrolysis would explain the observed loss in ester bonds. As pointed out by Van de Voort et al. [186], the appearance of negative bands in the FTIR spectra of an oxidized oil when ratioed against that of an un-oxidized oil does not necessarily indicate the loss of functional groups. Instead, this may indicate a "dilution" of the original chemical composition due to oxygen uptake, in particular for sp³ C-H and C=O (ester) stretching vibrations. Considering that

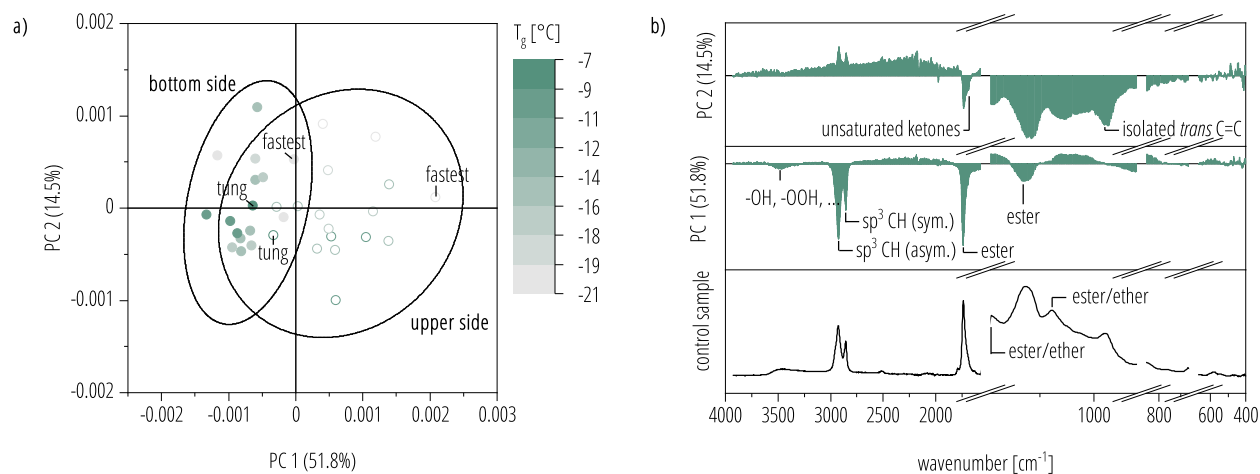


Figure 2.10: a) PCA score plot with 95 % confidence ellipses for the data points representing the upper (open circles) and bottom side (filled dots) FTIR spectra recorded after drying at 60 °C for 24 h and subsequent T_g analysis. The colour scale indicates the T_g but did not explain as much of the observed clustering of the data. For comparison with the previous graphs, the sample with 25 wt % FAME_{oz,20min} is labelled (fastest), as well as the control (pure tung oil). b) Loading plot showing how strongly different IR bands influenced PC 1 and PC 2. Breaks were included in regions of absorbance by the CaCO₃ filler.

the main O₂ uptake occurred after film formation (Figure 2.9), PCA shows that the most of the oxygen is incorporated into the upper layers of the film. Generally, this observation is in line with the known formation of a surface skin in conjugated drying oils, in particular tung oil, limiting the diffusion of O₂ to the layers beneath and resulting in the formation of a typical low-gloss surface [187–189].

2.3.3 Performance beyond the Box-Behnken design boundaries

2.3.3.1 Effect on tung oil at room temperature

The drying time analyses that were performed at 60 °C were less reproducible when performed at 25 °C (Figure A.10, A.2.4.1). Nonetheless, a significant (~30 %) shortening of the dry-through time at 25 °C was observed (with 25 wt % FAME_{oz,20min}), although less than that observed at 60 °C (~70 % reduction). Hence for a future study, further method development to overcome this reproducibility limitation, followed by a temperature-dependence study beyond the current scope, is desirable. However, air-drying at the elevated temperature of 60 °C is necessary to reduce the time required to conduct this study, and this temperature is commonly used in other literature [175] addressing the curing of drying oils, being a low enough temperature to avoid the risk of chain breaking reactions.

2.3.3.2 Use of higher concentrations of ozonized lipids in tung oil

On the basis of the promising findings from the Box-Behnken design, the effects of incorporating even higher levels of FAME_{oz,20min} in tung oil have also been studied. The results are shown in Figure 2.11. Further addition of the drying agent was effective in reducing the drying time from an average of 2.1 h with 25 wt %

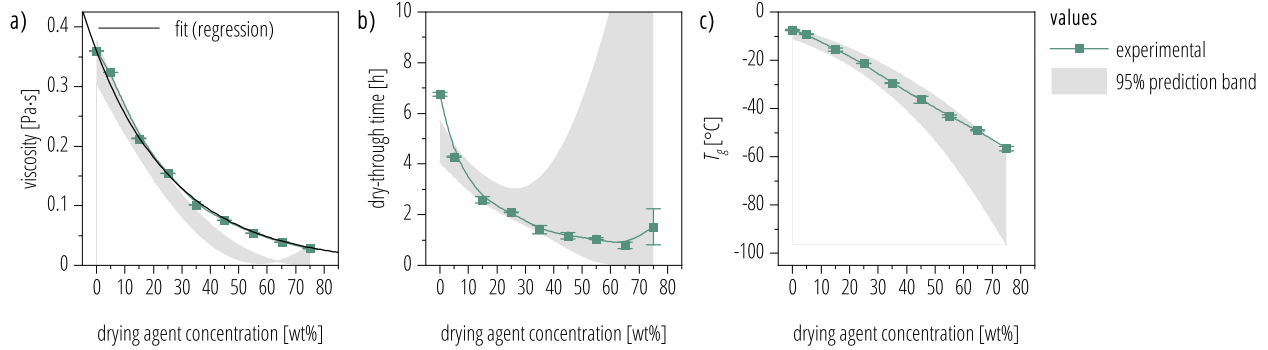


Figure 2.11: Reduction in **a)** viscosity, **b)** dry-through time, and **c)** T_g with further addition of $\text{FAME}_{\text{oz},20\text{min}}$ in tung oil. Error bars represent the standard deviation of the experimental data ($n = 2$) and comparison with the 95% prediction bands based on the derived regression models. Additionally, the viscosity data were fitted with the regression function derived from the Grunberg-Nissan relationship (based on weight fractions).

$\text{FAME}_{\text{oz},20\text{min}}$ to 0.8 h at 65 wt %, corresponding to an almost 90 % drying time reduction at 60 °C compared to pure tung oil. At concentrations above 75 wt % $\text{FAME}_{\text{oz},20\text{min}}$, the films no longer solidified. Additionally, this experimental data were compared with the predicted values from the regression models. The prediction bands increase with higher concentration for the drying time and to a much lower extent also for the T_g . While having a relatively narrow prediction band, the viscosity reduction is consistently overestimated throughout the tested viscosity range. A simpler and more accurate way to predict the viscosity (η_{mixture}) of this binary mixture (wt% of $\text{FAME}_{\text{oz},20\text{min}}$ (X) in tung oil) was found by regression analysis based on the Grunberg-Nissan relationship but by using weight rather than molar fractions:

$$\ln(\eta_{\text{mixture}}) = (1 - X/100) \cdot \ln(\eta_{\text{tung oil}}) + X/100 \cdot \ln(\eta_{\text{drying agent}}) + (1 - X/100) \cdot (X/100) \cdot G \quad (2.2)$$

While optimum drying time was not within the range of the tested Box-Behnken design, extending the model beyond its limits was able to predict the drying time and T_g within a 95% confidence band for the present case. However, the data also shows that the T_g continued to decrease almost linearly down to -50 °C for 65 wt % replacement of tung oil by the drying agent. In view of drying time optimization, application-dependent limits to the T_g would have to be taken into consideration. Nevertheless, the data shows that more than 50 wt % of tung oil could be replaced by the proposed ozonized linseed product. It is estimated that this would be of lower cost compared to tung oil, it would be locally sourced, and it would be a much faster polymerizing drying oil.

2.4 Outlook and future work

In addition to the proven ability to reduce the dry-through time and the viscosity of tung oil, the functionalization of FAME with O_3 also results in other properties, which may provide additional benefits for application in drying oils. As discussed in Section 2.1, ozonized vegetable oils have long been known as antimicrobials and most to-date applications seem to be related to according medical products. Delayed microbial colonization of wood varnishes, in particular of drying oils, is of great interest to prevent premature staining. Discoloration of drying oil-treated wood in outdoor applications is a common important reason for reapplying the drying oil. A preliminary study of the potential for $FAME_{oz,20min}$ to impart resistance to surface colonization by microbes has been initiated in collaboration with another University of Alberta research group.

2.4.1 Dispersion of CNC and formation of bionanocomposites

The reaction with O_3 results in lipid derivatives of significantly increased polarity, which could be beneficial in dispersing polar carbohydrate-based polymers. Therefore, a preliminary study was also conducted on the potential of $FAME_{oz,35min}$ and $TAG_{oz,35min}$ in tung oil mixtures to enhance the dispersion of CNC in producing bionanocomposites as discussed below. For the direct dispersion of dried CNC in the drying agents, a CNC aerogel was used to benefit from the high specific surface area. This so-called PGX-CNC is produced through a spray drying process that uses supercritical CO_2 and ethanol as the antisolvents to precipitate CNC from an aqueous suspension and to dry CNC into nano-structured morphologies due to homogeneous dehydration [190].

The ultrasonic dispersion of the PGX-CNC resulted in almost instantaneous gelling of the ozonized (35 min) linseed FAME and canola oil. The successful dispersion of the nanoparticles was further confirmed by the change in the rheological flow behaviour (Figure 2.12a)). $FAME_{oz,35min}$ and $TAG_{oz,35min}$ showed mostly Newtonian flow behaviour up to $3000s^{-1}$, whereas the incorporation of CNC resulted in a strong viscosity increase at low shear rates. This was followed by shear-thinning almost down to the viscosity of the drying agents as the shear rate increased above about $100s^{-1}$. Upon reducing the shear rate again, a memory effect was also observed as the materials returned to a more viscous state, which is characteristic for structured fluids. The tested CNC concentration of 0.5 wt %, is below what is typically reported as the percolation thresholds (minimum concentration required for the formation of a three-dimensional continuous network of connecting particles) [191, 192]). Therefore, the observed shear-induced viscosity drop indicates a shear-sensitive network formed between the nanoparticles and the ozonized lipids, a behaviour that has also been observed in the UV-curable polyurethane in Chapter 4. This effect was significantly more pronounced in the ozonized linseed FAME. In the case of dried (24 h at $60^\circ C$) films of the FAME-based nanodispersions in tung oil, the average T_g increased from $-48^\circ C$ for the control to $-44^\circ C$ in the presence of 0.25 wt % (Figure 2.12b)). However, more material would be needed to test for statistical significance.

Few studies have investigated the use of CNC in drying oils. Yoo and Youngblood [193] were able to produce CNC-reinforced tung oil films with CNC concentrations up to 10 wt %. Veigel et al. [194] used nanofibrillated

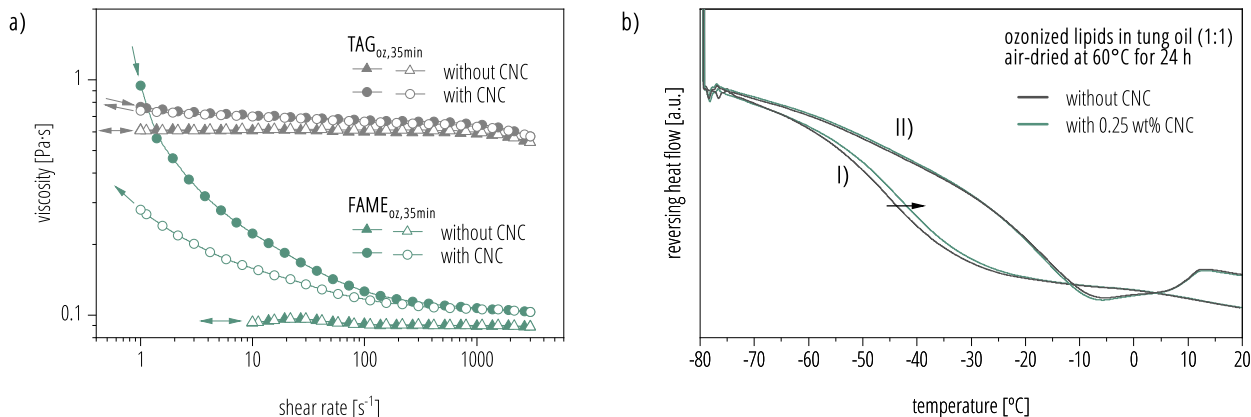


Figure 2.12: **a)** Shear rate dependence of the viscosity (25 °C) of ozonized (35 min) linseed FAME and canola oil and the effect of CNC (0.5 wt %). The arrows indicate the direction of the applied shear rate ramps. The neat drying agents showed Newtonian flow behaviour while, CNC imposed a structuring effect, in particular for the ozonized linseed FAME. **b)** MDSC graphs showing the reversing heat flow for films made from ozonized (35 min) lipids in tung oil (1:1 ratio) and CaCO₃ as a filler (50 wt %). I) Using ozonized linseed FAME as a carrier for CNC, a small but consistent increase in T_g was observed. II) In the case of ozonized canola oil, no change in the thermal properties was observed upon CNC addition. However, the transition range broadened and showed an additional exothermic peak due to further drying. The CNC concentration is given in wt % of the resin (not considering CaCO₃).

cellulose (1 wt % relative to linseed oil) to improve the mechanical properties, in particular the wear resistance, of linseed oil films. In both cases, the CNC was modified to aid in dispersion using poly(lactic acid) oligomers, oleic acid, or anhydrides, respectively, as well as thinners (up to 50 wt% relative to the oil).

Overall, this prestudy proved for the first time that unmodified CNC can be dispersed in ozonized lipids and subsequently incorporated into drying oils at a concentration sufficient to show nanoeffects owing to the good dispersion quality. The CNC dispersion quality was reflected by the formation of a reversible internal network with lipids and slightly higher T_g . For coating and paint applications, shear thinning, as observed in the nanodispersions, could be beneficial for uniform layer formation and for subsequent resistance to further flow to prevent sagging on a vertical surface. The low amounts needed and the transparency of the nanodispersions could also be potential advantages of CNC as a rheology modifier in drying oils. However, more research is needed to link the observed trend for slightly increased T_g to other nanoreinforcement effects in the films.

While nanoreinforcement effects at very low loading levels of PGX-CNC is promising for producing cost-effective materials, most dried CNC is produced through regular spray-drying causing significant CNC agglomeration, and attempts at dispersing spray- or freeze-dried CNC directly into the ozonized lipids were not successful. Therefore, the use of aqueous CNC suspensions collected prior to spray-drying was investigated for a different solvent-free coating system in Chapter 4, where CNC dispersion can be performed in the wet phase.

2.5 Conclusion

This study demonstrates the feasibility of using ozone-modified lipids as a reactive diluent for conjugated drying oils, resulting in faster curing and reduced viscosity without solvents. Kinetic analyses using FTIR spectroscopy strongly suggest that radical species from ozonized lipids have a tendency to add directly to conjugated $-\text{CH}=\text{CH}-$ over participating in H atom abstraction as most often seen with non-conjugated unsaturated lipids. This direct radical addition leads to cross-linking without terminating the radical chain reaction. As a result, accelerated tung oil polymerization beyond the observed reduced induction time occurs. Acceleration of linseed oil polymerization was not observed, although its viscosity and induction time were still decreased after incorporating FAME_{oz} . The concentration of ozonized lipid drying agents in tung oil had the strongest effect on the drying time reduction. In contrast, the ozonolysis time had less effect so likely partial ozonolysis is sufficient, which would be efficient for future scale-up. The low cost of producing FAME and performing ozonolysis suggest that the present approach could reduce the cost of the drying oil through the partial substitution of tung oil with a readily available lipid feedstock, giving a fully biobased product.

Inevitably, even solvent-free drying oils do emit some volatile compounds during film formation due to the low-molecular weight by-products of oxidation. The composition and implications of any VOC emissions still have to be established. Nevertheless, the results presented suggest that ozonized lipids could be used as solvent-free and fully biorenewable binders in oil-based coatings and paints.

Chapter 3

Epoxidized linseed lipids as a durable and fast-curing alternative to drying oils

Linseed and other unsaturated plant oils continue to be important natural finishes for wood protection. However, they suffer from long drying times and reduced durability due to their susceptibility to microbial colonization. Response surface methodology was used to study the curing behaviour of epoxidized linseed oil triacylglycerols (ELO) and fatty acid methyl esters (ELOME) under ultraviolet (UV) light, as an alternative to air-drying of linseed oil. Ether cross-links were formed following high degrees of epoxy group conversion ($\geq 80\%$) during photo-induced polymerization, reducing hydrolytic (abiotic and enzymatic) degradation by 20% compared to air-dried linseed oil. As an alternative to using a UV lamp, curing under solar irradiation when sensitized by curcumin was studied. This revealed that oxygen inhibition can limit cross-linking on wood surfaces and in thin films unless a tertiary amine is present to scavenge oxygen. A desirability function approach concluded that epoxidized linseed lipids containing a high content of ELOME (75 wt% to 85 wt%) and moderate concentrations of the photoinitiator (3 wt% to 5 wt%), are good alternatives to linseed oil, resulting in films with a similar glass transition temperature but with the benefits of faster curing (seconds to minutes, compared to days or weeks) and improved hydrolytic stability. Such films still maintain a biorenewable content of $>93\%$.

3.1 Introduction

Obtaining durable exterior wood finishes is challenging for multiple reasons. In addition to being exposed to a relatively harsh environment, dimensional changes of the wood substrate can strain the finishes and eventually result in crack formation [195]. Various wood pretreatments, such as the use of antimicrobials and the photostabilization of lignin, are able to improve weathering resistance. However, the flexibility of a finish throughout its service life has been found to be crucial in protecting the wood substrates [195–197], along with the ability of the coating to penetrate the wood [198].

Drying oils are highly unsaturated plant oils, which polymerize through air-induced autoxidation (see Section 1.1.1.1). They were one of the first binders used by humankind [9, 110], and they continue to be used as a natural wood finish or as a component of oil-based coatings, such as alkyds. While providing a fully biobased wood finish, they suffer from relatively long drying times and susceptibility to microbial colonization. The addition of metal driers [111, 123] or oxidative/thermal pretreatments [112, 113, 116] can be employed to substantially reduce the drying times, which would otherwise take to days or even weeks depending on the oil. However, rapid surface colonization by microbes and subsequent staining requires the drying oil finishes to be reapplied regularly. This staining has been linked to the formation of melanins by *Aureobasidium melanogenum*, formerly known as *Aureobasidium pullulans* [199]. Its growth was found to be dependent on the wood substrate and the drying oil type [200]. It is generally accepted that plant oil-based polymers are partially biodegradable due to the presence of ester linkages in the triacylglycerol (TAG) structure, which can be hydrolyzed under abiotic conditions or through the catalysis by lipases [201]. Therefore, the growth of *A. melanogenum* on drying oil films is inhibited with increasing cross-linking density [202, 203]. It is well-known that linseed oil films are more susceptible to microbial degradation than films prepared from tung oil [201, 204]. As a conjugated plant oil, tung oil has a high propensity for cross-linking through direct radical addition to conjugated double bonds (-CH=CH-). In drying oils with isolated -CH=CH- groups such as linseed oil, however, cross-linking occurs predominantly through radical combination upon reaction with oxygen and competes with various secondary oxidation reactions [32]. The rapid staining of linseed oil films on wood could be related to melanin production in the chlamydo spores of the colonizing fungi as a stress response to free radicals formed during autoxidation [202, 205]. At the same time, its lower cross-linking density compared to air-dried tung oil makes the polymer network more accessible as a nutrient source. However, other factors like unpolymerized oil in lower layers of the applied film, the availability of nutrients from the wood substrate, and the ability of spores to attach to the surface of the coating, also affect surface colonization of oil-treated woods [200].

Recent research suggests that intentional biofilms of drying oils colonized by *A. melanogenum* could be used as a wood stain, and biocide-free and self-healing protective coating [202, 203, 206]. In this work, a different approach has been used to improve the durability of linseed oil-based wood finishes. Here, the epoxidation of linseed lipids as a simple route to induce UV-curability *via* photo-induced cationic polymerization is described.

Epoxidized plant oils (see Section 1.2.2) are well known as economical, widely available, and environmentally friendly monomers with up to 100% biorenewable content [207]. The possibility for UV-curing offers an interesting opportunity to make plant-oil based coatings, which are solvent-free and do not require energy-intensive curing as in most conventional coatings [208, 209]. Furthermore, the relatively lower molecular weight will benefit the ability of the resin to penetrate into the wood substrate, which is critical for forming durable wood coatings [198].

While epoxidized acrylated plant oils, such as soybean oil, have already been commercialized for UV-induced radical polymerization (*e.g.* EBECRYL[®] 5848, with a viscosity of ~ 20 Pa s at 25 °C), it was focused on the direct use of epoxidized linseed lipids to avoid the need for further chemical conversion and increases

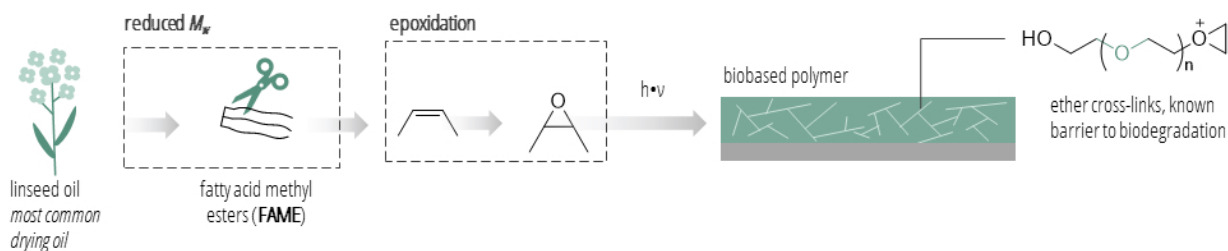


Figure 3.1: Schematic overview of the approach to use linseed lipid (TAG and FAME) epoxidation to develop UV-curable resins with a higher hydrolytic stability and faster curing compared to air-dried linseed oil due to UV-induced polymerization through ether linkages.

in molecular weight. Their ability to undergo UV-induced cationic polymerization instead of radical curing also precludes issues related to oxygen inhibition [64, 65], while offering the ability of dark curing (*cf.* Section 1.1.3). This phenomenon is related to the longer active life of the initiated species (hours or even days), which allows them to diffuse to non-irradiated areas of the coatings to induce polymerization [84].

In this study, an iodonium photoinitiator was used. It is believed that the excitation, fragmentation, and the initiation of the cationic epoxy polymerization follows the mechanism outlined in Chapter 1 (Eqs. 1.18 to 1.21) [80–82]. Both cationic and radical species from the fragmented photoinitiator can react with the epoxy monomers to yield the Brønsted acid HMtX_n [81], in the present case $\text{HB}(\text{C}_6\text{F}_5)_4$. The epoxy monomer is rapidly protonated by this superacid to form a secondary oxonium species (Eq. 1.19). Cationic ring-opening polymerization then proceeds *via* an $\text{S}_{\text{N}}2$ attack resulting in the formation of a tertiary oxonium species (Eq. 1.20). Chain growth occurs by the repetitive addition of monomers to the active chain end (Eq. 1.21). The absence of termination is considered to be the primary reason for the longevity of the active centres and therefore the ability of dark cure polymerization [84].

The use of epoxidized plant oils for cationic UV-curing has been described in several studies but to the best of the author’s knowledge, has not yet been commercialized. Their lower reactivity compared to cycloaliphatic epoxy monomers [80], the formation of soft films, and their relatively high viscosity are among the underlying reasons. Interestingly, the use of epoxidized lipid derivatives, such as fatty acid methyl esters (FAME) from plant oils has not been widely studied despite the opportunity for significantly reduced viscosity as compared to epoxidized TAG. In an attempt to produce an environmentally-friendly wood coating, however, these apparent disadvantages could be put to use in order to make a linseed oil-based alternative to its air-dried traditional product, which cures faster (minutes as opposed to days or weeks) but can still penetrate wood substrates and form flexible films to withstand dimensional changes in the substrate for improved durability. To test this, response surface methodology and a desirability assessment of different formulations based on mixtures of epoxidized linseed FAME (ELOME) and TAG (ELO) were performed. Furthermore, it was hypothesized that the formation of ether cross-links should increase the hydrolytic stability compared to films of air-dried linseed oil. This, in turn, may improve the durability of such films by delaying staining due to microbial colonization, since fewer microorganisms are able to cleave ether cross-links [210]. The main concepts of this study are illustrated in Figure 3.1.

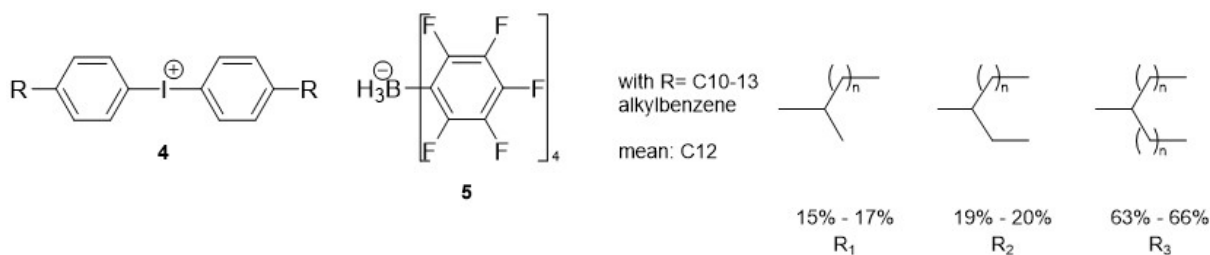


Figure 3.2: Chemical structure of the photoinitiator Silcolese UV Cata 243 (CAS 1115251-57-4) with the IUPAC name 4,4'-Bis[sec-alkyl(C10-C13)phenyl]iodonium tetrakis(pentafluorophenyl)borate.

3.2 Materials and methods

3.2.1 Materials

Epoxidized linseed oil and fatty acid methyl esters were prepared as previously described [156]. The obtained oxygen oxirane contents (OOC) were 9.55% and 9.46%, respectively. Boiled linseed oil (Recochem Inc.) was purchased from a local home improvement retailer. Silcolese UV Cata 243 (Figure 3.2), a cationic photoinitiator, was kindly donated by Elkem Silicones USA Corp. (East Brunswick, New Jersey, USA). Lipase from *Aspergillus niger* ($\sim 200 \text{ U g}^{-1}$) and ethylenediaminetetraacetic acid (EDTA, 99.995% trace metal basis) were purchased from Sigma-Aldrich Canada. The standards used for inductively coupled plasma mass spectrometry (ICP-MS) included the internal standard mix 2, SPEX CertiPrep (Metuchen, New Jersey, USA), iodine standard for ICP-MS in 1% TEA buffer (Inorganic Ventures, Christiansburg, Virginia, USA), and the cobalt reference standard solution (Fisher Scientific, Fair Lawn, New Jersey, USA). Trace metal grade nitric acid (67% to 70%), and hydrochloric acid (34% to 37%), trace metal grade, were obtained from Fisher Scientific (Nepean, Ontario, CA). Tetramethylammonium hydroxide, as 10% in water, was purchased from Acros Organics (Geel, BE). Certified ACS grade sodium phosphate dibasic anhydrous (Na_2HPO_4) and sodium phosphate monobasic monohydrate ($\text{NaH}_2\text{PO}_4 \cdot \text{H}_2\text{O}$) were obtained from Fisher Scientific (Fair Lawn, New Jersey, USA). Curcumin from *Curcuma longa* (turmeric) was purchased from Sigma-Aldrich Canada.

3.2.2 Methods

An overview of the conducted experiments and analyses is illustrated as a process flow diagram in Figure 3.3. The two main aspects of this research concern the systematic study of the UV-curing behaviour of ELOME/ELO mixtures through a central-composite experimental design, as well as the hydrolytic stability of the cured films compared to air-dried linseed oil films.

3.2.2.1 Central composite experimental design

The central composite experimental design (CCD) and statistical analyses were performed using the "Design of Experiments" app (file version 1.1) in OriginPro[®] 2020b. The effects of the ELOME:ELO ratio (X_1) and the photoinitiator (X_2) concentration on the UV-curing behaviour (including curing time, and rate/degree

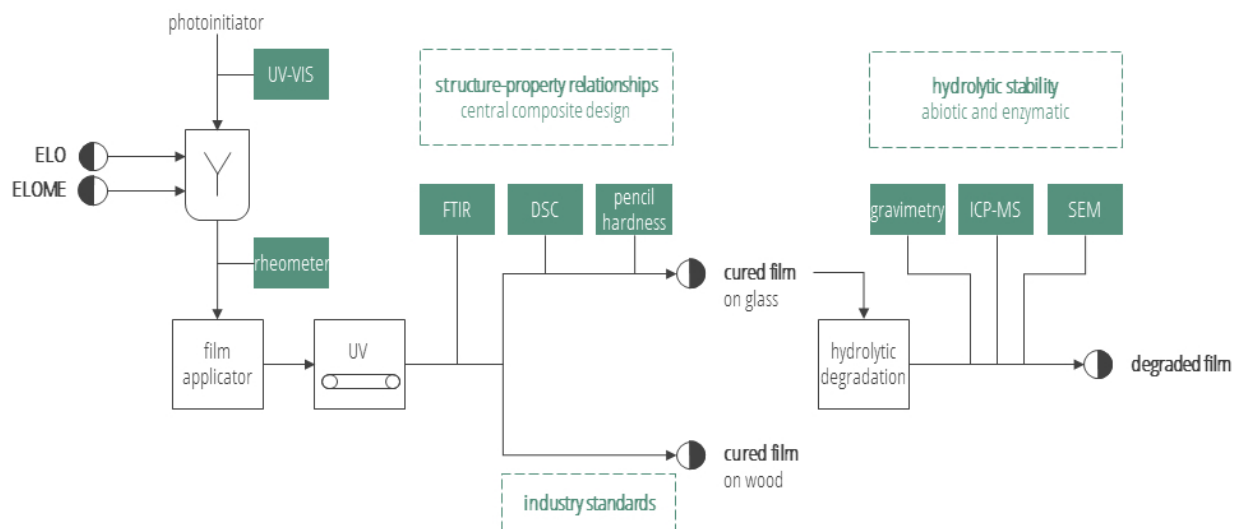


Figure 3.3: Simplified process flow diagram of the experimental setup and analyses to study the UV-curing behaviour of ELOME/ELO mixtures and the hydrolytic stability of the cured films compared to air-dried linseed oil films.

of epoxy group conversion) and glass transition temperature (T_g) were systematically studied through a full factorial and rotational ($\alpha = 1.414$) CCD at two levels using 4 centre points. The parameters and levels are shown in Table 3.1. The process for data transformation, model selection, and fitting is described in the Appendix B.2.7.

3.2.2.2 Resin rheology

Rotational rheology (Advanced Rheometer AR 2000, TA Instruments) at 25 °C using a plate/cone geometry (2°, 40 mm diameter, truncation gap distance of 52 μm) was used to study the rheological properties of the tested formulations under shear. Linear regression was performed to calculate the viscosity (first Newtonian plateau) over a shear rate range from 1000 s^{-1} to 100 s^{-1} (downramp) under steady state conditions (7 points per decade).

3.2.2.3 Film preparation and curing

For the central composite experimental design, the films were coated on microscope slides (Fisherbrand™ Frosted Microscope Slides, Pittsburgh, USA). Using cube applicators (TQC Cube Applicators, Paul N. Gardner Co., Inc, Pompano Beach, Florida, USA), films with a wet thickness of 50 μm and 30 μm for the epoxy and boiled linseed oil resins, respectively, and a film width of 12 mm, could be prepared. The boiled linseed oil films were air-dried for 4 days at ambient conditions. The epoxy resin films were cured in a lab-scale UV-curing unit (Mini Laboratory Unit with a medium vapour pressure mercury lamp 80 W cm^{-1} , GEW (EC) Limited, UK) at a conveyor belt speed of 10 m min^{-1} . This setup required multiple passes under the UV source (see Section 3.2.2.4). A sample support (18 mm) was used to reduce the distance to the lamp and increase the UV dose. The exposure time under these conditions was calculated to be 0.33 s per pass with a UV dosage of

Table 3.1: Central composite design matrix of the parameters and levels tested. X_1 and X_2 correspond to the ELOME:ELO ratio and the photoinitiator concentration, respectively.

	X_1	X_2	point type	
	[wt%]	[wt%]	coded	description
1	70	6.8	-1	star point
2	50	2	1	factorial point
3	90	2	1	factorial point
4	70	4	0	centre point
5	50	6	1	factorial point
6	90	6	1	factorial point
7	70	1.2	-1	star point
8	41.7	4	-1	factorial point
9	70	4	0	centre point
10	70	4	0	centre point
11	70	4	0	centre point
12	98.3	4	-1	factorial point

$95 \text{ J cm}^{-2} \text{ min}^{-1}$ based on the manufacturer's data. The dark cure time associated with reloading the films onto the conveyor belt and passing them under the UV source was determined to be 4 min per 40 passes on average with a standard deviation of 0.2 min ($n = 5$).

3.2.2.4 Epoxy conversion

Attenuated total reflectance Fourier transform infrared spectroscopy (ATR-FTIR) was used to monitor the monomer conversion during the UV-polymerization. Spectra of the films were recorded after different number of passes (up to 100 passes) under the UV-lamp. A total of 16 interferograms at a resolution of 4 cm^{-1} were summed before Fourier transformation (Platinum ATR Alpha, Bruker). Automatic baseline correction using the OPUS software (Bruker) was performed. The C-O-C stretching vibrations at $\sim 826 \text{ cm}^{-1}$ for the oxirane groups [211] were monitored. The relative loss in intensity during polymerization was determined from the peak height after calculating the second derivatives with a Norris filter (gap-segment = 3-1) for improved band separation. Additionally, the formation of -OH groups was monitored by calculating the integrated peak area between 3692 cm^{-1} to 3136 cm^{-1} .

3.2.2.5 Film properties

Glass transition temperature Differential scanning calorimetry (DSC) was used to determine the glass transition temperature (T_g) of the UV-cured films and the boiled linseed oil control using a differential scanning calorimeter (TA Q100, TA Instruments) and standard aluminum sample pans. The sample size was around 7 mg. The samples were first cooled to $-90 \text{ }^\circ\text{C}$ at a rate of $5 \text{ }^\circ\text{C min}^{-1}$ before applying a relatively fast ramp of $50 \text{ }^\circ\text{C min}^{-1}$, which was needed to detect the broad transition. The glass transition temperatures

were determined from the inflection point between onset and endpoint of the glass transition range using the TA analysis software (Universal Analysis 2000).

Pencil hardness The hardness of the films was determined by a pencil test according to ASTM D3363-05. Wood pencils (Mars[®] Lumograph[®], Nürnberg, DE) covering the scale range from 6B (softest) to 6H (hardest) were used and prepared as outlined in the ASTM method. Gauge and scratch hardness were determined for each film.

TABER abrasion resistance TABER abrasion resistance was determined using an abrasion tester (5130 Abraser, TABER Industries) based on the ASTM D4060-14 specifications but without conditioning. Two coats of the epoxy and boiled linseed oil resins were applied onto birch specimen plaques (S-17, TABER Industries). The epoxy resin was applied in the same traditional way as boiled linseed oil. First, the resins were rubbed onto the wood using a paper towel. After 15 min, excess resin was removed with a paper towel. The epoxy resin was cured under a UV-light until full conversion as determined in the central composite experiments (Section 3.2.2.4), while boiled linseed oil was dried for 24 h as per the manufacturers direction before a second coat was applied in the same manner. The samples were then kept for 4 days at ambient conditions before the abrasion testing. Two abrading wheels (CS-17, TABER Industries) with a load of 1000 g on each wheel were used. The weight loss was recorded after 100 cycles, 200 cycles, and subsequently after every 200 cycles up to 1000 cycles. The abrading wheels were resurfaced every 200 cycles. The wear index, I (1000 times the loss in weight in milligrams per cycle) was calculated for each sanding step. Three independent specimens were prepared for each treatment. Wood chips were cut out using a scalpel and ATR-FTIR spectra of their surfaces were recorded (see Section 3.2.2.4).

3.2.2.6 Hydrolytic stability

Abiotic and enzymatic hydrolytic degradation of the cured coatings Films of the centre point epoxy formulation and boiled linseed oil were applied to microscope slides as described in Section 3.2.2.3. The slides were immersed into 50 mL of a 0.1 M sodium phosphate buffer solution (pH = 7.0) containing lipase (1 U g⁻¹). A control experiment was performed in the absence of the enzyme to estimate the effect of abiotic hydrolysis. In both cases, the films were incubated at 37 °C and gently agitated using a tube rotator (Fisher Scientific) at 10 rpm. Weight changes were recorded after 45 min drying under vacuum at 25 °C. Samples of the buffer solution were taken for ICP-MS/MS analysis as described below.

Leaching of drying agent and photoinitiator Analysis of leached cobalt (Co), the main drier found in the boiled linseed oil, and iodine (I) was done on an Agilent 8800 Triple Quad ICP-MS/MS. Subsamples taken from the buffer solutions were diluted 2x using a matrix solution and then filtered using 0.2 µm syringe filter membranes. For Co analysis, the matrix solution was 2% nitric acid and 0.5% hydrochloric acid. Cobalt (m/z 59) was measured using He gas as a collision gas to cope with isobaric interferences and using Ge (m/z 72) as internal standard [212]. The calculated detection limit for Co was 8 ng L⁻¹. For I analysis, 0.5% tetramethyl ammonium hydroxide [213] was used as the matrix solution. Iodine (m/z 127) was measured

Table 3.2: Desired range for the responses considered for estimating the overall desirability.

$Y_i(X_1, X_2)$	unit	target T_i	desired range	constraint
photoinitiator concentration	[wt%]	0.5	$Y_1(X_1, X_2) < 8$	minimize
viscosity	mPa·s	34	$Y_2(X_1, X_2) < 500$	minimize
rate constant k (first-order)	[a.u.]	0.3	$Y_3(X_1, X_2) > 0.02$	maximize
T_g	[°C]	-12.6	$-60 < Y_4(X_1, X_2) < 10$	target

using O_2 as the reaction/collision gas and using In (m/z 115) as the internal standard. The calculated detection limit for I was $2 \mu\text{g L}^{-1}$.

3.2.2.7 Desirability assessment

The overall suitability of these biobased coatings as an alternative to air-dried linseed oil was determined using a desirability approach. The response values $Y_i(X_1, X_2)$ for the photoinitiator concentration ($Y_1(X_1, X_2)$), the viscosity ($Y_2(X_1, X_2)$), the rate constant k ($Y_3(X_1, X_2)$), and the T_g ($Y_4(X_1, X_2)$) were considered. Due to environmental concerns of photoinitiator migration and reduced biobased content of the coatings, the aim was to minimize the photoinitiator concentration. The upper limit U_1 and target concentration for the photoinitiator concentration was set to 8 wt % and the target to 0.5 wt %, respectively, following general recommendations for cationic photoinitiator use [209]. The coating viscosity plays a key role in processability. Generally, the viscosity of coatings or paints is in the range of 0.05 Pa·s to 0.5 Pa·s for application by spraying, brushing, or roll coating [214]. However, for wood coatings, penetration is also important. Therefore, the upper limit U_2 was set at 500 mPa·s and the viscosity of ELOME (34 mPa·s) was used as the target T_2 , corresponding to the lowest possible viscosity for the tested system. Considering efficiency and energy consumption, faster UV-curing is of advantage. Therefore, desirability was rated higher for treatments resulting in increased rate constants k for epoxy group conversion. Finally, the T_g determined for the boiled linseed oil control film was used as the target T_g as an approximation for "comparable" properties, while the range of determined T_g s of the epoxy formulations were used as the upper and lower limits. The desired ranges of the responses $Y_i(X_1, X_2)$ are listed in Table 3.2. The controllable factors for the coating formulations were the ELOME:ELO ratio X_1 and the photoinitiator concentration X_2 (as in the CCD).

The measured response values from the CCD are too sparse to study desirability. Therefore, fitted responses $\hat{Y}_i(X_1, X_2)$ were calculated from the fitting curves derived from the CCD (Equation B.1 and Equation B.3) and the approximation for the viscosity (Equation 3.5) for $40 \text{ wt \%} \leq X_1 \leq 100 \text{ wt \%}$ (interval of 5 wt %) and $1 \text{ wt \%} \leq X_1 \leq 7 \text{ wt \%}$ (interval of 1 wt %), which corresponds to a 13x7 2D mesh.

The desirability function to minimize $\hat{Y}_i(X_1, X_2)$ was defined as follows:

$$d_i(\hat{Y}_i(X_1, X_2)) \begin{cases} 1.0 & \text{if } \hat{Y}_i(X_1, X_2) < T_i \\ \left(\frac{\hat{Y}_i(X_1, X_2) - U_i}{T_i - U_i} \right)^s & \text{if } T_i \leq \hat{Y}_i(X_1, X_2) \leq U_i \\ 0.0 & \text{if } \hat{Y}_i(X_1, X_2) > U_i \end{cases} \quad (3.1)$$

The exponents s and t in all desirability functions were set to 1, corresponding to a linear increase of the desirability up to the target and default value [215]. The desirability function to maximize $\hat{Y}_i(X_1, X_2)$ was defined as follows:

$$d_i(\hat{Y}_i(X_1, X_2)) \begin{cases} 0.0 & \text{if } \hat{Y}_i(X_1, X_2) < L_i \\ \left(\frac{\hat{Y}_i(X_1, X_2) - L_i}{T_i - L_i} \right)^s & \text{if } L_i \leq \hat{Y}_i(X_1, X_2) \leq T_i \\ 1.0 & \text{if } \hat{Y}_i > T_i \end{cases} \quad (3.2)$$

The desirability function for a targeted $\hat{Y}_i(X_1, X_2)$ was defined as follows:

$$d_i(\hat{Y}_i(X_1, X_2)) \begin{cases} 0.0 & \text{if } \hat{Y}_i(X_1, X_2) < L_i \\ \left(\frac{\hat{Y}_i(X_1, X_2) - L_i}{T_i - L_i} \right)^s & \text{if } L_i \leq \hat{Y}_i(X_1, X_2) \leq T_i \\ \left(\frac{\hat{Y}_i(X_1, X_2) - U_i}{T_i - U_i} \right)^s & \text{if } T_i \leq \hat{Y}_i(X_1, X_2) \leq U_i \\ 0.0 & \text{if } \hat{Y}_i(X_1, X_2) > U_i \end{cases} \quad (3.3)$$

The overall desirability D was then computed as the geometric mean:

$$D = (d_1(\hat{Y}_1) \cdot d_2(\hat{Y}_2) \cdot d_3(\hat{Y}_3) \cdot d_4(\hat{Y}_4))^{1/4} \quad (3.4)$$

A surface plot was fitted for the data of overall desirability using OriginPro[®] 2020b (smoothing: total points increase factor 200, smoothing parameter 0.05).

3.2.2.8 Preliminary suitability assessment of curcumin-sensitized solar curing

Curing under solar radiation was tested for the medium photoinitiator concentration (4 wt %). Formulations with 3 levels of curcumin were prepared (0.1 wt %, 0.2 wt %, and 0.3 wt %). A drying time recorder (TQC Drying Time Recorder, Paul N. Gardner Company, Inc.) with 5 g needle weights was used to determine the curing time under direct solar irradiation according to ASTM D5895 [157] in Edmonton, Canada, (53.522° N,

113.505° W, facing west) between 3 PM to 5 PM during July 2020. Films with different wet thicknesses were prepared as described in Section 3.2.2.3. The dry-through time was determined based on the disappearance of a needle track on the films' surfaces. Samples were taken and analyzed using ATR-FTIR to determine the degree of conversion and ether bond cross-linking at the top surface of the films as described in Section 3.2.2.4.

3.2.2.9 Scanning electron microscopy

For scanning electron microscopy (SEM) samples were carbon coated (Leica EM SCD005 evaporative carbon coater) and analyzed on a Zeiss Sigma Field Emission SEM (300 VP-FESEM) in high vacuum mode with beam energy at 10.0 kV.

3.2.2.10 Additional tests

The method for identifying the main drier in the commercial boiled linseed oil sample is described in B.2.1. ECOSAR ecotoxicity characterization of the photoinitiator is described in B.1.2.2. Additional methods to test the film performance on wood included a hot and cold check resistance test (B.1.2.4) and resistance to liquid (household) chemicals (B.1.2.5).

3.3 Results and discussion

3.3.1 Central composite experimental design

3.3.2 Resin rheology

As expected, the viscosity of ELO (1300 mPas) was considerably higher than for epoxidized FAME with a viscosity of 34 mPas, and an ELOME:ELO ratio of $\geq 90\%$ is needed to reach the lower viscosity of pure linseed oil (about 40 mPas) within the shear rate range of 100 s^{-1} to 1000 s^{-1} (Figure 3.4a)). As shown in Figure 3.4b), the viscosity of the tertiary resin mixtures (ELOME, ELO, and photoinitiator) can be approximated as follows:

$$\ln(\eta_{mix}) \approx w_1 \cdot \ln(\eta_1) + w_2 \cdot \ln(\eta_2) + w_3 \cdot \ln(\eta_3), \quad (3.5)$$

corresponding to an extended expression of that proposed by Arrhenius [216] but using weight (w_i) rather than molar fractions.

3.3.3 UV-curing kinetics

Epoxidized plant oils have been associated with relatively low polymerization rates [217, 218]. This has been linked to the presence of an induction period [80, 219] due to the stabilization of secondary oxonium ions through hydrogen-bonding, which reduces the polymerization rate, especially at low temperatures [220]. The subsequent phase of increased polymerization rates, known as autoacceleration, occurs where increasing

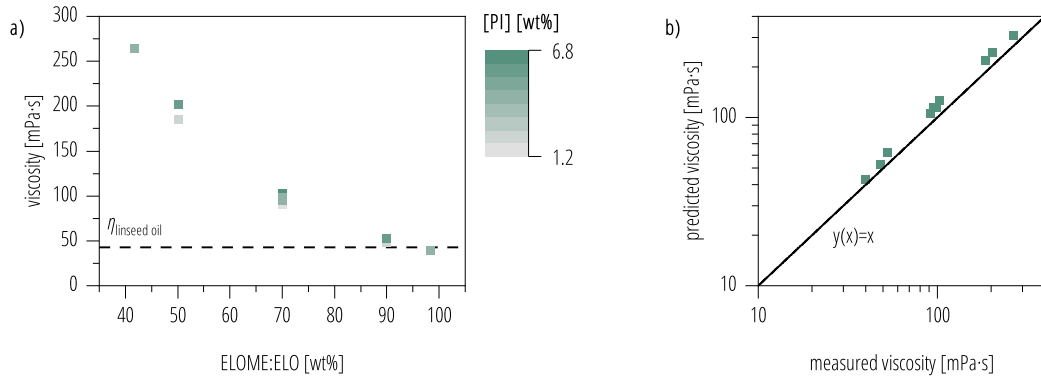


Figure 3.4: **a)** Viscosity-dependence on the ELOME:ELO ratio (at 25 °C). Higher photoinitiator concentrations [PI] resulted in small but measurable viscosity increases (as indicated with the colour map). **b)** Comparison of predicted (Equation 3.5) and observed viscosities for the tested resins.

viscosity leads to reduced rates of termination reactions in favour of chain propagation and increase in molecular weight [221]. In order to fit the conversion profiles and derive kinetic parameters, a model developed by Bera et al. [222] was applied:

$$Y = (1 - a) \cdot (1 - e^{-k \cdot \tau}) + \frac{a}{1 + e^{-k_{\text{autoacc.}} \cdot (x - \tau_{2, \text{max}})}} \quad (3.6)$$

with a corresponding to the epoxy fraction reacted through autoacceleration, k and $k_{\text{autoacc.}}$ being the rate constants for first-order and autoacceleration/deceleration epoxy group conversion, respectively, and $\tau_{2, \text{max}}$ as the "time" necessary to reach the maximum rate of autoacceleration. A selection of the fitted curves ($R^2 > 0.97$) are plotted in Figure 3.5.

The conversion data presented here are a result of pulsed UV irradiation and dark cure during the time needed to load the samples back onto the conveyor belt for a subsequent pass under the UV source. The reported induction period for epoxidized plant oils [219, 223] has not been observed in the present case. Rather, the conversion profiles followed predominantly first-order kinetics. Direct comparison with epoxidized oils exposed to constant UV irradiation is therefore difficult. Overall, the majority of formulations reached final conversion within ~ 10 s of effective UV exposure during a total run time of 3 min, as opposed to the days or weeks required for air-drying of linseed oil. As demonstrated in Figure 3.5, the ratio of ELOME:ELO mainly affected the final degree of epoxy conversion, while epoxy group conversion rate was mainly controlled by the photoinitiator concentration. These observations are based on a detailed statistical analysis (see details in Section 3.2.2.1) as outlined below.

Given the predominantly first-order kinetics, the effect of the resin composition on the rate constant k was further investigated. The data were fitted with a linear model with squares ($R^2 = 0.97$). Based on ANOVA (Table B.11, B.2.7.3), both the photoinitiator concentration and the ELOME:ELO ratio had a significant

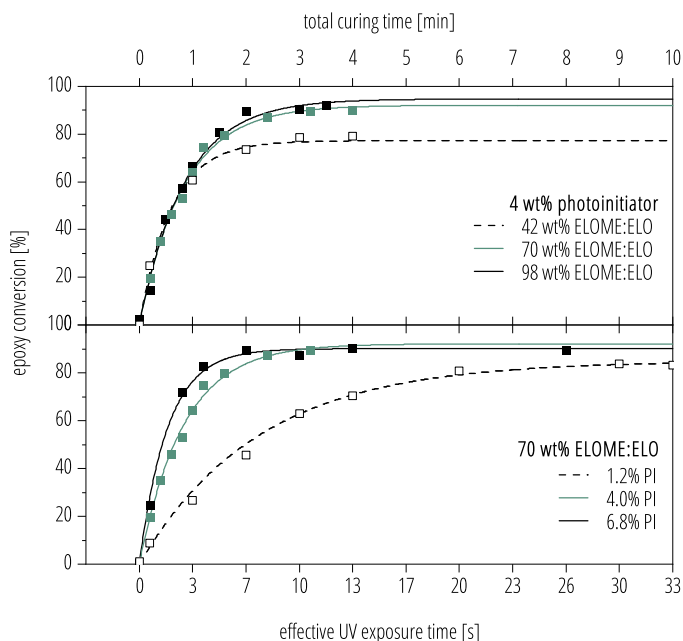


Figure 3.5: Selected conversion profiles for epoxy groups under pulsed UV irradiation (UV system with a conveyor belt and up to 100 passes corresponding to a total run time of 10 min). The consumption of epoxy groups was measured through ATR-FTIR analysis of the 826 cm^{-1} band (C-O-C stretching vibrations). In both graphs, the centre point formation is shown in green. The effect of varying ratios of ELOME:ELO is shown in the upper graph, and concentration-dependence on the photoinitiator (PI) in the lower graph.

effect on k (with $F(1,7) = 329$, $p < 0.0001$ and $F(1,7) = 58.4$, $p=0.005$), respectively. As can be seen in the effect size plot in Figure 3.6b), the photoinitiator had the strongest effect on k . The faster reaction rates with increasing photoinitiator concentration relate to the higher amount of photogenerated superacids to initiate the polymerization.

Interestingly, increasing the content of ELOME slowed down the polymerization rate, although this effect decreased with increasing concentration (significant square contribution $F(1,7) = 12.3$, $p < 0.04$). Unlike the epoxidized oils used by Chakrapani and Crivello [219], no quaternary ammonium phase transfer agents were used during epoxidation, which could have produced basic impurities which could neutralize the photogenerated acids [80, 219]. Furthermore, any remaining base catalyst (NaOH) from the transesterification step would likely have been neutralized during the subsequent performic acid epoxidation. It is therefore suggested, that the observed reduction in k with increasing contents of epoxidized linseed FAME is related to the epoxides' structure. Bulut and Crivello [80] proposed that with sufficient conformational freedom, hydrogen-bonded structures can be formed, which stabilize the secondary oxonium ion and thereby retard the nucleophilic attack by the monomer to form the propagating tertiary oxonium ion. It was hypothesized that the loss of the TAG backbone in ELOME may provide increased polymer chain flexibility to contribute to this effect. Unfortunately, in the FTIR spectra, the ether stretching bands between 1150 cm^{-1} and 1050 cm^{-1} cannot be easily resolved to reveal the contribution of free and hydrogen-bonded ether absorptions [224]. Therefore, the

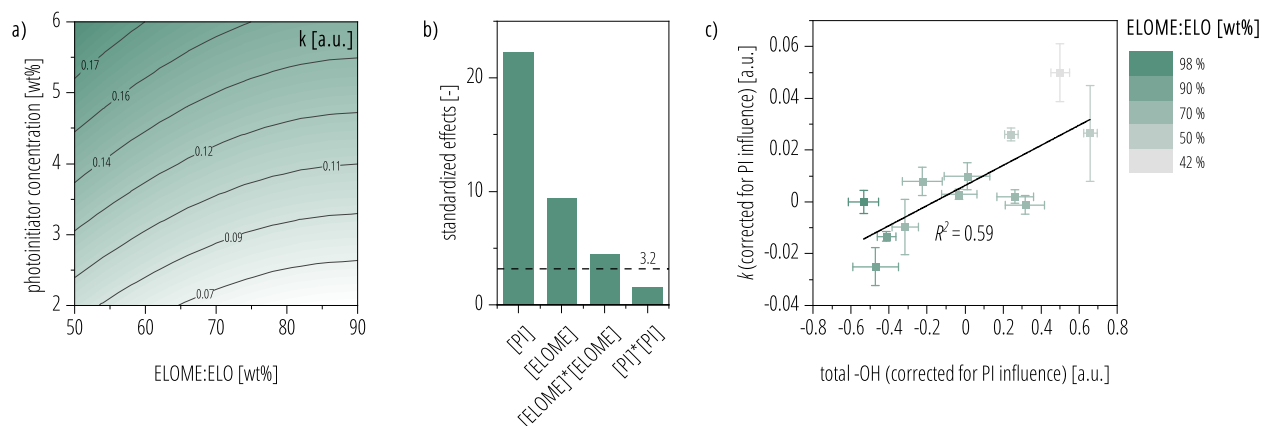


Figure 3.6: **a)** Contour plot showing the dependence of the rate constant k on the photoinitiator concentration and the ELOME:ELO ratio based on a linear model with squares ($R^2 = 0.96$). **b)** Effect size plot. The photoinitiator concentration and ELOME:ELO ratio are abbreviated as [PI] and [ELOME], respectively. **c)** Scatter plot to illustrate the relationship between the k and the formation of -OH group (due to tertiary oxonium ion formation) depending on the ELOME:ELO ratio. The data was corrected by the influence of the photoinitiator (PI) based on the fitted response surface models. Error bars represent the relative standard error of fit for the portion of the response variables from the CCD explained by the ELOME content.

relationship between k and the final intensity band area for O-H stretching vibrations (H-bonded) between 3550 cm^{-1} to 3200 cm^{-1} for the samples analyzed in the CCD was studied. A linear model was selected to fit the data for hydroxyl groups and used to calculate the portion of -OH formation explained by the ELOME:ELO ratio. Accordingly, the contribution of the epoxidized lipid composition on k was calculated. A scatter plot of the data (Figure 3.6c) indicates that fewer -OH groups were formed for higher contents of ELOME. Since the presence of -OH groups is indicative of tertiary oxonium ion formation, those results support the stronger stabilization of the secondary oxonium ion in the presence of ELOME and therefore lower k .

The reported degrees of epoxy group conversion for epoxidized linseed oil cured under cationic UV-polymerization vary between 25 % to 60 %, depending on the level of irradiation and photoinitiator type and concentration [217, 219, 225]. In the present case, the average conversion degree was 89 % with a 95 % confidence interval of 86 % to 92 %. ANOVA (Table B.13, B.2.7.3) of the linear regression model showed that the final conversion is only significantly impacted by the ELOME:ELO ratio, $F(1,9) = 75.1$, $p = 0.003$. However, the model cannot explain 37 % of the observed variation. This might be linked with the relatively small sample differences when compared to the sampling variation within the four centre point formulations ($M = 90\%$, $SD = 0.8\%$), with M and SD representing the sample mean and standard deviation, respectively. Overall, these results indicate, that the incorporation of ELOME can significantly increase the final conversion of epoxy groups compared to the use of the corresponding TAG. Given the nearly equal oxygen oxirane contents, this is likely a result of increased chain mobility in the formation of a three-dimensional polymer network due to the lack of the TAG backbone. The increase in final epoxy conversion degree is beneficial in

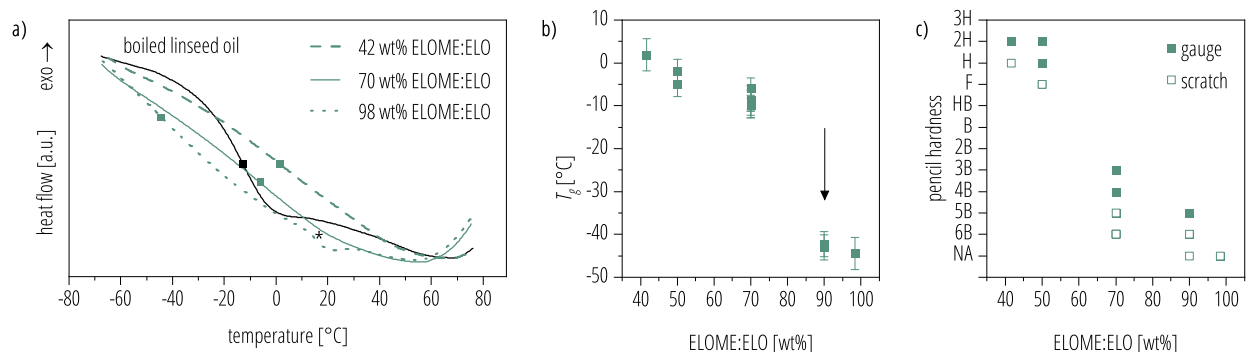


Figure 3.7: **a)** Heat flow curves (exo up) for films of boiled linseed oil and the two star point formulations of the CCD with the lowest and highest ratio of ELOME:ELO. Data points corresponding to the specific T_g are indicated with a square symbol. With ELOME:ELO ratios ≥ 90 wt %, a second transition (*) appeared. **b)** Scatter plot of T_g as a function of ELOME:ELO ratio. The main T_g for ELOME:ELO ≥ 90 wt % dropped significantly (indicated with an arrow). Error bars represent the standard error of fit. **c)** Dependence of gauge and scratch hardness on the ELOME:ELO ratio.

making use of the potential viscosity reduction achieved by incorporating ELOME, while still being able to form cross-linked films.

3.3.4 Glass transition temperature and pencil hardness

The T_g observed for air-dried films of boiled linseed oil ($M = -12.6^\circ\text{C}$, $SD = 0.6^\circ\text{C}$, $n = 3$) was within the range of T_g for the CCD formulations (-44°C to 2°C). Representative DSC traces are plotted in Figure 3.7a). Given the broad transition range, the determination of the T_g was challenging and became progressively more difficult to detect with an ELOME:ELO ratio of ≥ 90 wt %, where a second transition above 0°C appeared. This is consistent with the presence of heterogeneities in the forming polymer matrix. Figure 3.7b) shows a steep drop in T_g at high levels of ELOME. This would be expected to result in softer films, as was tested using a simple pencil hardness scratch test. Although this test involves large localized deformations, which may not correlate with dynamic properties [226], the results plotted in Figure 3.7c), do indicate that films with low ELOME content giving high T_g were indeed the hardest. The range shown covered levels from 2H and H for gauge and scratch resistance, respectively, down to 6B and lower, approaching the hardness of an air-dried boiled linseed oil film (a gauge hardness of 6B).

A linear model with squares was used to fit the T_g data ($R^2 = 0.95$) and the corresponding contour plot is shown in Figure 3.8a). ANOVA confirmed the observation that the ELOME:ELO ratio had the biggest effect on T_g (see Figure 3.8b)) and significantly reduced the T_g , $F(1,7) = 905$, $p < 0.0001$. The effect was found to be non-linear and amplified with increasing concentration. The drop in T_g by incorporating epoxidized FAME as opposed to TAG can be explained by the loss of the TAG backbone connecting the fatty acids.

The photoinitiator concentration had a minor effect on T_g . Previous research has suggested plasticizing effects by photoinitiator fragments that reduce the T_g at higher concentrations [227]. However, increasing the photoinitiator concentration also increases the number of initiated chains, as can be seen in Figure 3.8c),

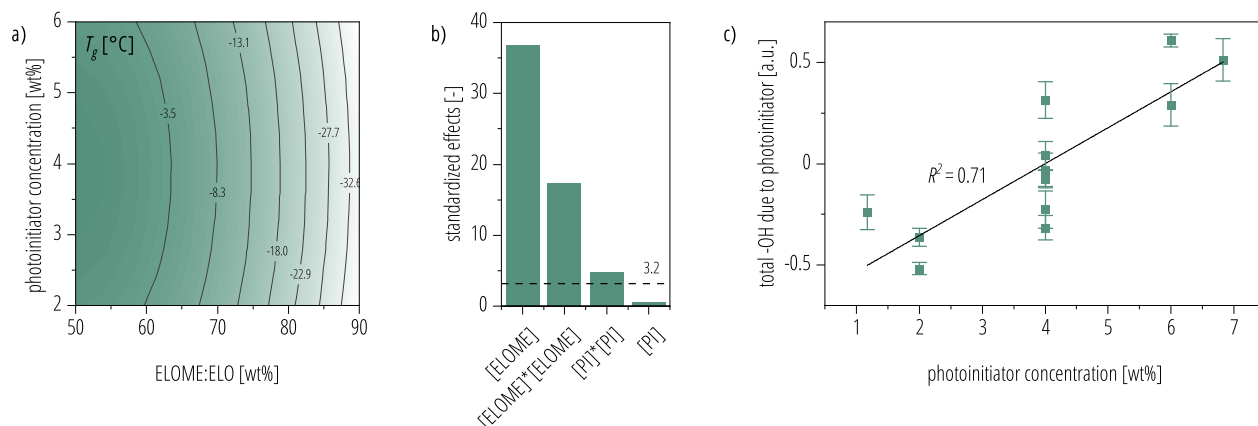


Figure 3.8: a) Contour plot showing the dependence of the T_g on the photoinitiator concentration and the ELOME:ELO ratio based on linear model with squares ($R^2 = 0.95$). b) Effect size plot. The photoinitiator concentration and ELOME:ELO ratio are abbreviated as [PI] and [ELOME], respectively. c) Scatter plot showing the dependence of the formation of -OH groups (due to tertiary oxonium ion formation) on the photoinitiator concentration for the formulations analyzed in the CCD. The data were corrected by the influence of varying ratios of ELOME:ELO based on the fitted response surface models. Error bars represent the relative standard error of fit for the portion of the response variables from the CCD explained by the photoinitiator content.

where the formation of -OH groups (see Section 3.2.2.4) in tertiary oxonium ions due to the presence of the photoinitiator is plotted against the photoinitiator concentration.

Overall, DSC analysis showed that UV-cured formulations based on epoxidized linseed FAME and TAG can be used to make films with a very similar T_g compared to air-dried linseed oil films. The relatively low T_g suggest the formation of soft and flexible films - properties that are useful for substrates undergoing volume changes, such as wood, as well as low-temperature flexibility.

3.3.5 TABER abrasion resistance

Abrasion resistance of a coated birch specimen was compared with resins of boiled linseed oil and the UV-cured epoxy (the centre point formulation with an ELOME:ELO ratio of 70:30, and 4 wt % photoinitiator). Drying oil coatings have long been known to have poor abrasion resistance [228]. Accordingly, relatively high TABER wear indices of >100 (determined over 100 cycles to 200 cycles) were measured here. Wear resistance was strongly dependent on the substrate depth. As can be seen in Figure 3.9a), there is a huge initial drop in the wear index within the first 200 cycles. This suggests high initial wear due to the possible combination of raised wood grain/surface roughness, and build up of cured resin on the wood substrate, which was even more pronounced in the UV-cured epoxy films. By only applying one coat of the epoxy, the total wear index over 1000 cycles was no longer statistically different (Figure 3.9b)) but still higher on average compared to the boiled linseed oil sample, and with a significant drop within the first 200 cycles.

Epoxy resin accumulation at the substrate's surface (formation of a top coat) is also supported the ATR-FTIR analysis of the coated wood surfaces (Figure 3.9c) upper graph) by the absence of significant absorbance

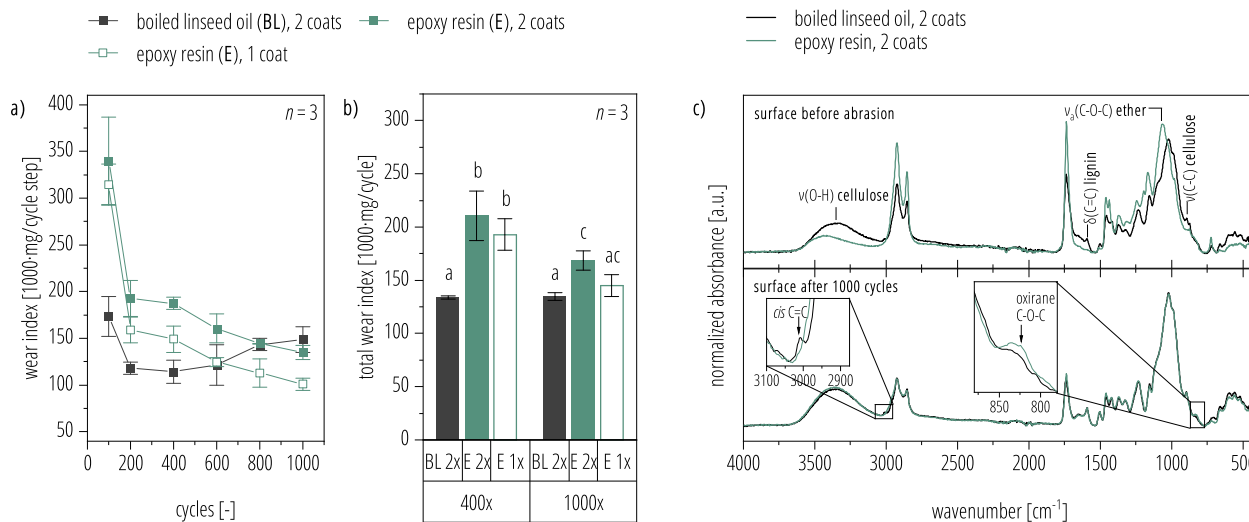


Figure 3.9: Comparison of wear resistance of air-dried films of boiled linseed oil (BL) and UV-cured epoxy resin (E) with the centre point formulation. **a)** Wear index for each additional rounds of abrasion. **b)** Total wear index over the course of 400 cycles and 1000 cycles. Means with different letters are significantly different (Bonferroni test for pairwise comparison of means, $\alpha = 0.05$). Error bars indicate the standard deviation ($n = 3$). **c)** ATR-FTIR spectra of coated birch specimen (upper graph) and after 1000 cycles of abrasion (lower graph). The inset graphs show the presence of unreacted boiled linseed oil (*cis* -CH=CH- at 3100 cm^{-1}) and epoxy resin (C-O-C at 826 cm^{-1}).

by bands related to ligno-cellulosic functional groups. While boiled linseed oil had more time to penetrate before solidification, the fast curing of the epoxy resin after coating may result in the formation of a soft top coat. ATR-FTIR spectra recorded on the sanded surfaces after 1000 cycles revealed the presence of unreacted double bonds (*cis* -CH=CH-) in the boiled linseed oil sample and unreacted epoxy groups in the epoxy resin sample. The presence of unreacted epoxy groups indicates, that dark polymerization did not proceed to deeper layers of the wood substrate. Since it has been reported that epoxy resins with thicknesses of up to several centimetres have been cured after being briefly illuminated on only one side [84], more research is needed to optimize the formulation and curing conditions to achieve better through-curing on wood.

The results highlight the importance of controlling the amount of resin applied and the time allowed to penetrate before UV-curing in order to avoid the build-up of top coat, which is poorly resistant to abrasive forces. However, the results also show that the epoxy resin was able to penetrate the wood substrate similar to drying oils, was not fully cured, and therefore requires shadow curing optimization.

3.3.6 Hydrolytic stability

The presence of unreacted linseed oil plays an important role in the colonization of linseed oil coated wood substrates by microbes due to lipase-catalyzed hydrolysis, making fatty acids available for assimilation. However, cross-linked linseed oil films were also shown to biodegrade [202, 203]. In the present study, the hydrolytic stabilities of films of cured boiled linseed oil and epoxy resin (centre point formulation) were compared by monitoring weight loss, as well as the leaching of cobalt (from the drier used in the boiled

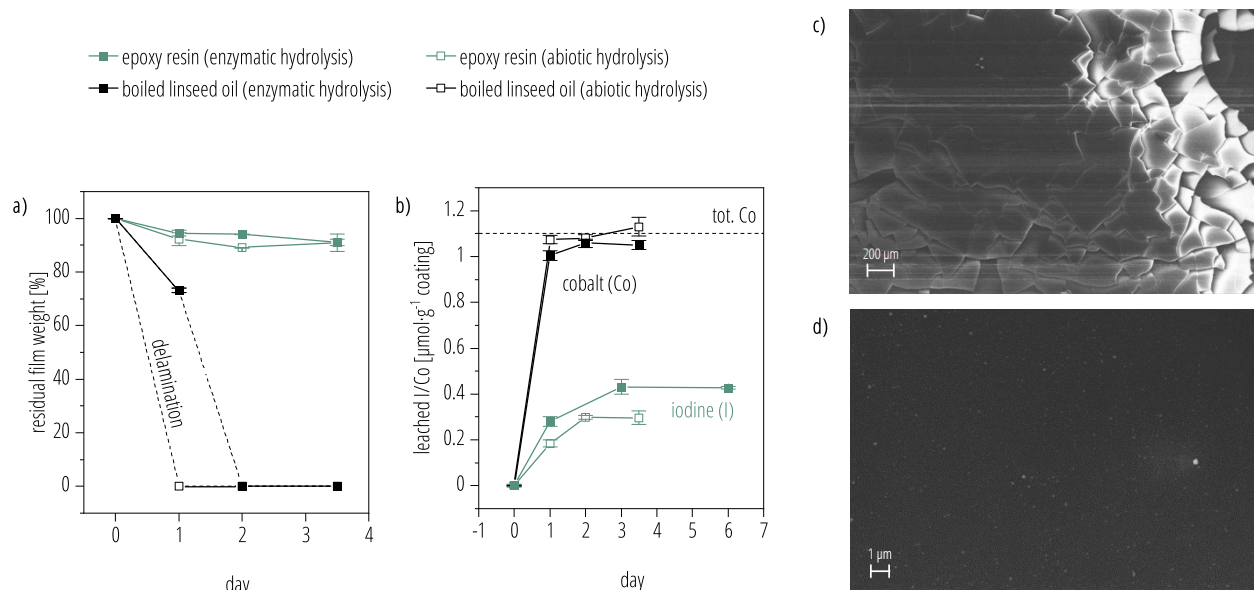


Figure 3.10: **a)** Monitoring of the residual film weight (error bars represent the standard deviation, $n = 2$). **b)** Leaching of cobalt (Co) from the boiled linseed oil films and (total) iodine (I) during the hydrolytic degradation as determined by ICP-MS/MS (dissolved or from colloids $<0.2\mu\text{m}$). Error bars represent the instrumental standard deviation, ($n = 4$). The dashed line indicates the total cobalt concentration that could be leached from the boiled linseed oil films based on digestion data (B.2.1). **c)** SEM image illustrating the effect of lipase-catalyzed hydrolysis on the surface erosion of the UV-cured epoxy resin. **d)** SEM image of a corresponding epoxy film exposed to abiotic hydrolysis with layered and homogeneous surface erosion. Colloidal particles probably precipitated on the film surface during the drying process.

linseed oil) and total iodine (originating from the iodonium cation (4, Section 3.2.1) of the photoinitiator used for the UV-curing of the epoxy resins).

Weight loss due to both abiotic and enzymatic hydrolysis was found to be much lower in the UV-cured epoxy films compared to that seen for the boiled linseed oil films (Figure 3.10a)). For example, while the weight of the boiled linseed oil film dropped by an average of 27% within the first 24 h of the test, the mean epoxy film weight was reduced by only 5%. In general, coated microscope slides provided a reproducible means to study hydrolytic degradation at application-relevant film thicknesses. However, after prolonged exposure to water, the boiled linseed oil films became turbid and started to delaminate and disintegrate, while the epoxy films showed no visual signs of surface damage and remained transparent. Drying oils, in particular linseed oil, are known to have relatively poor resistance to water immersion [228]. In a study by Rinse and Wiebols [229], air-dried linseed oil films of $20\mu\text{m}$ to $50\mu\text{m}$ were reported to absorb water between 100% to 330% of their weight. After subsequent drying of the turbid and tacky films, weight losses of $>20\%$ (compared to the unaltered film weight) were measured, which is in the range of what was observed in the present study.

Interestingly, the weight losses observed under abiotic conditions were similar to those observed in the presence of the lipase. However, the boiled linseed oil films appeared to delaminate even faster in the absence of the enzyme. It is suggested that high concentrations of lipase provided some protection to the film due to the

presence of lipophilic domains, possibly counteracting the swelling and subsequent film damage caused by water. While most studies on enzyme-catalyzed degradation of polymers at $\text{pH} = 7$, including the present one, are conducted in phosphate buffers [230–232], it is well-known that phosphate ions are very effective in catalyzing hydrolytic reactions [233]. This suggests that these studies show a combined effect of anionic and enzymatic catalysis of ester hydrolysis. For films of boiled linseed oil, the contribution of the solubilization of extractables (*e.g.* secondary oxidation products of low molecular weight), and the hydrolytic degradation cannot be separated based on the observed weight. Certainly, the high swelling of the boiled linseed oil films by water promoted rapid bulk degradation [234], while the epoxy films appeared to degrade only *via* surface erosion at consequently lower degradation rates.

Figure 3.10b) shows the amount of cobalt and total iodine (both $<0.2\ \mu\text{m}$) leached from the films during hydrolytic degradation as determined by ICP-MS/MS. Most of the cobalt drier present in the boiled linseed oil was leached into the buffer solution. These driers are typically used as metal carboxylates [111] and are not covalently bound to the drying oils matrix, making them prone to leaching during bulk degradation of the drying oil films. In the case of the enzymatically hydrolyzed epoxy resins, the faster rate and higher levels of dissolved and colloidal iodine, show that enzymatic hydrolysis of ester bonds had a significant effect on the release of iodine photoinitiator fragments, while the total weight loss was comparable to abiotic conditions within the 3.5 d period. These results are supported by SEM analysis (see Figure 3.10c) and d)), which showed a clear enzyme-effect on the surface erosion behaviour. Enzymatic hydrolysis resulted in surface penetration giving rise to erosion with a shattered surface appearance seen in Figure 3.10c). Increased solubilization and leaching of iodine would be expected to follow this increase in surface area. Interestingly, the surface pattern does not show the pits and cavities typically reported in other studies on the enzymatic hydrolysis of polymers [235–237]. This suggests a relatively low enzyme activity. In contrast to studies on biodegradable polyesters, ether cross-links were the most dominant in the present polymer. Whether surface weaknesses or the mode of lipase interaction with the surface eventually led to the observed crack formation requires further investigation. On the other hand, apart from occasional deposited colloidal polymer particles, a smooth film surface from surface erosion of the epoxy film was found under abiotic conditions (Figure 3.10d)), consistent with erosion occurring evenly downwards from the surface layer.

Overall, these results suggest that abiotic hydrolysis may be an underestimated cause of film degradation. Despite having comparable T_g , films of the epoxy resin were found to have a higher hydrolytic stability ($\sim 20\%$ less weight loss) within the tested time period compared to films of air-dried boiled linseed oil. This is probably related to the swelling behaviour of the latter, promoting bulk degradation with higher rates of hydrolytic degradation, whereas the epoxy films remained intact during the course of the investigation and were subject to surface erosion. While the epoxidation of plant oils preserves their biodegradability [238], less is known about the ability of microbes to breakdown cross-linked epoxidized lipids. Overall, the higher hydrolytic stability and absence of bulk degradation of the epoxy resin is expected to reduce its biodegradability compared to boiled linseed oil films. Whether higher hydrolytic stability can effectively delay staining due to microbial colonization still needs to be verified.

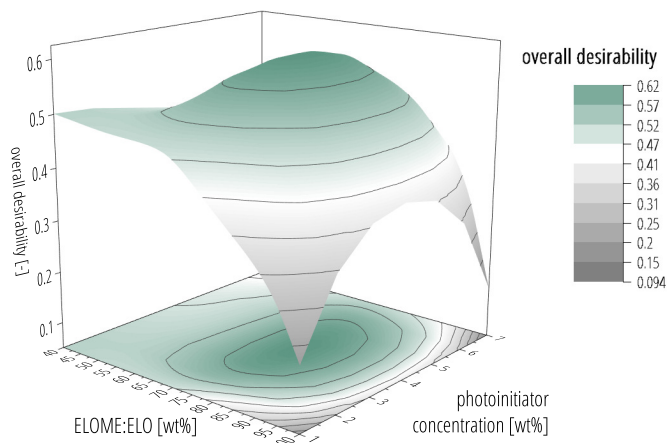


Figure 3.11: Overall desirability calculated based on minimized photoinitiator concentration, minimized viscosity, maximized polymerization rate, and similar T_g compared to the boiled linseed oil control sample.

3.3.7 Desirability assessment

The systematic analysis of the structure-property relationships discussed above, revealed a wide range of film properties that can be obtained from the photo-induced cationic polymerization of epoxidized linseed lipids. To produce an environmentally friendly alternative to air-dried linseed oil, the photoinitiator concentration should be minimized whilst achieving an acceptable viscosity and fast curing. Figure 3.11 shows a 3D colourmap surface and contour plot of the calculated overall desirability of formulations with different ELOME:ELO ratios and photoinitiator concentrations. The results indicate that high ratios of ELOME:ELO (75 wt % to 85 wt %) and moderate photoinitiator concentrations (3 wt % to 5 wt %) offer the best "compromise" as a potential alternative to air-dried linseed oil, with a similar T_g (between about $-10\text{ }^{\circ}\text{C}$ and $-15\text{ }^{\circ}\text{C}$) and resin viscosity acceptable for spraying applications.

A preliminary theoretical study of the photoinitiator ecotoxicity (B.2.2) supports the low toxicity claimed by the supplier. This might be related to its poor water solubility. However, based on the calculated $\log K_{ow}$ values, the photoinitiator and some of its fragments have the potential to bioaccumulate. Therefore, additional measures to decrease the curing time should be applied in order to minimize the photoinitiator concentration, such as the use of photosensitizers [80] or partial ring opening of the epoxy groups by alcohols to introduce hydroxyl groups for faster polymerization *via* an activated monomer mechanism [219] (*cf.* Eq. 1.24, Section 1.1.3).

In any case, the drying time compared to linseed oil is substantially reduced from days/weeks to just minutes. Depending on the application, the boundaries and targets of the response variables used will differ, but the studied formulations appear to cover the relevant range of compositions.

3.3.8 Preliminary suitability assessment of curcumin-sensitized solar curing

While the use of UV is advantageous for heat sensitive substrates like wood, equipment cost and safety issues could limit the use of the model system developed here as a drying oil alternative in the do-it-yourself (DIY) market. Since most cationic photoinitiators based on onium salts have absorption maxima in the UV-C and UV-B range [239], they are not activated under visible light. However, photosensitizers such as aryl ketones, 1,2-diketones, and quinones, can be used to extend the absorption range through an electron-transfer mechanism [239–244]. Curcumin was discovered to be an effective photosensitizer for diaryliodonium salt photoinitiators for various monomers used in cationic polymerization, including epoxies [245]. The commonly accepted mechanism is an electron transfer reaction involving the free-radical chain decomposition of the onium salt photoinitiator.

As can be seen in Figure 3.12a), solar curability could be reproduced in the current lipid-based system with curing times of 3 min to 4 min comparable to those obtained under pulsed UV irradiation (Section 3.3.3). However, it was found that the curing time increased significantly for films with a lower wet thickness of 20 μm (Figure 3.12b)) and the surfaces remained tacky. Considering that the proposed mechanism for curcumin-based photosensitization includes radical species, potential O_2 inhibition was suspected as the underlying cause for the increase in curing time (*cf.* Section 1.1.2.3).

The formation of unreactive peroxy radicals upon reaction with oxygen is a well-known issue [246] for UV-induced radical polymerization. It is of special relevance with thin films (diffusion of O_2 from the top down) and systems of lower reactivity (time dependence). Tertiary amines are known to react with O_2 to form peroxy radicals and thereby reduce the O_2 concentration in the film [65] (Eq. 1.17, Section 1.1.2.3). Here, the addition of $3 \cdot 10^{-2}$ wt % EDTA was able to reduce the curing time of films with a 20 μm wet thickness from an average of 6.5 min to 3.1 min, and resulted in tack-free surfaces. However, the curing time remained strongly temperature-dependent and increased to an average of 10 min with a 10 $^\circ\text{C}$ drop in air temperature from 26 $^\circ\text{C}$ to 16 $^\circ\text{C}$. The formation of charge complexes [245] with curcumin also causes a colour change from bright yellow to dark red (Figure B.2a), B.2.4). It was observed that over time, the colour changed irreversibly to olive green. At thin layers applied on wood substrate (Figure B.2b), B.2.4), however, the colour difference compared to UV-cured epoxy resin in the absence of curcumin was minimal, suggesting the general applicability of curcumin-sensitized formulations. Furthermore, the use of curcumin in these coatings, could have other benefits, such as imparting antimicrobial properties [247].

3.4 Conclusion

This feasibility study demonstrated that the epoxidation of linseed TAG and FAME can be used to make UV-curable films, as an alternative to its traditional use as a drying oil. The epoxidized linseed monomers offer much faster drying times and can be cured within minutes compared to the autoxidative polymerization of linseed oil, which takes days to weeks.

While the epoxy group conversion was mostly affected by the photoinitiator concentration, ATR-FTIR provided further evidence that chain flexibility is linked to secondary oxonium ion stabilization, which is con-

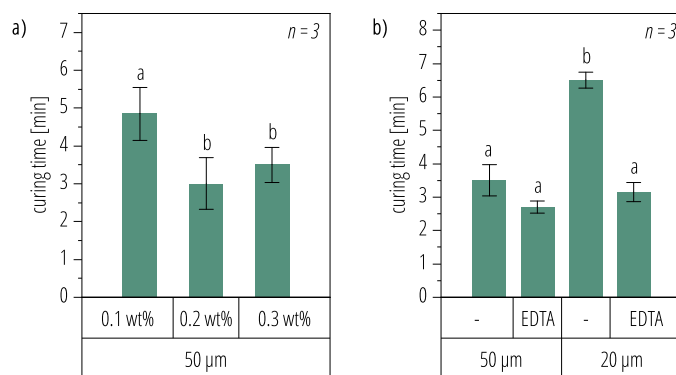


Figure 3.12: Determination of the dry-through time using a drying time monitor during solar curing with curcumin as the photosensitizer. **a)** Curing time dependence on the curcumin concentration (0.1 wt % to 0.3 wt %). **b)** Curing time-dependence on film thickness (20 μm versus 50 μm) due to suspected O₂ inhibition, which can be avoided by adding 3 · 10⁻² wt % EDTA. Error bars show the standard deviation ($n = 3$) and letters indicate significant differences based on a Bonferroni means comparison ($\alpha = 0.05$).

sidered to be one of the main reasons for the induction time observed in the photo-induced cationic polymerization of epoxidized plant oils. Films with a high content of ELOME had a high cross-linking efficiency ($\geq 80\%$ epoxy group conversion), resulting in a T_g comparable to films of boiled linseed oil despite the loss of the TAG backbone. This enables a resin viscosity close to that of linseed oil to be achieved. As with drying oils, the epoxy resin was found to provide poor protection against abrasive wear, in particular when the resin is applied in high amounts and cured before fully penetrating the wood substrate. Therefore, the amount of resin applied and the curing time should be controlled to obtain a penetrating finish without the buildup of a top coat.

The formation of ether cross-links *via* cationic polymerization was found to improve the hydrolytic stability of the epoxy films. While air-dried films of boiled linseed oil undergo rapid bulk degradation, the epoxy films were only hydrolyzed through surface erosion under both abiotic and enzymatic conditions. Future studies are needed to investigate how this might improve their durability with regards to weathering resistance and staining due to microbial colonization. Furthermore, colour stability should be investigated since a spruce specimen treated with the UV-cured epoxy formulation and stored for 6 months in the dark did not undergo the typical yellowing observed for boiled linseed oil (Figure B.4, B.2.6).

The use of curcumin offers a plant-based solution to the solar curability of these formulations with curing times similar to those under pulsed UV radiation. In this work, O₂ inhibition was found to significantly affect the drying time and surface tackiness when applying thin coats. However, the use of a low-cost tertiary amine circumvents this issue.

It is therefore proposed that epoxidized plant lipids, in particular epoxidized FAME, could serve as the basis for durable and faster curing alternatives to drying oil wood coating. These maintain the penetrating and flexible properties of cured linseed oil films at a $>93\%$ biorenewable content.

Chapter 4

Low concentration CNC as an adhesion promoter in a UV-curable coating

CNC at low loading levels were shown to reinforce a photocurable coating resulting in improved adhesion. A polyether polyol containing CNC at loading levels of up to 1.8 weight percent was grafted with 3-isopropenyl- α,α -dimethylbenzyl isocyanate to functionalize it with a photocurable group. The nanoparticles were kinetically stabilized in the rapidly forming prepolymer of high viscosity. Photoinitiators and a difunctional reactive diluent were added to produce optically transparent coatings and free films upon irradiation by UV light. This allowed evaluation of the effects of CNC at low loading levels in a glassy polymer matrix obtained through a rapid cure system. Incorporation of CNC nanoparticles in the polymer matrix resulted in an average improvement in adhesive strength of 150% while enhancing tensile strength by an average of 16%. The technique described could be used as a new approach to reduce adhesive failure in UV-curable coatings without sacrificing their mechanical strength.

4.1 Introduction

CNC has received attention as a potential reinforcing agent for polymeric matrices. As organic fillers obtained from biorenewable feedstock, they exhibit remarkable mechanical properties at low density. Compared to steel, CNC has an almost three times higher specific Young's modulus, the ratio of Young's modulus to density [103]. These properties could therefore satisfy the twin demand of high performance and renewability. In a recent review, Oksman et al. [248] highlighted the exponential increase in CNC nanocomposite research since the early pioneering work in the mid-90s, and the initial focus on solvent casting of water-soluble or water-dispersible (bio)polymers mixed with cellulosic nanomaterials [102, 249]. Impregnation [250, 251] and twin-screw extrusion were later investigated as ways of producing cellulose nanocomposites in thermoset and thermoplastic matrices, whereas the current trends are in areas such as nanocomposite foams and fibres [248]. Reinforcement in nanocomposites is largely based on the stress transfer through the large interfacial area

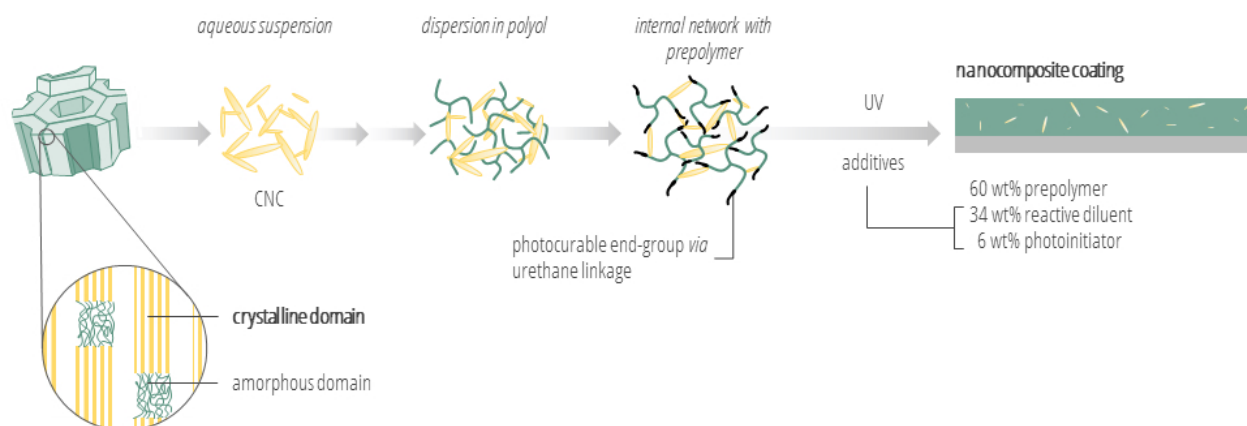


Figure 4.1: Schematic overview of the approach used to kinetically stabilize CNC in a photocurable prepolymer. Dispersion of CNC in polyol is obtained through a solvent-exchange process. In a next step, the polyol is reacted with isocyanate to form the viscous prepolymer, which forms an internal network with CNC and serves as the main component of the UV-curable resin.

shared between the nanoparticles and the matrix, which is much larger than the interface with conventional fillers [252]. Therefore, achieving a homogeneous dispersion of nanoparticles in the matrix is a key factor in exploiting nanoreinforcement. In the case of CNC, the abundance of surface hydroxyl groups and its strong tendency for hydrogen-bonded agglomeration makes dispersion in hydrophobic polymers quite challenging, requiring the use of surfactants [253] and surface modification (*cf.* Dufresne [103] for an extensive review).

The reported improvements in the mechanical properties of thermoplastic composites (*e.g.* abrasion resistance) makes CNC reinforcement an interesting approach for use in coatings that has only been explored in a few studies [254]. A fast-growing technology in the coating industry involves coatings curable by UV irradiation [50]. Unlike conventional coating systems, which mainly solidify through solvent evaporation and polymer entanglement, UV-curable coating components are used in their monomeric or oligomeric form and polymerize once exposed to high-intensity UV light. While this rapid polymerization allows for the immediate processing of the cured surface, it is also accompanied by substantial shrinkage resulting in the build-up of internal stresses. This can negatively impact mechanical properties such as adhesion to the substrate [255], and is one of the main drawbacks of UV-cured coatings [256]. Although the use of nanotechnology to improve scratch and abrasion resistance of UV-curable coatings has been well studied [257–263], its use in adhesion control has been less investigated despite poor adhesion being a major challenge for these coatings.

In this work, a combined approach of CNC nanoreinforcement and UV-curability was investigated. A summary of the literature describing CNC utilization in UV-curable nanocomposites is given in Table 4.1. These reports typically use relatively high CNC loading levels (>1%) and CNC surface modification in order to achieve sufficient compatibility with the matrix. Using CNC for nanoreinforcement of UV-curable coatings is of special interest since it lacks some of the negative impacts on the curing as reported for behaviour of more commonly explored inorganic nanoparticles which can absorb or diffuse UV radiation [264].

In this work, low concentrations of unmodified CNC to mitigate cost and concentration-dependent [265] agglomeration were investigated. As illustrated in Figure 4.1, the idea was to stabilize a CNC suspension in the main component of a UV-curable resin, a high viscosity prepolymer, and make use of the rapid polymerization under UV radiation to guarantee efficient entrapment of the nanoparticle suspension within the forming polymer matrix. It has been previously shown that CNC nanoreinforcement in polyurethanes can be achieved using low CNC loading levels [266]. This is based on the high dispersion qualities of CNC in polyol obtained through the developed solvent-exchange technology. In the present case, the polyol-CNC suspensions were used as the starting material to synthesize a photocurable urethane prepolymer. Urethane oligomers are commonly used in UV-coatings due to their excellent weathering stability. A simple one-step chemical transformation of the polyol into a photo-reactive prepolymer was achieved using an isocyanate bearing an α -methyl styrene moiety (*cf.* Eq. 1.29, Section 1.2.4). Unlike the acrylates (secondary radicals) that are often used to photopolymerize UV-curable coatings, the present system has much lower reactivity (tertiary radicals, see Section 1.1.2.1). Despite this disadvantage, the simplicity and controllability of the reaction used is an advantage for studying the CNC dispersibility and effects of CNC on the properties of a model system as the main objective of this study.

Table 4.1: Review of selected properties of UV-nanocomposites reinforced with CNC.

CNC	polymer matrix	CNC modification	rheology	T_g	mechanical properties	dispersibility	others	references
5 %, 10 %	methacrylic siloxane	NA	pseudoplastic	7 °C increase at 10% CNC	increase in storage and loss modulus	inconclusive (SEM)	retarded thermal degradation, reduced curing efficiency due to light scattering by CNC (>5%)	Cataldi et al. [267]
1 %	polyurethane acrylate (water-borne)	NA	NA	absence of noticeable effects by CNC	increased Young's modulus and tensile strength	NA	covalent linkages between CNC and matrix forming electron beam curing	Furtak-Wrona et al. [268]
2 %, 4 %, 8 %	epoxy acrylate (in dimethylformamide)	NA	NA	up to 40 °C increase in T_g	increased storage modulus	NA	slightly lower optical transmittance	Pan et al. [269]
0.5 %, 1 %, 1.5 %, 2 %, 3 %	polyurethane acrylate (water-borne)	cationic surfactant	strong increase in viscosity above 1.5% CNC	NA	30 % to 40 % increase in wear resistance (abrasion/scratch)	increased surface roughness at >2% CNC (atomic force microscopy)	increased contact angle due to modified CNC	Vardanyan et al. [254]
1 %, 3 %	epoxy acrylate	cationic surfactant	NA	slight decrease	NA	substantial agglomeration (polarized light microscopy)	decreased water vapour transmission rate	Kaboorani et al. [265]
1 %, 3 %	epoxy acrylate, methacrylate, acrylate	cationic surfactant	NA	NA	hardness, Young's modulus, tensile strength, and abrasion resistance were improved	increased surface roughness (atomic force microscopy)	increased thermal stability up to 430 °C, no effect on curing behaviour	Kaboorani et al. [264], Kaboorani et al. [270]
2 %	polyurethane acrylate (water-borne)	grafting	NA	NA	improved abrasion resistance (greater for modified CNC), decreased adhesion to wood	reduced surface roughness compared to unmodified CNC (atomic force microscopy)	haze/gloss apparatus: aesthetic appearance preserved	Poaty et al. [271]
1 %, 2 %	acrylated epoxidized soybean oil	grafting and cationic surfactant	NA	NA	Young's modulus, tensile strength, and hardness increased	aggregates (polarized light microscopy)	CNC acrylation increased fragility, cationic surfactant increased ductility	Auclair et al. [272]

4.2 Materials and methods

4.2.1 Materials

The CNC was supplied as a homogenous aqueous suspension from a previous study [273]. Carpol[®] GP 725 polyol with a hydroxyl number of 240 mg KOH g⁻¹ and viscosity of 0.25 Pa s (at 25 °C) was donated by Carpenter Co. (Richmond, Virginia, USA). 3-Isopropenyl- α,α -dimethylbenzyl isocyanate (TMI, CAS 2094-99-7), 95 % was purchased from Sigma Aldrich Canada. Umicore Speciality Materials Brugge NV (Bruges, BE) supplied the bismuth carboxylate catalyst (Valikat Bi 2010) used for the prepolymer synthesis. Rahn AG has (Aurora, Illinois, USA) has kindly provided Genomer 1225 (tri(ethyleneglycol) diacrylate), which was used as the reactive (difunctional) diluent. 2,2-Dimethoxy-2-phenylacetophenone (DMPA, CAS 2460-42-8), 99 % was purchased from Sigma-Aldrich Canada. Genocure LTD, a 50:50 wt% mixture of 2-hydroxy-2-methyl-1-phenylpropan-1-one (DMHA, CAS 7473-98-5) and 2,4,6-trimethylbenzoyl-diphenylphosphine oxide (TPO, CAS 75980-60-8) was kindly provided by Rahn USA (Aurora, Illinois, USA). Details of the utilized photoinitiators are listed in Table 4.2. They undergo fast homolytic cleavage when exposed to UV light following a Norrish type I mechanism (Eq. 1.16, Section 1.1.2.2) to generate free radicals.

Table 4.2: Specification of the used photoinitiators. The absorption maxima occur over a broad range of the UV spectrum (UV-C to UV-A).

photoinitiator	type	absorption maxima (λ_{\max})
DMHA	hydroxy alkyl phenone	247 nm, 277 nm
TPO	phosphine oxide	380 nm
DMPA	benzile ketal	250 nm, 340 nm

4.2.2 Methods

An overview of the conducted experiments and analyses is illustrated as a process flow diagram in Figure 4.2. The two main aspects of this research concern the dispersion of CNC in a UV-curable prepolymer, and to study its effect on the thermomechanical coating properties upon UV-curing.

4.2.2.1 Polyol-CNC suspension

Polyol-CNC suspensions were produced using a solvent exchange process as described earlier [266]. First, an aqueous suspension of CNC (10.3 wt %) was diluted to a CNC concentration of 2 wt % with 1,3-propanediol. Then, the H₂O-1,3-propanediol-CNC suspensions were mixed with various amounts of GP 725 polyol, and excess water and 1,3-propanediol were simultaneously removed using a wiped-film evaporator at low pressure. The final CNC concentrations in the polyol were: 0.4 wt %, 0.8 wt %, and 1.6 wt %. The remaining water and 1,3-propanediol concentrations were between 0.6 % to 1.3 % and 0.4 % to 1.0 %, respectively. Moisture uptake due to hygroscopicity of the polyol can be controlled by selecting appropriate processing conditions to avoid the formation of plasticizing byproducts during prepolymer synthesis. Residual 1,3-propanediol due to suboptimal solvent removal efficiency is less critical. During grafting with the isocyanate monomer, it will

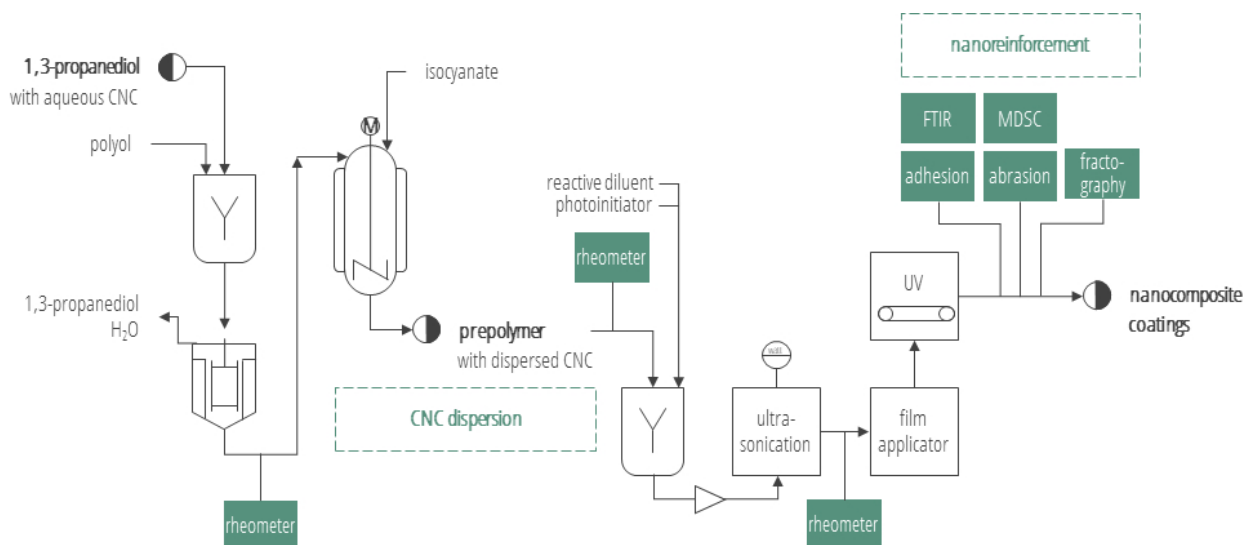


Figure 4.2: Simplified process flow diagram of the experimental setup and analyses to study the dispersion of CNC and its nanoreinforcement effects in a polyurethane-based UV-curable resin.

form a photocurable oligomer of lower molecular weight than the prepolymer and would increase the cross-linking density. Therefore, it would contribute to reinforcing effects, in contrast to other solvents commonly used in CNC processing, such as dimethylformamide, which may act as plasticizers in the matrix [266].

4.2.2.2 Prepolymer synthesis and characterization

Polyol grafting with TMI under nitrogen atmosphere was performed at a 1:1 molar ratio of OH:NCO functional groups and total weight of 20 g. The reaction was catalyzed using the bismuth carboxylate catalyst Valikat Bi 2010 (0.8 wt %). All chemicals were weighed into a 3-necked reactor equipped with a Teflon stirrer blade and the reaction was started immediately to prevent phase separation. The experimental setup is illustrated in Figure 4.3. Using an oil bath, the external temperature of the reactor was held at a temperature of 50 °C.

The structures of the reactants and proposed addition product, a star-shaped urethane styrene prepolymer, are shown in Figure 4.4. The prepolymers were used within 48 h of their synthesis to prepare the UV-curable resins. The same reaction conditions were applied to the polyol CNC suspensions.

ATR-FTIR monitoring of the grafting reaction The degree of isocyanate conversion was determined by monitoring the $\nu(\text{N}=\text{C}=\text{O})$ band in the FTIR spectra collected during the reaction using attenuated total reflectance Fourier transform infrared (ATR-FTIR) spectroscopy (Platinum ATR Alpha, Bruker). A total of 16 interferograms were summed before Fourier transformation. Using the OMNIC 8 software (Thermo Scientific), the peak areas were determined between 2330 cm^{-1} and 2187 cm^{-1} using the series function with automatic baseline correction. In order to estimate the initial isocyanate band area (time $t = 0\text{ min}$), a mixture of polyol and TMI was prepared (in the absence of the catalyst) to avoid preliminary reaction

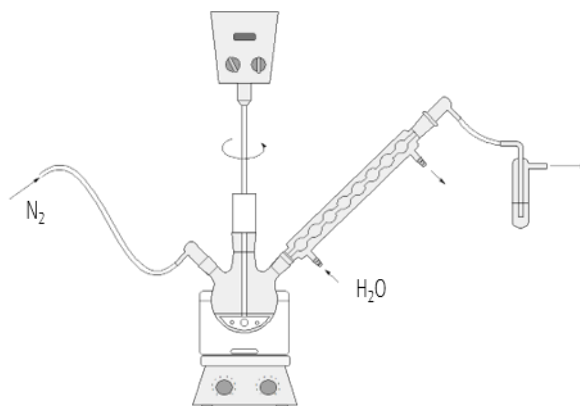


Figure 4.3: Experimental setup for the prepolymer synthesis. All chemicals were weighed into a 3-necked reactor equipped with a mechanical stirrer (Teflon stirrer blade) operating at 300 rpm and a reflux condenser under nitrogen atmosphere. The external temperature of the reactor vessel was adjusted to 50 °C using an oil bath.

between the polyol and TMI. To fit the isocyanate conversion data points, the average reaction rate constant, k , was determined from linear regression of $1/A_{NCO}$ plotted as a function of time t (between 0 min and 30 min). Then, k was used to model the conversion rate according to the following equation (4.1):

$$\text{conversion}[\%] = \frac{A_{NCO, t=0} - \frac{1}{k \cdot t + \frac{1}{A_{NCO, t=0}}}}{A_{NCO, t=0}} \quad (4.1)$$

Molecular size distribution analysis by GPC The grafting of the polyol was further confirmed by gel permeation chromatography (GPC). The chromatograms were acquired using an isocratic Agilent 1200 pump (Agilent Technologies) equipped with an evaporative light scattering detector (Alltech ELSD 2000, Mandel Scientific Company) at a tube temperature of 60 °C. A column ((300 × 4.6) mm² i.d.) with a particle

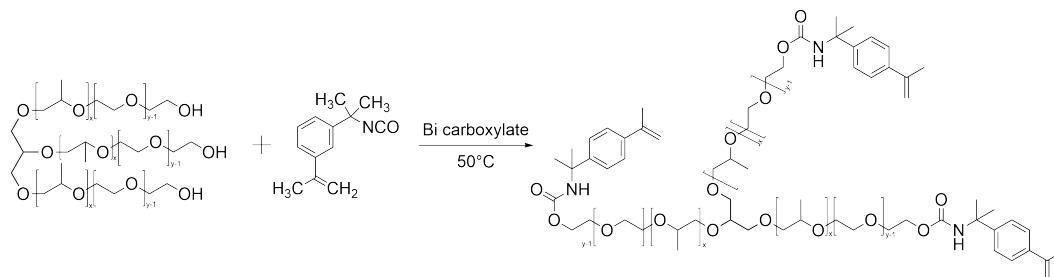


Figure 4.4: Grafting of a commercial polyol (GP 725) with TMI isocyanate through carbamate linkages (-NHCOO-). The addition reaction results in the formation of a star-shaped prepolymer with photocurable moieties (terminal geminal disubstituted double bonds).

Table 4.3: Resin formulation for the model coating system developed to study CNC behaviour in an according nanocomposite. Batch sizes of 4 g were prepared.

resin component	content [wt%]
CNC prepolymer suspension	60
reactive diluent (Genomer 1225)	34
photoinitiator blend	6 (total)
- DMHA/TPO (50:50 wt%)	4
- DMPA	2

size of 5 μm (Styragel HR 4E THF, Waters Corporation) was used under the following isocratic conditions: tetrahydrofuran (THF, HPLC-grade) as the mobile phase at a flow rate of 0.5 ml min^{-1} and injection volumes of 10 μl . The sample preparation included diluting 0.3 mg of the unreacted polyol and the prepolymer, respectively, into 10 ml of THF. Polystyrene standards with known molecular weights were used to generate a calibration curve. The prepolymer CNC suspensions could not be analyzed by GPC as the nanoparticles would damage the column.

Prepolymer viscosity Viscosity dependence of the prepolymer on the shear rate under steady state conditions was analyzed by rotational rheology (Advanced Rheometer AR 2000, TA instruments) at 35 $^{\circ}\text{C}$ using a plate/cone geometry (2 $^{\circ}$, 40 mm diameter, truncation gap distance of 52 μm). Up- and down-ramps applying shear rates from 0.01 s^{-1} to 3000 s^{-1} were applied to the sample. The analysis was preceded by a 5 min conditioning step at the measurement temperature, and a solvent trap was used to avoid photochemical oligomerization during the measurement.

4.2.2.3 Photocurable nanodispersion

A combination of photoinitiators (liquid blend of DMHA/TPO and DMPA) with absorption in the UV-C and UV-A regions was selected to increase the total absorption range for faster curing as well as to facilitate surface and through curing (Table 4.2). DMPA was added mainly due to its insensitivity towards photoinitiator quenching by styrene [50]. The photoinitiators were dissolved in the reactive diluent, forming a slightly yellowish (UV-VIS absorption by DMPA) but transparent solution. The mixtures could be blended with the prepolymer by applying 30 s of ultrasonication (Sonic Dismembrator Model 100, Fisher Scientific) followed by subsequent mixing using the vortex mixer (Fisher Scientific). The large amount of air introduced could be efficiently removed by a second application of ultrasonication, resulting in the formation of clear solutions. The formulation of the resin is listed in Table 4.3. The resulting CNC concentrations in the resin were: 0.1 wt %, 0.3 wt %, and 0.5 wt %.

After cooling to room temperature, the resin was coated onto cleaned glass plates with a wet film thickness of 120 μm using a 4-sided film applicator (1209468, BYK). The liquid films were cured in a lab-scale UV-curing unit (Mini Laboratory Unit with a medium vapour pressure mercury lamp, GEW (EC) Limited, UK) at a conveyor belt speed of 5 m min^{-1} . A sample support (2.5 cm) served to reduce the distance to the lamp and

thus increase the UV dose. Nested coating replicates ($n = 6$ with the exception of $n = 3$ for the abrasion analysis) were prepared from three replicate resins per treatment. To guarantee a stable and reproducible degree of curing (terminal double bond conversion), the photopolymerization kinetics were investigated in a pre-study, the details of which can be found in C.1.1. Stable maximum conversions at both the top and bottom side of the coatings were achieved upon 16 passes under the UV source (Figure C.2).

Resin viscosity The rheological properties of the resins under shear were investigated using the same method as applied to the prepolymer, details of which can be found in Section 4.2.2.2.

4.2.2.4 CNC-matrix interaction

The influence of CNC on thermal and mechanical properties (tensile and abrasion), as well as interfacial bonding failure between coating and substrate were investigated. While by definition, coatings are bonded to a substrate, some of the conducted tests, required the preparation of free films by peeling them off the glass substrates after UV-curing.

Modulated differential scanning calorimetry Modulated differential scanning calorimetry (MDSC) was used to determine the glass transition temperature (T_g) of the UV-cured films (2 mg to 3 mg) using a differential scanning calorimeter (TA Q100, TA Instruments) and standard aluminum sample pans. The samples were directly cooled to $-50\text{ }^\circ\text{C}$ at a rate of $5\text{ }^\circ\text{C min}^{-1}$. Then, a modulated heating profile up to $100\text{ }^\circ\text{C}$ was applied using a linear heating rate of $2\text{ }^\circ\text{C min}^{-1}$ and a modulated heating rate with a 60 s modulation period and $1\text{ }^\circ\text{C}$ temperature amplitude. The glass transition temperatures were determined from the reversing heat flow curve using the TA analysis software (Universal Analysis 2000) from the inflection point between onset and endpoint of the glass-rubber transition range.

Tensile properties and fractography The tensile tests were performed at room temperature following ASTM D882-12 using a Shimadzu AGS-X tester (Shimadzu Scientific Instruments) but without conditioning of the samples. Free-standing specimens with dimensions of 9 mm x 75 mm were prepared by peeling the UV-cured films from the glass substrate using a scalpel. The thickness of the specimen was estimated using an electronic digital caliper (PRO-MAX, Fowler). Based on the ASTM recommendation for samples with less than 20 % elongation, an initial strain rate of 0.1 min^{-1} was applied. The required rate of grip separation was then calculated as 5 mm min^{-1} for an initial gap separation of 5 cm. Toe compensations had to be made for the calculation of percentage elongation and plastic strain (ε_p) as described by the standard method. The elastic strain (ε_e) was calculated as the difference between the elongation at break and the plastic strain.

The overall fracture patterns were analyzed using a Super CoolScan 5000 ED Film Scanner (Nikon) and optical microscopy (DMRX, Leica Microsystems). This was complemented by scanning electron microscopy (SEM) to help identify the fracture mode. Conductive coatings of carbon were deposited using a Leica EM SCD005 evaporative carbon coater before analysis with a Zeiss Sigma Field Emission SEM (300 VP-FESEM). In both cases, ATR-FTIR analysis was used to determine the top surface of the film, which was investigated together with the fracture surface.

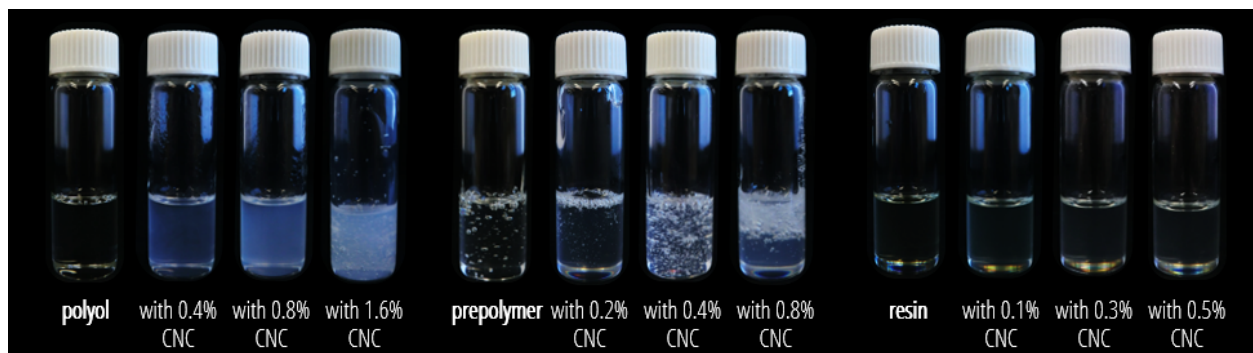


Figure 4.5: Images of the polyol, the prepolymer, and the resin, with CNC concentrations indicated as weight %. For the polyol and prepolymer suspensions, the turbidity increases with the CNC concentration. The viscosities of the prepolymer suspensions are the highest. Accordingly, those samples could hardly be degassed (*cf.* entrapped air bubbles) with the effect the strongest at higher CNC loading levels.

Abrasion resistance TABER abrasion resistance was determined using an abrasion tester (5130 Abraser, TABER Industries) based on the ASTM D4060-14 specifications without conditioning. Steel specimen plates (S-16, TABER Industries) were coated (about 280 μm wet thickness) using a film applicator (Universal Blade Applicator, Garoco Paul N. Gardner Company). Two abrading wheels (CS-17, TABER Industries) with a load of 1000 g on each wheel were used. The weight loss after 500 cycles was recorded and the wear index was calculated as 1000 times the loss in weight in milligrams per cycle. The wheels were resurfaced before testing each specimen and after every 500 cycles by resurfacing against the resurfacing medium (S-11 abrasive disk, TABER Industries) for 50 cycles. Three independent specimen were prepared for each treatment.

Pull-off adhesion strength Following the ASTM D4541-09 standard method, pull-off adhesion strength was measured using an adhesion tester (Elcometer 106, Elcometer Limited). P320 sandpaper was used to roughen the coating surfaces and test dolly faces. A cyanoacrylate instant adhesive (MC1500, 3M) was used to glue the dollies onto the coating surfaces and was allowed to cure overnight. The samples were cut around the base of the dollies and a base support ring was used to bring the adhesion tester into position. A stress rate of about 0.2 $\text{MPa}\cdot\text{s}^{-1}$ was applied. ATR-FTIR analysis of the coated dolly surfaces was used to verify that the adhesive did not penetrate the coatings. Since the nanodispersions were known to contain byproducts due to the presence water and 1,3-propanediol in the polyol CNC suspensions, control experiments were performed to exclude that the observed improvement of adhesion can be attributed to these compounds. This included the preparation of a polyol spiked with water and 1,3-propanediol concentrations of 0.6 % and 0.8 %, respectively. The chosen concentrations correspond to the levels detected in the polyol yielding the best adhesion properties (polyol with 0.8 wt % CNC).

4.2.2.5 Statistical analyses

To test whether CNC has a statistically significant impact ($\alpha = 0.05$) on the tested properties, one-way independent ANOVA statistical analyses were performed with subsequent Tukey *post hoc* tests for pairwise

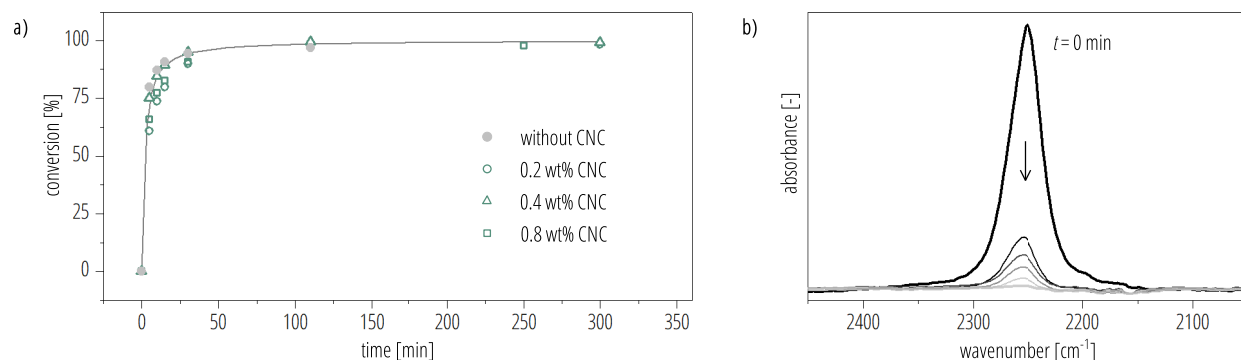


Figure 4.6: a) Calculated isocyanate conversion based on ATR-FTIR monitoring of the NCO stretching band intensity. Data without CNC was used for kinetic modelling of the conversion (solid line). b) Evolution of the NCO stretching band at $\sim 2250\text{ cm}^{-1}$ as a function of time.

comparisons. In case of unequal population variances, as assessed by performing Levene's test (absolute deviations, $\alpha = 0.05$), a Welch's correction for the ANOVA was applied to account for the small sample sizes ($n \leq 6$) followed by Games-Howell *post hoc* test. The Levene's test results are listed in Table C.1, C.1.3.1. All *p* values for the *post hoc* tests can be found in Table C.2, C.1.3.2. Statistical analysis was done using the R environment for statistical computing (RStudio Version 0.98.501) and OriginPro 9 (OriginLab Corporation).

4.3 Results and discussion

Photos of the main reagents (polyol, prepolymer, and resin) and the suspensions obtained over the course of the different processing stages leading to the photocurable resin formulation are shown in Figure 4.5. While the polyol suspensions with CNC concentrations of 0.4 wt % and 0.8 wt % were optically transparent, increasing the CNC to 1.6 wt % resulted in turbidity. No visible micro- or macro-sized agglomerates were detectable in any of the CNC prepolymer or resin suspensions.

4.3.1 Prepolymer synthesis

Preventing early agglomeration of the predispersed CNC during prepolymer synthesis was critical. Two characteristics of the reaction were thought to be advantageous - the high reaction speed and the accompanying increase in viscosity, as discussed in the following sections.

4.3.1.1 ATR-FTIR monitoring of the grafting reaction

Grafting of the polyol by isocyanate monomers was monitored by ATR-FTIR spectroscopy as illustrated in Figure 4.6. Around 75% conversion of the isocyanate monomers could be obtained within the first 5 min following the initial 2nd order reaction kinetics. Full conversion was reached within ~ 2 h. Some grafting of isocyanate onto the nanoparticles may have occurred but this could not be verified using FTIR spectroscopy.

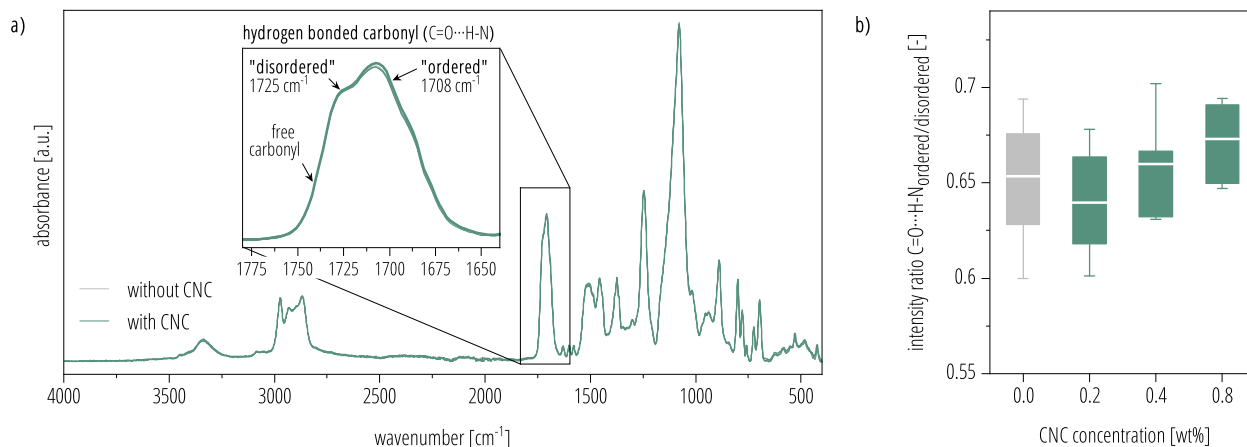


Figure 4.7: **a)** ATR-FTIR spectra (not normalized) recorded of the prepolymer and prepolymer CNC suspensions (0.2 wt %, 0.4 wt %, and 0.8 wt %). The inset graph of the carbonyl $\nu_s(\text{C}=\text{O})$ region indicates the modes for the different types of hydrogen-bonded carbonyl groups. **b)** Box plot showing the mean, lower (Q1) and upper (Q3) quartiles, and minimal and maximal values of the intensity ratio between bands for ordered and disordered hydrogen-bonded carbonyls in the prepolymer ($-\text{NH}\cdots\text{O}=\text{C}$) for each treatment. No statistically significant difference could be detected by performing a one-way ANOVA ($n = 6$).

Analysis of the carbonyl hydrogen bonding pattern ($-\text{NH}\cdots\text{O}=\text{C}$) using FTIR spectroscopy has been used to investigate the dispersion quality of CNC and its participation in the reaction with the isocyanate monomers through the surface hydroxyl groups [266, 274–276]. Hydrogen bonding elongates the $\text{C}=\text{O}$ bond length, which decreases the bonding force constant and therefore the vibration frequency of the bond [277]. Here, the hydrogen-bonding patterns of the $\nu_s(\text{C}=\text{O})$ band ($\sim 1750\text{ cm}^{-1}$ to $\sim 1675\text{ cm}^{-1}$) of the prepolymer and CNC prepolymer suspensions are illustrated in Figure 4.7. Two unresolved bands were detected at around 1725 cm^{-1} and 1708 cm^{-1} , which most likely correspond to hydrogen bonded carbonyl groups, with some degree of "order" in the latter case [278]. The band for free $\text{C}=\text{O}$ ($\sim 1740\text{ cm}^{-1}$) can hardly be detected. This indicates that the prepolymers exhibit substantial hydrogen bonding between the carbamate groups. As highlighted in the Figure 4.7 inset, there is a small variation in the intensity distribution around the hydrogen-bonded $\nu_s(\text{C}=\text{O})$ bands with CNC concentration. Due to the signal overlap, their intensity ratio was calculated using the same data transformation as described in C.1.1. A box plot with the results is given in Figure 4.7b). The observed average values correspond to the trend observed for both thermal (Section 4.3.3.1) and some of the tensile properties (Section 4.3.3.2) but the influence of CNC was not statistically significant, $F(3, 20) = 1.46$ and $p = 0.26$.

This behaviour differs from other reports, which found an intensity shift for bands characteristic for free and hydrogen-bonded carbonyls upon incorporation of CNC [266, 279]. CNC's ability to reduce hydrogen-bonding between the carbamate groups was reported to indicate sufficient CNC dispersion [274]. In the present case, the $\text{C}=\text{O}$ groups remained hydrogen-bonded, which may be related to the low loading levels of CNC used here.

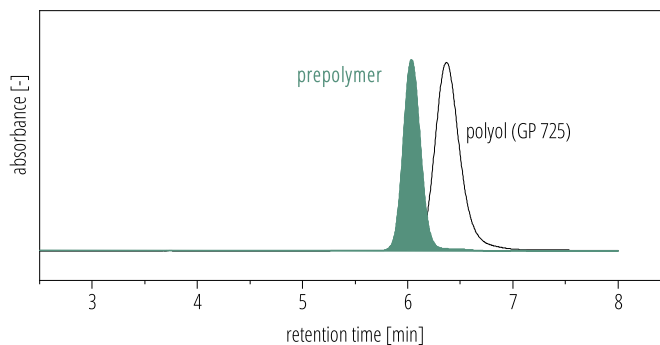


Figure 4.8: GPC separation of the polyol (GP 725) and the star-shaped prepolymer resulting from the addition reaction with TMI isocyanate to endcap the polyol and introduce a photocurable functional group. The GPC traces indicate high monodispersity.

4.3.1.2 Molecular size distribution analysis by GPC

The GPC traces for the GP 725 polyol and star-shaped prepolymer obtained after endcapping of the polyol with TMI are shown in Figure 4.8. The separation yielded a monodisperse polyol and reaction product (prepolymer), indicating that functionalization of the polyol occurred as expected with an estimated molecular weight of around 1300 g mol^{-1} .

4.3.1.3 Prepolymer viscosity

As expected, the dynamic viscosity of the prepolymer depends on the shear rate. Within the studied shear rate range of 0.01 s^{-1} to 3000 s^{-1} , there appears to be a first Newtonian plateau (almost 15 Pa s at $35 \text{ }^\circ\text{C}$) followed by a transition area and shear thinning (Figure 4.9a)) due to orientation of the prepolymer chains. In the presence of CNC, the viscosity increased remarkably. Due to the difficulties in removing entrapped air, the viscosity could only be accurately determined at CNC concentrations up to $0.4 \text{ wt } \%$. The prepolymer CNC suspensions were characterized by an initial drop in viscosity at low shear rates until they reached a viscosity similar to the neat prepolymer. This indicates a shear-induced breakup of an internal network formed by CNC nanoparticles. Given the low loading levels, this structuring effect is likely to involve interaction with the prepolymer (CNC concentrations are below those of regularly reported percolation thresholds [191, 192]), which indicates good dispersion of the nanoparticles. A memory effect was also observed, as seen by the viscosity increase upon release of the applied stress (downramp). This memory effect is typical for structured fluids. The high viscosity of the prepolymer can be expected to stabilize the CNC dispersion by limiting the diffusion of the nanoparticles. Hence, close approaches between the nanoparticles, which can result in agglomeration when attractive interactions (hydrogen bonding) overcome repulsive forces (negatively charged sulfonic groups originating from the acid hydrolysis treatment) are avoided. Furthermore, the presence of the hydroxyl groups and carbamate linkages in the prepolymer promote favourable prepolymer-CNC interactions to compete with CNC self-aggregation. These effects combined with the fast transformation, facilitated the stabilization of the nanodispersions.

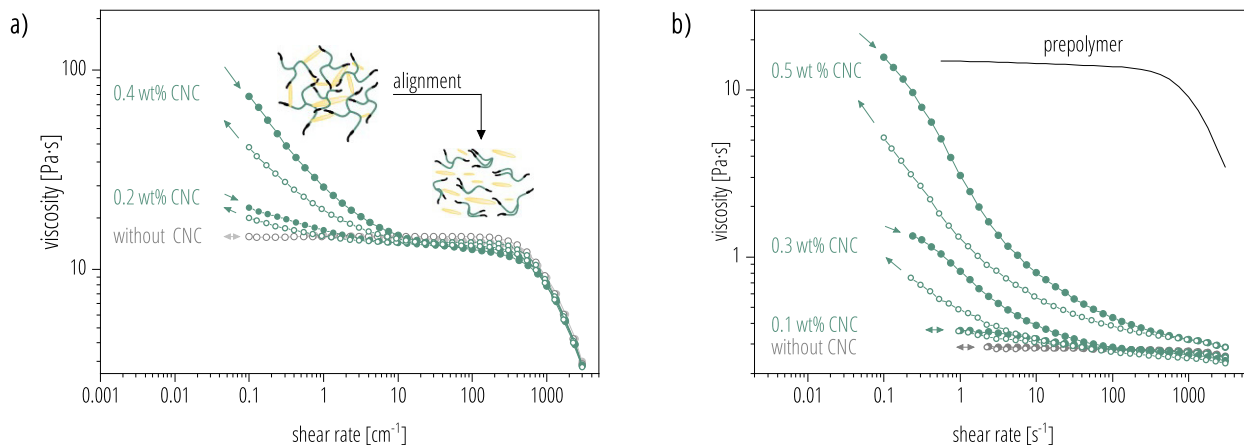


Figure 4.9: **a)** Shear rate dependency of the prepolymer viscosity at 35 °C with up to 0.4 wt% CNC. The filled scatter points correspond to the initial upramp (increasing shear rate) and the corresponding open scatter points represent the downramp (decreasing shear rate). CNC imposed a strong structuring effect on the nanodispersions. As expected from the molecular structure of the prepolymer, the fluids showed strong shear thinning behaviour. **b)** Shear-rate dependence of the resin viscosity showing an extended first Newtonian plateau and much lower viscosity upon addition of the reactive diluent and photoinitiators compared to the prepolymer (at 35 °C). Distinct hysteresis is observable in the shear thinning behaviour of the resin containing CNC at lower shear rates. Representative curves are shown.

4.3.2 Photocurable nanodispersion

4.3.2.1 Resin viscosity

The change in viscosity of the resins with shear rate is shown in Figure 4.9b). As expected, the addition of the reactive diluent (and photoinitiators) resulted in a strong viscosity reduction compared to the prepolymer, as well as in the extension of the first Newtonian plateau. However, the resins still behaved as structured fluids in the presence of CNC as was observed for the CNC prepolymer suspensions. This flow behaviour is most likely due to a hydrogen-bonded network at rest, involving both interparticle and particle-resin interactions. Formation of this network was time-dependent and the viscosity did not follow the same path on structure breakdown (with increasing shear rate) and recovery (with subsequently decreasing shear rate), as seen in Figure 4.9b). Even though the analyses were performed at 35 °C, the results suggest that weak shearing can already result in the breakdown of the internal structure of the resin that is present at rest. For a coating application, the thixotropic nature of the nanodispersion has interesting features being in a stable form at rest but becoming fluid when agitated, facilitating the wetting and penetration of the substrate upon shear, whereas subsequent regaining of structuring with an increase in viscosity avoids drips and runs.

This rheological behaviour represents another advantage of utilizing such low CNC concentrations and avoiding the viscosity issues that have been observed at higher concentrations [271].

4.3.3 CNC-matrix interaction

4.3.3.1 Modulated dynamic scanning calorimetry

In all samples, only one T_g was observed within the chosen temperature range (-50°C to 100°C , which corresponds to the glass-rubber transition of the polymeric matrix. ANOVA analysis with Welch's correction showed a significant main effect of the CNC concentration on T_g , $F(3, 5.77) = 21.3$ and $p = 0.002$. The Games-Howell *post hoc* test revealed that CNC at a 0.5 wt % concentration significantly increased T_g compared to the neat polymer coatings ($p = 0.010$). At the lowest tested CNC concentration of 0.1 wt %, the average T_g was lower than in any other treatment groups, however, this difference is only statistically significant when compared to 0.3 wt % ($p = 0.003$) and 0.5 wt % CNC ($p = 0.030$). These findings are illustrated as box plots in Figure 4.10a). On average, the T_g increased from 39°C to 44°C upon incorporating 0.5 wt % CNC. A growing body of literature has examined the T_g changes in nanocomposites. When using CNC as the nanofiller, T_g was typically found to remain the same or slightly decrease, whereas other researchers report an increase in T_g with increasing CNC concentration until a plateau region over which there is little increase in T_g [265–268]. In 2012, Pan et al. [269] reported a substantially higher increase in T_g up to 40°C by incorporating 8 % CNC into an epoxy acrylate resin. Here, the observed changes in T_g with CNC concentration are less pronounced and may be influenced by multiple mechanisms, including 1) the plasticizing effect of side reaction products between TMI and absorbed moisture in the polyol during prepolymer formation (reducing T_g), 2) competing hydrogen bonding between the polymer chains and CNC [274], 3) increasing T_g due to grafting of residual 1,3-propanediol with TMI forming a difunctional and photocurable oligomer, and 4) potential grafting of the nanoparticles with isocyanate (CNC functioning as a crosslinker [266]).

Interestingly, when exposing the same samples to a 2nd heating cycle to eliminate the thermal history, the effect was lost (*cf.* T_g drop for the nanocomposite with 0.5 wt % CNC in Figure 4.10a)). It can be concluded that the nanocomposites structurally rearranged into a lower energy state similar to the neat polymer, when given enough thermal energy. This indicates a confining effect on the nanoparticles in the polymer matrix formation during photopolymerization (*cf.* C.1.1 about the anomalous polymerization kinetics). This results in a different, but reversible, structural arrangement of the glassy polymer matrix.

4.3.3.2 Tensile properties

The tensile properties of the free-standing films were subject to high variability (relative standard deviations as high as 60 %). Representative engineering stress curves are plotted in Figure 4.10b). The tensile properties were derived from the stress-strain data. The findings of the ANOVA analyses (with Welch's correction in the case of the Young's modulus) are indicated in the box plots in Figure 4.11. The fracture of the film samples under uniaxial tensile load always occurred in the plastic region in a mostly "hard and strong" fashion.

The relatively low Young's moduli (in the order of 10^9 Pa) indicate that the elastic deformation was dominated by relatively weak intermolecular interactions [280]. Accordingly, the average values followed the trend observed for T_g but the influence of CNC was not significant, $F(3, 8.60) = 2.95$ and $p = 0.09$. CNC significantly affected the tensile strength, $F(3, 16) = 3.88$ and $p = 0.03$. The Tukey *post hoc* test revealed

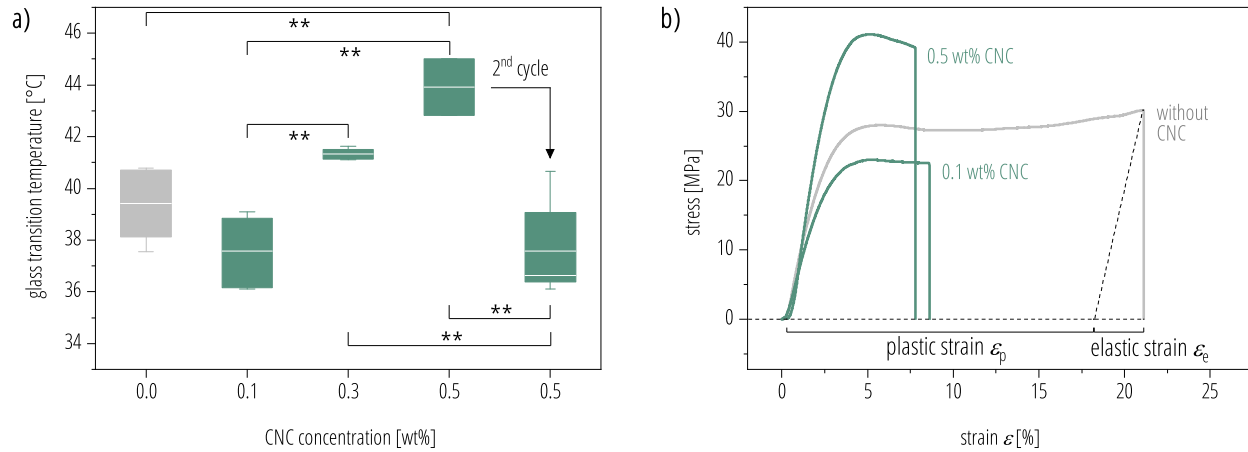


Figure 4.10: **a)** Dependence of T_g on the CNC concentration illustrated as a box plot showing the mean, lower (Q1), and upper (Q3) quartiles, and minimal and maximal values. Statistical significance values were derived from pairwise comparisons using the Games-Howell *post hoc* test ($n = 6$). When subjecting the samples to a 2nd heating cycle, the increase in T_g was lost (illustrated for the nanocomposite with 0.5 wt % CNC). **b)** Engineering stress-strain curves of the tested samples representing the average properties observed. Compared to the neat coating, the nanocomposites with 0.5 wt % exhibited higher tensile strength and reduced elongation at break.

that increasing the CNC concentration from 0.1 wt % to 0.5 wt % significantly increased the tensile strength ($p = 0.02$), while the comparison of the other means did not show any significant difference. The results substantiate the nanoreinforcement of CNC corresponding to an increase in tensile strength of about 16 % on average, indicating good stress transfer at the filler-polymer interface. The deformation in response to the applied stress was significantly smaller for the nanocomposites containing 0.3 wt % and 0.5 wt % CNC ($p = 0.02$ in both cases). In all cases, fracture occurred at a few percent of strain ranging from 15 % on average for the neat polymer film to only 6 % for the nanocomposites at the two highest CNC loading levels. The glassy polymer and nanocomposite films were only linear elastic up to relatively small strains and underwent plastic deformation before fracture. No statistically significant effects of CNC on the elastic strain was detected, $F(3, 16) = 0.54$ and $p = 0.66$. Plastic strain (refers to ductility), on the other hand, was significantly affected by CNC, $F(3, 16) = 6.14$ and $p = 0.006$. The nanocomposites with 0.3 wt % and 0.5 wt % had a significantly lower plastic strain as determined by a Tukey *post hoc* test ($p = 0.02$ in both cases). While the polymer nanoparticle interface increased tensile strength, the decreased ability for efficient energy dissipation through plastic deformation resulted in the reduced deformability observed as the reduction in elongation. The toughness of the free films can be correlated to the energy absorbed to break and was significantly affected by CNC, $F(3, 16) = 5.79$ and $p = 0.007$. The Tukey *post hoc* test revealed that incorporating 0.3 wt % and 0.5 wt % CNC resulted in a statistically significant reduction in toughness with $p = 0.01$ and $p = 0.02$, respectively. Under the chosen loading conditions, the balance of strength and ductility was unfavourable for the nanocomposites with the reduction in plastic deformation dominating the impaired dissipation of energy. Overall, the increase in strength at cost of elongation upon CNC incorporation

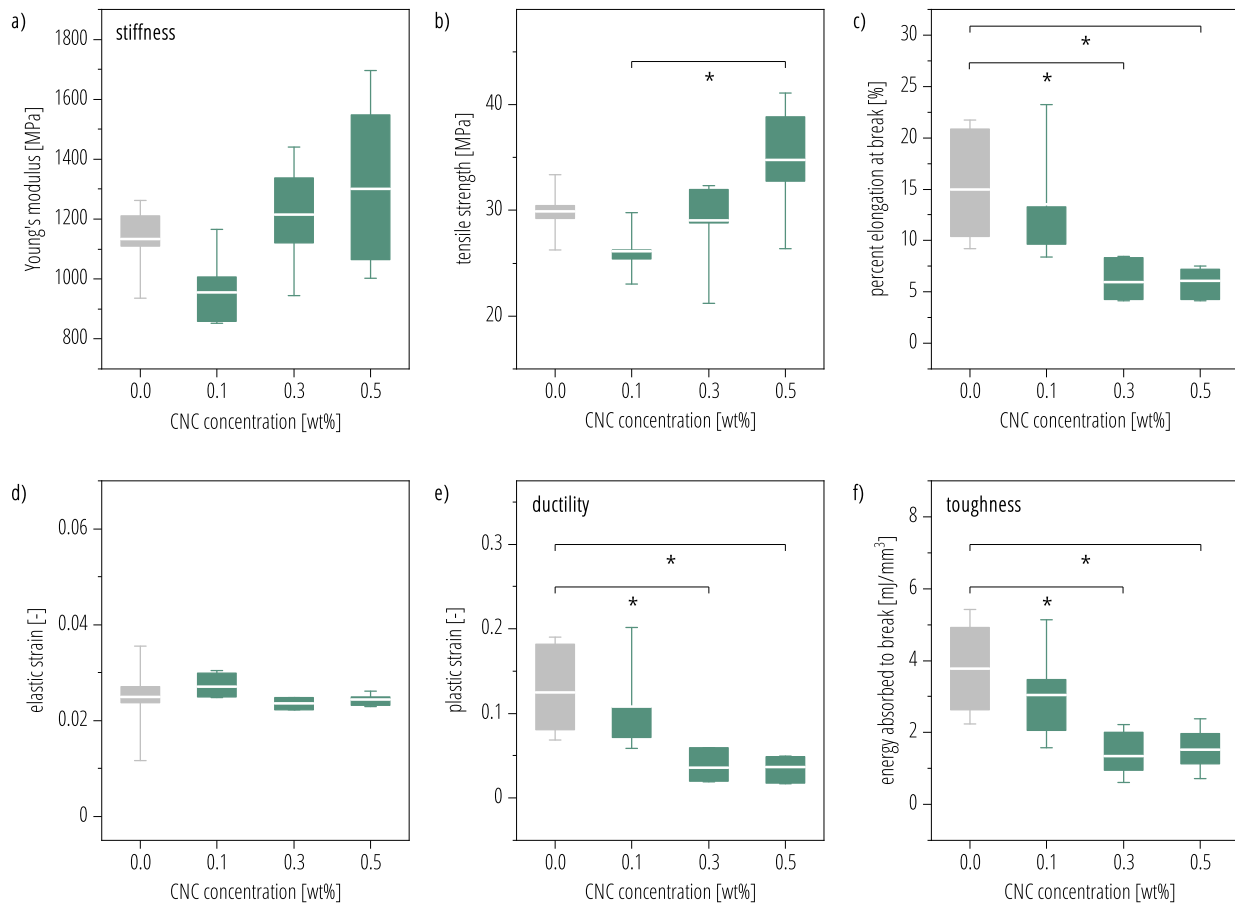


Figure 4.11: Box plots show the mean, lower (Q1), and upper (Q3) quartiles, and minimal and maximal values of the following tensile properties for each treatment: **a)** Young's modulus, **b)** tensile strength, **c)** percent elongation at break, **d)** elastic strain, **e)** plastic strain, and **f)** energy absorbed to break. Statistical significance values were derived from pairwise comparisons using the Tukey *post hoc* test ($n = 6$) as the variance was equal for the cases with a statistically significant effect of CNC on the tensile properties.

could translate into nanocomposite coatings with increased hardness but reduced flexibility. Future work is needed to establish how this would affect the durability and long-term performance of the coatings.

Fracture topography The reduced ability of the nanocomposites to undergo plastic deformation for energy dissipation could also be observed when analyzing the fracture surfaces after the tensile tests by SEM (Figure 4.12). In all samples, mostly brittle normal-planar crack fracture was observed. In the neat polymer films, the fractures were dominated by stress cracking in the form of isolated V-shaped fracture parabolas. Thin microcracks were rare and the deformed borders of the parabolic markings showed evidence of plastic deformations such as waving (Figure 4.12a). Fracture parabolas can be formed when a primary crack front reaches a local stress concentration caused by an inhomogeneity in the material, resulting in crack branching with the formation of a parabolic propagation front where the two cracks intersect as indicated

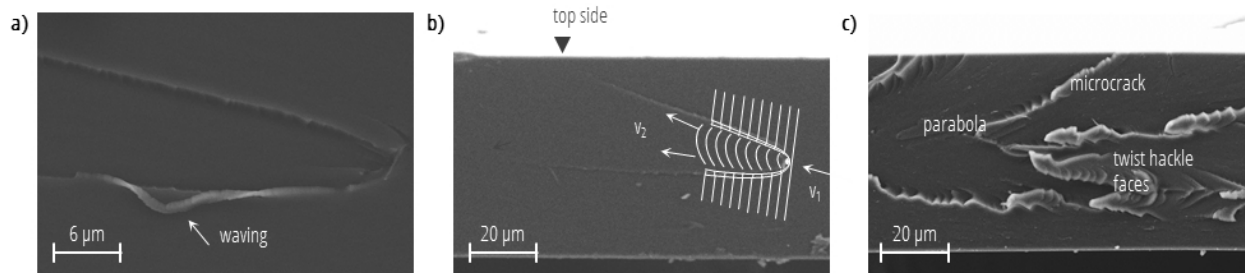


Figure 4.12: Selected SEM images of the fracture surfaces (top side facing upwards) to illustrate the parabolic markings, the main fracture features, with some plastic deformation along the secondary crack front in the absence of CNC (**a**) and **b**). **c**) Upon incorporating CNC (nanocomposite with 0.5 wt% CNC) the roughness of the fracture surface increased noticeably and additional fracture features along ramps/steps, which could have been a result of more frequent distortions on the crack front. All tested samples shared fracture behaviour characteristic for brittle materials.

in Figure 4.12b) [281, 282]. With increasing CNC concentration, the parabolas took the form of ramps or steps and the density of the fracture features was increased compared to the neat polymer films with increased prevalence of vertical displacements (Figure 4.12c)). More of the microcracks were also seen and the roughness of the fracture plane increased. This could indicate increased crack branching due to the presence of the nanoparticles as well as changes in fracture velocity. The surface roughness was a result of tiny fracture features with a relatively uniform distribution. It has been reported that energy dissipation through plastic deformation is estimated to be greater by several orders of magnitude than through the creation of new surfaces [282], the latter being more pronounced in the nanocomposites. The observed significant reduction of plastic strain with increasing CNC concentration may thus have been the major reason behind the reduced toughness but is inconclusive over the nature of nanoreinforcement by CNC.

4.3.3.3 Abrasion resistance

The average values for the determined wear indices obtained from the TABER abrasion test and 95 % confidence intervals (two-tailed independent *t*-test) are summarized in Table 4.4. No statistically significant effect of CNC on the wear index could be established, $F(3, 8) = 1.99$ and $p = 0.19$. The wear indices of all specimens were very low (average values (*M*) between 18 and 20), corresponding to excellent abrasion resistance in all cases. A different industrial test method, such as sand abrasion might be more conclusive. With the current test conditions, it was found that the incorporation of CNC appeared to reduce the wear index averages, however, the effect was not strong enough to cause a significant improvement.

4.3.3.4 Pull-off adhesion strength

Adhesive failure of all tested coatings occurred between the substrate (glass plate) and the coating (100 % A/B) but was subject to high variability due to the nature of this test with relative standard deviations between 10 % and 35 %. ANOVA analysis revealed a significant effect of CNC concentration on the pull-off adhesion strength, $F(4, 10.979) = 15.01$ and $p = 0.0002$). CNC significantly improved the tensile pull-off strength at a concentrations of 0.1 wt % and 0.3 wt % CNC with $p = 0.008$ and $p = 0.009$, respectively. These

Table 4.4: Wear index determined after 500 cycles ($n = 3$) at a load of 1 kg on each wheel (CS-17) and 95 % confidence intervals (two-tailed independent t -test). The incorporation of CNC did not cause a statistically significant improvement in the abrasion resistance.

[CNC] [wt%]	wear index [-]
	$M \pm 95\% \text{ CI}$
0.0	19.7 ± 1.1
0.1	17.7 ± 0.9
0.3	18.0 ± 1.4
0.5	18.1 ± 1.5

findings are illustrated as box plots in Figure 4.13a. Additionally, the results for the control experiment are also shown and represent the adhesion performance of the neat resin in the presence of byproducts originating from residual water and 1,3-propanediol in the polyol, as is the case in the nanocomposites. The presence of these byproducts did not significantly affect the required tensile pull-off stress but the samples showed evidence of increased variation compared to the coating based on the pure prepolymer. As shown in Figure C.4 (C.1.2), reacting polyol containing trace amounts of water and 1,3-propanediol with TMI results in a prepolymer with visible turbidity, indicating phase separation. While 1,3-propanediol gets endcapped by TMI forming a difunctional oligomer, the reaction of water with TMI is more complex. Isocyanates can react with water to form an intermediate carbamic acid, which can decompose into CO_2 and an amine. The latter can further react again with isocyanate to yield urea linkages [283]. The diverse reaction pathways in combination with the instability of the multicomponent system could account for some of variability in the observed properties of the nanocomposites.

On average, the addition of CNC at such low concentrations increased the tensile pull-off adhesion stress required to detach the coatings in vertical direction from 0.2 MPa to 0.4 MPa and 0.5 MPa, respectively, more than a two-fold increase. Incorporation of 0.5 wt % CNC did not result in a statistically significant improvement compared to the neat coating but still represented a medium effect (Cohen's $d = 0.57$, pooled standard deviations). It appears that the effect is characteristic for low loading level CNC applications and might be reduced at higher concentrations. In an ideal case, the resin would undergo uniform shrinkage upon curing. Due to this interaction between the coating and substrate in the form of adhesion ($\sigma_{adhesion}$), shrinkage is restricted into that one direction and results in the build-up of internal stresses ($\sigma_{internal}$) as illustrated in Figure 4.13b. The coating shrinkage (contraction) is therefore counteracted by shear stresses (τ_{shear}) at the interface. To prevent detachment in the tangential direction, a minimum shear friction and thus a certain minimum adhesive stress ($\sigma_{adhesion,min}$) is required. This ultimately reduces the minimal amount of pull-off force which has to be applied to detach the coating from the substrate in normal direction.

Internal stresses depend on both the Young's modulus (E) and the strain (ε):

$$\sigma_{internal} \approx E \cdot \varepsilon \quad (4.2)$$

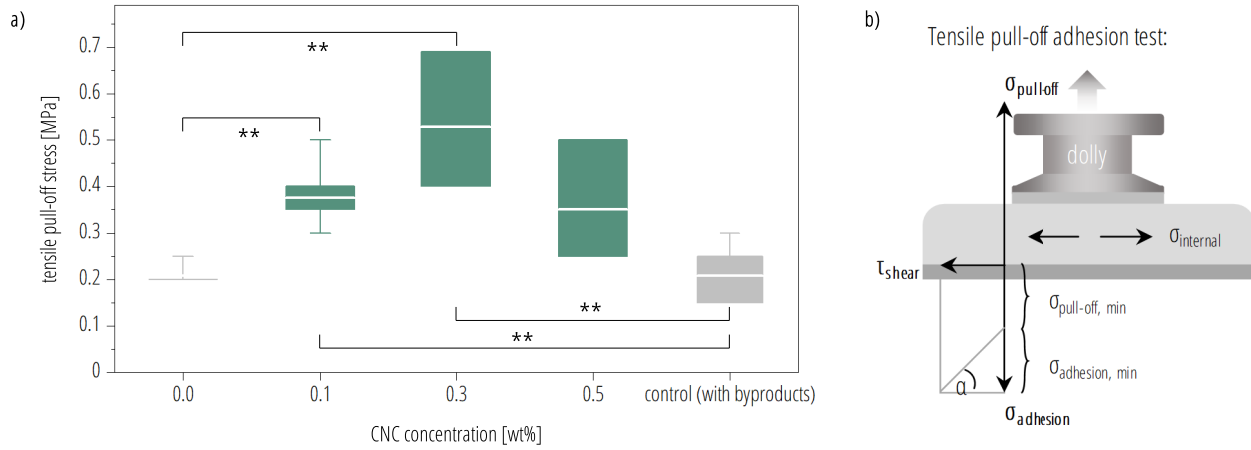


Figure 4.13: **a)** Tensile pull-off force for each treatment illustrated as a box plot showing the mean, lower (Q1), and upper (Q3) quartiles, and minimal and maximal values. Statistical significance values were derived from pairwise comparisons using the Games-Howell *post hoc* test ($n = 6$). **b)** Simplified scheme illustrating the acting stresses at the interface between the coating and the substrate upon curing. Adhesion to the substrate results in the development of internal stresses due to restricted shrinkage. A minimum adhesion stress is required to develop a threshold static friction at the interface that can counteract the shrinkage in tangential direction. This reduces the minimal tensile pull-off stress required for detachment in normal direction.

The same holds true for the shear stress, with an additional dependence on the dimensions of the coatings:

$$\tau_{shear} \approx \frac{E \cdot \varepsilon \cdot A_{cross-section}}{A_{interface}} \approx \frac{E \cdot \varepsilon \cdot thickness}{length} \quad (4.3)$$

As revealed by the tensile data, increasing CNC concentration tends to increase Young's modulus (E), which increases the internal stresses, assuming no effects on the adhesive strength due to increasing restriction of deformation (Equation 4.2). On the other hand, the nanoparticles themselves cannot shrink and also have strong interaction with the polymeric matrix, which could decrease the strain (ε) due to shrinkage. Therefore, it is possible to have an intermediate optimum concentration, as indicated by the results of the pull-off adhesion test. Further research is needed to elucidate the underlying mechanism and whether it indeed represents a type of reinforcement by CNC which is limited to very low filler levels, as explored here for the first time in such a system. The structuring of the resin in the presence of CNC, as revealed by rheological characterization, together with the observed effect of relaxation processes on the glass transition temperature, further support the conclusion that the polymer-CNC interface and its effect on rapid polymerization under UV play a significant role in shaping the properties of the resulting nanocomposites. A similar concept has been applied to resin-based composites for dental restoration, a review of which is given by Giachetti et al. [71]. The results presented here suggest the potential for CNC to find use as an adhesion promoter. This would be an alternative strategy to common practices used in UV-curing industries to overcome adhesive failure such as increasing the molecular weight relative to the functionality or introducing adhesion-promoting functional groups [50, 284, 285], often accompanied by a lower cross-linking density of the matrix.

4.4 Conclusions

These findings suggest a technique for introducing unmodified CNC into UV-curable resins at low loading levels to result in nanoreinforcement effects that are distinct from those observed at the high levels typically studied. This strategy results in lower incremental costs due to the small quantities used and the absence of CNC surface modification. The effects of CNC nanoparticles are attributed to the fast transformation of a polyol-CNC suspension into a high viscosity photocurable CNC prepolymer suspension and the subsequent establishment of a hydrogen-bonded network between the nanoparticles and the forming polymer matrix. This resulted in a large increment in the tensile pull-off strength of 154 % on average at a CNC loading level of only 0.3 wt %. The model system studied is not highly photoreactive, but the principle could be applied to using more reactive photocurable urethane prepolymers as the major component of UV-curable formulations, by endcapping the isocyanate monomers with appropriately reactive photosensitive functional groups. The low filler amount used is promising for applications where optical and other thermo-mechanical properties should not be altered significantly by its presence. The observed enhancement of adhesion properties is likely due to the reduction of internal stresses during the UV-curing. This suggests the potential for CNC utilization as an adhesion promoter and new strategy to tackle adhesive failure in UV-curable coatings without sacrificing cross-linking density, since the functionality of the resin components is preserved.

Chapter 5

General conclusion

Coating materials are important for substrate protection as well as for decorative purposes. Recent work by McDonald et al. [3] brought new attention to the contribution to urban air pollution of the volatile organic compounds (VOC) emitted from by coatings and paints. This is mostly related to the volatilization of solvents from these coatings. In this work, the use of oleochemical reactions and photo-chemistry to develop biobased coatings was demonstrated. These coatings can potentially contribute to lowering urban air pollution due to their very low emission of VOC, and can reduce the consumption of fossil feedstocks. In contrast to physical drying, the films are applied as monomeric or oligomeric structures which polymerize upon exposure to radiation or air. Physical drying, which is typically an energy intensive processing step, that even compromises the environmental benefit of using water-based over solvent-borne coatings and paints, can thus be avoided [286]. While traditional drying oils are one of the oldest man-made coatings that are solvent-free and have outstanding wood protection properties, synthetic polymers became more and more dominant with the rise of the chemical industry in the early 20th century. The versatility and quick drying times of synthetic coatings were decisive for their success.

5.1 Three new low-emission coating systems

5.1.1 A fully biobased reactive accelerant and diluent for drying oils

In contrast to conventional strategies to reduce the drying time of drying oils, the ozonized lipids developed in this work can be used to avoid potentially toxic metal driers, while also serving as a reactive diluent. Based on the autoxidative polymerization chemistry that is inherent to drying oils, the carbon-carbon double bonds in lipids were reacted with ozone to introduce functional groups capable of releasing reactive radicals which can participate in autoxidative polymerization. In addition, the use of fatty acid methyl esters (FAME) was pursued as a possibility to reduce the viscosity of such plant oil-based coatings.

ATR-FTIR analysis proved suitable in this work to study possible cross-linking mechanisms and polymerization kinetics. In Chapter 2, it could be determined that the radical decomposition products of the ozonized lipids had a higher propensity to directly add to conjugated double bonds rather than participating in hydrogen atom abstraction reactions. Hence, the reactivity was very high in conjugated tung oil, which is the fastest polymerizing natural drying oil, but also relatively expensive. When using tung oil mixtures containing 25 wt % of ozonized linseed FAME, the dry-through time and viscosity could be reduced by 70 % and 60 %, respectively. Although the glass transition temperature (T_g) was reduced compared to films of pure tung oil, the T_g was comparable to that of cured films of linseed oil, suggesting similar coating flexibility. This approach of using ozonized lipids, in particular FAME, could improve the performance of conjugated drying oils by providing a metal- and solvent-free way to obtain significantly shorter drying times than any natural drying oil, and with the added benefits of reduced viscosity, and a high content of low-cost and locally sourced lipids. Since conjugated lipids are also used for oxidative polymerization in oil-based alkyds (see section 1.1.1.3), this work could serve as the basis for developing reactive diluents for oil-based alkyd resins to reduce the use solvents, and explore possible benefits of the antimicrobial properties associated with ozonized lipids.

5.1.2 Epoxidized lipids as a durable and fast-curing alternative to drying oils

While drying oil-based coatings are still widely used, radiation-curing is the fastest growing (solvent-free) coating industry. As opposed to the slow propagating peroxy radicals in drying oils, carbon-centred radicals in radical polymerization or oxonium species in cationic curing, allow curing times of seconds or minutes compared to days or even weeks as in the case of drying oils. Therefore, Chapter 3 aimed at the modification of linseed oil to induce UV-curability through the functionalization of $-\text{CH}=\text{CH}-$ through epoxidation.

Using desirability optimization methodology, it was found that mixtures with high contents of epoxidized FAME relative to triacylglycerols (TAG) provide a fast-curing alternative to air-dried linseed oil. In the absence of a UV lamp, polymerization of these mixtures can also be obtained under solar radiation when sensitized by curcumin, a plant pigment. In this way, curing times of <5 min, similar to that obtained with UV-curing, were achieved, which is considerably faster than any drying oil system. Additionally, the ease of use benefits dark curing, since areas not directly irradiated by the UV source can still polymerize.

Not only can such mixtures of epoxidized lipids be produced at low cost and up to 100 % biobased content, the networks formed through ether linkages were shown to be significantly more stable towards hydrolytic degradation compared to linseed oil films. This could improve the film durability compared to traditional drying oils, perhaps leading to a higher resistance to wood staining due to microbial surface colonization, if confirmed by future weather studies. The demonstrated significance of abiotic hydrolysis in both cases highlights the importance of also considering abiotic processes when studying the natural weathering of such materials, which appear to be underrepresented in the literature. Furthermore, the role of non-cross-linked fatty acids and low molecular weight byproducts (*e.g.* secondary oxidation products in air-dried oil films) have to be studied in the lipase-catalyzed biodegradation of these plant oil-based polymer matrices.

Within the scope of this work, the suitability of epoxidized lipids to be a faster curing alternative to drying oils and their higher hydrolytic stability was demonstrated. However, more research is needed to better evaluate the weathering stability and aging of such films. For example, the epoxidation of the double bonds in linseed lipids considerably reduced the yellowing of the films during sample storage for 6 months. This is due to the absence of the abundant $-\text{CH}=\text{CH}-$ which can isomerize to form conjugated systems, and which in turn absorb visible light. While drying oils continue to penetrate the wood as they start to slowly solidify from the top down upon contact with air, rapid UV-curing of the epoxy coatings occurs before proper penetration into the substrate happens. This results in the formation of soft top coat on the surface. Similar to drying oils, the cross-linked epoxy formulations are flexible coatings resulting in a lower susceptibility towards cracking as a result of dimensional changes in the wood substrate. However, the formation of a top coat on the wood substrate should be avoided by controlling the amount of resin applied and time given to penetrate the substrate before UV curing, as the coating flexibility offers little abrasion resistance.

Figure 5.1 is a scatter plot of the molecular weight (M_w) of commercial coating components and the T_g of the cured films based on a literature database [287] in comparison to the materials developed in this work. Obviously, the T_g of coatings is influenced by numerous parameters and not just the T_g of the main polymeric constituents. However, the graph illustrates that most commercial coatings are thermoplastic resins, which mostly dry through evaporation of the solvent, which is needed to solubilize the coating polymers. Air- and UV-curable coatings, on the other hand, are of lower M_w and polymerize during chemical curing.

Nevertheless, the high-lipid based coatings developed in this thesis (Chapter 2 and Chapter 3) are on the lower end of the scale with regards to their T_g . Traditionally, those were properties made use of for applying a fully natural and durable finish to wood substrates, where the penetration due to low M_w and high flexibility avoided cracking or peeling of the paint. With the two new approaches presented here, the issues of slow drying time and poor hydrolytic stability are diminished significantly using green chemistry approaches, while maintaining an up to 100% biorenewable content. Further modification of the lipids to produce polymer networks with higher T_g is possible, such as acrylated epoxidized soybean oligomers for radical UV-curing. One of the challenges faced is the high viscosity due to longer side chains as the lipids are grafted with other monomers. For applications on wood, where penetration into the substrate is important for durability purposes, this can be a disadvantage while also further increasing the cost of the material without providing significant functional advantages compared to conventional polymers.

5.1.3 Biobased nanotechnology for improved adhesion of UV-cured coatings

UV-curable coatings of higher strength (*e.g.* higher abrasion resistance) and durability are often based on polyurethanes. Technically, those types of monomers/oligomers could be produced using lipid feedstocks. But for the reasons discussed in the previous section, a more targeted way was chosen to use plant biomass targeting performance improvement over maximized biorenewable content. UV-curable coatings have one major drawback, which is a direct result of their instant curing: reduced adhesive strength due to accumulating polymerization stresses. This was the first study to show how CNC nanoparticles can be used to reduce these stresses and accordingly increase adhesive strength (Chapter 4). In this model system, a more than a 150%

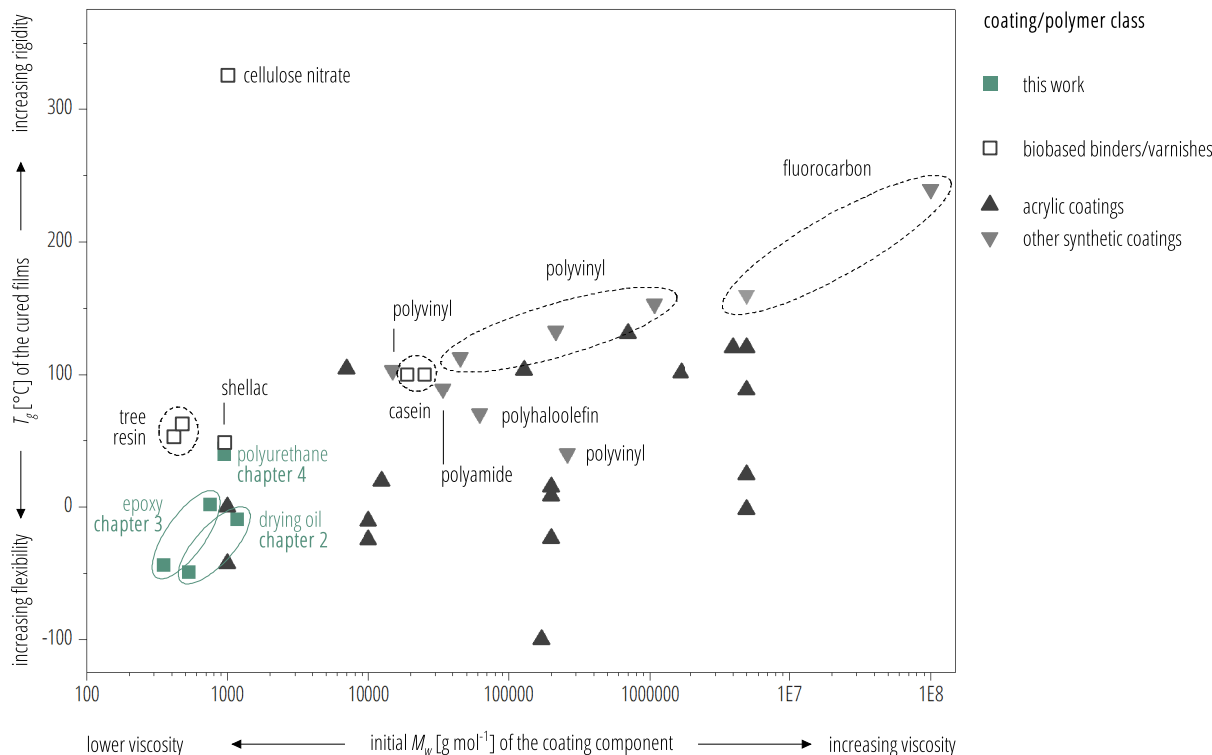


Figure 5.1: Comparison of (initial) molecular weight M_w and T_g for the coatings developed in this thesis and polymers used in coatings based on a literature database [287]. Missing M_w data was derived based on the CAS-number except for cellulose nitrate [288] and Teflon AF 1600/AF 2400 [289]. Data for the tree resins (dammar and mastic), shellac, and casein were derived from literature [290, 291, 291, 292, 292, 293]. For simplicity, two data points per resin were plotted: lowest M_w/T_g and highest M_w/T_g . Due to the thermosetting properties, the resin systems developed in this thesis offer low M_w in the uncured state and accordingly reduce the need for solvent use. Given the relatively high flexibility and low initial M_w , suggests applicability as wood finishes. Similar properties to the polyurethane resin developed in Chapter 4 would be expected when using a lipid-based polyol. However, biorenewable content is sacrificed for a higher T_g compared to the other two resins.

improvement in adhesive strength was obtained using only 0.3 wt % unmodified CNC. In contrast to many other publications on the utilization of CNC in UV-curable coatings, a highly dispersed CNC suspension was targeted in order to observe true nanoparticle effects, as opposed to reinforcement that can be attributed to the presence of CNC agglomerates. This made it possible to study new effects in these rather complex curing systems. Surprisingly, it was found that these nanoparticles can counteract poor adhesive strength, one of the main drawbacks of UV-curing. Furthermore, the CNC-induced thixotropic flow behaviour is an additional benefit for coating applications due to reduced sagging of the applied coatings on a non-horizontal plane. The low amount of CNC used and the absence of any surface modification is also a big advantage for the cost-effective use of CNC, and could facilitate its commercialization as a plant-derived nanomaterial.

While those results are very promising and generally applicable to formulations containing polyurethane-based oligomers as the main component, more research will be needed to better understand this behaviour

and define the range of compatible resin formulations. It will be interesting to study whether the observed improvements in adhesive strength could also be applied to stereolithography (photo-curing 3D-printing) for reduced weakness between added layers of UV-polymerized resins.

5.2 Potential implications on coating sustainability

Similar to most plastics, the production of coatings and paints relies heavily on fossil feedstocks and a significant material value of coatings and paints is lost after a first use. The present work has been centred around the use of low-emission coating technologies and incorporation of biobased feedstock in the synthesis of coating building blocks in an attempt to improve sustainability. Below, these parameters are briefly discussed in the perspective of externalities related to the use of such materials and coatings/paints in general.

5.2.1 Emissions

While VOC emissions from coatings applied in an industrial setting can be managed [5], the low energy requirements for UV-curing still offers an advantage for a reduced carbon footprint over conventional and water-borne coatings [8]. Furthermore, the significant contribution of VOC pollutants in urban air originating from coating and paints demonstrates that current measures to contain VOC emissions are not sufficient. These pollutants pose potential health risks [3] and can contribute to atmospheric ozone formation [15]. However, even natural drying oil can give off volatile oxidation products on drying, such as the emission of hexanal and propanal from linoleic and linolenic acid-rich oil paints [185]. On the other hand, VOC emissions in UV-curable coatings are more often related to the use of solvents when lower viscosities are needed, for example in spray-applications [294].

The use of biobased feedstocks to produce coating building-blocks could reduce consumption of fossil-based feedstocks, and thereby decrease net carbon dioxide emissions. While CNC can be produced from cellulosic agricultural waste and forestry waste [295, 296], the use of so-called 1st generation biofeedstocks (can be used as food or animal feed), has (rightly) received much critical attention due to issues such as competition with food production, land use, or biodiversity [297]. Currently, about 15 % of the global production of vegetable oil is used in non-food applications, such lubricants, biodiesel, or as drying oils/ink formulations [298]. Without elaborating on the fact that approximately 70 % of the global agricultural area is used as pasture, the lipid-based drying agent and epoxidized linseed lipids developed in this thesis can be obtained through modification of linseed oil already produced for application as a drying oil, thereby improving product performance without the immediate need of additional oilseed feedstocks. Nevertheless, future work should explore the use of algae-sourced lipids and non-food plant oils as a feedstock in the preparation of such coating building blocks to avoid the creation of significant undesirable consequences in other domains.

5.2.2 Recyclability

Waste generation during coating/paint application, in particular spraying (*e.g.* overspray), cannot be fully prevented but various strategies are in place to recycle [5] or reuse the forming "paint sludge" as an alter-

native to incineration/combustion [299], the current major route of paint sludge disposal [300]. However, an effective after-use strategy for coatings is challenging and recycling is limited to paint stripping to recycle the substrate, such as wood [301] or packaging material [5], or the recovery of additives and pigments like titanium dioxide [302]. In the present case, additives like photoinitiators could prevent wood substrates from subsequent composting and render it a hazardous material instead. However, the all-lipid resin from Chapter 2 is likely more environmentally-benign as drying oils are considered biodegradable finishes [303].

5.2.3 Leaking of non-volatiles

Issues related to the leaking of degrading plastics into the environment are not just related to the polymeric constituents alone, but also to the various additives present in plastics. For example, an estimated 23 million tonnes of plastic additives have leaked into the oceans alone [297]. In this work, the transition from air-curable ozone-modified lipids to the two UV-curable systems also entailed the use of photoinitiators and also a bismuth catalyst, in the case of the UV-curable urethane prepolymers. Although photoinitiator-free UV-curable coatings based on thiol-ene photoclick chemistry [304], radical generating nanoparticles [305], or short-wavelength vacuum-UV irradiation [306] are under investigation, the wide-spread use of photoinitiators are under close scrutiny for their potential negative health effects in humans and biota [307, 308]. Attempts to reduce the migration of photoinitiators can come at the expense of increased bioaccumulation due to poor water solubility. This suggests the need for additional research on the environmental fate of these additives in addition to polymer degradation.

In fact, paints and coatings were found to be a significant source of microplastic found in the environment [309]. While clothing was the main source for plastic particles, they also found a significant amount of primary microparticles originating from coatings and paints, mainly coloured microbeads (5 μm to 30 μm). In addition to their reported aerosolization of these contaminants during the spray-application of paints, the release also occurs directly as consumers clean brushes and rollers with tap water [310], and as secondary microplastics through coating degradation through wear and weathering processes. This applies in particular to road markings and direct release of microplastic from commercial and leisure boats into water bodies [311].

In the present case, the persistence of the coating building blocks in the environment have to be evaluated for both the uncured monomers and the thermoset polymer matrices. While ozonized and epoxidized oils are known to biodegrade, the biodegradability for the cured systems developed in this thesis is expected to decrease in the order of drying oil > epoxy > polyurethane/styrene with a transition from bulk degradation to surface erosion and increasing T_g . With the utilization of these resins in transparent finishes, the photoinitiators are likely the additives of most concern in the two UV-curable coatings. Considering the industrial use of plastic microfibrils (among silicates and other thixotropic agents) to achieve thixotropic paint flow behaviour [312], utilization of CNC as proposed in this work, could offer a microplastic-free and transparent alternative.

5.3 Summary

Plant oils have been used as coating materials since prehistoric times. While long drying times are one of the main reasons for the use of modified or synthetic fast-drying alternatives, the fully biobased nature of drying oils is of great interest in sustainable construction. This thesis provides two new approaches to significantly reduce the drying times from weeks/days down to hours/minutes while maintaining an up to 100% biobased content. Rather than sacrificing the natural origin of these materials, the focus was to tune the drying behaviour for increased performance in areas where the high flexibility and low M_w of lipid-based coatings are of advantage, such as wood finishes. With the move to UV-polymerizable coatings, also plant-derived pigments and CNC additives can significantly improve coating performance - not as bulk ingredients like lipids but for targeted property tuning. The combined use of biobased feedstocks and low-emission curing technologies has the potential to reduce the carbon footprint and VOC emissions of these materials. Since these parameters are strongly dependent on coating durability, life-cycle analysis is required to obtain a realistic estimate of any reduced environmental impacts. Meanwhile, the increasing consumer demand for more biobased coating materials such as those developed here, could contribute to the advancement of local and global oleochemistry and cellulose processing. This has significant commercialization potential owing to the relatively simple chemistry and processing developed.

Bibliography

- [1] O. Association. *Surface Coatings: Volume 1 Raw Materials and Their Usage*. Surface Coatings. Springer Netherlands, 1993. ISBN 9780412552106.
- [2] G. R. Pilcher and M. Rezai. The global paint and coating industry. *European Coatings Journal*, 10, 2018.
- [3] B. C. McDonald, J. A. de Gouw, J. B. Gilman, S. H. Jathar, A. Akherati, C. D. Cappa, J. L. Jimenez, J. Lee-Taylor, P. L. Hayes, S. A. McKeen, et al. Volatile chemical products emerging as largest petrochemical source of urban organic emissions. *Science*, 359(6377):760–764, 2018.
- [4] G. R. Pilcher. The demand for coatings raw materials to 2022. *European Coatings Journal*, 4, 2018.
- [5] A. Goldschmidt and H. Streitberger. *BASF Handbook on Basics of Coating Technology*. American Coatings Literature. Vincentz Network, 2003. ISBN 9783878707981.
- [6] W. Freitag and D. Stoye. *Paints, Coatings and Solvents*. Wiley, 2008. ISBN 9783527611850.
- [7] A. Bahadori. *Essentials of Coating, Painting, and Lining for the Oil, Gas and Petrochemical Industries*. Elsevier Science, 2015. ISBN 9780128016657.
- [8] H.-D. Hwang, C.-H. Park, J.-I. Moon, H.-J. Kim, and T. Masubuchi. UV-curing behavior and physical properties of waterborne UV-curable polycarbonate-based polyurethane dispersion. *Progress in Organic Coatings*, 72(4):663–675, 2011.
- [9] D. Chiriu, P. C. Ricci, C. M. Carbonaro, D. Nadali, A. Polcaro, and F. Mocci. Drying oil detected in mid-third Millennium BC Mesopotamian clay artifacts: Raman spectroscopy and DFT simulation study. *Microchemical Journal*, 124:386–395, 2016.
- [10] Y. Taniguchi, H. Otake, M. Cotte, and E. Checroun. The painting techniques, materials and conservation of Bamiyan Buddhist mural paintings in Afghanistan. In *ICOM Committee for Conservation, ICOM-CC, 15th Triennial Conference New Delhi, 22-26 September 2008: preprints*, volume 1, pages 553–560, 2008.

- [11] A. Lluveras-Tenorio, R. Vinciguerra, E. Galano, C. Blaensdorf, E. Emmerling, M. Perla Colombini, L. Biolo, and I. Bonaduce. GC/MS and proteomics to unravel the painting history of the lost Giant Buddhas of Bāmiyān (Afghanistan). *PLOS ONE*, 12(4):e0172990, 2017.
- [12] M. Cotte, J. Susini, V. A. Solé, Y. Taniguchi, J. Chillida, E. Checroun, and P. Walter. Applications of synchrotron-based micro-imaging techniques to the chemical analysis of ancient paintings. *Journal of Analytical Atomic Spectrometry*, 23(6):820–828, 2008.
- [13] R. Terrill. Dehydration of castor oil. *Journal of the American Oil Chemists Society*, 27(11):477–481, 1950.
- [14] G. Sward. *Paint Testing Manual: Physical and Chemical Examination of Paints, Varnishes, Lacquers, and Colors*. ASTM special technical publication. American Society for Testing & Materials, 1972. ISBN 9780803100992.
- [15] J. V. Koleske. *Paint and coating testing manual: of the Gardner-Sward handbook*, volume 17. ASTM International, West Conshohocken, 1995. doi: 10.1002/col.5080200415.
- [16] H. Wexler. Polymerization of drying oils. *Chem. Rev.*, 64:591–611, 1964.
- [17] M. M. Piskur. Annual Review of literature on fats, oils, and soaps. Part 1. *Journal of the American Oil Chemists' Society*, 26(4):179–194, April 1949. ISSN 0003-021X.
- [18] D. Min and J. Boff. Chemistry and reaction of singlet oxygen in foods. *Comprehensive Reviews in Food Science and Food Safety*, 1(2):58–72, 2002.
- [19] M. Tolinski. *Additives for polyolefins: getting the most out of polypropylene, polyethylene and TPO*. William Andrew, 2015.
- [20] F. Gunstone. *The Chemistry of Oils and Fats: Sources, Composition, Properties and Uses*. Blackwell Publishing Ltd, Oxford, 2009. ISBN 1405150025.
- [21] E. Frankel. *Lipid Oxidation*. Elsevier, Oxford, 2 edition, 2014. ISBN 9780857097927.
- [22] D. Wheeler. The chemistry of drying oils. *Journal of the American Oil Chemists' Society*, 27(11):440–445, 1950.
- [23] B. Maillard, K. Ingold, and J. Scaiano. Rate constants for the reactions of free radicals with oxygen in solution. *Journal of the American Chemical Society*, 105(15):5095–5099, 1983.
- [24] M. Soucek, T. Khattab, and J. Wu. Review of autoxidation and driers. *Progress in Organic Coatings*, 73(4):435–454, 2012.
- [25] L. Marnett. Peroxyl free radicals: potential mediators of tumor initiation and promotion. *Carcinogenesis*, 8(10):1365–1373, 1987.
- [26] N. A. Porter. Mechanisms for the autoxidation of polyunsaturated lipids. *Accounts of Chemical Research*, 19(9):262–268, 1986.

- [27] N. A. Porter, B. A. Weber, H. Weenen, and J. A. Khan. Autoxidation of polyunsaturated lipids. factors controlling the stereochemistry of product hydroperoxides. *Journal of the American Chemical Society*, 102(17):5597–5601, 1980.
- [28] C. Schneider. An update on products and mechanisms of lipid peroxidation. *Molecular Nutrition & Food Research*, 53(3):315–321, 2009.
- [29] N. Porter, S. Caldwell, and K. Mills. Mechanisms of free radical oxidation of unsaturated lipids. *Lipids*, 30(4):277–290, 1995.
- [30] J. Mallégol, J. Gardette, and J. Lemaire. Long-term behavior of oil-based varnishes and paints. Photo- and thermooxidation of cured linseed oil. *Journal of the American Chemical Society*, 77(3):257–263, 2000.
- [31] A. Hellgren, M. Wallin, P. Weissenborn, P. McDonald, P. Glover, and J. Keddie. New techniques for determining the extent of crosslinking in coatings. *Progress in Organic Coatings*, 43(1):85–98, 2001.
- [32] Z. O. Oyman, W. Ming, and R. der Linde. Oxidation of drying oils containing non-conjugated and conjugated double bonds catalyzed by a cobalt catalyst. *Progress in Organic Coatings*, 54(3):198–204, 2005.
- [33] R. F. Paschke, J. E. Jackson, and D. H. Wheeler. Thermal Polymerization of Drying Oils Isomers of Methyl Linoleate. *Chemistry & Industry*, 44(5):1113–1118, May 1952. doi: 10.1021/ie50509a051.
- [34] Z. W. Wicks. Drying Oils. In *Kirk-Othmer Encyclopedia of Chemical Technology*, pages 142–155. John Wiley & Sons, Inc., Hoboken, NJ, USA, December 2000. doi: 10.1002/0471238961.0418250923090311.a01.pub2.
- [35] G. Moad and D. Solomon. *The Chemistry of Radical Polymerization*. The Chemistry of Radical Polymerisation. Elsevier Science, 2006. ISBN 9780080442884.
- [36] J. Mallégol, J. Lemaire, and J. Gardette. Yellowing of oil-based paints. *Studies in Conservation*, pages 121–131, 2001.
- [37] A. Elm. Deterioration of dried oil films. *Industrial & Engineering Chemistry Research*, 41(2):319–324, 1949.
- [38] J. Honzíček. Curing of air-drying paints: A critical review. *Industrial & Engineering Chemistry Research*, 58(28):12485–12505, 2019.
- [39] O. Privett, M. Blank, J. Covell, and W. Lundberg. Yellowing of oil films. *Journal of the American Oil Chemists' Society*, 38(1):22–27, 1961.
- [40] L. O'Neill, S. Rybicka, and T. Robey. Yellowing of drying oil films. *Chemistry & Industry*, 41:1796–1797, 1962.
- [41] R. Kumarathasan, A. Rajkumar, N. Hunter, and H. Gesser. Autoxidation and yellowing of methyl linolenate. *Progress in Lipid Research*, 31(2):109–126, 1992.

- [42] H. A. Standeven. *House paints, 1900-1960: History and use*. Getty Publications, 2011.
- [43] P. Oldring and G. Hayward. *Resins for Surface Coatings: Manual for*. SITA Technology, 1987.
- [44] G. Gündüz, A. Khalid, I. Mecidoğlu, and L. Aras. Water-borne and air-drying oil-based resins. *Progress in Organic Coatings*, 49(3):259–269, 2004.
- [45] K. Holmberg and J. Johansson. Addition of maleic anhydride to esters of mono-unsaturated fatty acids. *Acta Chemica Scandinavica*, 36(7), 1982.
- [46] F. Stefanoiu, L. Candy, C. Vaca-Garcia, and E. Borredon. Kinetics and mechanism of the reaction between maleic anhydride and fatty acid esters and the structure of the products. *European Journal of Lipid Science and Technology*, 110(5):441–447, 2008.
- [47] N. Engineers. *The Complete Book on Water Soluble Polymers*. NIIR Project Consultancy Services, 2009. ISBN 9788178331232.
- [48] Y. Huang, G. Ye, and J. Yang. Synthesis and properties of UV-curable acrylate functionalized tung oil based resins via diels–alder reaction. *Progress in Organic Coatings*, 78:28–34, 2014.
- [49] M. Derrick, D. Stulik, and J. Landry. *Infrared Spectroscopy in Conservation Science*. Scientific Tools for Conservation. Getty Conservation Institute, 2000. ISBN 9780892364695.
- [50] P. Glöckner. *Radiation curing: Coatings and printing inks; technical basics, applications and trouble shooting*. Vincentz Network GmbH & Co KG, 2008.
- [51] R. Schwalm. *UV Coatings: Basics, Recent Developments and New Applications*. Elsevier Science, 2006. ISBN 9780080466897.
- [52] J. M. Tedder and J. C. Walton. The kinetics and orientation of free-radical addition to olefins. *Accounts of Chemical Research*, 9(5):183–191, 1976.
- [53] J. Bentley and G. Turner. *Introduction to Paint Chemistry and principles of paint technology, Fourth Edition*. Taylor & Francis, 1997. ISBN 9780412723308.
- [54] N. Ballard and J. M. Asua. Radical polymerization of acrylic monomers: An overview. *Progress in Polymer Science*, 79:40–60, 2018.
- [55] N. M. Ahmad, F. Heatley, and P. A. Lovell. Chain transfer to polymer in free-radical solution polymerization of n-butyl acrylate studied by NMR spectroscopy. *Macromolecules*, 31(9):2822–2827, 1998.
- [56] C. Plessis, G. Arzamendi, J. Leiza, H. Schoonbrood, D. Charnot, and J. Asua. A decrease in effective acrylate propagation rate constants caused by intramolecular chain transfer. *Macromolecules*, 33(1): 4–7, 2000.
- [57] R. S. Davidson. *Exploring the science, technology and applications of UV and EB curing*. Sita Technology, 1999.

- [58] J.-P. Fouassier and A. Merlin. Laser investigation of norrish type I photolysis in the photoinitiator irgacure (2, 2-dimethoxy 2-phenyl-acetophenone). *Journal of Photochemistry*, 12(1):17–23, 1980.
- [59] J. A. Arceneaux. UV/EB chemistry and technology. *Printers' Guide*, 2016.
- [60] J. Bennett. Measuring UV curing parameters of commercial photopolymers used in additive manufacturing. *Additive Manufacturing*, 18:203–212, 2017.
- [61] U. Kolczak, G. Rist, K. Dietliker, and J. Wirz. Reaction mechanism of monoacyl- and bisacylphosphine oxide photoinitiators studied by ^{31}P -, ^{13}C -, and ^1H -CIDNP and ESR. *Journal of the American Chemical Society*, 118(27):6477–6489, 1996.
- [62] A. Albini, T. Costa, F. Barigelletti, and M. Jimenez. *Photochemistry. SPR - photochemistry*. Royal Society of Chemistry, 2010. ISBN 9781847550545.
- [63] N. S. Allen, P. J. Robinson, N. J. White, R. Clancy, and J. Luc-Gardette. Photo-oxidative stability and photoyellowing of electron-beam- and UV-cured multi-functional amine-terminated diacrylates: a monomer/model amine study. *Journal of Photochemistry and Photobiology A: Chemistry*, 47(2):223–247, 1989.
- [64] A. K. O'Brien and C. N. Bowman. Impact of oxygen on photopolymerization kinetics and polymer structure. *Macromolecules*, 39(7):2501–2506, 2006.
- [65] S. C. Ligon, B. Husar, H. Wutzel, R. Holman, and R. Liska. Strategies to reduce oxygen inhibition in photoinduced polymerization. *Chemical Reviews*, 114(1):557–589, 2014.
- [66] R. Davidson. The role of amines in UV curing. *Radiation Curing in Polymer Science and Technology*, 3:153–76, 1993.
- [67] Z. Wicks Jr, F. Jones, S. Pappas, and D. Wicks. *Organic coatings: science and technology*. John Wiley & Sons, Hoboken, 2007.
- [68] S. Pappas. *Radiation Curing: Science and Technology*. Topics in Applied Chemistry. Springer US, 2013. ISBN 9781489907127.
- [69] A. Walls, J. McCabe, and J. Murray. The polymerization contraction of visible-light activated composite resins. *Journal of Dentistry*, 16(4):177–181, 1988.
- [70] R. Labella, P. Lambrechts, B. Van Meerbeek, and G. Vanherle. Polymerization shrinkage and elasticity of flowable composites and filled adhesives. *Dental Materials*, 15(2):128–137, 1999.
- [71] L. Giachetti, D. Scaminaci Russo, C. Bambi, and R. Grandini. A review of polymerization shrinkage stress: current techniques for posterior direct resin restorations. *Journal of Contemporary Dental Practice*, 7(4):79–88, 2006.
- [72] K. Baroudi, A. M. Saleh, N. Silikas, and D. C. Watts. Shrinkage behaviour of flowable resin-composites related to conversion and filler-fraction. *Journal of Dentistry*, 35(8):651–655, 2007.

- [73] K. Mittal. *Progress in Adhesion and Adhesives*. Wiley, 2018. ISBN 9781119526391.
- [74] J. R. Condon and J. L. Ferracane. Reduced polymerization stress through non-bonded nanofiller particles. *Biomaterials*, 23(18):3807–3815, 2002.
- [75] B. S. Dauvillier, P. F. Hübsch, M. P. Aarnts, and A. J. Feilzer. Modeling of viscoelastic behavior of dental chemically activated resin composites during curing. *Journal of Biomedical Materials Research: An Official Journal of The Society for Biomaterials, The Japanese Society for Biomaterials, and The Australian Society for Biomaterials*, 58(1):16–26, 2001.
- [76] B. S. Dauvillier, A. J. Feilzer, A. De Gee, and C. Davidson. Visco-elastic parameters of dental restorative materials during setting. *Journal of Dental Research*, 79(3):818–823, 2000.
- [77] J. Li, H. Li, A. S. Fok, and D. C. Watts. Multiple correlations of material parameters of light-cured dental composites. *Dental Materials*, 25(7):829–836, 2009.
- [78] N. Abdulsamee, A. Elkhadem, and P. Nagi. Shrinkage of dental composite resin: Contemporary understanding its enigmas and how to solve? A review. *EC Dental Science*, 19:03–17, 2020.
- [79] W. Green. *Industrial Photoinitiators: A Technical Guide*. CRC Press, 2010. ISBN 9781439827468.
- [80] U. Bulut and J. V. Crivello. Investigation of the reactivity of epoxide monomers in photoinitiated cationic polymerization. *Macromolecules*, 38(9):3584–3595, 2005.
- [81] J. V. Crivello and J. Lam. Diaryliodonium salts. a new class of photoinitiators for cationic polymerization. *Macromolecules*, 10(6):1307–1315, 1977.
- [82] J. Crivello, B. Falk, and M. Zonca. Study of cationic ring-opening photopolymerizations using optical pyrometry. *Journal of Applied Polymer Science*, 92(5):3303–3319, 2004.
- [83] T. H. Chiang and T.-E. Hsieh. A study of monomer’s effect on adhesion strength of UV-curable resins. *International Journal of Adhesion and Adhesives*, 26(7):520–531, 2006.
- [84] B. A. Ficek, A. M. Thiesen, and A. B. Scranton. Cationic photopolymerizations of thick polymer systems: Active center lifetime and mobility. *European Polymer Journal*, 44(1):98–105, 2008.
- [85] C. Decker, T. Nguyen Thi Viet, and H. Pham Thi. Photoinitiated cationic polymerization of epoxides. *Polymer International*, 50(9):986–997, 2001.
- [86] R. Bongiovanni, E. Turcato, A. Di Gianni, and S. Ronchetti. Epoxy coatings containing clays and organoclays: Effect of the filler and its water content on the UV-curing process. *Progress in Organic Coatings*, 62(3):336–343, 2008.
- [87] S. Penczek, P. Kubisa, and R. Szymański. Activated monomer propagation in cationic polymerizations. *Makromolekulare Chemie. Macromolecular Symposia*, 3(1):203–220, 1986.
- [88] Z. Liu and G. Kraus. *Green materials from plant oils*. Royal Society of Chemistry, 2014.

- [89] S. Miao, P. Wang, Z. Su, and S. Zhang. Vegetable-oil-based polymers as future polymeric biomaterials. *Acta Biomaterialia*, 10(4):1692–1704, 2014.
- [90] C. Li, Z. Xiao, L. He, M. Di Serio, and X. Xie. *Industrial Oil Plant: Application Principles and Green Technologies*. Springer Singapore, 2020. ISBN 9789811549205.
- [91] F. Su and Y. Guo. Advancements in solid acid catalysts for biodiesel production. *Green Chemistry*, 16(6):2934–2957, 2014.
- [92] A. Demirbaş. Biodiesel fuels from vegetable oils via catalytic and non-catalytic supercritical alcohol transesterifications and other methods: a survey. *Energy Conversion & Management*, 44(13):2093–2109, 2003.
- [93] A. Demirbaş. Biodiesel from vegetable oils via transesterification in supercritical methanol. *Energy Conversion & Management*, 43(17):2349–2356, 2002.
- [94] T. S. Omonov and J. M. Curtis. Plant oil-based epoxy intermediates for polymers. In S. A. Madbouly, C. Zhang, and M. R. Kessler, editors, *Bio-Based Plant Oil Polymers and Composites*, chapter 7, page 232. William Andrew, 2015.
- [95] F. P. Greenspan and R. J. Gall. *In situ* epoxidation of oleic acid using formic acid, December 18 1956. US Patent 2,774,774.
- [96] P. Theato. *Multi-Component and Sequential Reactions in Polymer Synthesis*. Advances in Polymer Science. Springer International Publishing, 2015. ISBN 9783319207209.
- [97] M. Desroches, M. Escouvois, R. Auvergne, S. Caillol, and B. Boutevin. From vegetable oils to polyurethanes: synthetic routes to polyols and main industrial products. *Polymer Reviews*, 52(1):38–79, 2012.
- [98] X. Kong, G. Liu, H. Qi, and J. M. Curtis. Preparation and characterization of high-solid polyurethane coating systems based on vegetable oil derived polyols. *Progress in Organic Coatings*, 76(9):1151–1160, 2013.
- [99] E. Delebecq, J.-P. Pascault, B. Boutevin, and F. Ganachaud. On the versatility of urethane/urea bonds: reversibility, blocked isocyanate, and non-isocyanate polyurethane. *Chemical Reviews*, 113(1):80–118, 2012.
- [100] M. Bertoldo, C. Cappelli, S. Catanorchi, V. Liuzzo, and S. Bronco. Understanding the accelerating effect of ϵ -caprolactam on the formation of urethane linkages. *Macromolecules*, 38(4):1385–1394, 2005.
- [101] M. Modesti and A. Lorenzetti. An experimental method for evaluating isocyanate conversion and trimer formation in polyisocyanate–polyurethane foams. *European Polymer Journal*, 37(5):949–954, 2001.
- [102] V. Favier, G. Canova, J. Cavaillé, H. Chanzy, A. Dufresne, and C. Gauthier. Nanocomposite materials from latex and cellulose whiskers. *Polymers for Advanced Technologies*, 6(5):351–355, 1995.
- [103] A. Dufresne. Nanocellulose: a new ageless bionanomaterial. *Materials Today*, 16(6):220–227, 2013.

- [104] H. Kargarzadeh, M. Ioelovich, I. Ahmad, S. Thomas, and A. Dufresne. Methods for extraction of nanocellulose from various sources. *Handbook of Nanocellulose and Cellulose Nanocomposites*, 1:1–51, 2017.
- [105] H. A. Khalil, A. Bhat, and A. I. Yusra. Green composites from sustainable cellulose nanofibrils: A review. *Carbohydrate Polymers*, 87(2):963–979, 2012.
- [106] P. Lu and Y.-L. Hsieh. Preparation and properties of cellulose nanocrystals: rods, spheres, and network. *Carbohydrate Polymers*, 82(2):329–336, 2010.
- [107] M. Roman and W. T. Winter. Effect of sulfate groups from sulfuric acid hydrolysis on the thermal degradation behavior of bacterial cellulose. *Biomacromolecules*, 5(5):1671–1677, 2004.
- [108] M. V. Zimmermann, C. Borsoi, A. Lavoratti, M. Zanini, A. J. Zattera, and R. M. Santana. Drying techniques applied to cellulose nanofibers. *Journal of Reinforced Plastics and Composites*, 35(8):628–643, 2016.
- [109] Y. Peng, D. J. Gardner, and Y. Han. Drying cellulose nanofibrils: in search of a suitable method. *Cellulose*, 19(1):91–102, 2012.
- [110] Z. W. Wicks Jr. Drying oils. *Kirk-Othmer Encyclopedia of Chemical Technology*, 2000.
- [111] R. Van Gorkum and E. Bouwman. The oxidative drying of alkyd paint catalysed by metal complexes. *Coordination Chemistry Reviews*, 249(17-18):1709–1728, 2005.
- [112] P. Fryer and F. Weston. *Technical Handbook of Oils, Fats and Waxes*. Number 2 in The Cambridge Technical Series. Cambridge University Press, 2013. ISBN 9781107660885.
- [113] N. Board. *The Complete Technology Book on Printing Inks*. Asia Pacific Business Press, 2003. ISBN 9788178330488.
- [114] E. Frankel. Lipid oxidation. *Progress in Lipid Research*, 19(1-2):1–22, 1980.
- [115] S. Coffey. III. the mechanism of the oxidation of drying oils as elucidated by a study of the true oxygen absorption. Part III. The action of driers. *Journal of the Chemical Society, Transactions*, 121:17–23, 1922.
- [116] K. van den Berg, I. Bonaduce, A. Burnstock, B. Ormsby, M. Scharff, L. Carlyle, G. Heydenreich, and K. Keune. *Conservation of Modern Oil Paintings*. Springer International Publishing, 2020. ISBN 9783030192549.
- [117] J. D. Van Den Berg, N. D. Vermist, L. Carlyle, M. Holčapek, and J. J. Boon. Effects of traditional processing methods of linseed oil on the composition of its triacylglycerols. *Journal of Separation Science*, 27(3):181–199, 2004.
- [118] C. Boelhouwer, J. T. Knegtel, and M. Tels. On the mechanism of the thermal polymerization of linseed oil. *Fette, Seifen, Anstrichmittel*, 69(6):432–436, 1967.

- [119] F. Browne. Paint thinners. *Industrial & Engineering Chemistry*, 23(8):868–874, 1931.
- [120] W. Kubie and J. Cowan. Linseed oil emulsions for protecting concrete. *Journal of the American Oil Chemists' Society*, 44(3):194–196, 1967.
- [121] F. Boig. Laboratory experiments dealing with the manufacture of paints. *Journal of Chemical Education*, 24(12):594, 1947.
- [122] T. Estlander, R. Jolanki, and L. Kanerva. *Paints, lacquers and varnishes*. Springer, 2004.
- [123] J. Lindeboom. Air-drying high solids alkyd pants for decorative coatings. *Progress in Organic Coatings*, 34(1):147–151, 1998.
- [124] F. Heaton and N. Uri. The aerobic oxidation of unsaturated fatty acids and their esters: cobalt stearate-catalyzed oxidation of linoleic acid. *Journal of Lipid Research*, 2(2):152–160, 1961.
- [125] J. Mallécol, J. Lemaire, and J.-L. Gardette. Drier influence on the curing of linseed oil. *Progress in Organic Coatings*, 39(2-4):107–113, 2000.
- [126] C. Bawn, A. Pennington, and C. Tipper. The catalyzed oxidation of trimethyl-ethylene in solution. *Discussions of the Faraday Society*, 10:282–291, 1951.
- [127] C. W. McGlinchey. Thermal analysis of fresh and mature oil paint films: The effect of pigments as driers and the solvent leaching of mature paint films. *MRS Online Proceedings Library Archive*, 185, 1990.
- [128] U. Biermann, W. Butte, R. Holtgreffe, W. Feder, and J. O. Metzger. Esters of calendula oil and tung oil as reactive diluents for alkyd resins. *European Journal of Lipid Science and Technology*, 112(1):103–109, 2010.
- [129] C. Stenberg, M. Svensson, E. Wallström, and M. Johansson. Drying of linseed oil wood coatings using reactive diluents. *Surface Coatings International Part B: Coatings Transactions*, 88(2):119–126, 2005.
- [130] C. D. Harries. *Untersuchungen Über das Ozon und Seine Einwirkung auf Organische Verbindungen (1903–1916)*. Springer-Verlag, 2013.
- [131] E. Molinari and E. Soncini. Constitution der Oelsäure und Einwirkung von Ozon auf Fette. *Berichte der deutschen chemischen Gesellschaft*, 39(3):2735–2744, 1906.
- [132] T. Harada. Olive oil ozonide and its fungicidal quality. *Bulletin of the Chemical Society of Japan*, 9(4):192–197, 1934.
- [133] F. G. Fischer, H. Düll, and L. Ertel. Über die katalytische Hydrierung von Ozoniden. *Berichte der deutschen chemischen Gesellschaft (A and B Series)*, 65(8):1467–1472, 1932.
- [134] C. Noller and R. Adams. The preparation and use of aldehyde esters formed by ozonation of the methyl esters of various unsaturated acids. *Journal of the American Chemical Society*, 48(4):1074–1080, 1926.

- [135] C. G. Goebel, A. C. Brown, H. F. Oehlschlaeger, and R. P. Rolfes. Method of making azelaic acid, November 12 1957. US Patent 2,813,113.
- [136] J. Riebsomer and R. C. Tallman. A method for an oxidizing hydrolysis of ozonides prepared from unsaturated acids. In *Proceedings of the Indiana Academy of Science*, volume 43, pages 136–138, 1933.
- [137] M. F. Díaz, J. A. Gavín, M. Gómez, V. Curtielles, and F. Hernández. Study of ozonated sunflower oil using ¹H NMR and microbiological analysis. *Ozone: Science & Engineering*, 28(1):59–63, 2006.
- [138] M. F. Díaz, N. Núñez, D. Quincose, W. Díaz, and F. Hernández. Study of three systems of ozonized coconut oil. *Ozone: Science & Engineering*, 27(2):153–157, 2005.
- [139] K. Skalska, S. Ledakowicz, J. Perkowski, and B. Sencio. Germicidal properties of ozonated sunflower oil. *Ozone: Science & Engineering*, 31(3):232–237, 2009.
- [140] P. Guerra-Blanco, T. Poznyak, A. Pérez, Y. Gómez y Gómez, M. Bautista-Ramírez, and I. Chairez. Ozonation degree of vegetable oils as the factor of their anti-inflammatory and wound-healing effectiveness. *Ozone: Science & Engineering*, 39(5):374–384, 2017.
- [141] H. Kataoka, M. Semma, H. Sakazaki, K. Nakamuro, T. Yamamoto, S. Hirota, K. Tazuya-Murayama, and A. Ichikawa. Proinflammatory event of ozonized olive oil in mice. *Ozone: Science & Engineering*, 31(3):238–246, 2009.
- [142] R. G. Kadesch. Ozonolysis of fatty acids and their derivatives. *Progress in the Chemistry of Fats and other Lipids*, 6:291–312, 1963.
- [143] V. Kulçitki, A. Bourdelais, T. Schuster, and D. Baden. Synthesis of a functionalized furan via ozonolysis—further confirmation of the Criegee mechanism. *Tetrahedron Letters*, 51(31):4079–4081, 2010.
- [144] C. A. Taatjes, D. E. Shallcross, and C. J. Percival. Research frontiers in the chemistry of Criegee intermediates and tropospheric ozonolysis. *Physical Chemistry Chemical Physics*, 16(5):1704–1718, 2014.
- [145] R. Criegee. Mechanism of ozonolysis. *Angewandte Chemie International Edition in English*, 14(11):745–752, 1975.
- [146] F. Cataldo. Chemical and thermochemical aspects of the ozonolysis of ethyl oleate: Decomposition enthalpy of ethyl oleate ozonide. *Chemistry and Physics of Lipids*, 175:41–49, 2013.
- [147] O. Privett and E. Nickell. Recent advances in the determination of the structure of fatty acids via ozonolysis. *Journal of the American Oil Chemists Society*, 43(6):393–400, 1966.
- [148] O. Privett and E. C. Nickell. Studies on the ozonization of methyl oleate. *Journal of the American Oil Chemists Society*, 41(1):72–77, 1964.
- [149] M. D. Lundin, A. M. Danby, G. R. Akien, T. P. Binder, D. H. Busch, and B. Subramaniam. Liquid CO₂ as a safe and benign solvent for the ozonolysis of fatty acid methyl esters. *ACS Sustainable Chemistry & Engineering*, 3(12):3307–3314, 2015.

- [150] M. D. Lundin, A. M. Danby, G. R. Akien, P. Venkitasubramanian, K. J. Martin, D. H. Busch, and B. Subramaniam. Intensified and safe ozonolysis of fatty acid methyl esters in liquid CO₂ in a continuous reactor. *AIChE Journal*, 63(7):2819–2826, 2017.
- [151] Society of Chemical Industry (Great Britain). *Journal of the Society of Chemical Industry*, volume 16. Eyre and Spottiswoode, 1897.
- [152] J. B. C. Kershaw. The production of ozone, and a comparison of its cost with that of other oxidising agents. In *The Electrical Review*, volume 43, pages 151–153. H. Alabaster, Gatehouse & Co., London, 1899.
- [153] O. Lange. *Chemisch-Technische Vorschriften: Ein Handbuch der Speziellen Chemischen Technologie insbesondere für Chemische Fabriken und Verwandte Technische Betriebe Enthaltend Vorschriften aus allen Gebieten der Chemischen Technologie mit Umfassenden Literaturnachweisen III. Band: Harze, Öle, Fette*. Springer-Verlag Berlin Heidelberg, 1923. ISBN 978-3-662-31453-1.
- [154] M. Doerner. *Malerei und seine Verwendung im Bilde*. Ferdinand Enke Verlag Stuttgart, 6 edition, 1938.
- [155] F. E. Hartman. Apparatus for the treatment and purification of liquids, 1937. URL <https://patents.google.com/patent/US2089793A/en>. Patent No. 2089793, Filed January 1st., 1934, Issued Aug. 10th., 1937.
- [156] T. S. Omonov, E. Kharraz, and J. M. Curtis. The epoxidation of canola oil and its derivatives. *RSC Advances*, 6(95):92874–92886, 2016.
- [157] ASTM International. Standard test methods for evaluating drying or curing during film formation of organic coatings using mechanical recorders. Standard ASTM D5895-13, ASTM International, 100 Barr Harbor Drive, PO Box C700, West Conshohocken, PA 19428-2959, United States, 2016.
- [158] C. S. Tumosa and M. F. Mecklenburg. Oil paints: the chemistry of drying oils and the potential for solvent disruption. In *New Insights into the Cleaning of Paintings: Proceedings from the Cleaning 2010 International Conference, Universidad Politecnica de Valencia and Museum Conservation Institute*, pages 51–58. Smithsonian Institution, 2013.
- [159] N. U. Soriano Jr, V. P. Migo, and M. Matsumura. Functional group analysis during ozonation of sunflower oil methyl esters by ft-ir and nmr. *Chemistry and Physics of Lipids*, 126(2):133–140, 2003.
- [160] M. Wu, D. F. Church, T. J. Mahier, S. A. Barker, and W. A. Pryor. Separation and spectral data of the six isomeric ozonides from methyl oleate. *Lipids*, 27(2):129–135, 1992.
- [161] R. Murray, Y. Wallace, D. Raymond, and P. R. Story. Ozonolysis. steric and stereochemical effects in the olefin. *Journal of the American Chemical Society*, 89(10):2429–2434, 1967.
- [162] V. Vacque, B. Sombret, J. Huvenne, P. Legrand, and S. Suc. Characterisation of the O-O peroxide bond by vibrational spectroscopy. *Spectrochimica Acta Part A: Molecular and Biomolecular Spectroscopy*, 53(1):55–66, 1997.

- [163] F. Cataldo. Ethyl oleate and ethyl elaidate ozonides: thermal decomposition and photolysis. *Ozone: Science & Engineering*, 37(5):431–440, 2015.
- [164] M. Anachkov, S. Rakovsky, R. Fotty, and A. Stoyanov. DSC study of the thermal decomposition of 1-decene ozonide. *Thermochimica Acta*, 237(1):213–217, 1994.
- [165] F. Cataldo. Thermal stability, decomposition enthalpy, and raman spectroscopy of 1-alkene secondary ozonides. *Tetrahedron Letters*, 56(8):994–998, 2015.
- [166] United States. Office of the Federal Register. *Code of Federal Regulations: 2000-*. U.S. General Services Administration, National Archives and Records Service, Office of the Federal Register, 2015.
- [167] A. Joglekar and A. May. Product excellence through design of experiments. *Cereal Foods World*, 32(12):857, 1987.
- [168] L. De Viguerie, P. Payard, E. Portero, P. Walter, and M. Cotte. The drying of linseed oil investigated by fourier transform infrared spectroscopy: Historical recipes and influence of lead compounds. *Progress in Organic Coatings*, 93:46–60, 2016.
- [169] N. Board. *Modern Technology of Paints, Varnishes & Lacquers (2nd Edition)*. NIIR Project Consultancy Services, 2007. ISBN 9788178330884.
- [170] T. A. Girard, M. Beispiel, and C. E. Bricker. The mechanism of cobalt drier action. *Journal of the American Oil Chemists' Society*, 42(10):828–833, 1965.
- [171] M. P. Bertrand and J.-M. Surzur. Reactivite des radicaux alkoxy vis a vis des olefines une interpretation basee sur les effets orbitalaires. *Tetrahedron Letters*, 17(38):3451–3454, 1976.
- [172] W. A. Pryor, F. Y. Tang, R. H. Tang, and D. F. Church. Chemistry of the tert-butyl radical: polar character, . rho. value for reaction with toluenes, and the effect of radical polarity on the ratio of benzylic hydrogen abstraction to addition to aromatic rings. *Journal of the American Chemical Society*, 104(10):2885–2891, 1982.
- [173] J. C. Ewing, D. F. Church, and W. A. Pryor. Thermal decomposition of allylbenzene ozonide. *Journal of the American Chemical Society*, 111(15):5839–5844, 1989.
- [174] L. Hull, I. Hisatsune, and J. Heicklen. Vapor-phase thermal decomposition of some simple ozonides. *Journal of Physical Chemistry*, 76(19):2659–2665, 1972.
- [175] J. Mallécol, J.-L. Gardette, and J. Lemaire. Long-term behavior of oil-based varnishes and paints I. Spectroscopic analysis of curing drying oils. *Journal of the American Oil Chemists' Society*, 76(8):967–976, 1999.
- [176] R. Lee, G. Gryn'Ova, K. Ingold, and M. L. Coote. Why are *sec*-alkylperoxyl bimolecular self-reactions orders of magnitude faster than the analogous reactions of *tert*-alkylperoxyls? The unanticipated role of CH hydrogen bond donation. *Physical Chemistry Chemical Physics*, 18(34):23673–23679, 2016.

- [177] H. W.-S. Chan, G. Levett, and J. A. Matthew. The mechanism of the rearrangement of linoleate hydroperoxides. *Chemistry and Physics of Lipids*, 24(3):245–256, 1979.
- [178] A. Schönemann and H. G. Edwards. Raman and ftir microspectroscopic study of the alteration of chinese tung oil and related drying oils during ageing. *Analytical and Bioanalytical Chemistry*, 400(4):1173–1180, 2011.
- [179] J. Conant and C. Tongberg. Polymerization reactions under high pressure. i. some experiments with isoprene and butyraldehyde. *Journal of the American Chemical Society*, 52(4):1659–1669, 1930.
- [180] R. C. Houtz and H. Adkins. The catalysis of polymerization by ozonides. *Journal of the American Chemical Society*, 53(3):1058–1063, 1931.
- [181] R. C. Houtz and H. Adkins. The catalysis of polymerization by ozonides. II¹. *Journal of the American Chemical Society*, 55(4):1609–1617, 1933.
- [182] M. Tatimori. Polymerisation of tung oil. V. Effects of treated fatty oils upon the gelation of tung oil. *Bulletin of the Chemical Society of Japan*, 16(2):45–50, 1941.
- [183] J. C. Ewing, J. P. Cosgrove, D. H. Giamalva, D. F. Church, and W. A. Pryor. Autoxidation of methyl linoleate initiated by the ozonide of allylbenzene. *Lipids*, 24(7):609, 1989.
- [184] M. Lazzari and O. Chiantore. Drying and oxidative degradation of linseed oil. *Polymer Degradation and Stability*, 65(2):303–313, 1999.
- [185] P. Fjällström, B. Andersson, C. Nilsson, and K. Andersson. Drying of linseed oil paints: a laboratory study of aldehyde emissions. *Industrial Crops and Products*, 16(3):173–184, 2002.
- [186] F. Van de Voort, A. Ismail, J. Sedman, and G. Emo. Monitoring the oxidation of edible oils by Fourier transform infrared spectroscopy. *Journal of the American Oil Chemists' Society*, 71(3):243–253, 1994.
- [187] L. Goldblatt. The tung industry. II. Processing and utilization. *Economic Botany*, 13(4):343, 1959.
- [188] H. Dannenberg, J. Wagers, and T. Bradley. Frosting and gas-checking of conjugated drying oils. *Industrial & Engineering Chemistry*, 42(8):1594–1599, 1950.
- [189] S. K. Basu, L. Scriven, L. Francis, and A. McCormick. Mechanism of wrinkle formation in curing coatings. *Progress in Organic Coatings*, 53(1):1–16, 2005.
- [190] D. A. Osorio, B. Seifried, P. Moquin, K. Grandfield, and E. D. Cranston. Morphology of cross-linked cellulose nanocrystal aerogels: cryo-templating versus pressurized gas expansion processing. *Journal of Materials Science*, 53(13):9842–9860, 2018.
- [191] J. Bras, D. Viet, C. Bruzzese, and A. Dufresne. Correlation between stiffness of sheets prepared from cellulose whiskers and nanoparticles dimensions. *Carbohydrate Polymers*, 84(1):211–215, 2011.
- [192] Y. Cao, P. Zavattieri, J. Youngblood, R. Moon, and J. Weiss. The relationship between cellulose nanocrystal dispersion and strength. *Construction and Building Materials*, 119:71–79, 2016.

- [193] Y. Yoo and J. P. Youngblood. Tung oil wood finishes with improved weathering, durability, and scratch performance by addition of cellulose nanocrystals. *ACS applied Materials & Interfaces*, 9(29):24936–24946, 2017.
- [194] S. Veigel, E.-M. Lems, G. Gröll, C. Hansmann, T. Rosenau, T. Zimmermann, and W. Gindl-Altmutter. Simple green route to performance improvement of fully bio-based linseed oil coating using nanofibrillated cellulose. *Polymers*, 9(9):425, 2017.
- [195] L. Podgorski and M. Roux. Wood modification to improve the durability of coatings. *Surface Coatings International*, 82(12):590, 1999.
- [196] P. D. Evans, J. G. Haase, A. S. Seman, and M. Kiguchi. The search for durable exterior clear coatings for wood. *Coatings*, 5(4):830–864, 2015.
- [197] R. S. Williams, P. Sotos, and W. C. Feist. Evaluation of several finishes on severely weathered wood. *Journal of Coatings Technology*, 71(895):97–102, 1999.
- [198] J. Van den Bulcke, V. Rijckaert, J. Van Acker, and M. Stevens. Quantitative measurement of the penetration of water-borne coatings in wood with confocal lasermicroscopy and image analysis. *Holz als Roh-und Werkstoff*, 61(4):304–310, 2003.
- [199] Y. Lingappa, A. S. Sussman, and I. A. Bernstein. Effect of light and media upon growth and melanin formation in *aureobasidium pullulans* (de By.) Arn.(= *pullularia pullulans*). *Mycopathologia et Mycologia applicata*, 20(1-2):109–128, 1963.
- [200] E. J. van Nieuwenhuijzen, M. F. Sailer, L. R. Gobakken, O. C. Adan, P. J. Punt, and R. A. Samson. Detection of outdoor mould staining as biofinish on oil treated wood. *International Biodeterioration & Biodegradation*, 105:215–227, 2015.
- [201] R. L. Shogren, Z. Petrovic, Z. Liu, and S. Z. Erhan. Biodegradation behavior of some vegetable oil-based polymers. *Journal of Polymers and the Environment*, 12(3):173–178, 2004.
- [202] L. H. Peeters, H. P. Huinink, B. Voogt, and O. C. Adan. Oil type and cross-linking influence growth of *aureobasidium melanogenum* on vegetable oils as a single carbon source. *MicrobiologyOpen*, 7(6):e00605, 2018.
- [203] E. J. van Nieuwenhuijzen, M. F. Sailer, E. R. van den Heuvel, S. Rensink, O. C. Adan, and R. A. Samson. Vegetable oils as carbon and energy source for *aureobasidium melanogenum* in batch cultivation. *MicrobiologyOpen*, 8(6):e00764, 2019.
- [204] D. Torgeson. *Fungicides: Agricultural and industrial applications; environmental interactions*. Fungicides: An Advanced Treatise. Academic Press, 1967.
- [205] E. S. Jacobson. Pathogenic roles for fungal melanins. *Clinical Microbiology Reviews*, 13(4):708–717, 2000.

- [206] E. J. van Nieuwenhuijzen, J. A. Houbraken, M. Meijer, O. C. Adan, and R. A. Samson. *Aureobasidium melanogenum*: a native of dark biofinishes on oil treated wood. *Antonie van Leeuwenhoek*, 109(5): 661–683, 2016.
- [207] S. Tan and W. Chow. Biobased epoxidized vegetable oils and its greener epoxy blends: a review. *Polymer-Plastics Technology and Engineering*, 49(15):1581–1590, 2010.
- [208] A. Javadi, H. S. Mehr, M. Sobani, and M. D. Soucek. Cure-on-command technology: A review of the current state of the art. *Progress in Organic Coatings*, 100:2–31, 2016.
- [209] P. Glöckner. *Radiation Curing*. American coatings literature. Elsevier Science, 2009. ISBN 9783866309074.
- [210] G. F. White, N. J. Russell, and E. C. Tidswell. Bacterial scission of ether bonds. *Microbiological reviews*, 60(1):216, 1996.
- [211] M. H. Tavassoli-Kafrani, F. R. van de Voort, and J. M. Curtis. The use of atr-ftir spectroscopy to measure changes in the oxirane content and iodine value of vegetable oils during epoxidation. *European Journal of Lipid Science and Technology*, 119(7):1600354, 2017.
- [212] K. Sakai. Routine soil analysis using an Agilent 8800 ICP-QQQ. *Agilent Technologies. Application Note 5991-6409EN*, 2015.
- [213] Y. Shikamori, K. Nakano, N. Sugiyama, and S. Kakut. The ultratrace determination of iodine 129 using the Agilent 8800 triple quadrupole ICP-MS in MS/MS mode. *Agilent Technologies. Application Note 5991-0321EN*, 2015.
- [214] A. Port, C. Cameron, J. Warnon, P. Reynolds, W. Dunk, A. Guy, A. Milne, and A. Marrion. *The Chemistry and Physics of Coatings*. Royal Society of Chemistry, 2007. ISBN 9781847558206.
- [215] J. García-Alcaraz, G. Alor-Hernández, A. Maldonado-Macías, and C. Sánchez-Ramírez. *New Perspectives on Applied Industrial Tools and Techniques*. Management and Industrial Engineering. Springer International Publishing, 2017. ISBN 9783319568713.
- [216] S. Arrhenius. Über die innere Reibung verdünnter wässriger Lösungen. *Zeitschrift für Physikalische Chemie*, 1(1):285–298, 1887.
- [217] J. Wu, Z. Zong, P. Chittavanich, J. Chen, and M. D. Soucek. UV-curable, seed oil-based coatings by cationic photopolymerization: Part 2. *Radtech Report*, 3:30–39, 2013.
- [218] J. Chen, M. D. Soucek, W. J. Simonsick Jr, and R. W. Celikay. Epoxidation of partially norbornylized linseed oil. *Macromolecular Chemistry and Physics*, 203(14):2042–2057, 2002.
- [219] S. Chakrapani and J. V. Crivello. Synthesis and photoinitiated cationic polymerization of epoxidized castor oil and its derivatives. *Journal of Macromolecular Science, Part A: Pure and Applied Chemistry*, 35(1):1–20, 1998.

- [220] L. Yang, J. Yang, J. Nie, and X. Zhu. Temperature controlled cationic photo-curing of a thick, dark composite. *RSC Advances*, 7(7):4046–4053, 2017.
- [221] J. Gooch. *Encyclopedic Dictionary of Polymers*, volume 1 of *Encyclopedic Dictionary of Polymers*. Springer, 2010. ISBN 9781441962461.
- [222] O. Bera, R. Radičević, D. Stoiljković, M. Jovičić, and J. Pavličević. A new approach for the kinetic modeling of free radical bulk polymerization of styrene. *Polymer Journal*, 43(10):826–831, 2011.
- [223] J. Crivello and R. Narayan. Epoxidized triglycerides as renewable monomers in photoinitiated cationic polymerization. *Chemistry of Materials*, 4(3):692–699, 1992.
- [224] S. Thomas, Y. Grohens, and P. Jyotishkumar. *Characterization of polymer blends: miscibility, morphology and interfaces*. John Wiley & Sons, 2014.
- [225] R. A. Ortiz, D. P. López, M. d. L. G. Cisneros, J. C. R. Valverde, and J. V. Crivello. A kinetic study of the acceleration effect of substituted benzyl alcohols on the cationic photopolymerization rate of epoxidized natural oils. *Polymer*, 46(5):1535–1541, 2005.
- [226] G. Sward and J. Koleske. Paint and coating testing manual 15th edition of the gardner-sward handbook. *ASTM International West Conshohocken PA*, page 1026, 2012.
- [227] A. Udagawa, Y. Yamamoto, Y. Inoue, R. Chūjō, T. Sasaki, and I. Ishigaki. Plasticization and antiplasticization effects of sulphonium salt initiator fragments remaining in cycloaliphatic epoxy resins cured by electron beam and ultraviolet irradiation. *Polymer*, 33(2):264–267, 1992.
- [228] United States. National Bureau of Standards. *Building Science Series*. Number 7 in Building Science Series. The Bureau, 1968.
- [229] J. Rinse and W. Wiebols. Swelling of drying oil films in water. *Industrial & Engineering Chemistry*, 29(10):1149–1154, 1937.
- [230] E. L. Kostoryz, K. Dharmala, Q. Ye, Y. Wang, J. Huber, J.-G. Park, G. Snider, J. L. Katz, and P. Spencer. Enzymatic biodegradation of HEMA/bisGMA adhesives formulated with different water content. *Journal of Biomedical Materials Research Part B: Applied Biomaterials*, 88(2):394–401, 2009.
- [231] C. J. Blackwell, K. Haernvall, G. M. Guebitz, M. Groombridge, D. Gonzales, and E. Khosravi. Enzymatic degradation of star poly (ϵ -caprolactone) with different central units. *Polymers*, 10(11):1266, 2018.
- [232] H. S. Azevedo and R. L. Reis. Understanding the enzymatic degradation of biodegradable polymers and strategies to control their degradation rate. *Biodegradable Systems in Tissue Engineering and Regenerative Medicine*, 2005.
- [233] G. Zaikov. Quantitative aspects of polymer degradation in the living body. *Journal of Macromolecular Science-Reviews in Macromolecular Chemistry and Physics*, 25(4):551–597, 1985.

- [234] C.-C. Lin and K. S. Anseth. The biodegradation of biodegradable polymeric biomaterials. In *Biomaterials science*, pages 716–728. Elsevier, 2013.
- [235] S. D. Sommerfeld, Z. Zhang, M. C. Costache, S. L. Vega, and J. Kohn. Enzymatic surface erosion of high tensile strength polycarbonates based on natural phenols. *Biomacromolecules*, 15(3):830–836, 2014.
- [236] K. Shi, J. Jing, L. Song, T. Su, and Z. Wang. Enzymatic hydrolysis of polyester: Degradation of poly(ϵ -caprolactone) by candida antarctica lipase and fusarium solani cutinase. *International Journal of Biological Macromolecules*, 144:183–189, 2020.
- [237] H. P. Austin, M. D. Allen, B. S. Donohoe, N. A. Rorrer, F. L. Kearns, R. L. Silveira, B. C. Pollard, G. Dominick, R. Duman, K. El Omari, et al. Characterization and engineering of a plastic-degrading aromatic polyesterase. *Proceedings of the National Academy of Sciences*, 115(19):E4350–E4357, 2018.
- [238] X. Wu, X. Zhang, S. Yang, H. Chen, and D. Wang. The study of epoxidized rapeseed oil used as a potential biodegradable lubricant. *Journal of the American Oil Chemists' Society*, 77(5):561–563, 2000.
- [239] J. V. Crivello and M. Sangermano. Visible and long-wavelength photoinitiated cationic polymerization. *Journal of Polymer Science Part A: Polymer Chemistry*, 39(3):343–356, 2001.
- [240] J. Crivello and J. Lee. Photosensitized cationic polymerizations using dialkylphenacylsulfonium and dialkyl (4-hydroxyphenyl) sulfonium salt photoinitiators. *Macromolecules*, 14(5):1141–1147, 1981.
- [241] H. Gu, W. Zhang, K. Feng, and D. C. Neckers. Photolysis of ((3-(trimethylsilyl) propoxy) phenyl) phenyliodonium salts in the presence of 1-naphthol and 1-methoxynaphthalene. *Journal of Organic Chemistry*, 65(11):3484–3488, 2000.
- [242] Y. Chen, T. Yamamura, and K. Igarashi. Photosensitization of carbazole derivatives in cationic polymerization with a novel sensitivity to near-UV light. *Journal of Polymer Science Part A: Polymer Chemistry*, 38(1):90–100, 2000.
- [243] E. Nelson, T. Carter, and A. B. Scranton. The role of the triplet state in the photosensitization of cationic polymerizations by anthracene. *Journal of Polymer Science Part A: Polymer Chemistry*, 33(2):247–256, 1995.
- [244] J. Kampmeier and T. W. Nalli. Initiation of cationic polymerization of cyclic ethers by redox radical-chain reactions of onium salts. *Journal of Organic Chemistry*, 59(6):1381–1388, 1994.
- [245] J. V. Crivello and U. Bulut. Curcumin: A naturally occurring long-wavelength photosensitizer for diaryliodonium salts. *Journal of Polymer Science Part A: Polymer Chemistry*, 43(21):5217–5231, 2005.
- [246] S. P. Pappas. Photochemical aspects of UV curing. *Progress in Organic Coatings*, 2(4):333–347, 1974.
- [247] M. Condat, P.-E. Mazeran, J.-P. Malval, J. Lalevée, F. Morlet-Savary, E. Renard, V. Langlois, S. A. Abdalloussi, and D.-L. Versace. Photoinduced curcumin derivative-coatings with antibacterial properties. *RSC Advances*, 5(104):85214–85224, 2015.

- [248] K. Oksman, Y. Aitomäki, A. P. Mathew, G. Siqueira, Q. Zhou, S. Butylina, S. Tanpichai, X. Zhou, and S. Hooshmand. Review of the recent developments in cellulose nanocomposite processing. *Composites Part A: Applied Science and Manufacturing*, 83:2–18, 2016.
- [249] V. Favier, H. Chanzy, and J. Cavaille. Polymer nanocomposites reinforced by cellulose whiskers. *Macromolecules*, 28(18):6365–6367, 1995.
- [250] S. Iwamoto, A. N. Nakagaito, H. Yano, and M. Nogi. Optically transparent composites reinforced with plant fiber-based nanofibers. *Applied Physics A*, 81(6):1109–1112, 2005.
- [251] H. Yano, J. Sugiyama, A. N. Nakagaito, M. Nogi, T. Matsuura, M. Hikita, and K. Handa. Optically transparent composites reinforced with networks of bacterial nanofibers. *Advanced Materials*, 17(2):153–155, 2005.
- [252] B. Fiedler, F. H. Gojny, M. H. Wichmann, M. C. Nolte, and K. Schulte. Fundamental aspects of nano-reinforced composites. *Composites Science and Technology*, 66(16):3115–3125, 2006.
- [253] L. Heux, G. Chauve, and C. Bonini. Nonflocculating and chiral-nematic self-ordering of cellulose microcrystals suspensions in nonpolar solvents. *Langmuir*, 16(21):8210–8212, 2000.
- [254] V. Vardanyan, B. Poaty, G. Chauve, V. Landry, T. Galstian, and B. Riedl. Mechanical properties of UV-waterborne varnishes reinforced by cellulose nanocrystals. *Journal of Coatings Technology and Research*, 11(6):841–852, 2014.
- [255] Y. He, M. Yao, and J. Nie. Shrinkage in UV-curable coatings. In *Protective Coatings*, pages 195–223. Springer, 2017.
- [256] Y. Jian, Y. He, T. Jiang, C. Li, W. Yang, and J. Nie. Volume shrinkage of UV-curable coating formulation investigated by real-time laser reflection method. *Journal of Coatings Technology and Research*, 10(2):231–237, 2013.
- [257] F. Bauer, R. Flyunt, K. Czihal, H. Langguth, R. Mehnert, R. Schubert, and M. R. Buchmeiser. UV curing and matting of acrylate coatings reinforced by nano-silica and micro-corundum particles. *Progress in Organic Coatings*, 60(2):121–126, 2007.
- [258] E. Amerio, P. Fabbri, G. Malucelli, M. Messori, M. Sangermano, and R. Taurino. Scratch resistance of nano-silica reinforced acrylic coatings. *Progress in Organic Coatings*, 62(2):129–133, 2008.
- [259] F. Bauer and R. Mehnert. UV curable acrylate nanocomposites: properties and applications. *Journal of Polymer Research*, 12(6):483–491, 2005.
- [260] F. Bauer, R. Flyunt, K. Czihal, M. R. Buchmeiser, H. Langguth, and R. Mehnert. Nano/micro particle hybrid composites for scratch and abrasion resistant polyacrylate coatings. *Macromolecular Materials and Engineering*, 291(5):493–498, 2006.

- [261] K. Xu, S. Zhou, and L. Wu. Dispersion of γ -methacryloxypropyltrimethoxysilane-functionalized zirconia nanoparticles in UV-curable formulations and properties of their cured coatings. *Progress in Organic Coatings*, 67(3):302–310, 2010.
- [262] S. Zhou and L. Wu. Phase separation and properties of UV-curable polyurethane/zirconia nanocomposite coatings. *Macromolecular Chemistry and Physics*, 209(11):1170–1181, 2008.
- [263] A. Revis and L. J. Cottingham. Radiation curable abrasion resistant coatings from colloidal silica and acrylate monomer, June 30 1992. US Patent 5,126,394.
- [264] A. Kaboorani, N. Auclair, B. Riedl, O. Hosseinaei, and S. Wang. Cellulose nanocrystal (CNC)-based nanocomposites for UV curable high-solid coating systems. *Journal of Coatings Technology and Research*, 14(5):1137–1145, 2017.
- [265] A. Kaboorani, N. Auclair, B. Riedl, and V. Landry. Physical and morphological properties of UV-cured cellulose nanocrystal (CNC) based nanocomposite coatings for wood furniture. *Progress in Organic Coatings*, 93:17–22, 2016.
- [266] X. Kong, L. Zhao, and J. M. Curtis. Polyurethane nanocomposites incorporating biobased polyols and reinforced with a low fraction of cellulose nanocrystals. *Carbohydrate Polymers*, 152:487–495, 2016.
- [267] A. Cataldi, C. E. Corcione, M. Frigione, and A. Pegoretti. Photocurable resin/nanocellulose composite coatings for wood protection. *Progress in Organic Coatings*, 106:128–136, 2017.
- [268] K. Furtak-Wrona, P. Kozik-Ostrówka, K. Jadwiszczak, J. Maigret, V. Aguié-Béghin, and X. Coqueret. Polyurethane acrylate networks including cellulose nanocrystals: a comparison between UV and EB-curing. *Radiation Physics and Chemistry*, 142:94–99, 2018.
- [269] H. Pan, L. Song, L. Ma, and Y. Hu. Transparent epoxy acrylate resin nanocomposites reinforced with cellulose nanocrystals. *Industrial & Engineering Chemistry Research*, 51(50):16326–16332, 2012.
- [270] A. Kaboorani, N. Auclair, B. Riedl, and V. Landry. Mechanical properties of UV-cured cellulose nanocrystal (CNC) nanocomposite coating for wood furniture. *Progress in Organic Coatings*, 104: 91–96, 2017.
- [271] B. Poaty, V. Vardanyan, L. Wilczak, G. Chauve, and B. Riedl. Modification of cellulose nanocrystals as reinforcement derivatives for wood coatings. *Progress in Organic Coatings*, 77(4):813–820, 2014.
- [272] N. Auclair, A. Kaboorani, B. Riedl, V. Landry, O. Hosseinaei, and S. Wang. Influence of modified cellulose nanocrystals (CNC) on performance of bionanocomposite coatings. *Progress in Organic Coatings*, 123:27–34, 2018.
- [273] X. Kong, J. Wolodko, L. Zhao, and J. M. Curtis. The preparation and characterization of polyurethane reinforced with a low fraction of cellulose nanocrystals. *Progress in Organic Coatings*, 125:207–214, 2018.

- [274] A. Pei, J.-M. Malho, J. Ruokolainen, Q. Zhou, and L. A. Berglund. Strong nanocomposite reinforcement effects in polyurethane elastomer with low volume fraction of cellulose nanocrystals. *Macromolecules*, 44(11):4422–4427, 2011.
- [275] Y. Li, H. Ren, and A. J. Ragauskas. Rigid polyurethane foam/cellulose whisker nanocomposites: preparation, characterization, and properties. *Journal of Nanoscience and Nanotechnology*, 11(8):6904–6911, 2011.
- [276] A. I. Cordero, J. I. Amalvy, E. Fortunati, J. M. Kenny, and L. M. Chiacchiarelli. The role of nanocrystalline cellulose on the microstructure of foamed castor-oil polyurethane nanocomposites. *Carbohydrate Polymers*, 134:110–118, 2015.
- [277] A. K. Mishra, D. Chattopadhyay, B. Sreedhar, and K. Raju. FT-IR and XPS studies of polyurethane-urea-imide coatings. *Progress in Organic Coatings*, 55(3):231–243, 2006.
- [278] J. Mattia and P. Painter. A comparison of hydrogen bonding and order in a polyurethane and poly(urethane-urea) and their blends with poly(ethylene glycol). *Macromolecules*, 40(5):1546–1554, 2007.
- [279] Y. Tien and K. Wei. Hydrogen bonding and mechanical properties in segmented montmorillonite/polyurethane nanocomposites of different hard segment ratios. *Polymer*, 42(7):3213–3221, 2001.
- [280] R. N. Haward. *The physics of glassy polymers*. Springer Science & Business Media, 2012.
- [281] W. Grellmann and B. Langer. *Deformation and Fracture Behaviour of Polymer Materials*. Springer Series in Materials Science. Springer International Publishing, 2017. ISBN 9783319418797.
- [282] A. International and S. Lampman. *Characterization and Failure Analysis of Plastics*. ASM International, 2003. ISBN 9781615030736.
- [283] G. Shkapenko, G. Gmitter, and E. Gruber. Mechanism of the water-isocyanate reaction. *Industrial & Engineering Chemistry*, 52(7):605–608, 1960.
- [284] J. Florio and D. Miller. *Handbook Of Coating Additives*. CRC Press, 2004. ISBN 9781482276671.
- [285] L. Burak. Ensuring proper adhesion of UV-curable coatings to plastic substrates. *Paint & Coatings Industry*, 2003.
- [286] I. D. Dobson. Life cycle assessment for painting processes: putting the voc issue in perspective. *Progress in Organic Coatings*, 27(1-4):55–58, 1996.
- [287] B. Ellis and R. Smith. Polymers: A property database, 2019. Data retrieved from applications citing "coatings", <http://poly.chemnetbase.com/>.
- [288] National Center for Biotechnology Information. Pubchem compound summary for CID 44263835, nitrocellulose, 2020. URL <https://pubchem.ncbi.nlm.nih.gov/compound/Nitrocellulose>. Retrieved August 24.

- [289] P. R. Resnick and W. H. Buck. Teflon of amorphous fluoropolymers. *Modern Fluoropolymers*, pages 397–419, 1997.
- [290] M. R. Schilling. The glass transition of materials used in conservation. *Studies in Conservation*, 34(3): 110–116, 1989.
- [291] H. Weinberger and W. H. Gardner. Chemical composition of shellac. *Industrial & Engineering Chemistry*, 30(4):454–458, 1938.
- [292] S. Zumbühl, R. Knochenmuss, S. Wülfert, F. Dubois, M. J. Dale, and R. Zenobi. A graphite-assisted laser desorption/ionization study of light-induced aging in triterpene dammar and mastic varnishes. *Analytical Chemistry*, 70(4):707–715, 1998.
- [293] W. Eigel, J. Butler, C. Ernstrom, H. Farrell Jr, V. Harwalkar, R. Jenness, and R. M. Whitney. Nomenclature of proteins of cow’s milk: fifth revision. *Journal of Dairy Science*, 67(8):1599–1631, 1984.
- [294] L. Cox. *Ultraviolet and electron beam (UV/EB) cured coatings, inks and adhesives*. DIANE Publishing, 2001. ISBN 9781428901285.
- [295] G. Kandhola, A. Djioleu, K. Rajan, N. Labbé, J. Sakon, D. J. Carrier, and J.-W. Kim. Maximizing production of cellulose nanocrystals and nanofibers from pre-extracted loblolly pine kraft pulp: a response surface approach. *Bioresources and Bioprocessing*, 7:1–16, 2020.
- [296] M. Rajinipriya, M. Nagalakshmaiah, M. Robert, and S. Elkoun. Importance of agricultural and industrial waste in the field of nanocellulose and recent industrial developments of wood based nanocellulose: a review. *ACS Sustainable Chemistry & Engineering*, 6(3):2807–2828, 2018.
- [297] L. Neufeld, F. Stassen, R. Sheppard, and T. Gilman. The new plastics economy: rethinking the future of plastics. In *World Economic Forum*, volume 7, 2016.
- [298] N. Karak. *Vegetable Oil-Based Polymers: Properties, Processing and Applications*. Woodhead Publishing in materials. Elsevier Science, 2012. ISBN 9780857097149.
- [299] B. Ruffino, A. Farina, D. Dalmazzo, G. Blengini, M. Zanetti, and E. Santagata. Cost analysis and environmental assessment of recycling paint sludge in asphalt pavements. *Environmental Science and Pollution Research*, pages 1–11, 2020.
- [300] G. Salihoglu and N. K. Salihoglu. A review on paint sludge from automotive industries: Generation, characteristics and management. *Journal of Environmental Management*, 169:223–235, 2016.
- [301] P. J. Dolan, R. G. Lampo, and J. C. Dearborn. *Concepts for Reuse and Recycling of Construction and Demolition Waste*. DIANE Publishing, 1999. ISBN 9781428912007.
- [302] M. C. Karlsson, Z. Abbas, R. Bordes, Y. Cao, A. Larsson, P. Taylor, and B.-M. Steenari. Characterisation of silicon, zirconium and aluminium coated titanium dioxide pigments recovered from paint waste. *Dyes and Pigments*, 162:145–152, 2019.

- [303] X. Yang, S. Zhang, and W. Li. The performance of biodegradable tung oil coatings. *Progress in Organic Coatings*, 85:216–220, 2015.
- [304] Q. Wang, G. Chen, Y. Cui, J. Tian, M. He, and J.-W. Yang. Castor oil based biothiol as a highly stable and self-initiated oligomer for photoinitiator-free UV coatings. *ACS Sustainable Chemistry & Engineering*, 5(1):376–381, 2017.
- [305] M. Sangermano, L. Vescovo, N. Pepino, A. Chiolerio, P. Allia, P. Tiberto, M. Coisson, L. Suber, and G. Marchegiani. Photoinitiator-free UV-cured acrylic coatings containing magnetite nanoparticles. *Macromolecular Chemistry and Physics*, 211(23):2530–2535, 2010.
- [306] F. Bauer, U. Decker, S. Naumov, and C. Riedel. UV curing and matting of acrylate nanocomposite coatings by 172 nm excimer irradiation, part 2. *Progress in Organic Coatings*, 69(3):287–293, 2010.
- [307] M. A. Lago, A. Rodriguez-Bernaldo de Quiros, R. Sendón, J. Bustos, M. T. Nieto, and P. Paseiro. Photoinitiators: a food safety review. *Food Additives & Contaminants: Part A*, 32(5):779–798, 2015.
- [308] R. Liu, Y. Lin, F. Hu, R. Liu, T. Ruan, and G. Jiang. Observation of emerging photoinitiator additives in household environment and sewage sludge in china. *Environmental Science & Technology*, 50(1):97–104, 2016.
- [309] J. Brahney, M. Hallerud, E. Heim, M. Hahnenberger, and S. Sukumaran. Plastic rain in protected areas of the United States. *Science*, 368(6496):1257–1260, 2020.
- [310] S. Hamm, C. Sherrington, O. Jamieson, M. Hickman, P. Kershaw, A. Bapasola, and G. Cole. Investigating options for reducing releases in the aquatic environment of microplastics emitted by (but not intentionally added in) products. *Report for DG ENV EC*, 2018.
- [311] J. Boucher and D. Friot. *Primary microplastics in the oceans: a global evaluation of sources*. IUCN Gland, Switzerland, 2017.
- [312] T. Brock, M. Groteklaes, and P. Mischke. *European Coatings Handbook*. Coatings compendia. Vincentz, 2000. ISBN 9783878705598.
- [313] The Rot Doctor, Inc. Penetration test: Ours vs. theirs, 2020. URL <https://www.rotdoctor.com/test/penetration.html>. Accessed: 2020-01-30.
- [314] EPA. Acid digestion of oils for metals analysis by atomic absorption or icp spectrometry. test methods for evaluating solid waste, physical/chemical methods. method 3031, 1996. URL <https://www.epa.gov/sites/production/files/2015-12/documents/3031.pdf>. Accessed: 2020-07-19.
- [315] F. A. Gobas, W. de Wolf, L. P. Burkhard, E. Verbruggen, and K. Plotzke. Revisiting bioaccumulation criteria for POPs and PBT assessments. *Integrated Environmental Assessment and Management: An International Journal*, 5(4):624–637, 2009.
- [316] European Chemicals Agency. Registered dossier 27652, 2020. URL <https://echa.europa.eu/registration-dossier/-/registered-dossier/27652/1>. Last modified: 2020-05-25.

-
- [317] C. Decker, B. Elzaouk, and D. Decker. Kinetic study of ultrafast photopolymerization reactions. *Journal of Macromolecular Science, Part A: Pure and Applied Chemistry*, 33(2):173–190, 1996.
- [318] C. Decker. Kinetic study and new applications of UV radiation curing. *Macromolecular Rapid Communications*, 23(18):1067–1093, 2002.
- [319] J. G. Kloosterboer. Network formation by chain crosslinking photopolymerization and its applications in electronics. In *Electronic applications*, pages 1–61. Springer, 1988.
- [320] S.-Y. Zhu, H. Li, X.-M. Zhang, W.-X. Chen, and L.-F. Feng. Synthesis, copolymer composition, and rheological behavior of functionalized polystyrene with isocyanate and amine side groups. *Designed Monomers and Polymers*, 18(3):232–241, 2015.
- [321] C. Decker and A. D. Jenkins. Kinetic approach of oxygen inhibition in ultraviolet- and laser-induced polymerizations. *Macromolecules*, 18(6):1241–1244, 1985.

Appendix A

Appendix Chapter 2

A.1 Materials and methods

A.1.1 Methods

A.1.1.1 Demonstration of penetration and film appearance on wood

In an attempt to visualize the preservation of the drying oil character when using ozonized (20 min) linseed FAME ($\text{FAME}_{\text{oz},20\text{min}}$) in tung oil, wood specimens (cedar, poplar, and spruce) were coated following the standard craftsman practice. The wood surface was sanded (down to 400 grit) and wiped with a damp cloth to raise the wood grain with subsequent sanding thereof. Three oil formulations were compared: pure tung oil, boiled linseed (Recochem Inc., Edmonton, Alberta, CA), and 25 wt% ozonized (20 min) linseed FAME ($\text{FAME}_{\text{oz},20\text{min}}$) in tung oil. The oils were "generously" rubbed onto the wood using a paper towel. After 15 min, excess oil was removed with a paper towel. The oils were allowed to dry for two days as by the manufacturer's direction for the boiled linseed oil, before a second coat was applied in the same manner.

To illustrate the improvement in penetration speed by incorporating the drying agent into tung oil, an approach from a wood preservation company was used [313]. In brief, using a 10 mm drill bit, a hole was drilled in the centre of $(3.5 \times 3.5 \times 1.5) \text{ cm}^3$ spruce specimen, down to approximately one half of the specimen thickness. The cavity was then filled with 0.15 g of the oils and allowed to penetrate at ambient condition. Penetration of the oils into the longitudinal direction of the wood fibres was visually compared as the cross-sectional area filled with oil. The results can be found in A.2.5.

A.2 Results and discussion

A.2.1 Drying agent synthesis

Photographic coverage of the synthesized drying agents is given in Figure A.1. With the increase in polarity and molecular weight, the reaction mixture underwent phase separation as witnessed by an increase in turbidity and eventual deposition of material on the reactor wall. The modified lipids were significantly bleached with increasing duration of ozonolysis and formed clear solutions after solvent evaporation. They were all characterized by a slight fruity/cucumber-like aldehyde odour.

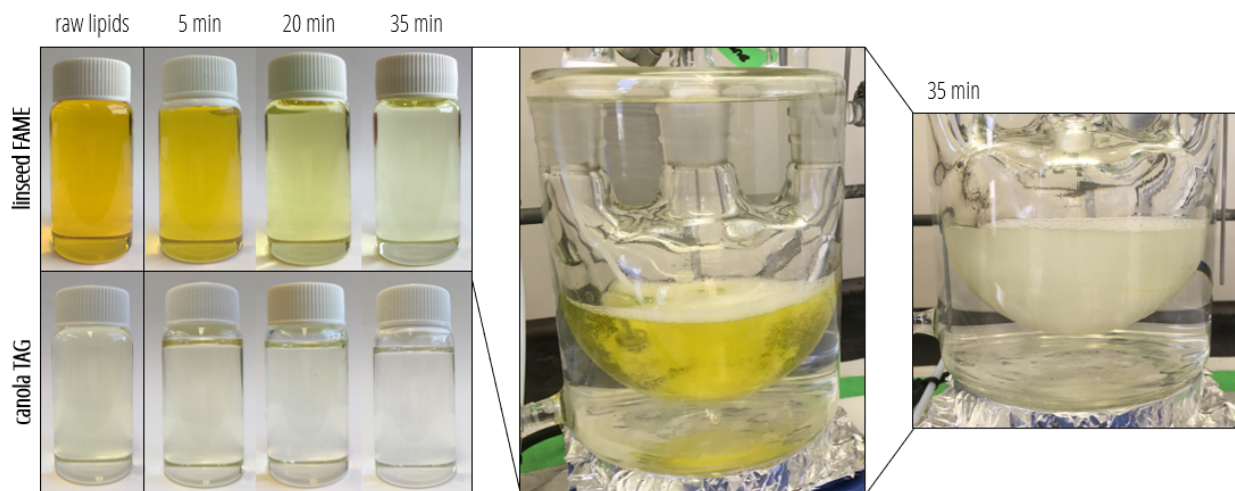


Figure A.1: Images of the ozonized lipids obtained after 5 min, 20 min, and 35 min of ozonolysis and subsequent solvent evaporation. The inset photos show the reaction mixture of hexanes and linseed FAME during the first minutes of ozonolysis and the increase in turbidity and bleaching effect over the course of 35 min of ozonolysis.

A.2.2 Systematic drying agent performance analysis in tung oil

A.2.2.1 Results from the drying time recorder

In Figure A.2, pictures of the coated glass slides are displayed for the Box-Behnken design and pure tung oil. The marks from the needle indicate the different phases for drying.

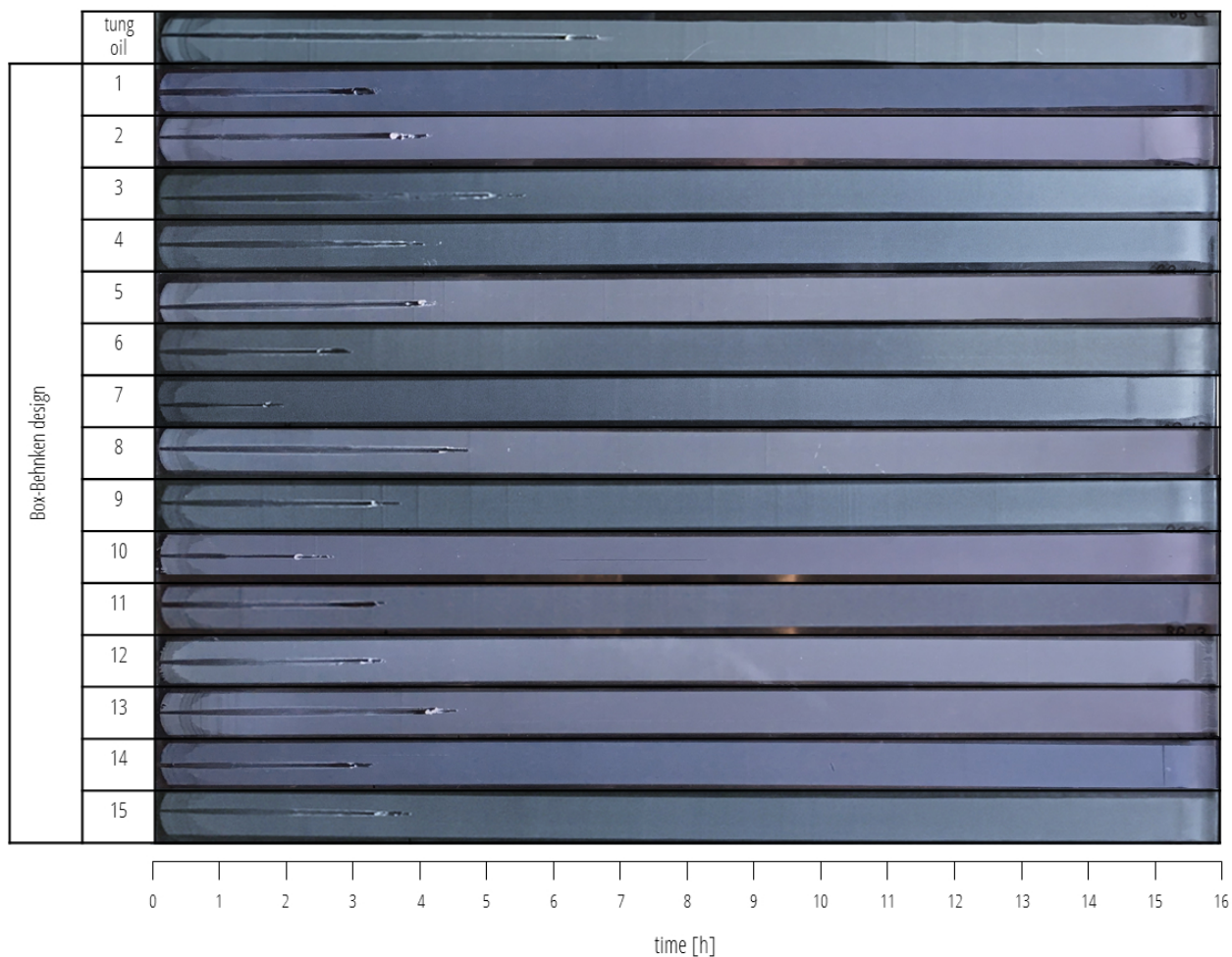


Figure A.2: Drying behaviour at 60 °C monitored for 16 h using a drying time recorder to study the effect of the drying agents on the drying time of tung oil (with CaCO_3 as the filler).

A.2.2.2 Effect of the drying agent on the kinetics of tung oil drying

In Section 2.3.2.2, the diagnostic bands of the spectra were discussed and a potential explanation of drying agent mechanism developed. Figure A.3 shows that the overall changes in the functional groups during the autoxidative drying were not significantly altered by the drying agent, while significant differences in the rates could be observed. For reference, also the individual ATR-FTIR spectra are plotted (Figure A.4).

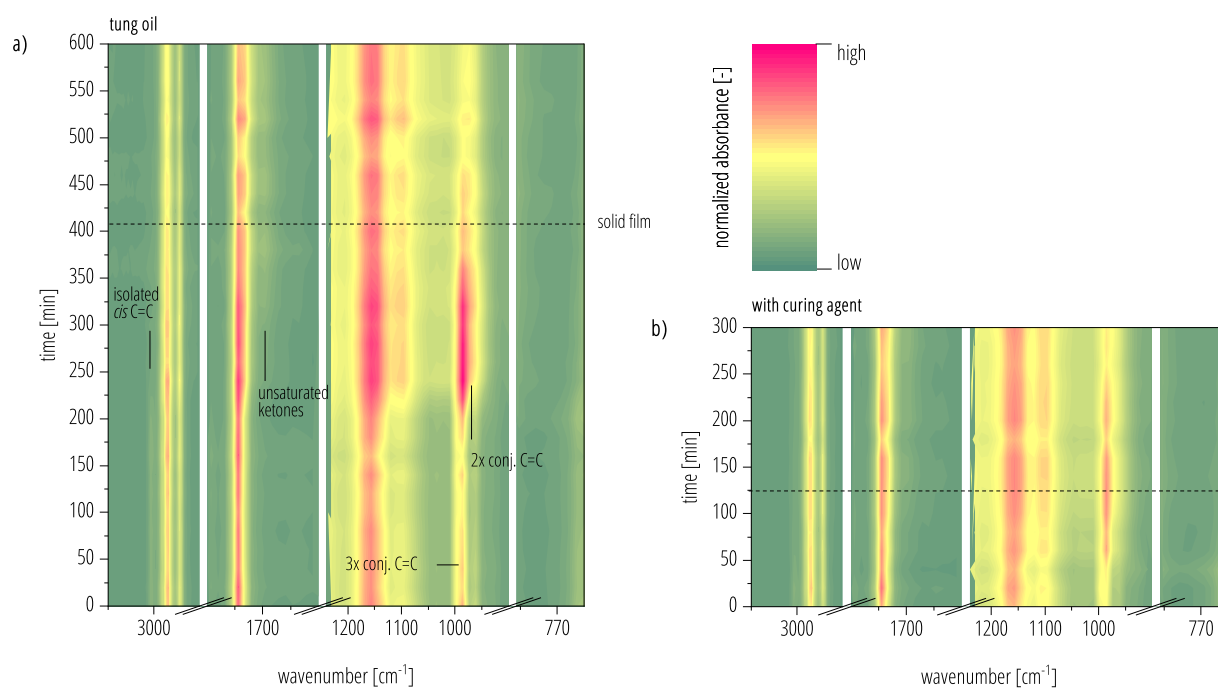


Figure A.3: Contour plot showing the temporal changes in the ATR-FTIR spectra recorded on the top side of the films for **a)** pure tung oil, and **b)** in presence of 25 wt % ozonized (20 min) linseed FAME at 60 °C. Breaks were included in regions of absorbance by the CaCO_3 filler.

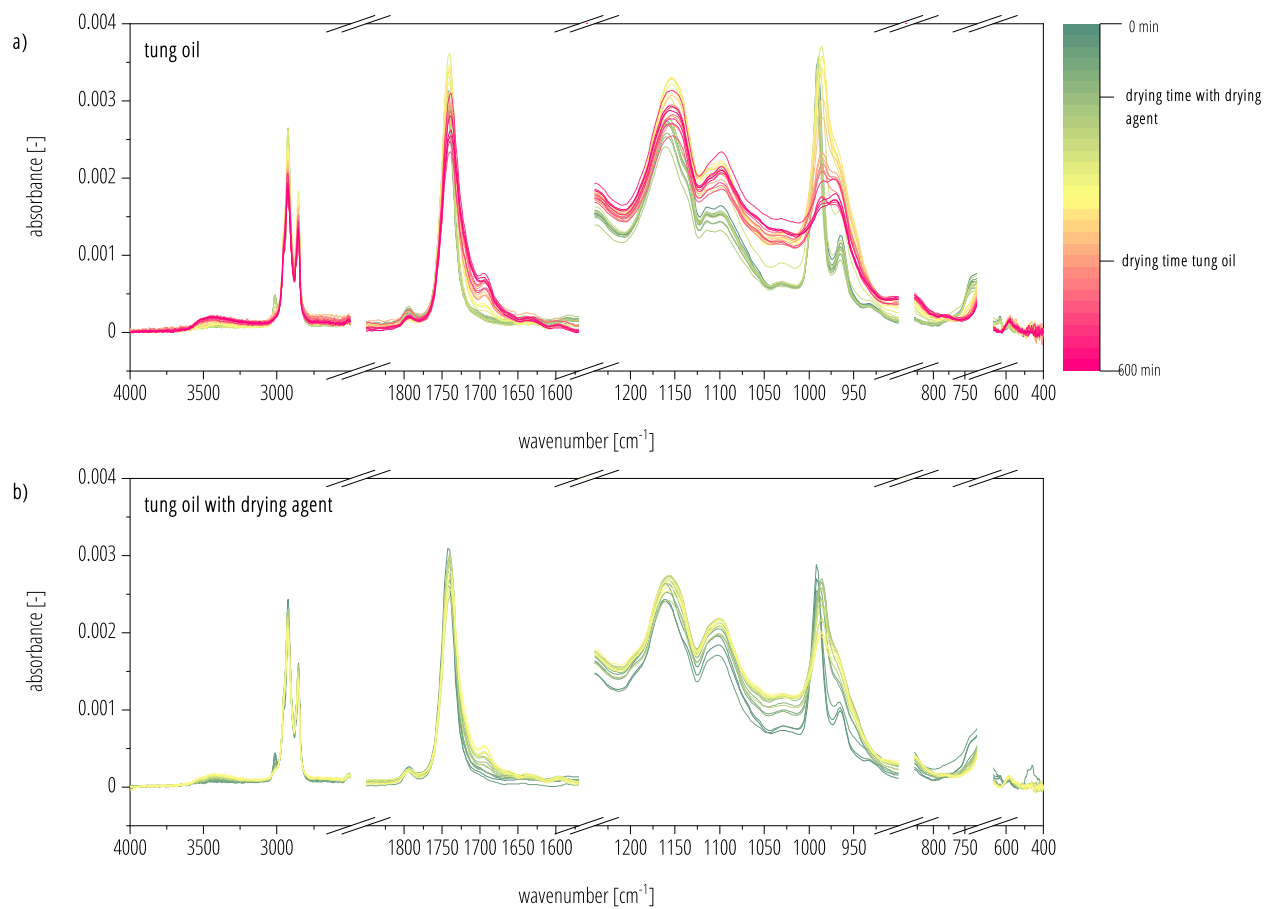


Figure A.4: ATR-FTIR spectra recorded on the top side of the films for **a)** pure tung oil, and **b)** in the presence of 25 wt % ozonized (20 min) linseed FAME. Breaks were included in regions of absorbance by the CaCO₃ filler. The colour map indicates the drying time, and the time after which the spectra were recorded during drying at 60 °C.

A.2.2.3 Structural and chemical changes after film formation

In Figure A.5, major bands associated with the autoxidative drying of tung oil are labelled based on a literature review by De Viguerie et al. [168]. After film formation, significant changes related to the uptake and reaction with O₂ are observed.

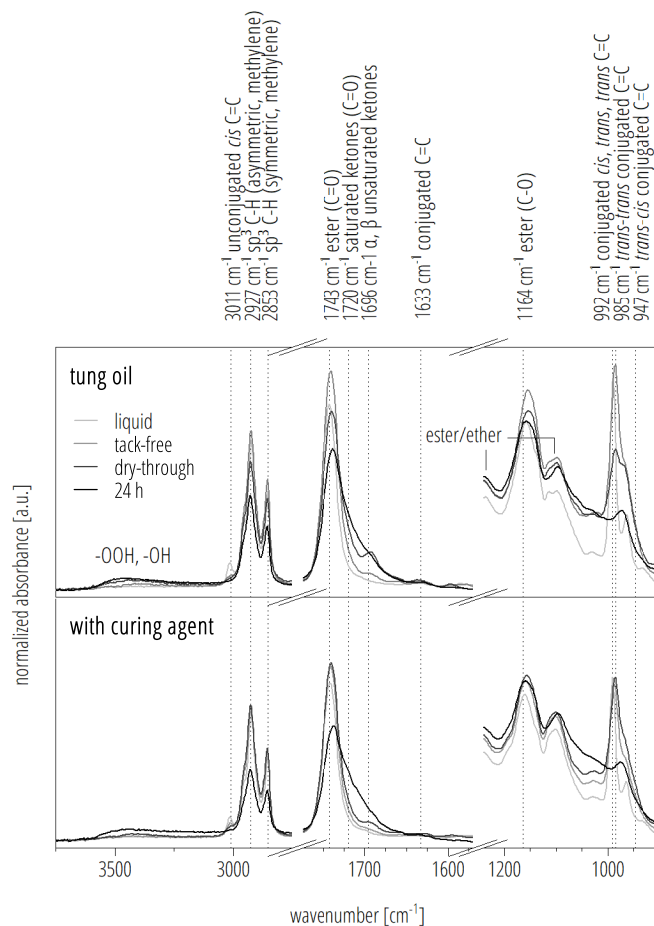


Figure A.5: Changes in the ATR-FTIR spectra of the upper side of a tung oil film during polymerization at 60 °C by addition of 25 wt % ozonized (20 min) linseed FAME. Breaks are inserted for band areas overlapping with CaCO₃, the filler used to make the films. Representative spectra are shown.

A.2.3 Control experiments in cold-pressed linseed oil

While using 5 wt % and 25 wt % ozonized (20 min) linseed FAME in cold-pressed linseed oil resulted in fully dried films over the 96 h drying period at 60 °C, the dry-through time determination using the drying time recorder was not very reproducible and indicated a slight increase in the drying time (Figure A.6). Likely, the films are very soft and keep being ruptured by the needle (with oil residues being ripped off and eventually solidifying on the needle) even after film formation. The transition of the needle track from dislocating a soft film to leave a thinner mark corresponds to the visually observed solidification of the films.

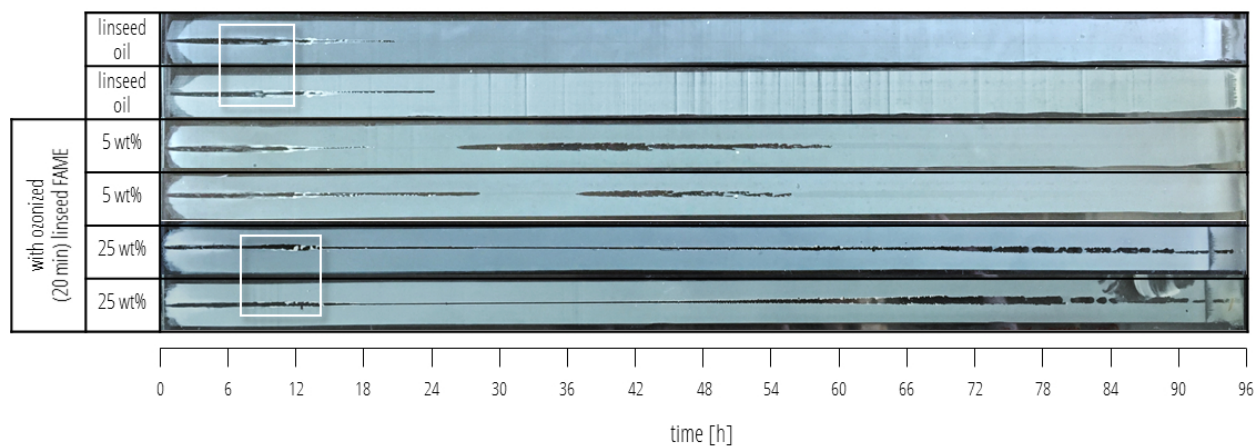


Figure A.6: Drying behaviour at 60 °C monitored for 96 h using a drying time recorder for coated glass slides and effect of ozonized (20 min) linseed FAME on the drying time of cold-pressed linseed oil (with CaCO₃ as the filler). The white boxes indicate the periods of main O₂ absorption as determined by TAG (Figure A.9a)).

The effect of incorporating 25 wt % FAME_{oz,20min} on the kinetics of linseed oil autoxidation at 60 °C is illustrated in Figure A.8. For reference, the individual ATR-FTIR spectra from which the calculations were derived, are shown in Figure A.7.

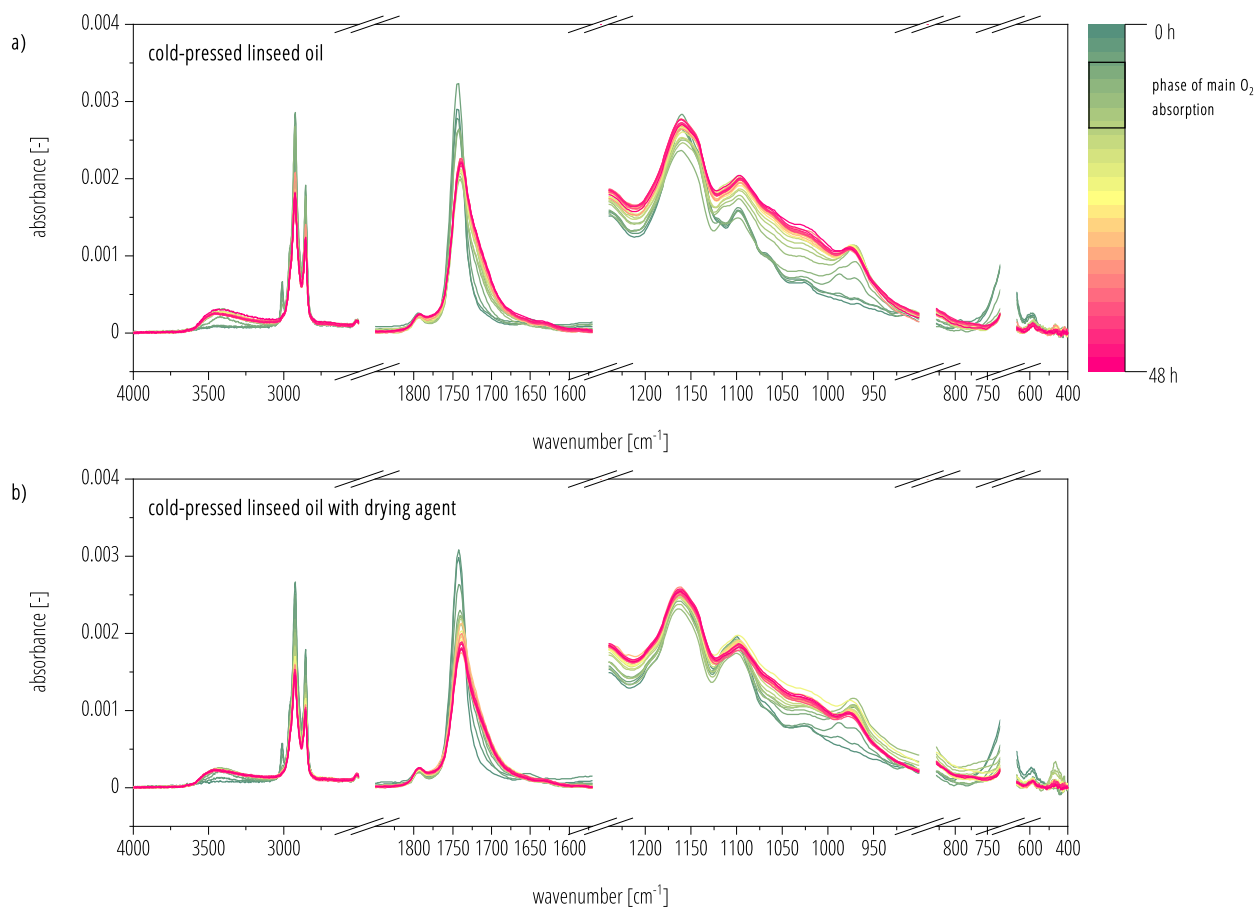


Figure A.7: ATR-FTIR spectra recorded on the top side of the films for **a)** pure cold-pressed linseed oil, and **b)** in the presence of 25 wt % ozonized (20 min) linseed FAME. Breaks were included in regions of absorbance by the CaCO₃ filler. The colour map indicates the time after which the spectra were recorded during drying at 60 °C. Additionally, the time frame for the main O₂ uptake is indicated.

As in tung oil, the drying agent reduced the induction time significantly (ca. 2 h at 60 °C), which indicates the formation of radicals by the drying agents, which would partially compensate for antioxidants present in the drying oils. However, changes in the rates for reactions during autoxidation were less evident. The isomerization of isolated -CH=CH- upon H atom abstraction into conjugated -CH=CH- can be well observed for the band at 985 cm^{-1} for conjugated *trans-trans* -CH=CH- [168] at the very beginning of autoxidative polymerization. From the time intervals studied, it remains inconclusive whether the drying agents resulted in a faster consumption of these conjugated double bonds. Even if addition reaction with the decomposition products of the drying agent with those conjugated -CH=CH- occurred, these cross-linking reactions have to compensate for the absence of the ether linkages in the FAME-based drying agent. However, the data also suggest that FTIR kinetics should be done with shorter sampling intervals at the beginning in order to

better understand the role of $-\text{CH}=\text{CH}-$ and detect potential effects by the drying agent on the kinetics of conjugated double bonds.

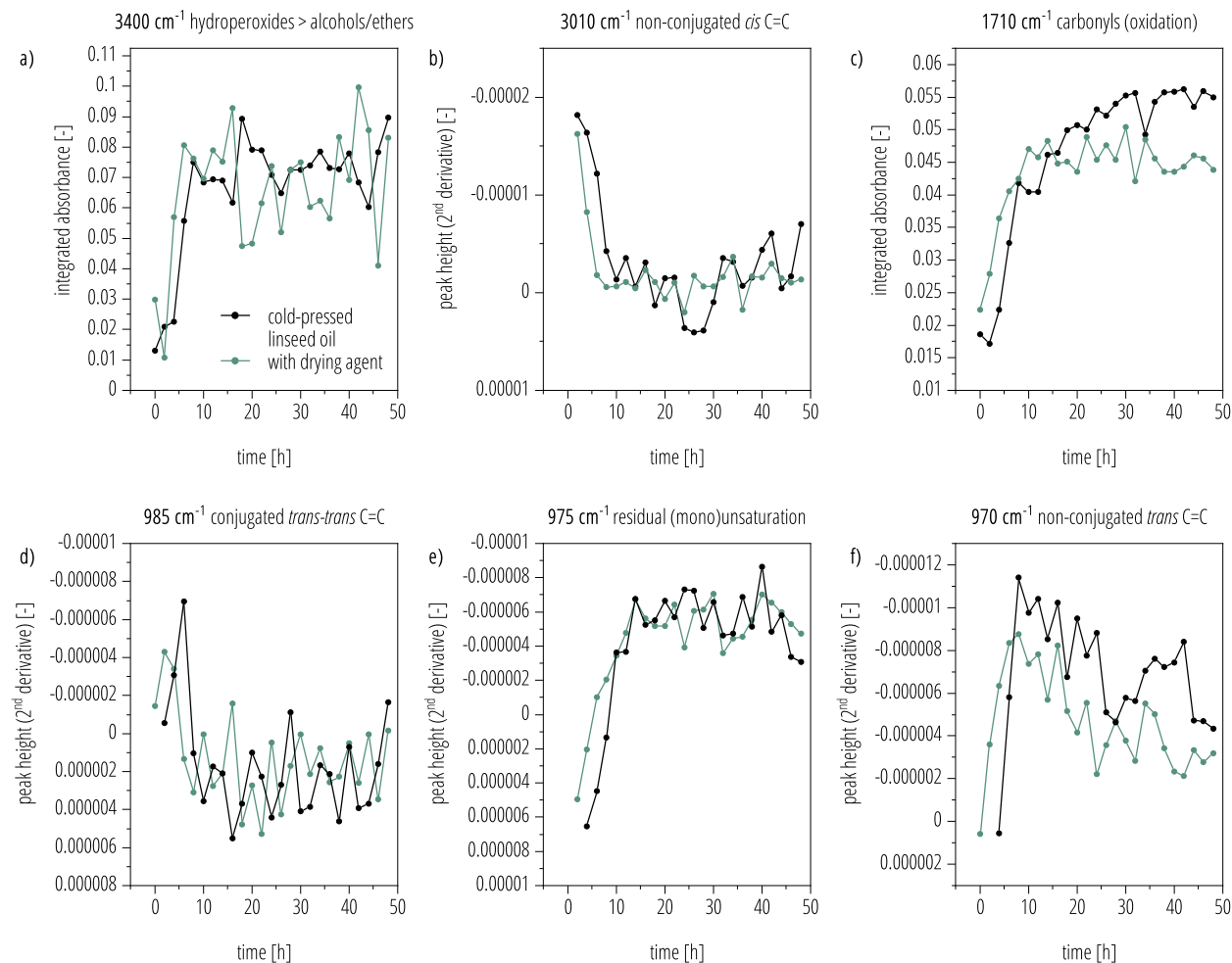


Figure A.8: Drying kinetics analysis using ATR-FTIR ($n = 1$) at 60°C of cold-pressed linseed oil (dark grey) and with 25 wt % ozonized (20 min) linseed FAME (green). **a)** and **c)** Integrated peak area for the following ROI 3400 cm^{-1} (3692 cm^{-1} to 3136 cm^{-1}), and 1710 cm^{-1} (1734 cm^{-1} to 1672 cm^{-1}) based on De Viguerie et al. [168]. **b)** and **d)-f)** Peak height of second derivatives with Norris filter (segment length 1 and gap of 2) for different double bond configurations at 3010 cm^{-1} , 992 cm^{-1} , 985 cm^{-1} , and 947 cm^{-1} .

Data comparison with TGA (Figure A.9a)) showed that solidification occurs shortly after the main O_2 absorption. Despite the shorter induction time in the presence of the drying agent, the O_2 absorption is slightly delayed and occurs over a longer period of time when the drying agent is added. As observed in tung oil, the drying agents reduced the net uptake of O_2 , which was discussed to result from the lower abundance of radicals reacting with O_2 to participate in autoxidation.

DSC analysis (Figure A.9b)) showed that the T_g for the films with 25 wt % drying agent kept increasing during the first 38 h, while pure cold-pressed linseed oil films became soon stable with regard to their T_g . In fact, the drying agent caused the T_g to rise for long after the main O_2 absorption occurred, which is also reflected by the increasing film damage of the needle as it kept moving through the soft but hardening films.

In comparison with the observations from the experiments conducted with tung oil, the lower propensity of the drying agent decomposition products to abstract H atoms compared to direct radical addition to conjugated $-CH=CH-$, was considered to be the most plausible explanation for the difference in reactivity of the two oils compared. While FAME_{oz} could be used as a reactive diluent in linseed oil as well, the use of conjugated FAME is likely more useful as it may allow to increase polymerization rate due to the higher abundance of conjugated $-CH=CH-$ during the autoxidative polymerization. For alkyd resins, this has already been proven (see publication by Biermann et al. [128]).

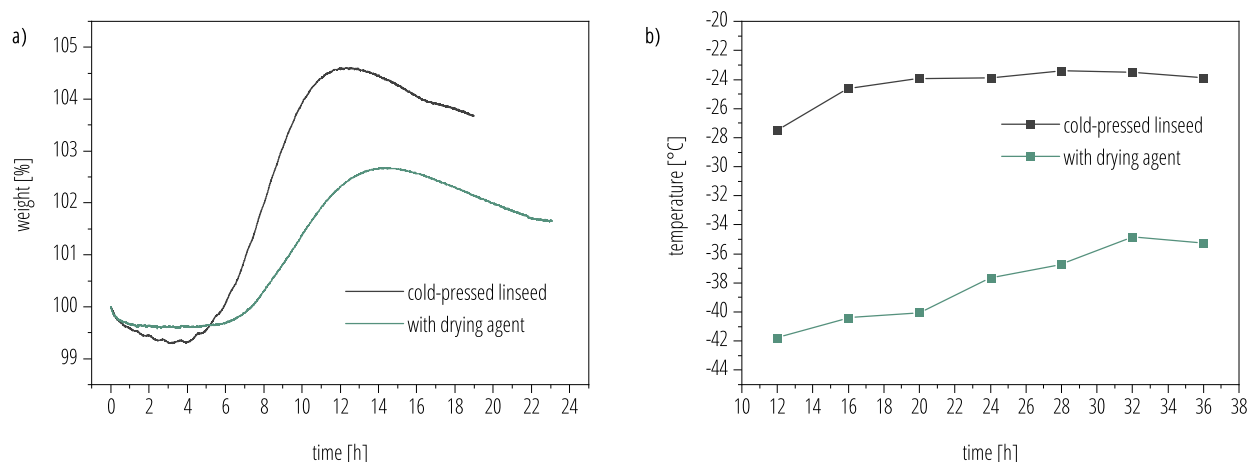


Figure A.9: **a)** Percentage weight change over time recorded by TGA for cold-pressed linseed oil and a mixture with 25 wt % ozonized (20 min) linseed FAME, and $CaCO_3$ as filler at 60 °C. Representative TGA traces are shown. **b)** Effect of 25 wt % ozonized (20 min) linseed FAME in cold-pressed linseed oil on T_g ($n = 1$) after film formation and continued drying at 60 °C.

A.2.4 Performance beyond the Box-Behnken design boundaries

A.2.4.1 Effect on tung oil at room temperature

Ozonized linseed FAME was also screened as a drying agent in tung oil at room temperature. As can be seen in Figure A.10, the dry-through time cannot be determined reproducibly. On average, incorporation of 5 wt % and 25 wt % FAME_{oz,20min} resulted in a slight reduction of the dry-through time but the effect was less than 50 % of what was observed at 60 °C.

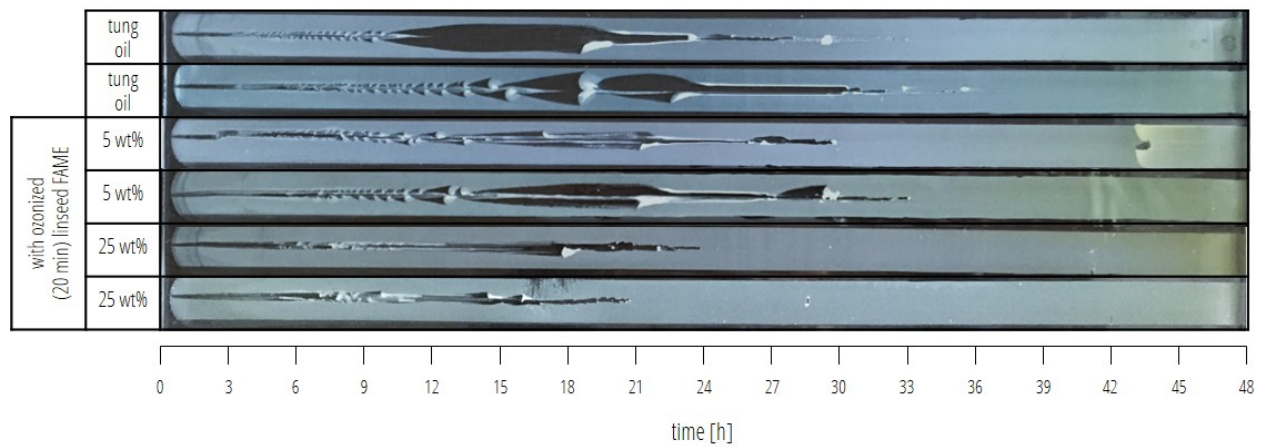


Figure A.10: Drying behaviour at 25 °C and 20 % rel. humidity monitored for 48 h using a drying time recorder for coated glass slides, and the effect of ozonized (20 min) linseed FAME on the drying time of tung oil (with CaCO_3 as the filler).

A.2.5 Demonstration of penetration and film appearance on wood

For visualization purposes only, double coated wood specimen were prepared as outlined in A.1.1.1. As shown in Figure A.11, in the short term, no obvious visual or tactile differences were observed between the different drying oils. However, the anticipated penetration speed increase was demonstrated qualitatively. In both cases, the oil solidified before fully penetrating away from the cavity.

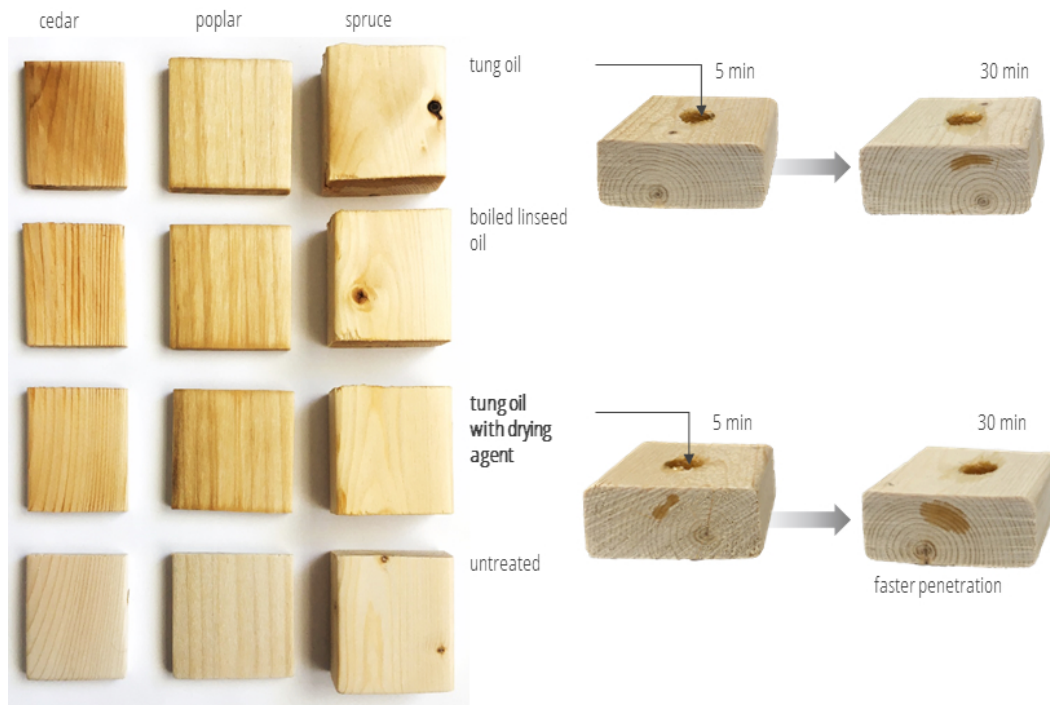


Figure A.11: Incorporation of the drying agent (25 wt %, ozonized (20 min) linseed FAME) into tung oil did not alter the overall appearance based on visual inspection in the short term when applied as two coats on cedar, poplar, and spruce specimen when compared to pure tung oil and boiled linseed oil. As expected from the reduced viscosity, the drying agent was shown to speed up the penetration of tung oil in a spruce wood specimen.

A.2.6 Statistics

A.2.6.1 Box-Behnken Design

Model adequacy The accuracy of the following models were tested to fit the results for drying time (Table A.1), viscosity (Table A.2), and T_g (Table A.3): linear, linear + squares, linear + interactions, and full quadratic. Many studies refer to Joglekar and May [167] and name a minimum R^2 of 0.80 for a good fit of a model. The degrees of freedom are abbreviated as *df*.

Table A.1: Adequacy of different models (linear, linear + squares, linear + interactions, and full quadratic) to fit the data for the drying time after a Box-Cox power transformation.

Lack of fit							
source	<i>df</i>	sum of squares	mean square	<i>F</i> value	Prob > <i>F</i>	remarks	
Linear	9	0.58	0.06	20.40	0.0476	significant	
Linear + squares	6	0.26	0.04	13.83	0.0690	not significant	
Linear + interactions	6	0.48	0.08	25.12	0.0388	significant	
Full quadratic	3	0.16	0.05	16.71	0.0570	not significant	
Model summary statistics							
source	<i>df</i>	root mean square of error	<i>R</i> ²	adjusted <i>R</i> ²	residual sums of squares	predicted <i>R</i> ²	remarks
Linear	11	0.23	0.92	0.90	0.59	0.87	-
Linear + squares	8	0.18	0.96	0.93	0.27	0.86	suggested
Linear + interactions	8	0.25	0.94	0.89	0.48	0.80	-
Full quadratic	5	0.18	0.98	0.94	0.16	0.67	overfitting

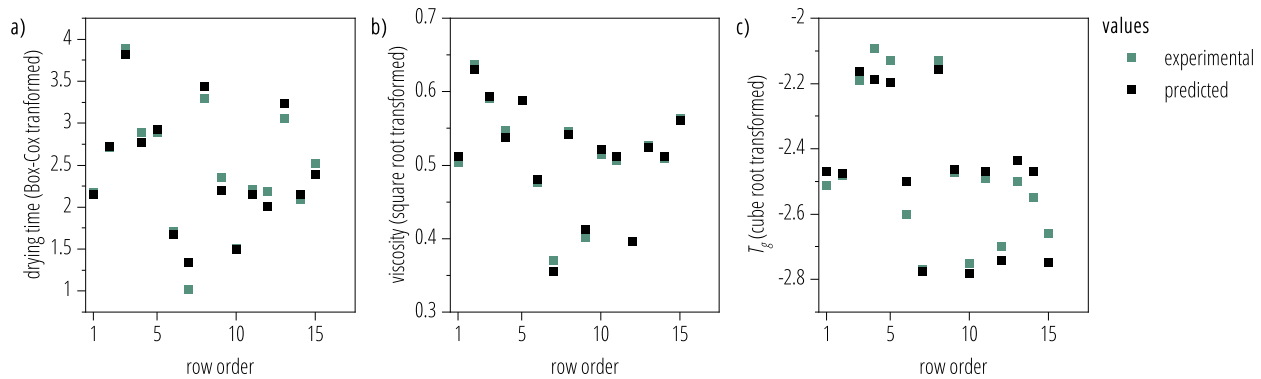
Table A.2: Adequacy of different models (linear, linear + squares, linear + interactions, and full quadratic) to fit the data for the viscosity after square root transformation.

Lack of fit							
source	<i>df</i>	sum of squares	mean square	<i>F</i> value	Prob > <i>F</i>	remarks	
Linear	9	0.00819	9.10152E-4	147.39559	0.00676	significant	
Linear + squares	6	0.00795	0.00132	214.47653	0.00465	significant	
Linear + interactions	6	6.44617E-4	1.07436E-4	17.39887	0.05534	not significant	
Full quadratic	3	3.99467E-4	1.33156E-4	21.56403	0.04464	significant	
Model summary statistics							
source	<i>df</i>	root mean square of error	<i>R</i> ²	<i>R</i> ²	residual sums of squares	predicted <i>R</i> ²	remarks
Linear	11	0.02731	0.89741	0.86943	0.0082	0.8019	-
Linear + squares	8	0.03154	0.90048	0.82584	0.00796	0.63819	-
Linear + interactions	8	0.00906	0.99178	0.98562	6.56967E-4	0.96195	suggested
Full quadratic	5	0.00908	0.99485	0.98558	4.11817E-4	0.92014	-

Table A.3: Adequacy of different models (linear, linear + squares, linear + interactions, and full quadratic) to fit the data for T_g after cube root transformation.

Lack of fit							
source	df	sum of squares	mean square	F value	Prob > F	remarks	
Linear	9	0.04687	0.00521	5.58016	0.16116	not significant	
Linear + squares	6	0.01873	0.00312	3.34375	0.24805	not significant	
Linear + interactions	6	0.0296	0.00493	5.28542	0.16763	not significant	
Full quadratic	3	0.00145	4.83333E-4	0.51786	0.71093	not significant	
Model summary statistics							
source	df	root mean square of error	R^2	adjusted R^2	residual sums of squares	predicted R^2	remarks
Linear	11	0.06657	0.93392	0.9159	0.04874	0.8786	inhomogeneity of variance
Linear + squares	8	0.05073	0.97208	0.95115	0.02059	0.89568	overfitting
Linear + interactions	8	0.06271	0.95734	0.92535	0.03147	0.83086	overfitting
Full quadratic	5	0.02576	0.9955	0.98741	0.00332	0.96302	suggested

The most accurate model was chosen based on non-significance for the lack-of-fit test ($\alpha=0.05$) and least discrepancy between R^2 and predicted R^2 (avoid overfitting by reducing the number of terms added to the model). The drying time was best fitted with a linear+squares regression model. A linear regression with interactions was chosen for the viscosity, while the T_g data were best fitted with a fully quadratic model. A comparison of the experimental data *versus* the predicted values is shown in Figure A.12.

**Figure A.12:** Scatter plots of experimental *versus* predicted values for a) Box-Cox transformed drying time data, b) square root transformed viscosity, and c) cube root transformed T_g .

Coded coefficients The regression coefficients for the models derived for the drying time, viscosity, and T_g are listed in Table A.4, Table A.5, Table A.6, respectively.

The following model for the drying time was derived after a Box-Cox power transformation with the following coded parameters X_1 (ozonolysis time), X_2 (drying agent concentration), and X_3 (FAME_{oz}:TAG_{oz} ratio):

$$\begin{aligned}
 Y' &= (Y^{0.86} - 1)/0.86 \\
 &= 2.2 - 0.3 \cdot X_1 - 0.7 \cdot X_2 - 0.5 \cdot X_3 + 0.1 \cdot X_1^2 + 0.2 \cdot X_2^2 + 0.2 \cdot X_3^2
 \end{aligned}
 \tag{A.1}$$

Table A.4: Coded coefficients for the linear model with squares to fit the drying time data.

linear with squares	value	standard error
(intercept)	2.16253	0.10566
ozonolysis time	-0.25869	0.0647
concentration	-0.71726	0.0647
ratio	-0.52394	0.0647
ozonolysis time*ozonolysis time	0.09432	0.09524
concentration*concentration	0.2164	0.09524
ratio*ratio	0.20276	0.09524

The following model was derived for fitting the viscosity data after a square root transformation:

$$\begin{aligned}
 Y' &= \sqrt{Y} \\
 &= 0.51 + 0.04 \cdot X_1 - 0.05 \cdot X_2 - 0.07 \cdot X_3 + 0.02 \cdot X_1 \cdot X_2 - 0.01 \cdot X_1 \cdot X_3 - 0.04 \cdot X_2 \cdot X_3
 \end{aligned}
 \tag{A.2}$$

Table A.5: Coded coefficients for the linear model with interactions to fit the viscosity data.

linear with interactions	value	standard error
(Intercept)	0.51212	0.00234
ozonolysis time	0.04322	0.0032
concentration	-0.05343	0.0032
ratio	-0.06517	0.0032
ozonolysis time*concentration	0.01953	0.00453
ozonolysis time*ratio	-0.00923	0.00453
concentration*ratio	-0.03769	0.00453

The T_g was fitted by the following model after cube root transformation:

$$\begin{aligned}
 Y' &= \sqrt[3]{Y} \\
 &= -2.47 - 0.02 \cdot X_1 - 0.29 \cdot X_2 - 0.01 \cdot X_3
 \end{aligned}
 \tag{A.3}$$

Table A.6: Coded coefficients for the linear model to fit the T_g data.

linear	value	standard error
(Intercept)	-2.468	0.01719
ozonolysis time	-0.02	0.02353
concentration	-0.2925	0.02353
ratio	-0.0125	0.02353

ANOVA of the regression coefficients The significance of the regression coefficients derived from ANOVA for the experimental data is listed in Table A.7 for the drying time, Table A.8 for the viscosity, and Table A.9 for the T_g .

Table A.7: ANOVA of the linear regression model with quadratic terms for the drying time after the Box-Cox power transformation.

ANOVA	df	sum of squares	mean square	F value	Prob >F	remarks
ozonolysis time	1	0.53536	0.53536	169.84985	0.00584	**
concentration	1	4.11569	4.11569	1305.7454	7.64967E-4	***
ratio	1	2.19607	2.19607	696.7255	0.00143	**
ozonolysis time*ozonolysis time	1	0.01548	0.01548	4.90966	0.15706	ns
concentration*concentration	1	0.14977	0.14977	47.5166	0.0204	*
ratio*ratio	1	0.1518	0.1518	48.16034	0.02014	*
Error	8	0.26795	0.03349			
Lack of fit	6	0.26164	0.04361	13.83488	0.06893	ns
Pure Error	2	0.0063	0.00315			
Total	22	7.70006				

Table A.8: ANOVA of the linear regression model with interactions for the viscosity after square root transformation.

ANOVA	df	sum of squares	mean square	F value	Prob >F	remarks
ozonolysis time	1	0.01494	0.01494	2420.00654	4.12966E-4	***
concentration	1	0.02284	0.02284	3699.18762	2.7022E-4	***
ratio	1	0.03398	0.03398	5502.68332	1.8168E-4	***
ozonolysis time*concentration	1	0.00153	0.00153	247.0209	0.00402	**
ozonolysis time*ratio	1	3.4078E-4	3.4078E-4	55.18801	0.01764	*
concentration*ratio	1	0.00568	0.00568	919.95819	0.00109	**
Error	8	6.56967E-4	8.21209E-5			
Lack of fit	6	6.44617E-4	1.07436E-4	17.39887	0.05534	ns
Pure Error	2	1.23498E-5	6.1749E-6			
Total	22	0.08062				

Table A.9: ANOVA of the linear regression model for the T_g after cube root transformation.

ANOVA	df	sum of squares	mean square	F value	Prob >F	remarks
ozonolysis time	1	0.0032	0.0032	3.42857	0.20528	ns
concentration	1	0.68445	0.68445	733.33929	0.00136	**
ratio	1	0.00125	0.00125	1.33929	0.3667	ns
Error	11	0.04874	0.00443			
Lack of fit	9	0.04687	0.00521	5.58016	0.16116	ns
Pure Error	2	0.00187	9.33333E-4			
Total	25	0.78638				

Interaction plots Interaction effects were only present in the model for the viscosity. All individual and interaction terms were significant (Table A.8 and Figure A.13). The benefit of using FAME_{oz} compared to TAG_{oz} was stronger at higher drying agent concentrations and longer ozonolysis times as a result of elevated oligomerization with increasing ozonolysis time and higher initial molecular weight, which increases the viscosity.

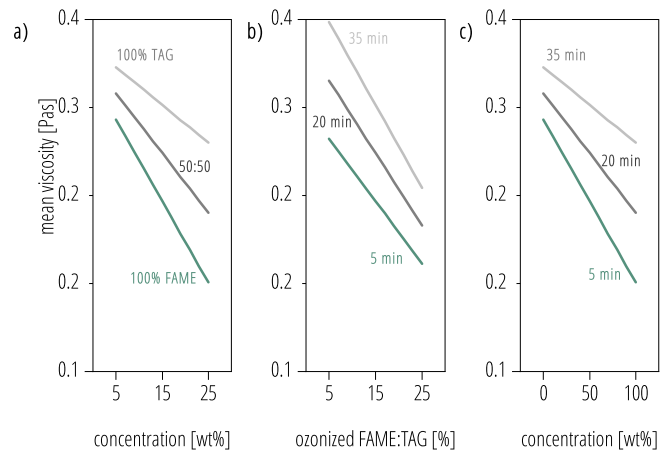


Figure A.13: Interaction plots for the mean viscosity of tung oil with added $\text{FAME}_{\text{oz}}/\text{TAG}_{\text{oz}}$. **a)** The concentration effect is stronger for FAME-based drying agents. **b)** Longer ozonolysis times of TAG results in a bigger disadvantage to reduce the viscosity. **c)** The concentration effect is strongest at short ozonolysis times.

Diagnostic plots for the regression models Reasonable linearity in the normal plots of residuals and random scattering of the residuals was assumed based on the data shown in Figure A.14 for the drying time, Figure A.15 for the viscosity, and Figure A.16 for the T_g .

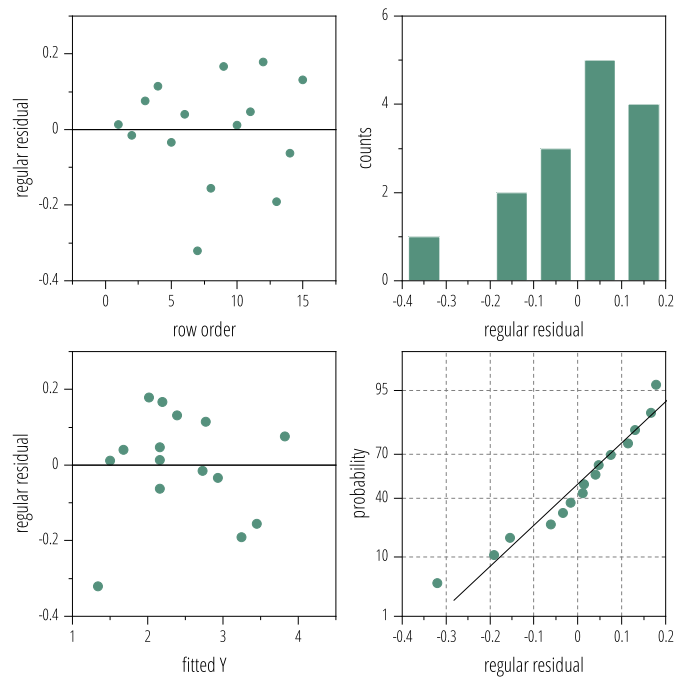


Figure A.14: Diagnostic plots for the regression analysis of the drying time in order to verify the model adequacy.

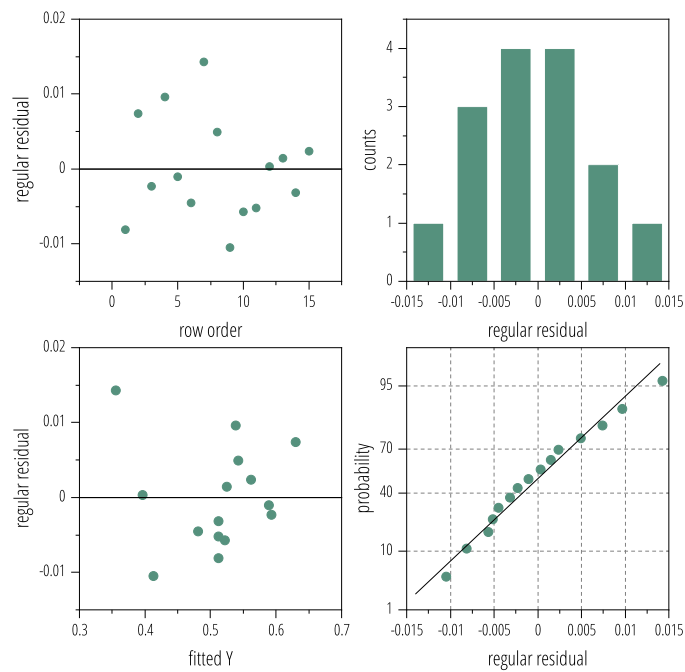


Figure A.15: Diagnostic plots for the regression analysis of the viscosity in order to verify the model adequacy.

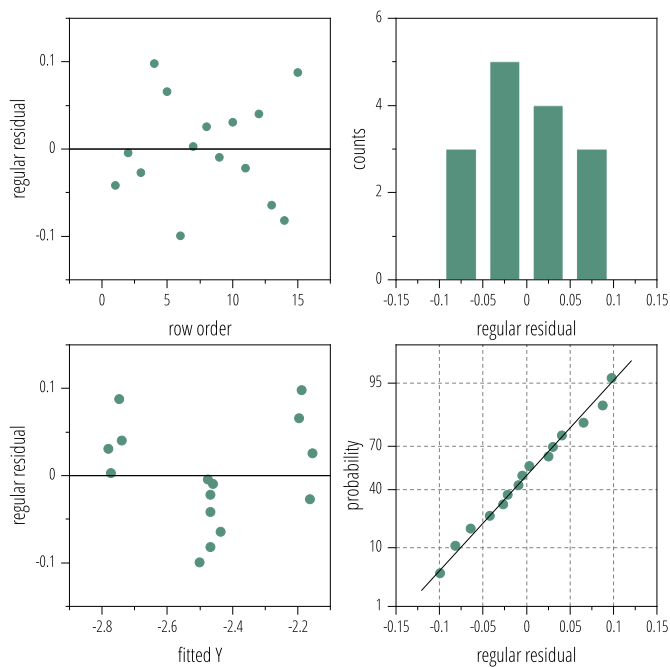


Figure A.16: Diagnostic plots for the regression analysis of the T_g in order to verify the model adequacy.

A.2.6.2 Independent t -tests

Statistical results for the independent t -tests comparing the decomposition enthalpies and temperatures of the drying agents are given in Table A.10 and Table A.11, respectively.

Table A.10: Pair-wise two-tailed independent t -test for the decomposition enthalpy (ΔH_{dec}) of the ozonized lipids ($n = 3$).

time	ozonized oil	ΔH_{dec} [W/g]		t statistics with Welch correction			power	remarks
		M	SD	t value	df	p value		
5 min	linseed FAME	173.06667	1.23423	-2.62896	2.03552	0.11721	0.51457	inconclusive
	canola oil	193.03333	13.09669					
20 min	linseed FAME	636.7	32.51015	6.87018	2.45414	0.01167	0.99834	*
	canola oil	500.53333	11.02648					
35 min	linseed FAME	933.26667	52.14886	-1.75163	2.04996	0.21887	0.27174	inconclusive
	canola oil	986.33333	5.82866					
5 min	linseed FAME	173.06667	1.23423	-24.68332	2.00577	0.00161	1	**
20 min		636.7	32.51015					
20 min	linseed FAME	636.7	32.51015	21.9251	2.63249	4.7013E-4	1	***
5 min	canola oil	193.03333	13.09669					
5 min	linseed FAME	173.06667	1.23423	-51.11954	2.05011	3.24595E-4	1	***
20 min	canola oil	500.53333	11.02648					
5 min	canola oil	193.03333	13.09669	-31.10949	3.88716	8.3092E-6	1	*****
20 min		500.53333	11.02648					
5 min	linseed FAME	173.06667	1.23423	-25.2419	2.00224	0.00156	1	**
35 min		933.26667	52.14886					
35 min	linseed FAME	933.26667	52.14886	23.84532	2.25129	9.4001E-4	1	***
5 min	canola oil	193.03333	13.09669					
20 min	linseed FAME	636.7	32.51015	-8.35879	3.35057	0.00234	0.99995	**
35 min	linseed FAME	933.26667	52.14886					
35 min	linseed FAME	933.26667	52.14886	14.06173	2.17847	0.00353	1	**
20 min	canola oil	500.53333	11.02648					
5 min	linseed FAME	173.06667	1.23423	-236.42849	2.179	7.5975E-6	1	*****
35 min	canola oil	986.33333	5.82866					
5 min	canola oil	193.03333	13.09669	-95.85079	2.76236	6.0008E-6	1	*****
35 min		986.33333	5.82866					
20 min	linseed FAME	636.7	32.51015	-18.33514	2.12844	0.00222	1	**
35 min	canola oil	986.33333	5.82866					
20 min	canola oil	500.53333	11.02648	-67.46427	3.03675	6.35694E-6	1	*****
35 min		986.33333	5.82866					

Table A.11: Pairwise two-tailed independent *t*-test for the peak decomposition temperature of the ozonized lipids ($n = 3$).

time	ozonized oil	decomposition temperature [°C]		<i>t</i> statistics with Welch's correction			power	remarks
		<i>M</i>	<i>SD</i>	<i>t</i> value	<i>df</i>	<i>t</i> value		
5 min	linseed FAME	147.26	0.42	-24.87449	2.11781	0.00119	1	**
	canola oil	153.38	0.07211					
20 min	linseed FAME	145.60667	0.20599	-49.97587	3.82375	1.5833E-6	1	*****
	canola oil	153.23333	0.16563					
35 min	linseed FAME	146.69	1.20528	-12.26331	2.01221	0.00644	1	**
	canola oil	155.23667	0.06658					
5 min	linseed FAME	147.26	0.42	6.12159	2.90957	0.00957	0.99275	**
20 min		145.60667	0.20599					
20 min	linseed FAME	145.60667	0.20599	-61.68967	2.48293	5.09142E-5	1	****
5 min	canola oil	153.38	0.07211					
5 min	linseed FAME	147.26	0.42	-22.91605	2.60738	4.437E-4	1	***
20 min	canola oil	153.23333	0.16563					
5 min	canola oil	153.38	0.07211	1.40625	2.7319	0.26264	0.1936	inconclusive
20 min		153.23333	0.16563					
5 min	linseed FAME	147.26	0.42	0.7735	2.47866	0.50621	0.093	inconclusive
35 min		146.69	1.20528					
35 min	linseed FAME	146.69	1.20528	-9.59672	2.01432	0.01044	1	*
5 min	canola oil	153.38	0.07211					
20 min	linseed FAME	145.60667	0.20599	-1.53456	2.11674	0.25797	0.22091	inconclusive
35 min	linseed FAME	146.69	1.20528					
35 min	linseed FAME	146.69	1.20528	-9.31557	2.07551	0.01005	1	*
20 min	canola oil	153.23333	0.16563					
5 min	linseed FAME	147.26	0.42	-32.48949	2.10047	7.13107E-4	1	***
35 min	canola oil	155.23667	0.06658					
5 min	canola oil	153.38	0.07211	-32.76471	3.97482	5.4979E-6	1	*****
35 min		155.23667	0.06658					
20 min	linseed FAME	145.60667	0.20599	-77.04685	2.4134	3.75665E-5	1	****
35 min	canola oil	155.23667	0.06658					
20 min	canola oil	153.23333	0.16563	-19.43773	2.62996	6.48005E-4	1	***
35 min		155.23667	0.06658					

Appendix B

Appendix Chapter 3

B.1 Materials and methods

B.1.1 Materials

The chemicals listed below were only used for experiments described in the appendix. For the digestion of the boiled linseed oil, sulfuric acid 95%-98%, trace metal grade, potassium permanganate $\geq 99.0\%$, and hydrogen peroxide 30% (certified ACS) were purchased from Fisher Scientific (Ontario, CA). HPLC grade acetonitrile was obtained from Fisher Scientific. ACS grade ($\geq 99.5\%$) acetone was purchased from Fisher Scientific Company (Ottawa, ON, Canada). Distilled water and commercial grape juice, instant coffee, and mustard were used for the chemical resistance testing towards household chemicals.

B.1.2 Methods

B.1.2.1 Identification of the metal drier in boiled linseed oil

In order to identify the main drying agent in the commercial boiled linseed oil, the liquid oil was digested according to the EPA method 3031 [314]. A sample of 0.1 g of oil was taken and mixed with 0.1 g of potassium permanganate. Thereafter, the sample was continuously amended with acid: 0.2 mL of sulfuric acid, 0.4 mL of nitric acid, and 2 mL of hydrochloric acid. The mixtures were kept at 120 °C until the liquid turned yellow. Blanks were used to account for trace metals in chemicals added. Partial polymerization was observed, leading to some transparent residues. The digested samples were then diluted with ultrapure water and analyzed by inductively coupled plasma mass spectrometry/mass spectrometry (ICP-MS/MS) as described in Section 3.2.2.6.

B.1.2.2 ECOSAR ecotoxicity characterization

In order to estimate potential risks related to the leaching of the cationic photoinitiator during hydrolytic film degradation, the ECOSAR (Application 2.0) program by the United States Environmental Protection Agency was used as a computerized predictive system to estimate aquatic toxicity. The toxicological profile was complemented by consulting the ECOTOX Knowledgebase (United States Environmental Protection Agency). The concern concentration (CC) was calculated as the lowest chronic value (ChV) divided by an uncertainty factor of 10 rounded to one significant digit. The following photoinitiator components were considered: ArI with R₁ (C10), ArI with R₃ (C13), and HMTX_n (see Figure 3.2).

B.1.2.3 UV-VIS spectroscopy

UV-VIS spectroscopy (Thermo Scientific Evolution 60S UV-Visible Spectrophotometer) was used to determine the absorption spectra for the cationic photoinitiator ($1 \cdot 10^{-4}$ M) and curcumin ($3 \cdot 10^{-5}$ M) in acetonitrile.

B.1.2.4 Hot and cold check resistance

The ability of the finishes to withstand cycles of hot and cold temperatures for prolonged periods was tested following the industry protocols by ANSI/KCMA A161.1-2012. Two coats were applied to poplar wood specimen ($(36 \times 36 \times 5)$ mm³) in a same manner as described in Section 3.2.2.5.

B.1.2.5 Effect of household chemicals

The chemical resistance towards substances typically found in households was studied using a spot test (covered) following the ASTM D1308-02 method at 15 min, 1 h, and 16 h intervals. The studied liquids were distilled water (ambient temperature), acetone (ambient temperature), mustard (ambient temperature), coffee (80 °C), and grape juice (ambient temperature).

B.2 Results and discussion

B.2.1 Boiled linseed oil digestion

Digestion of the boiled linseed oil suggests that cobalt was the main drier with an elemental concentration of 65 µg per g oil (see Table B.1).

Table B.1: Composition of metal elements in the boiled linseed oil resin ($n = 2$).

element	concentration [$\mu\text{g per g oil}$]	<i>SD</i>
B	ND	NA
Na	ND	NA
Mg	ND	NA
Al	0.298	0.184
Si	ND	NA
Ti	7.56	0.234
P	ND	NA
Ca	3.42	0.811
V	ND	NA
Fe	ND	NA
Co	65.0	0.533
Ni	ND	NA
Cu	ND	NA
Zn	ND	NA
Cr	0.371	0.0441
As	0.00577	0.00499
Se	ND	NA
Br	ND	NA
Sr	0.0202	0.0102
Mo	0.0539	0.00400
Cd	0.469	0.0273
Ba	ND	NA
Ce	0.000525	0.000218
Pb	0.0188	0.000823

B.2.2 ECOSAR ecotoxicity characterization

The used cationic photoinitiator, Silcolease UV Cata 243, is promoted as a low-toxicity catalyst by the manufacturer. Ecotoxicity estimation using ECOSAR (see Table B.2) supports the poor water solubility and therefore low migration in an aqueous environment. Based on the Stockholm convention, all three tested byproducts of the photoinitiator would be considered bioaccumulative due to their $\log K_{OW} > 5$ [315]. With regards to toxicological effects, the anion appears to be of lower concern than the aryl iodine compounds (mostly due to lower water solubility). Chronic and/or acute effects are expected in fish, mysids, green algae, and daphnids. Based on these estimates presented in Table B.2, the concern concentration (CC) was calculated to be $2 \cdot 10^{-5}$ ppb for ArI with R_1 (C10), $3 \cdot 10^{-7}$ ppb for ArI with R_3 (C13), and $3 \cdot 10^{-9}$ ppb for the anion. The results do not account for synergistic effects or degradation products of the those photoinitiator components. In the Registered Dossier 27652 by the European Chemicals Agency [316], reports of preliminary studies on acute aquatic toxicity (daphnid) were submitted. However, the tested concentrations of

(unreacted) photoinitiator were all above the saturation limit (a water solubility range between 0.02 mg L⁻¹ to 0.665 mg L⁻¹ was reported). While the results from ECOSAR are not directly comparable (no interaction), the estimated effect levels for daphnid acute toxicity suggest that no effects at saturation would be observed, which is consistent with the results reported for the ECHA registration dossier. Comparison with possible decomposition products from the photoinitiator indicates a potential higher risk compared to the photoinitiator anion. Overall, this preliminary ecotoxicological characterization shows that the photoinitiator and decomposition products are likely bioaccumulative due to their lipophilicity and that aqueous exposure is therefore not the predominant form of chemical uptake. Furthermore, decomposition products would have to be investigated for potentially increased toxicity.

Table B.2: Ecotoxicity characterization using ECOSAR. Chronic toxicity (long-term exposure) is indicated by the chronic value (ChV), which is defined as the geometric mean between the lowest observed effect level and no observed effect level. * indicates a low concern as no effects at saturation would be observed. † indicates that there are no effects at saturation or effects occur.

property	unit	Arl with R ₁ (C10)		Arl with R ₃ (C13)		superacid HMTX _n		
		effect concentration	ratio of effect concentration: water solubility	effect concentration	ratio of effect concentration: water solubility	effect concentration	ratio of effect concentration: water solubility	
structure	formula (SMILES)	-	c1cc(ccc1C(C)CCCCCCC)I	c1cc(ccc1C(C)CCCCCCC)I		Fc1c(F)c(F)c(c(F)c1(F))B(c2c(F)c(F)c(F)c(F)c2(F))C3=C(F)C(F)=C(F)C(F)=C3(F))C4=C(F)C(F)=C(F)C(F)=C4(F)		
	molecular weight	g mol ⁻¹	344.28	386.36		679.05		
solubility (estimated)	water solubility	mg L ⁻¹	8.882E-4	2.7167E-5		1.0971E-8		
	log K _{OW}	-	8.054	9.5272		11.293		
organic module result (prediction)	fish (LC50, 96 h)	mg L ⁻¹	0.00103	1.16412*	5.51337E-5	2.02944*	2.51453E-6	229.19774†
	fish (ChV)	mg L ⁻¹	0.00103	1.156*	6.27275E-5	2.30896*	3.36749E-6	306.94426†
	fish SW (LC50, 96 h)	mg L ⁻¹	0.00771	8.68549*	8.27118E-4	30.4457†	8.71334E-5	7942.15751†
	fish SW (ChV)	mg L ⁻¹	1.95414E-4	0.22001	1.22336E-5	0.45031	6.76263E-7	61.64094†
	daphnid (LC50, 48 h)	mg L ⁻¹	4.74443E-4	0.53416	4.23247E-5	1.55794*	3.57688E-6	326.03024†
	daphnid (ChV)	mg L ⁻¹	0.00701	7.89783*	0.00102	37.48047†	1.54223E-4	14057.34664†
	green algae (EC50, 96 h)	mg L ⁻¹	0.00135	1.51963*	7.26085E-5	2.67267*	3.34671E-6	305.05071†
	green algae (ChV)	mg L ⁻¹	1.6607E-5	0.0187	3.29295E-7	0.01212	4.58899E-9	0.41828
	mysid (LC50, 96 h)	mg L ⁻¹	0.00591	6.65014*	7.81271E-4	28.75809†	1.05858E-4	9648.84969†
	mysid SW (ChV)	mg L ⁻¹	2.387E-7	2.68746E-4	3.05868E-9	1.12588E-4	2.52585E-11	0.0023
earthworm (LC50, 14 d)	mg L ⁻¹	141.03441	158786.771†	111.33335	4098109.83914†	128.35559	1.16995E10†	

B.2.3 UV-VIS spectroscopy

UV-VIS spectroscopy revealed that the cationic photoinitiator has one absorption maximum in the UV-B range (approx. 288 nm) in acetonitrile. The absorption maximum of curcumin is in the visible range (approx. 418 nm).

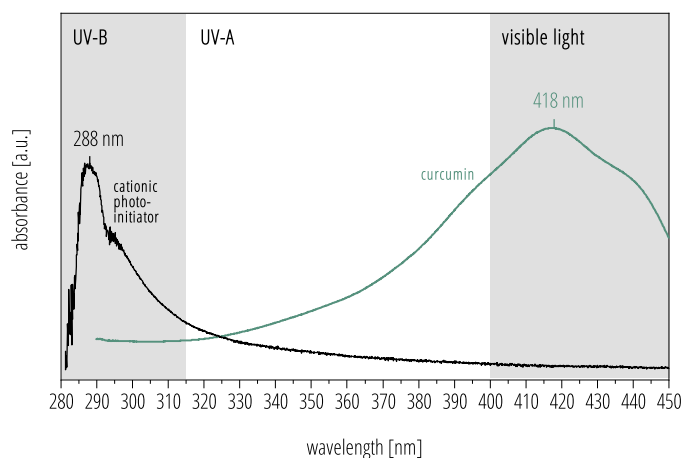


Figure B.1: UV-VIS spectra for the cationic photoinitiator and curcumin in acetonitrile.

B.2.4 Preliminary suitability assessment of curcumin-sensitized solar curing

To illustrate the colour changes during the solar radiation sensitized by curcumin, photos during the polymerization and after storage are shown in Figure B.2a). Application on a wood specimen demonstrates that solar curing in the presence of an agent to reduce oxygen inhibition allows to form finishes with a similar appearance to what is obtained by UV radiation (Figure B.2b)). As discussed in Section 3.3.8, also similar curing times can be achieved depending on the temperature and solar irradiation.

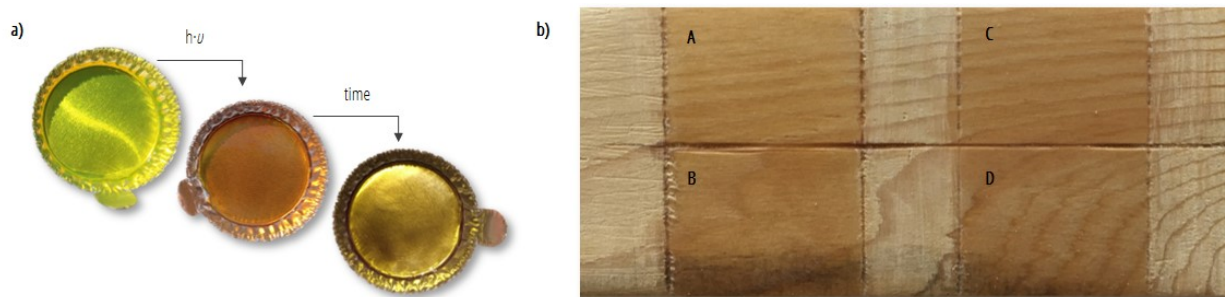


Figure B.2: a) Colour change in the epoxy resin with 0.2 wt% curcumin due to the formation of a exciplex with the photoinitiator and subsequent bleaching with time. b) Illustration of solar cured (A and B) versus UV-cured (C and D) epoxy resin coated on a cedar specimen for 1 coat (bottom) and 2 coats (top). In all cases, the epoxy resin with the centre point formulation was used. For solar curing, the formulation with added EDTA was used to avoid issues of oxygen inhibition.

B.2.5 Hot and cold check resistance

As can be seen in Figure B.3, the boiled linseed oil coated poplar specimen showed surface "bleeding", resulting from uncured resin being expelled to the surface upon dimensional changes during the hot and cold check test. Visual observation did not show major changes in the epoxy coated wood specimen. However, SEM analysis showed that surface roughness slightly increased and is best seen at the edge of the sample with less coating protection to counteract grain raising due to uptake of moisture and dimensional changes in the wood substrate.

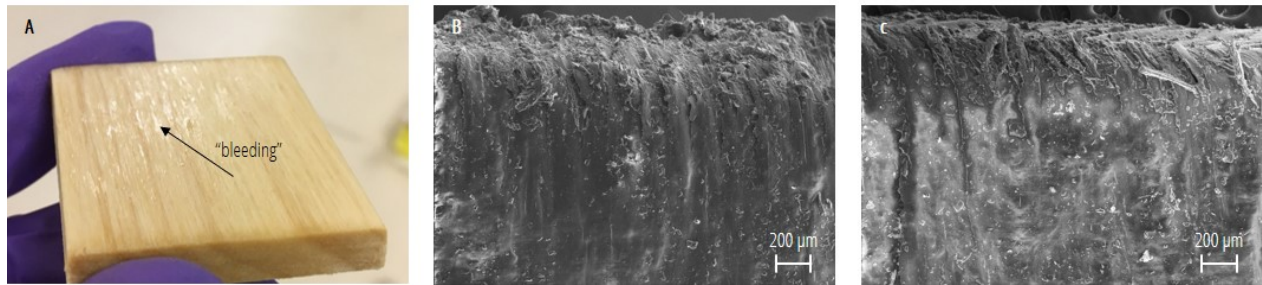


Figure B.3: **A** Illustration of surface "bleeding" through the expulsion of uncured boiled linseed oil from lower depths in the substrate upon artificial aging during the hot and cold check. **B** SEM image (without carbon coating) of the poplar specimen coated with the UV-curable epoxy resin (2 coats). The wood substrate is not well visible due to the surface layer formation. **C** Same as in B but after the hot and cold check test. No bleeding as for the drying oil sample was visually observed but the surface roughness still increased, which was most prevalent at the wood sample's edge, where grain raising was most dominant.

B.2.6 Effect of household chemicals

The specimens were only visually assessed for discoloration and erosion. The results are summarized in Table B.3. Mustard caused significant staining in all cases. The effects of coffee and grape juice were strongest at 16 h and left particular strong stains on the boiled linseed oil films.

Due to the transparency of the films, visualization of the effects of water and acetone were difficult. Overall, surface roughness appeared to be increased in the epoxy coated wood specimen.

As discussed in Section 3.3.5, the epoxy coatings resulted in the deposition of a top coat on the substrate surface (in particular with 2 coats), whereas boiled linseed oil kept penetrating during the much slower polymerization without building up a film at the wood surface. Accordingly, the specimen with the epoxy coating had a shiny surface, much more like a lacquer. Therefore, direct comparison of performance in this test is difficult. Rather, the results confirm that film formation as opposed to penetration of the wood substrate in case of the epoxy resin require for better control of applied amount and timing of the UV-curing to achieve a similar type of wood finish as with traditional linseed oil.

Table B.3: Test report for the resistance of spruce specimen with treatments of cured boiled linseed oil and epoxy (2 coats) to household chemicals. Rating was assessed on a 5-point rating scale: 5=no change, 4=minor change, 3=moderate change (visible from several viewing directions), 2=significant change in colour or gloss, slight change of structure, 1=strong change.

staining agent	coating	contact time		
		15 min	1 h	16 h
distilled water	boiled linseed oil	5	5	5
	epoxy	4	4	3
acetone	boiled linseed oil	5	5	5
	epoxy	4	4	4
mustard	boiled linseed oil	2	1	1
	epoxy	2	1	1
coffee	boiled linseed oil	3	2	1
	epoxy	4	3	2
grape juice	boiled linseed oil	3	2	1
	epoxy	4	3	2

Interestingly though, over 6 months of storage in the dark at ambient temperature, significant yellowing in the (control) samples was observed for the boiled linseed oil treated wood samples only (Figure B.4). This behaviour related to residual unsaturation is well-known for drying oils and oil-based paints upon aging [36, 39] (see Section 1.1.1.2).

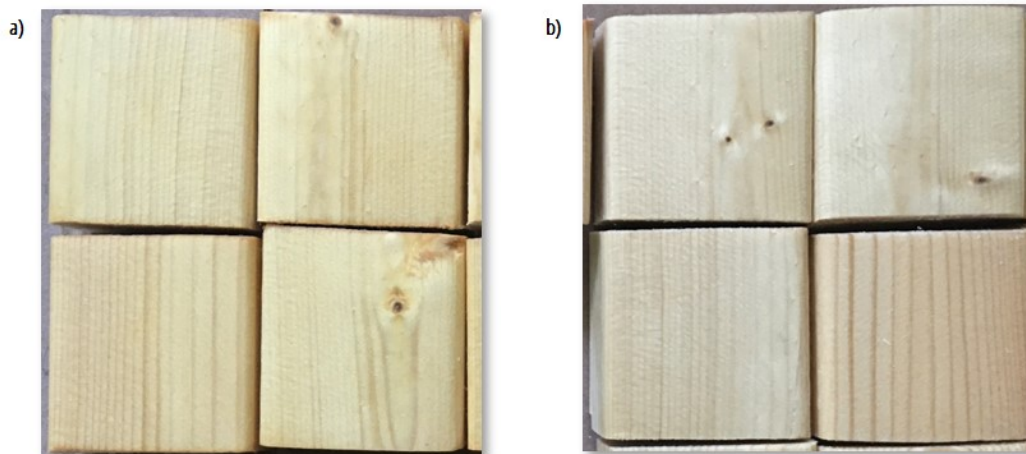


Figure B.4: Control specimen coated with two coats of **a)** boiled linseed and **b)** UV-cured epoxy (centre point formulation) after 6 months of storage in the dark at ambient temperature. The samples with the boiled linseed oil finish underwent apparent yellowing in contrast to the more colour-stable epoxy films.

B.2.7 Statistics

B.2.7.1 Data transformation

Data transformation was only performed for the final degree of epoxy conversion as the data were negatively skewed. Therefore reverse score transformation and subsequent square root transformation was performed.

B.2.7.2 Model accuracy and selection

The test statistics for fitting linear, linear+squares, linear+interactions, and full quadratic models for the rate constant k (first-order) and final conversion are listed in Table B.4 and Table B.5, respectively.

Table B.4: Test statistics for the different models to fit the rate constant k (first-order reaction).

model	df	root mean square of error	R^2	adj. R^2	residual sums of squares	predicted R^2	remarks
linear	9	0.0123	0.94082	0.92767	0.00136	0.88455	
linear + squares	7	0.0093	0.97369	0.95865	6.05125E-4	0.90123	suggested
linear + interactions	8	0.01287	0.94241	0.92081	0.00132	0.87062	
full quadratic	6	0.00974	0.97527	0.95466	5.68704E-4	0.86629	overfitted

Table B.5: Test statistics for the different models to fit the final conversion after reverse score and square root transformation to correct for negative skew.

model	df	root mean square of error	R^2	adj. R^2	residual sums of squares	predicted R^2	remarks
linear	9	0.06187	0.69666	0.62925	0.03446	0.50742	suggested
linear + squares	7	0.0647	0.74201	0.59458	0.0293	0.12843	likely overfitted
linear + interactions	8	0.0621	0.72842	0.62657	0.03085	0.28134	likely overfitted
full quadratic	6	0.06544	0.77376	0.58523	0.0257	-0.19982	likely overfitted

The test statistics for fitting linear, linear+squares, linear+interactions, and full quadratic models for the T_g are listed in Table B.6.

Table B.6: Test statistics for the different models to fit the T_g .

model	df	root mean square of error	R^2	adj. R^2	residual sums of squares	predicted R^2	remarks
linear	9	8.28022	0.80761	0.76485	617.0584	0.69634	
linear + squares	7	4.75802	0.95059	0.92236	158.471	0.78221	suggested
linear + interactions	8	8.76055	0.80857	0.73678	613.97837	0.47882	overfitted
full quadratic	6	5.08906	0.95155	0.91118	155.39098	0.68501	

The test statistics for lack of fit tests for the rate constant k (first-order) and final conversion are listed in Table B.7 and Table B.8, respectively.

Table B.7: Lack of fit test for the modelling the rate constant k (first-order).

model	df	sum of squares	mean square	F value	Prob>F	remarks
Linear	6	0.00119	1.98912E-4	3.56408	0.16215	ns
linear + squares	4	4.37695E-4	1.09424E-4	1.96064	0.30345	ns
linear + interactions	5	0.00116	2.31411E-4	4.14638	0.13564	ns
full quadratic	3	4.01273E-4	1.33758E-4	2.39665	0.24581	ns

Table B.8: Lack of fit test for the modelling the final conversion after reverse score and square root transformation to correct for negative skew.

model	df	sum of squares	mean square	F value	Prob>F	remarks
Linear	6	0.03153	0.00525	5.38115	0.09772	ns
linear + squares	4	0.02638	0.00659	6.75298	0.07427	ns
linear + interactions	5	0.02792	0.00558	5.71857	0.09101	ns
full quadratic	3	0.02277	0.00759	7.77262	0.06305	ns

Table B.9: Lack of fit test for the modelling the T_g .

model	df	sum of squares	mean square	F value	Prob>F	remarks
Linear	6	608.47132	101.41189	35.42949	0.00706	**
linear + squares	4	149.88393	37.47098	13.09095	0.03051	*
linear + interactions	5	605.3913	121.07826	42.30018	0.00555	**
full quadratic	3	146.8039	48.93463	17.09591	0.02168	*

B.2.7.3 Regression coefficients and derived models

An often cited publication by Joglekar and May [167], suggests a minimum R^2 of 0.80 as an indication for a good fit of a model. In addition to that, non-significance for the lack-of-fit test ($\alpha = 0.05$) and least discrepancy between R^2 and predicted R^2 (avoid overfitting by reducing the number of terms added to the model) was considered to chose the "best" model.

The rate constant k (first-order reaction) was used to investigate the polymerization rate. The data was fitted with a linear model with squares (adj. $R^2 = 0.96$) as follows:

$$Y = 0.12 - 0.02 \cdot X_1 + 0.05 \cdot X_2 + 0.01 \cdot X_1^2 - 0.003 \cdot X_2^2 \quad (\text{B.1})$$

with X_1 and X_2 representing the coded values for the ELOME:ELO ratio and photoinitiator concentration, respectively (see Table 3.1 for the parameters and levels). The coded coefficients and results of the ANOVA can be found in Table B.10 and Table B.11, respectively.

Table B.10: Coded coefficients for the linear model with squares to fit the data of the rate constant k .

linear with interactions	value	standard error
(Intercept)	0.11706	0.00465
ELOME content	-0.02018	0.00329
photoinitiator	0.04793	0.00329
ELOME content*ELOME content	0.00949	0.00368
photoinitiator*photoinitiator	-0.00329	0.00368

Table B.11: ANOVA for the linear model to fit the rate constant k (first-order).

	<i>df</i>	sum of squares	mean square	<i>F</i> value	Prob> <i>F</i>	remarks
ELOME content	1	0.00326	0.00326	58.37756	0.00466	**
photoinitiator (PI) concentration	1	0.01838	0.01838	329.31186	3.65033E-4	***
ELOME content*ELOME content	1	6.86479E-4	6.86479E-4	12.30023	0.03928	*
PI concentration*PI concentration	1	6.93004E-5	6.93004E-5	1.24171	0.34638	<i>ns</i>
error	7	6.05125E-4	8.64465E-5			
lack of fit	4	4.37695E-4	1.09424E-4	1.96064	0.30345	<i>ns</i>
pure error	3	1.67431E-4	5.58102E-5			
total	18	0.0236				

The final conversion (Y) was fitted with a linear model as follows:

$$Y' = \sqrt{(0.95 - Y)} = 0.22 - 0.1 \cdot X_1 - 0.03 \cdot X_2 \quad (\text{B.2})$$

The coded coefficients and results of the ANOVA for the regression coefficients can be found in Table B.12 and Table B.13, respectively.

Table B.12: Coded coefficients for the linear model with squares to fit the final conversion data.

linear with interactions	value	standard error
(Intercept)	0.21893	0.01786
ELOME content	-0.09573	0.02188
photoinitiator	-0.02696	0.02188

Table B.13: ANOVA for the linear model to fit the final conversion after reverse score and square root transformation.

	<i>df</i>	sum of squares	mean square	<i>F</i> value	Prob> <i>F</i>	remarks
ELOME content	1	0.07332	0.07332	75.08408	0.00323	**
photoinitiator concentration	1	0.00582	0.00582	5.95697	0.09244	<i>ns</i>
error	9	0.03446	0.00383			
lack of fit	6	0.03153	0.00525	5.38115	0.09772	<i>ns</i>
pure error	3	0.00293	9.76445E-4			
total	20	0.14804				

The dependence of the T_g on the ELOME:ELO ratio and the photoinitiator concentration could be fitted with a linear model with squares:

$$Y = -8.3 - 18 \cdot X_1 - 0.28 \cdot X_2 - 8.4 \cdot X_1^2 - 2.3 \cdot X_2^2 \quad (\text{B.3})$$

The coded coefficients and results of the ANOVA for the regression coefficients can be found in Table B.14 and Table B.15, respectively.

Table B.14: Coded coefficients for the linear model with squares to fit the T_g data.

linear with interactions	value	standard error
(Intercept)	-8.3425	2.37901
ELOME content	-17.99161	1.68221
photoinitiator	-0.27625	1.68221
ELOME content*ELOME content	-8.44062	1.88077
photoinitiator*photoinitiator	-2.31562	1.88077

Table B.15: ANOVA for the linear model with squares to fit the T_g .

	<i>df</i>	sum of squares	mean square	<i>F</i> value	Prob> <i>F</i>	remarks
ELOME content	1	2589.58636	2589.58636	904.70376	8.07208E-5	***
photoinitiator (PI) concentration	1	0.61051	0.61051	0.21329	0.67563	<i>ns</i>
ELOME content*ELOME content	1	424.26985	424.26985	148.22388	0.00119	**
PI concentration*PI concentration	1	34.31754	34.31754	11.98926	0.04056	*
error	7	158.471	22.63871			
lack of fit	4	149.88393	37.47098	13.09095	0.03051	*
pure error	3	8.58707	2.86236			
total	18	3365.72627				

B.2.7.4 Diagnostic plots

Linearity in the normal plots of residuals and random scattering of the residuals was considered reasonable, but lowest performance for the rate constant k . Diagnostic plots for the regression analysis of the rate constant k , final conversion, and T_g are shown in Figure B.5, Figure B.6, and Figure B.7, respectively.

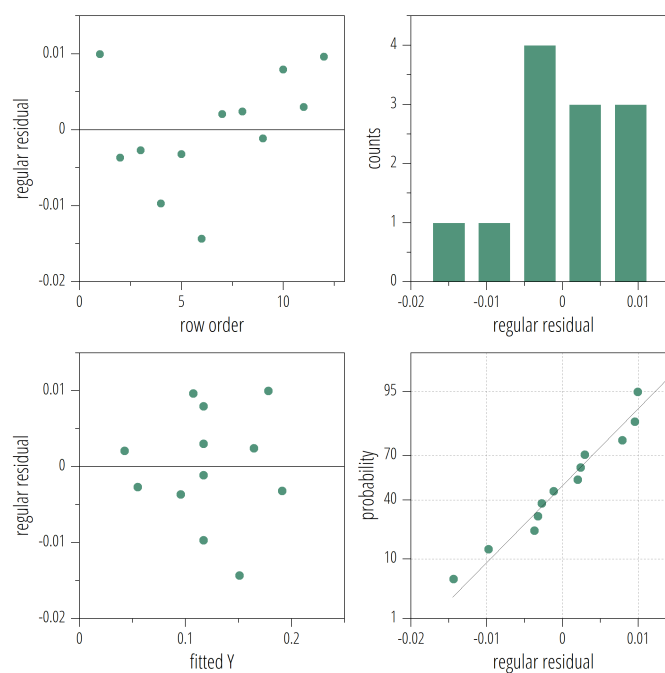


Figure B.5: Diagnostic plots for the regression analysis of the rate constant k .

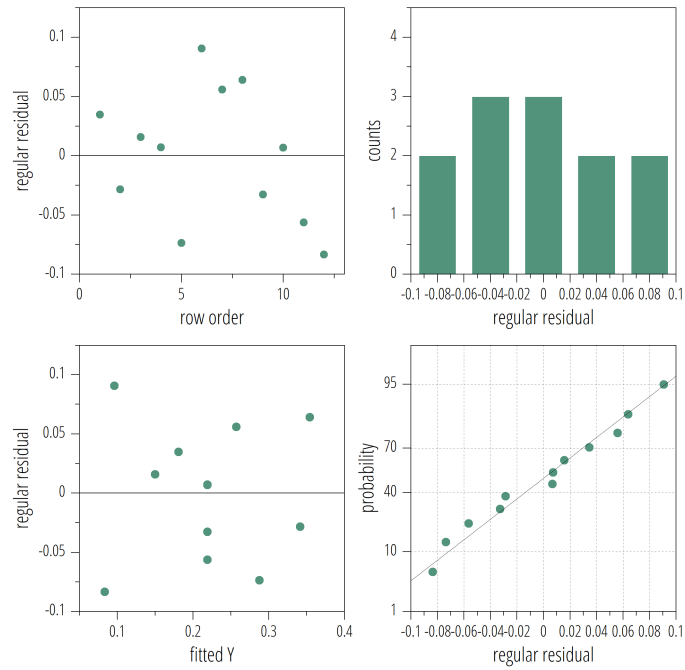


Figure B.6: Diagnostic plots for the regression analysis of the final conversion after reverse score and square root transformation.

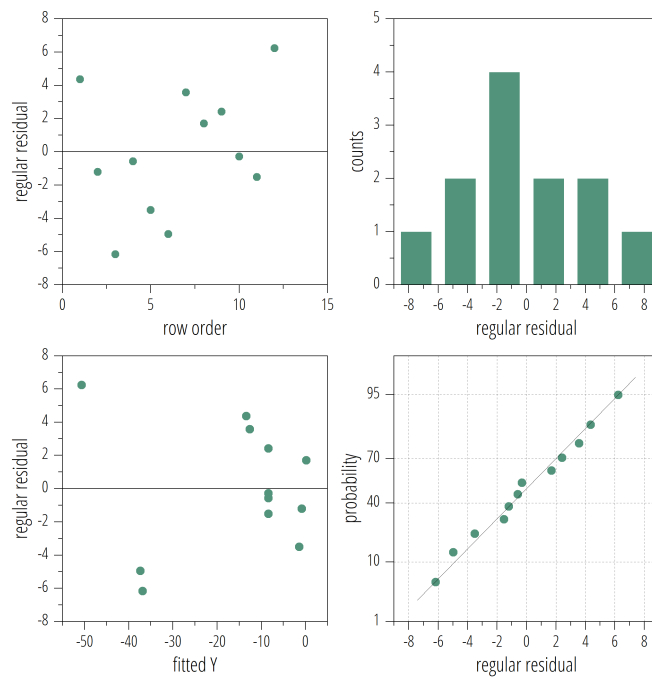


Figure B.7: Diagnostic plots for the regression analysis of the T_g .

B.2.7.5 Pairwise comparison of means

Bonferroni pairwise comparison of means was used after confirming that population variances are not significantly different (Levene's test).

TABER abrasion resistance The test statistics for the total wear indices is listed in Table B.16

Table B.16: Bonferroni test statistics for the pairwise comparison of the mean total wear index ($n = 3$, $\alpha = 0.05$) after 400 cycles (400x) and 1000 cycles (1000x) for birch specimen coated with 2 coats (2x) of boiled linseed oil (BL) and the epoxy resin (E), for which specimen with 1 coat (1x) and 2 coats (2x) were prepared. Sig equals 1 indicates that the difference of the means is significant at the 0.05 level. SEM stands for the standard error of the mean.

	MeanDiff	SEM	q Value	Prob	Alpha	Sig	LCL	UCL
400x BL2x:400x E2x	81.20833	10.50711	10.93031	2.47385E-5	0.05	1	46.74572	115.67095
400x BL2x:400x E1x	63.5	11.23257	7.99484	6.83288E-4	0.05	1	26.65792	100.34208
400x E2x:400x E1x	-17.70833	10.50711	2.38347	0.56156	0.05	0	-52.17095	16.75428
400x BL2x:1000x BL2x	5.28333	11.23257	0.66519	0.9965	0.05	0	-31.55875	42.12542
400x E2x:1000x BL2x	-75.925	10.50711	10.2192	5.2708E-5	0.05	1	-110.38761	-41.46239
400x E1x:1000x BL2x	-58.21667	11.23257	7.32965	0.00156	0.05	1	-95.05875	-21.37458
400x BL2x:1000x E2x	39.28333	10.50711	5.28738	0.02168	0.05	1	4.82072	73.74595
400x E2x:1000x E2x	-41.925	9.72769	6.09507	0.00757	0.05	1	-73.83118	-10.01882
400x E1x:1000x E2x	-24.21667	10.50711	3.25946	0.25475	0.05	0	-58.67928	10.24595
1000x BL2x:1000x E2x	34	10.50711	4.57626	0.05411	0.05	0	-0.46261	68.46261
400x BL2x:1000x E1x	15.45	11.23257	1.9452	0.74019	0.05	0	-21.39208	52.29208
400x E2x:1000x E1x	-65.75833	10.50711	8.8508	2.45978E-4	0.05	1	-100.22095	-31.29572
400x E1x:1000x E1x	-48.05	11.23257	6.04964	0.00803	0.05	1	-84.89208	-11.20792
1000 BL2x:1000x E1x	10.16667	11.23257	1.28001	0.93884	0.05	0	-26.67542	47.00875
1000x E2x:1000x E1x	-23.83333	10.50711	3.20787	0.26879	0.05	0	-58.29595	10.62928

Preliminary suitability assessment of curcumin-sensitized solar curing The test statistics for the comparison of curing time in dependence of the curcumin concentration can be found in Table B.17.

Table B.17: Bonferroni test statistics for the pairwise comparison of the curing time ($n = 4$, $\alpha = 0.05$) depending on the curcumin concentration. Sig equals 1 indicates that the difference of the means is significant at the 0.05 level. SEM stands for the standard error of the mean.

	MeanDiff	SEM	q Value	Prob	Alpha	Sig	LCL	UCL
low:medium	-1.847	0.44313	-4.16808	0.00726	0.05	1	-3.14684	-0.54716
low:high	-1.3525	0.44313	-3.05216	0.04123	0.05	1	-2.65234	-0.05266
medium:high	0.4945	0.44313	1.11593	0.88008	0.05	0	-0.80534	1.79434

Effects of film thickness and presence of the tertiary amine (EDTA) was also analyzed and results of the pairwise comparison of the mean curing time can be found in Table B.18.

Table B.18: Bonferroni test statistics for the pairwise comparison of the curing time ($n = 3$, $\alpha = 0.05$) depending on the film thickness (20 μm and 50 μm) and presence of EDTA. Sig equals 1 indicates that the difference of the means is significant at the 0.05 level. SEM stands for the standard error of the mean.

	MeanDiff	SEM	q Value	Prob	Alpha	Sig	LCL	UCL
50(-):20(-)	3.28833	0.27121	12.12485	4.04512E-4	0.05	1	2.14403	4.43264
50(-):50(EDTA)	-0.51667	0.27121	-1.90507	0.69067	0.05	0	-1.66097	0.62764
50(EDTA):20(-)	-3.805	0.29709	-12.8075	3.09867E-4	0.05	1	-5.05852	-2.55148
50(-):20(EDTA)	-0.10667	0.27121	-0.3933	1	0.05	0	-1.25097	1.03764
20(-):20(EDTA)	-3.395	0.29709	-11.42746	5.39161E-4	0.05	1	-4.64852	-2.14148
50(EDTA):20(EDTA)	0.41	0.29709	1.38005	1	0.05	0	-0.84352	1.66352

Appendix C

Appendix Chapter 4

C.1 Results and discussion

C.1.1 Prestudy: photopolymerization kinetics and oxygen inhibition

The films were peeled off the glass substrates after different number of passes under the UV source. ATR-FTIR spectra (settings as described in Section 4.2.2.2) were recorded at both the top and bottom side of the film (if strong enough to be peeled off), and compared to the spectra obtained from the uncured resin. To accommodate for the overlapping bands of the different types of terminal double bonds (geminal disubstituted alkene in the case of TMI *versus* the monosubstituted C=C double bond originating from the acrylated reactive diluent) as shown in Figure C.1, the spectra were transformed by calculating the 2nd derivative and applying a Norris filter using a gap-segment (GS) of 1-2 to obtain band separation. Band intensity was calculated by determining the band height. The OMNIC 8 software (Thermo Scientific) was used to for spectra transformation and analysis.

In Figure C.1, the FTIR spectra recorded for the isocyanate monomer and the reactive diluent (Genomer 1225) are shown. The following bands related to the different terminal double bonds for the evaluation of the curing progression, were identified: 1636 cm⁻¹ (ν_s (*cis* C=C)), 1620 cm⁻¹ (ν_s (*trans* C=C)), and 1408 cm⁻¹ (δ_s =CH₂).

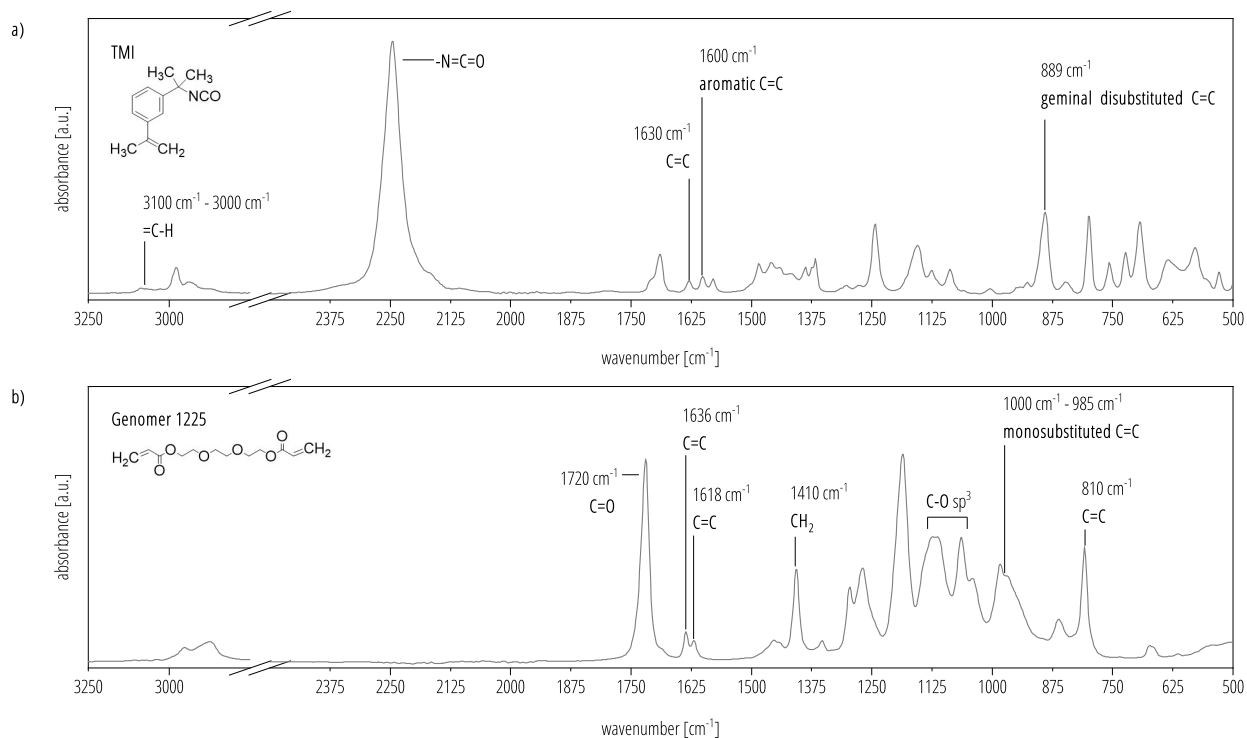


Figure C.1: Comparison of the IR-absorption by the different terminal double bonds present in **a)** the isocyanate monomer (TMI) and **b)** the reactive diluent Genomer 1225 obtained from ATR-FTIR analysis. The shift in wavenumber due to the different nature of the terminal C=C bonds (geminal disubstituted *versus* monosubstituted) is indicated, making monitoring of their conversion during the course of radical polymerization challenging due to band broadening.

Ensuring maximal curing of the coatings required 16 passes under the UV source. In Figure C.2a, the calculated conversions of the terminal double bonds upon polymerization (absorbance decrease in the 1637 cm⁻¹ band) are plotted against the number of passes under the UV source for the neat coating. Upon the first pass, the coatings were still liquid and therefore, only the top surface was analyzed. Between 2 and 4 passes, the surface solidified but was not yet tack-free and remained too weak to be peeled off at conversions of under 20%. Another 4 passes were required to reach almost 80% conversion and to render the films easily peelable. The polymerization rate levelled off before reaching almost 100% (after 12 passes). No apparent bands for the terminal double bonds could be detected in the ATR-FTIR spectra recorded on the top side (almost full conversion), whereas the bottom side seemed to have reached a slightly lower level (around 92%). A one-sided independent *t*-test confirmed that there was no statistically significant difference in the conversion between 12 passes to 16 passes at neither the top nor the bottom side of the films with $p = 0.42$ and $p = 0.34$, respectively. By applying 16 passes under the UV source, the sensitivity to small deviations in the curing conditions was considered to be reduced to an acceptable level and maximum conversion should be reached for all samples.

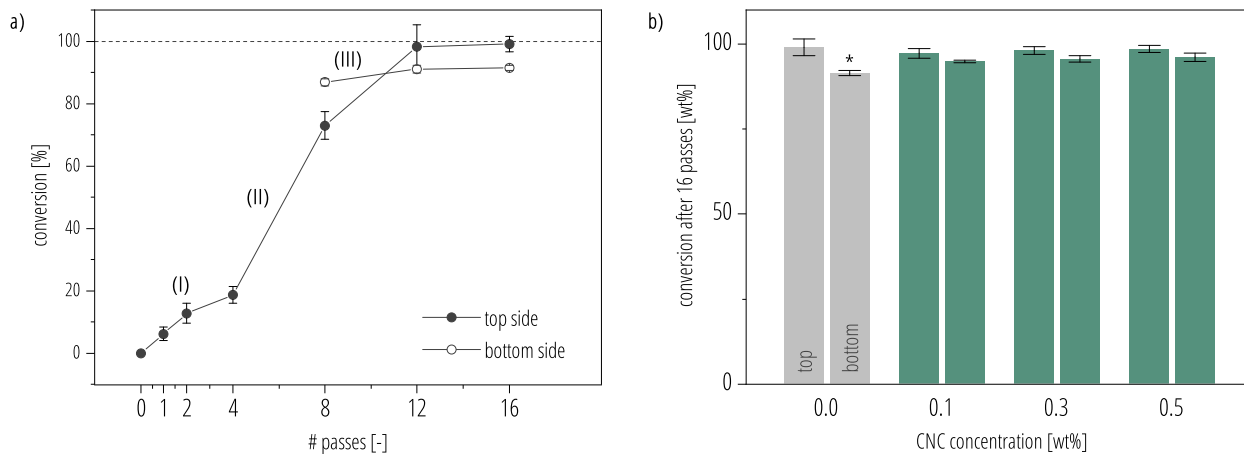


Figure C.2: **a)** Mean values of the calculated terminal C=C bond conversion of the neat coating based on the ATR-FTIR monitoring of the decrease in absorption at 1637 cm^{-1} with the standard deviation being represented as error bars for the independent experiments ($n = 3$). The theoretical phases of the kinetic profile, (I) autoacceleration, (II) constant reaction rate, and (III) autodeceleration, are indicated. Deviation from the expected photopolymerization rate increase during (I) are thought to be a result of post curing due to the time lag between UV exposure and ATR-FTIR analysis. **b)** Average conversion after 16 passes as a function of CNC concentration at the top and bottom side of the films. The error bars represent the standard deviation from independent experiments ($n = 3$). Only the bottom side of the neat polymer film was significantly different.

In Figure C.2a, the three theoretical phases of photopolymerization as described by Decker et al. [317] are indicated: (I) autoacceleration, (II) constant reaction rate (radical formation and propagation compensated by bimolecular termination reactions), and (III) autodeceleration (propagation also becomes diffusion-controlled). Upon initial photopolymerization, the polymeric radicals become more restricted in their mobility and termination through the dimerization of two radicals becomes diffusion-controlled. This results in the accumulation of radicals, and an according increment in the polymerization rate [317].

In the present case, the first phase does not represent an autoacceleration phase but shows an intermediate deceleration phase. It was assumed that this is a result of significant post curing of the coatings during the transfer from the UV unit onto the ATR-crystal and subsequent analysis, leading to a higher conversion than what would be measured if the analysis was performed online. As a result, it is not possible to derive the maximum polymerization rate ($R_{p,max}$) accurately. However, the results corroborate with the previously reported range of 10% to 30% conversion at the end of the autoacceleration phase (I) in most systems [318]. Decker et al. [317] also summarized two peculiarities related to the fast polymerization, which are the emergence of structural heterogeneities resulting from the formation of microgels and volume shrinkage effects on the kinetics. The latter is a result of the time lag between the conversion and shrinkage (change in intermolecular distance from van der Waals to covalent bond lengths), generating a temporary excess of free volume allowing for increased mobility of unreacted double bonds and subsequently higher conversion [317, 319].

Overall, the conversion of this model system was very slow. This can be traced back to prepolymer's structure since vinyl double bonds result in less reactive radical species compared to acrylates (see Section 1.1.2.1). Radical polymerization *via* the TMI moiety is also less favorable because of steric hindrance [320].

Furthermore, the low polymerization rate makes the system more susceptible to oxygen inhibition resulting in quenching of the activated photoinitiator and an additional decrease in the rate of radical propagation due to the formation of weak propagating radicals upon scavenging of triplet oxygen with carbon-based free radicals (see Section 1.1.2.3). This can result in diminished coating properties or even uncured liquid surfaces [321]. Differences between the surface chemistry at the top and bottom side of the films due to oxygen inhibition were investigated by ATR-FTIR and are illustrated in Figure C.3. One new band observed for the top side, corresponds to an alcohol -OH stretch (3600 cm^{-1} to 3200 cm^{-1}), which supports the suggestion that oxygen inhibition plays a role. Reduced intensity for the C-H sp^3 stretching vibration band between 3000 cm^{-1} and 2850 cm^{-1} compared to the bottom side of the film might also imply less cross-linking. While the intensity of the carbonyl band at 1720 cm^{-1} for the top side of the film is reduced, the band is also broadened. This could imply that the broadening of the carbonyl band (centred at about 1720 cm^{-1}) at the upper surface of the film due to potential O_2 inhibition, could mask the band used for monitoring the double bond conversion (1636 cm^{-1}). In that case, the observed higher conversion at the top side of the film would be an artifact. Monitoring the absorption at 1408 cm^{-1} ($\delta_s =\text{CH}_2$) revealed slightly reduced conversion at the top surface (data not shown). Thus, it would be plausible that in the presence of oxygen inhibition (top side), the photopolymerization was indeed impeded.

To test if the CNC nanocomposites behaved similarly to the neat polymer, normalized FTIR spectra were overlaid. However, no clear differences between the absorption spectra of the nanocomposites and neat polymer films after 16 passes could be observed. The conversion degree at the top side of the films was not significantly affected by the presence of CNC as indicated by ANOVA analysis, $F(3,8) = 1.89$ and $p = 0.21$ but in the presence of CNC, the conversion on the bottom sides was slightly increased (Figure C.2b).

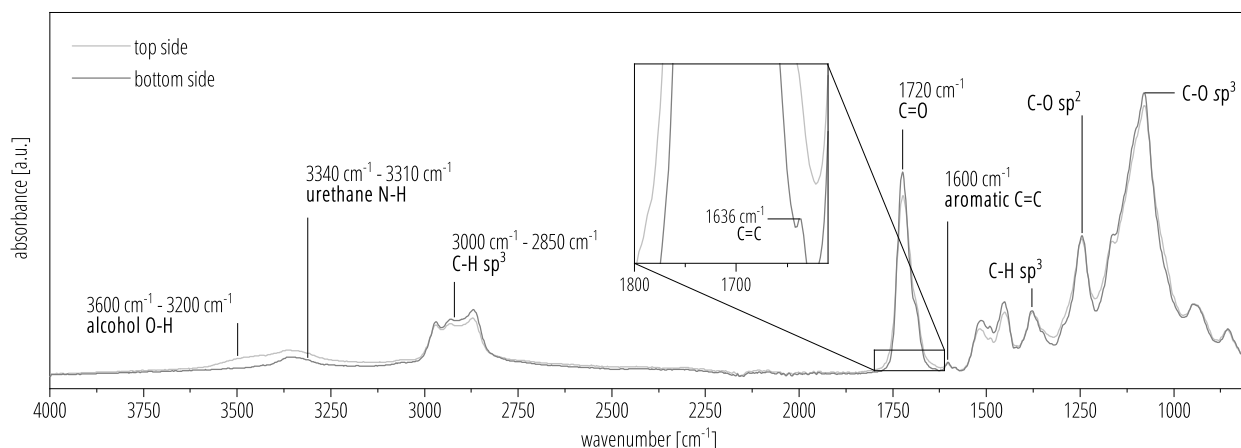


Figure C.3: ATR-FTIR spectra (representative curves) recorded on the top (light grey) and bottom side (dark grey) of the neat polymer coating (after 16 passes). Oxygen inhibition affecting mainly the top surface of the film, resulted in a broadening of the carbonyl band and appearance of alcoholic -OH functional groups.

C.1.2 CNC-matrix interaction

In a control experiment to test whether or not the byproducts in the prepolymer originating from the reaction of trace amounts of water and 1,3-propanediol account for the improvement in adhesion (see Section 4.3.3.4), the prepolymer was synthesized in the presence of the two trace compounds. Figure C.4 illustrates how this resulted in a turbid reaction mixture, which was not observed when reacting pure polyol with TMI.

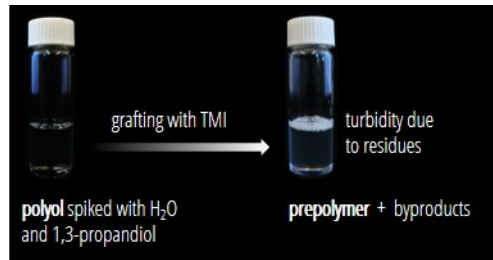


Figure C.4: Illustration of the turbid reaction mixture obtained when reacting polyol containing trace amounts of water and 1,3-propanediol at concentrations of 0.6 % and 0.8 %, respectively, with TMI to form the photocurable prepolymer.

C.1.3 Statistics

C.1.3.1 Levene's Test

A summary of the results from the Levene's tests are listed in Table C.1. A significant test result indicates unequal population variances and required a Welch correction for ANOVA analysis.

Table C.1: Summary of the Levene's test results to assess the equality of variances. In case of the adhesion strength, the results include the data from the control experiment.

Property	sample size (<i>n</i>)	<i>F</i> value	<i>p</i> value	significance
Conversion (top side)	3	1.89	0.21	<i>ns</i>
Conversion (bottom side)	3	1.24	0.36	<i>ns</i>
Modulated DSC	6	6.04	0.01	**
Abrasion resistance	3	3.35	0.08	<i>ns</i>
Pull-off adhesion strength	6	4.80	0.01	**
<i>Tensile properties</i>				
Young's modulus	6	3.72	0.03	*
Tensile strength	6	1.26	0.32	<i>ns</i>
% elongation at break	6	2.95	0.06	<i>ns</i>
Elastic strain	6	2.89	0.07	<i>ns</i>
Plastic strain	6	2.91	0.07	<i>ns</i>
Energy absorbed to break	6	1.53	0.25	<i>ns</i>

C.1.3.2 Pair-wise comparisons

A summary of the test results for the pair-wise comparisons after ANOVA analysis are listed in Table C.2. Additionally, the p -values for the Games-Howell *post hoc* test for comparing the adhesive strength of the control group and the nanocomposites (with increasing CNC concentration from 0.0 wt % to 0.5 wt % CNC), were as follows : 1.000, 0.008(**), 0.006(**), and 0.179.

Table C.2: Summary of the results for the pair-wise comparisons of the effect for different CNC loading levels (0.0 wt % to 0.5 wt %) on the properties, which were significantly influenced by the presence of CNC as revealed by ANOVA analysis. Statistically significant results are indicated with asterisks.

Property	Post hoc test		p value					
	pair-wise	com- parison	0.0:0.1	0.0:0.3	0.0:0.5	0.1:0.3	0.1:0.5	0.3:0.5
Conversion (bot- tom side)	Tukey		0.005 (**)	0.002 (**)	0.0001 (**)	0.784	0.381	0.869
Modulated DSC	Games-Howell		0.157	0.077	0.010 (*)	0.003 (**)	0.003 (**)	0.128
Pull-off adhesion strength	Games-Howell		0.008 (**)	0.009 (**)	0.162	0.175	0.991	0.179
Tensile strength	Tukey		0.486	0.988	0.268	0.678	0.019 (*)	0.159
% elongation at break	Tukey		0.951	0.022 (*)	0.025 (*)	0.063	0.068	1.000
Plastic strain	Tukey		0.922	0.020 (*)	0.021 (*)	0.068	0.070	1.000
Energy absorbed to break	Tukey		0.730	0.014 (*)	0.024 (*)	0.106	0.164	0.994